Contribution to the development of a high-power low-voltage DC-DC converter for proton exchange membrane electrolyzer applications

Burin Yodwong

Ecole Doctorale Informatique Automatique Électronique-Électrotechnique Mathématiques
Laboratoire GREEN

King Mongkut's University of Technology North Bangkok

Thèse

Présentée et soutenue publiquement pour l'obtention du titre de

DOCTEUR DE l'UNIVERSITE DE LORRAINE

Mention : GÉNIE ÉLECTRIQUE

par **Burin YODWONG**

Sous la direction de Prof.Dr.Melika HINAJE

Contribution to the development of a high-power low-voltage DC-DC converter for proton exchange membrane electrolyzer applications

10th June 2022

Membres du jury :

Directeur de thèse :	**Prof. Dr. Melika HINAJE**	**Université de Lorraine, GREEN**
Président de jury :	**Prof. Dr. Hamid GUALOUS**	**Université de Caen Normandie, LUSAC**
Rapporteurs :	**Prof. Dr. Christophe TURPIN**	**LAPLACE**
	Prof. Dr. Yuttana KUMSUWAN	**Chiang Mai University, Thailand**
Examinateurs :	**Assoc. Prof. Dr. Damien GUILBERT**	**Université de Lorraine, GREEN (Co-directeur de thèse)**
	Prof. Dr. Matheepot PHATTANASAK	**King Mongkut's University of Technology North Bangkok, Thailand (Co-directeur de thèse)**
	Asst. Prof. Dr. Wattana KAEWMANEE	**King Mongkut's University of Technology North Bangkok, Thailand**
	Assoc. Prof. Napat WATJANATEPIN	**Rajamangala University of Technology Suvarnabhumi, Thailand**

Abstract

This Ph.D. work has been carried out within the framework of a cotutelle agreement between the Group of Research in Electrical Engineering of Nancy (GREEN), Université de Lorraine, IUT de Longwy section, France, and Renewable Energy Research Centre (RERC), Thai French innovation institute, Faculty of technical education, King Mongkut's University of Technology North Bangkok, Thailand. Besides, this Ph.D. comes within the scope of the 2019 Franco-Thai Scholarship Program supported by the French Embassy in Thailand and Campus France. Also, Dr. Surin Tohtubtiang distinguished Member of the KMUTNB council committee who supported the finances in Thailand. The major goal of this Ph.D. work is to develop a high-power low voltage step-down DC-DC converter and a non-linear control algorithm for PEM electrolyzer applications.

First, the electrolyzer technologies and power electronics topologies for hydrogen production systems relying on water electrolysis process have been thoroughly studied. Besides, a literature review of PEM electrolyzer models has been carried out to investigate static and dynamic behaviors. In this work, PEM electrolyzer technology has been considered due to their main advantages such as high current densities, fast dynamic responses, and large partial load range. Hence, this technology is perfectly fit to be coupled with renewable energy sources. However, PEM electrolyzers are low-voltage high-current electrochemical loads requiring the use of a suitable step-down DC-DC converter. After reviewing the most used topologies and topologies candidates for this application, a three-level interleaved buck converter (TLIBC) has been chosen because of their main benefits. Indeed, the main features of the TLIBC are low output current ripple, low step-down conversion ratio gain, and availability in case of electrical failures.

Second, a PEM electrolyzer emulator has been designed and implemented based on the static and dynamic behavior of a commercial PEM electrolyzer. This emulator has been used with the TLIBC to avoid critical operating conditions that may damage a real electrolyzer during experimental tests.

Finally, to ensure excellent performance of the system, a non-linear improved sliding-mode control (SMC) has been designed for the TLIBC. The choice of this controller has been motivated by its major benefits such as fast dynamic response and robustness against parameters uncertainties. Then, the TLIBC driven by the improved SMC has been tested in simulation and experimentally. Both obtained simulation and experimental results have demonstrated the robustness of proposed control laws in managing the output inductor current (i.e., hydrogen flow rate) that precisely follows its reference with very low current ripple, while guaranteeing the balance of both input capacitors voltages with respect to the dynamic operating condition and uncertainty parameters.

Résumé

Cette thèse de doctorat a été réalisée dans le cadre d'un accord de cotutelle entre l'Université de Lorraine, IUT de Longwy, laboratoire GREEN et Renewable Energy Research Centre (RERC), King Mongkut's University of Technology North Bangkok, Thaïlande. Par ailleurs, cette thèse s'inscrit dans le cadre du programme de bourses Franco-Thaï 2019 soutenu par l'ambassade de France en Thaïlande et Campus France. L'objectif principal de cette thèse est de développer un convertisseur DC-DC dévolteur basse tension haute puissance et un algorithme de contrôle non linéaire pour des applications d'électrolyseurs PEM.

Tout d'abord, les technologies d'électrolyseurs et les topologies de convertisseurs DC-DC pour des systèmes de production d'hydrogène reposant sur le processus d'électrolyse de l'eau ont été étudiées avec attention. De plus, une étude bibliographique des modèles d'électrolyseurs PEM a été réalisée pour analyser les comportements statiques et dynamiques de ces derniers. Dans ce travail, la technologie d'électrolyseur PEM a été considérée en raison de ses avantages principaux tels que sa densité de courant élevée, sa réponse rapide aux sollicitations dynamiques, et sa large plage de fonctionnement. De là, cette technologie est particulièrement bien adaptée pour être couplée avec des sources d'énergies renouvelables. Cependant, les électrolyseurs peuvent être vus comme des charges électrochimiques basse tension fort courant exigeant en conséquence un convertisseur DC-DC dévolteur adapté. Après avoir effectué une analyse bibliographique sur les convertisseurs DC-DC les plus utilisés et les topologies candidates pour cette application, un convertisseur buck entrelacé trois niveaux (communément appelé *three-level interleaved buck converter (TLIBC)*) a été choisi dû à ses caractéristiques principales. En effet, cette topologie est caractérisée par une ondulation de courant de sortie faible, une conversion en tension faible, et une disponibilité en cas de défaillances électriques.

Dans un second temps, un émulateur d'électrolyseur PEM a été conçu et implémenté en s'appuyant sur les comportements statiques et dynamiques d'un électrolyseur PEM commercial. Cet émulateur a été utilisé avec le convertisseur buck entrelacé trois niveaux pour éviter toute condition de fonctionnement critique qui pourrait endommager un électrolyseur physique pendant les phases d'expérimentation.

Enfin, pour assurer d'excellentes performances du système, un contrôle non-linéaire mode glissant (communément appelé *sliding-mode control (SMC)*) amélioré a été conçu pour le convertisseur étudié. Le choix de ce contrôleur est motivé par ses bénéfices en termes de réponse dynamique et robustesse contre les incertitudes de paramètres du système. Ensuite, le convertisseur piloté par le contrôle non-linéaire mode glissant a été testé en simulation et expérimentalement. Les résultats obtenus à la fois en simulation et en pratique ont démontré la robustesse du contrôleur proposé dans la gestion du courant de sortie (i.e. réglage du débit d'hydrogène) qui suit avec précision une référence donnée avec une faible ondulation de courant de sortie, tout en garantissant l'équilibre des tensions des deux condensateurs d'entrée en conditions de fonctionnements dynamiques et d'incertitudes des paramètres.

Acknowledgment

This Ph.D. work has come within the scope of a co-mentorship agreement between the Group of Research in Electrical Engineering of Nancy (GREEN), Université de Lorraine, IUT de Longwy section, France, and Renewable Energy Research Centre (RERC), Thai French Innovation Institute (TFII), Faculty of technical education, King Mongkut's University of Technology North Bangkok (KMUTNB), Thailand under the direction and supervision by Professor Dr. Melika Hinaje, Professor Dr. Matheepot Phattanasak, Associate Professor Dr. Damien Guilbert and Assistant Professor Dr. Wattana Kaewmanee.

First and foremost, I would like to express my sincere gratitude to my supervisor from French side Professor Dr. Melika Hinaje for her advice and constant support professionally and educationally throughout my Ph.D. thesis. She is a dynamic and motivating supervisor. Moreover, she always answered my questions and provided me the excellent opportunity in my research works.

Second, I would like to provide my sincere appreciation to my supervisor from Thai side Professor Dr. Matheepot Phattanasak for his guidance and continuous assistance of my thesis work. He has always had an answer for me when I have a question of my research work. Furthermore, after fruitful discussions with him, I always got the excellent results of research and feel confident.

Third, I would like to express my heartfelt appreciation to my co-supervisor from French side Associate Professor Dr. Damien Guilbert for his valuable advice, extensive knowledge, ambition, motivation, and eagerness. He has a deep understanding of a wide range of research issues, and I really appreciated his assistance and helpful advice as I struggled in my thesis work. Besides, he is a model to me as lecturer and researcher. Moreover, thank to him, I had the opportunity to meet a lot of researchers in the fields of electrical engineering and automatic control during my stay in France, which had positive impacts on my thesis work and future work.

Fourth, my gratitude is also extended to my co-supervisor from Thai side Assistant Professor Dr. Wattana Kaewmanee for his guidance and constant support over the last seven years. He has inspired me since I finished my bachelor's degree and providing me the opportunity to do a research internship and study in France. Besides, he pushed me to moving out the comfort zone and trying to do new things.

Furthermore, I am sincerely thankful to the members of my Ph.D. defense committee and the progress thesis committee: Professor Dr. Hamid Gualous, Professor Dr. Yuttana Kumsuwan, Professor Dr. Christophe Turpin, Associate Professor Napat Watjanatepin, Professor Dr. Stéphane Rael, Professor Dr. Noureddine Takorabet, Professor Dr. Michel Zasadzinski, and Professor Dr. Gianpaolo Vitale for their perceptive and valuable suggestions to enhance the quality of my thesis dissertation.

Afterward, I would like to express my sincere gratefulness to all members of both laboratories: (GREEN in Nancy and IUT de Longwy section and RERC, TFII) who have engaged in this Thesis work in terms of administration or scientific.

Specifically, I would like to express my appreciativeness to Professor Dr. Bernard Davat, the former director of the GREEN, Professor Dr. Noureddine Takorabet, the current director of the GREEN, Assistant Professor Dr. Panarit Sethakul, the former director of TFII, and Professor Dr. Phatiphat Thounthong for their constant collaboration between both country and their helpful administrative support. Also, I would like to thank Ms. Sylvie Colinet, secretary of GREEN and Ms. Sukanjana Lekapat, for their valuable administrative assistance and support. I warmly thank Mr. Serge Merafina for many tricks and his experimental advice. Furthermore, I wish to express my appreciation to all my colleagues in both laboratory: Mr. Pongsiri Mungporn, Mr. Suwat Sikkabut, Mr. Amorn Bunseng, Professor Dr. Poom Kuman, Dr. Songklod Sriprang, Ms. Thanaporn Sommajcha, Ms. Anwida Teekasap, Ms. Kanokwan Jitngamkam, Ms. Yaowaret Maiket, Dr. Hugues Rafaralahy, Dr. Vittorio Guida, Dr. Ángel Hernández-Gómez, Dr. Rebah Maamouri, Dr. Mourad Rahim, Dr. Frank Gambou, Mr. Olivier Di Pillo, Mr. Nicolas Ponsart, Dr. Marouane Alma, Dr. Feriel Mustapha, Ms. Christelle Perrin-Starck, Mr. Sebastien Moneret, Mr. Fares Zamalkani, Ms. Marie-Francoise Fronieux, Ms. Marlene Baldassi, Ms. Virginie Avian, Ms. Célia Coquillard, Ms. Iryna Bevza, Mr. Mathieu Christen, and Mr. Sadick Abdi for their professional guidance, technical assistance and friendship. In addition, I also express appreciation to all my Thai friends in France who have always been supportive of me. Mr. Paisak Poolphaka, Ms. Benjamas Poolphaka, Ms. Apinya Siangsanoh, Ms. Akitna Phachop, Dr. Suphaporn Arunthanayothin and Ms. Kanokporn Nuantang.

Moreover, I would like to acknowledge French Embassy in Bangkok, Thailand, and Campus France who generously gave financial support during my Ph.D. program in France with the framework of 2019 Franco-Thai Scholarship Program. Also, I would like to thank Ms. Marie-Christine Marchal at Campus France Nancy, Ms. Wanpen Sirapat, and Ms. Salisa Limsakul at the French Embassy in Bangkok for their well-managed of my scholarship. In addition, I am sincerely grateful to Dr. Surin Tohtubtiang distinguished Member of the KMUTNB council committee who graciously supported me financially during my Ph.D. studies in Thailand.

Finally, from the bottom of my heart, I would like to send my heartfelt to my adoring grandparents (Mr. Chan Yodwong, Mrs. Por Yodwong, Mr. Inchan Kaewchan, and Mrs. Mine Kaewchan), parents (Mr. Niramit Juttupa Mrs. Pongsri Juttupa, Mr. Sirboonruang Yodwong, and Mrs. Bairin Yodwong), wife (Ms. Jirarat Surinta), sister (Ms. Salinrat Yodwong), brother-in-law (Mr. Arbit Nokhan), and niece (Ms. Sarinporn Yodwong), who are always there for me with their unending love and unwavering support. Without that love, this thesis work would not have been possible. Thank you all for the strength you gave me.

Contents

List of Tables

List of Figures

General Introduction

Nowadays, the action of human society to reduce the impact of climate change is critical by developing low-carbon energy sources. Low-carbon energy sources can play an important role in reducing greenhouse gas emissions to meet with the Paris agreement. The agreement sets a target of limiting global average temperature rises well below 2°C.

There are four main types of low-carbon energy sources: wind, solar, hydro, and nuclear energy to generate electricity. The first three energy are renewable energy sources (RES), which means that they are environmentally friendly. However, RESs have a strong intermittent characteristic depending strongly on weather conditions. Therefore, wind turbines and photovoltaic systems cannot generate electricity continuously. Hence, the nuclear energy is useful when RESs are unavailable and when the user needs more load demand.

On the other side, hydrogen is the simplest and most abundant element on Earth. However, it is usually combined with other elements and must be produced from them that contain it. For example, it can be merged with oxygen in water (H_2O) as well as carbon (e.g., oil, natural gas). Currently, 96% of global hydrogen production using the reformation method comes from fossil fuels such as natural gas, oil, and coal. Hydrogen generated by using fossil fuels features low gas purity and it is well-known as grey hydrogen due to the release of high amounts of greenhouse gases.

Furthermore, the water electrolysis process in global hydrogen production represents around 4%. To deal with the high usage and depletion of fossil fuels to meet the growing demand for hydrogen, the hydrogen production via water electrolysis process supplied by low-carbon energy sources (i.e., wind and solar energy) is regarded as a compelling and promising alternative. Besides, the water electrolysis process allows generating hydrogen with a high gas purity and may be ecologically friendly if the used power source features low-carbon emissions. In brief, by combining this process and low-carbon sources, green hydrogen can be obtained. For this reason, in this Ph.D. Thesis, the research works are focused on the use of the water electrolysis process.

The water electrolysis process consists of using electricity from low-carbon energy sources to split deionized water into oxygen and hydrogen. It is carried out by an electrolyzer. At the present time, there are four main types of electrolyzers: alkaline electrolyzer, proton exchange membrane (PEM) electrolyzer, solid oxide (SO) electrolyzer and more recently anion exchange membrane (AEM) electrolyzers have been introduced. Alkaline electrolyzer and PEM electrolyzer are commercially available, whereas SO electrolyzer and AE electrolyzer still remain in research and development.

On one hand, alkaline electrolyzer is the most mature and widespread used technology for large-scale systems. The strengths of this technology are cheap capital cost, high lifespan due to the catalyst material based on Nickel material, high energy efficiency, and coupling with RES. However, alkaline electrolyzers have several disadvantages such as low current density, flexibility, maintenance (due to the use of a liquid solution for the electrolyte).

On the other hand, PEM electrolyzers have been developed since the 1960s to cope with the issues of alkaline electrolyzers. This technology provides high current density, high partial load range (0-100%), fast response to dynamic operating conditions, making them suitable to be coupled with RESs. Nevertheless, the main drawback is the high capital cost due to the use of noble catalyst materials (e.g., iridium, platinum, and titanium). Given that the PEM electrolyzer has attracting features, this technology is considered in this Ph.D. Thesis.

In addition, power electronics is compulsory to interface RESs and electrolyzers and to meet several issues such as voltage conversion ratio, energy efficiency, reliability, and current ripple. Usually, RESs generate high DC voltage (around a hundred volts) while the electrolyzers require low DC voltage (around ten volts). For this reason, this Ph.D. Thesis aims at developing and realizing a step-down DC-DC converter with a suitable controller for PEM electrolyzer applications to overcome the above issues and increase the hydrogen production, reliability of the system, and life span of the PEM electrolyzer.

The PhD dissertation is divided into four chapters that are introduced briefly below:

In chapter 1, the current state-of-the-art of alkaline electrolyzer and PEM electrolyzer including their major features based on commercial electrolyzers available in the market is introduced. Moreover, the types of hydrogen production systems by using water electrolysis have been classified depending on the used low-carbon energy sources. Also, a literature review focused on power electronics (i.e., AC-DC converter and DC-DC converter) fit for electrolyzer applications is provided. Finally, a review of PEM electrolyzer modeling (i.e., resistive, static, and dynamic models) is given.

In chapter 2, a PEM electrolyzer emulator based on an equivalent electrical scheme is introduced. This emulator has been designed by considering the static and dynamic behavior of the real PEM electrolyzer. It is useful to test and evaluate the performance of power electronics and their control without using a real PEM electrolyzer that may be damaged during experiments. It has been realized and tested to validate its performance compared to the real PEM electrolyzer.

In chapter 3, the choice of the DC-DC converter investigated in this Ph.D. Thesis is discussed. The principle of operation of a three-level interleaved buck converter is described including the electrical scheme and operating waveforms. Afterward, the three-level interleaved buck converter has been designed and sized for the hydrogen production systems based on low-carbon energy sources. Besides, non-linear control algorithm and the mathematical modeling of the three-interleaved buck converter are detailed. At the end of this chapter, simulations have been carried out in MATLAB®—Simulink environment to evaluate the performance of the converter and proposed control laws.

In chapter 4, the performance validation of the three-level interleaved buck converter with the developed non-linear controller is presented. Subsequently, the realization of all elements in the studied converter have been detailed. Consequently, the experimental platform including the converter prototype in the studied hydrogen production system has been realized and described. Finally, the experimental results are given and analyzed to assess the effectiveness of the designed controller.

Chapter 1
State-of-the-art of Electrolyzer Systems: Technologies, Power Electronics, and Modeling

1.1 Introduction

Hydrogen production based on the water electrolysis process is an attractive approach to deal with global warming and the depletion of fossil resources [1]. In fact, the source of electricity used to supply the electrolyzer is the main variable to decreasing the carbon footprint [1]. For instance, the electricity from the grid is not a definitive choice for the electrolyzer since most electricity is generated by power plants based on fossil fuels, that emit greenhouse gases (i.e., coal and natural gas-fired power station). On the contrary, a low-carbon energy source such as renewable energy sources (RES) (e.g., wind, solar, and hydro energy) and nuclear energy provides a feasible pathway to fulfill the increasing demand for energy while also addressing the worldwide desire to reduce carbon emissions. Nevertheless, intermittent energy discontinuities are typically met when RESs are used [2], [3].

As a result, energy storage devices, such as hydrogen buffer storage, can be employed to face discontinuities issues. For example, produced and stored hydrogen can be used for a variety of purposes in hydrogen production processes based on RESs, as shown in Figure 1-1[4], [5].

- Energy storage: To deal with intermittent energy interruptions, surplus energy can be stored in hydrogen during periods of low energy demand and then utilized to balance the grid during periods of high energy demand. Consequently, hydrogen storage can maintain a balance between production and consumption.

- Transportation: hydrogen can be used for fuel cell electric vehicles. Hydrogen is stored in pressurized tanks (around 700 bar) and enables supplying PEM fuel cells. Some manufacturers have already developed fuel cell electric vehicles such as Hyundai (Nexo model and HDC-6 Neptune), Toyota (Mirai II model), and Honda (Clarity model).

- Industry: Hydrogen can be utilized in a wide range of industrial processes, including chemical (e.g., ammonia synthesis, methanol production), electronic (e.g., semiconductor manufacturing), and metallurgical (e.g., metalworking, carbon steels)

- Power-to-Gas: it consists of converting hydrogen into green methane gas that can be pumped into pipelines and subterranean facilities via the methanation process. It is an alternate storage capacity that may be used where and when it is needed, allowing the power system to be more flexible.

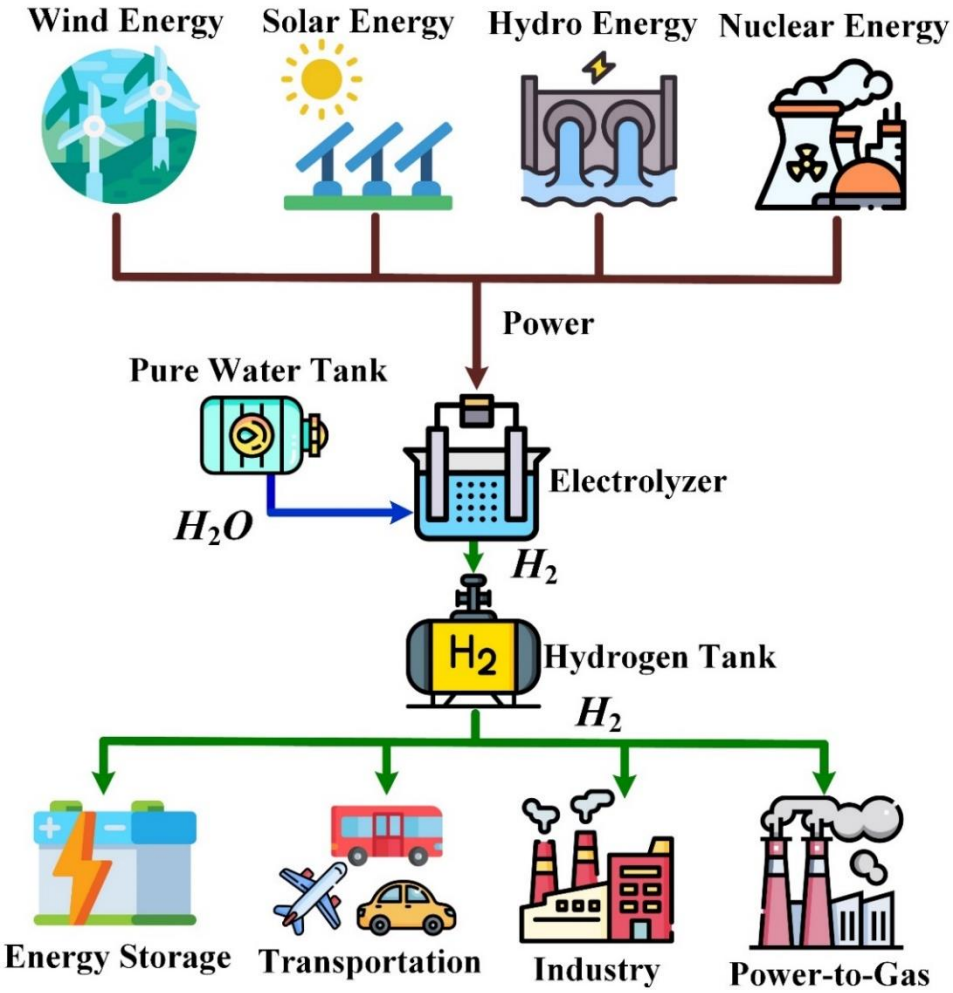

Figure 1-1: Overview of applications based on water electrolysis process supplied by low-carbon energy sources

The main objective of the first chapter is to present the state-of-the-art of electrolyzer technologies including the principle of operation and the most important features of alkaline and PEM electrolyzers. Afterward, different types of hydrogen production systems by using water electrolysis process have been analyzed depending on the used low-carbon energy sources. Furthermore, a literature survey dealing with power electronics (i.e., AC-DC converter and DC-DC converter) suitable for electrolyzer applications is given. Finally, modeling of electrolyzers (i.e., resistive, static, and dynamic models) is discussed with the goal to design an electrolyzer emulator.

1.2 Alkaline and PEM electrolyzer technologies

1.2.1. Alkaline electrolyzers

Alkaline electrolyzer is the most mature technology since the concept of operation was first established over 200 years ago [6], [7]. This technology has drawn a rising interest in the dissemination of large research projects (in the kilowatt scale) to overcome oil crisis appeared since the 1970s. Afterward, the power range has been increased to megawatts, permitting for the large-scale development of this technology for industrial applications [8], [9].

In alkaline electrolyzers, the chemical reaction takes place between two electrodes in an aqueous solution of pure water and potassium hydroxide (25-30% KOH). These electrodes are located between one or two diaphragms, that separate the produced gases from both electrodes while transporting hydroxide ions (OH^-) from the cathode to the anode. The chemical reactions of the alkaline water electrolysis process are given by the following expression [6]:

$$\text{Cathode} \qquad 2H_2O + 2e^- \rightarrow H_2 + 2OH^- \tag{1.1}$$

$$\text{Anode} \qquad 2OH^- \rightarrow 1/2\ O_2 + H_2O + 2e^- \tag{1.2}$$

$$\text{Global} \qquad 2H_2O \rightarrow 2H_2 + O_2 \tag{1.3}$$

From the chemical reaction (1.1), two water molecules are broken into hydrogen and hydroxide ions because of electrons at the cathode side. After that, from equation (1.2), hydroxide ions move into the electroyte and pass through the diaphragm to the anode side, where they interact with electrons to form oxygen. The fundamental operation of alkaline electrolyzer is depicted in Figure 1-2. On one hand, the key benefits of this technology are its maturity (well-established), cheap catalysts without no noble metals (e.g., nickel, cobalt, iron), excellent long-term stability (exchangeable electrolyte), and a high hydrogen generation rate of up to 3880 $Nm3.h^{-1}$ (atmospheric alkaline electrolyzer A3880 from NEL Company). On the other hand, this technology has a low current density (resulting in bulky electrolyzers) and restrictive partial load range (limiting its application in high-potential sectors like wind energy) [6], [10]. Thus, the remaining challenges for this technology include the increase in current densities and the expansion of partial load range. Recently, novel electrocatalysts have been used to minimize overpotentials and enhance the energy efficiency, and new diaphragms have been designed to extend partial load range while reducing ohmic losses in alkaline electrolyzers [2], [7].

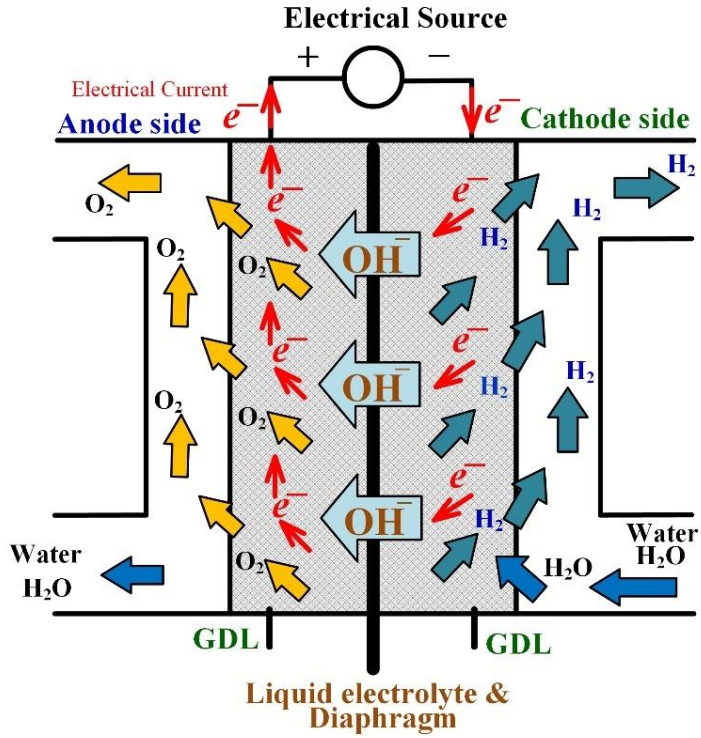

Figure 1-2: Principle of operation of alkaline electrolyzers.

Currently, alkaline electrolyzers are developed by a few manufacturers and a synthesis of the most significant specifications for different models is provided in Table 1-1. Normally, most manufacturers provide information such as hydrogen flow rate ($Nm3.h^{-1}$), specific energy consumption ($kWh.Nm^{-3}$), and partial load range (%). Potassium hydroxide is used as an electrolyte by all manufacturers, as seen in Table 1-1 (concentration between 25-30 %).

Table 1-1. Summary of leading manufacturers of alkaline electrolyzers.

Manufac-turer	**Series and Operating Pressure**	**Hydrogen flow rate ($Nm^3.h^{-1}$)[1]**	**Energy Consumption ($kWh.Nm^{-3}$ H_2)**	**Load Range (%)**	**Electrolyte**	**Power**
Hydrogenics [11]	HYSTAT / 10–25 bar	10–60 max.15/stack	4.9–5.4 (AC system all included)	40–100 (25–100 as an option)	H_2O + 30% wt. KOH	100 kVA–515 kVA
McPhy [12]	McLyzer / 10–30 bar	10–800	4.43–5.25 DC system at nominal flow rate	No details	No details	57 kW–4 MW
Teledyne Energy Systems [13]	TITAN HMXT 10 bar	2.8–11.2	No details	No details	No details	No details
Teledyne Energy Systems [14]	TITAN EL–N 10 bar	56–78	No details	No details	No details	No details
Wasserelektro-lyse Hydrotechnik [15]	EV 50–EV 150 Atmospheric 4 bar	75–220	5.28 depending on the operating temperature and the load	20–100	30% KOH	No details
NEL [16]	A Series 1–200 bar	50–3880	3.8–4.4	15–100	25% KOH Aqueous Solution	up to 2.2 MW
Nuberg PERIC [17]	ZDQ 5–600 15 bar to 20 bar	5–600	4.6 DC system	No details	30% KOH (by weight)	23.7kW – 2.74MW
Sagim S.A. [18]	M–series 7 bar	1.5–5	5	No details	No details	14–42k VA
Tianjin Mainland Hydrogen Equipment [19]	FDQ series 3 bar to 5 bar	2–1000	4.4–4.9 DC system	40–100	30% KOH	No details
Green Hydrogen [20]	A-Series 35 bar	2.7–8.1	4.69–4.82 system	No details	No details	125–450 kW

Generally, potassium hydroxide is often chosen over sodium hydroxide (NaOH) because it is more conductive [10]. This technology can operate at pressures ranging from 3 to 35 bars. The range of hydrogen flow rate is between 1.5 and 3880 $Nm^3.h^{-1}$, while the specific energy consumption is between 3.8 and 5.4 $kWh.Nm^{-3}$, depending on the power of the electrolyzer stack (from kW to MW). The partial load range is another essential characteristic given by the manufacturers. Indeed, the normal partial load range is 40-100 %; however, few

manufacturers (such as Hydrogenics and NEL) provide partial load ranges of 25-100 % and 15-100 %, respectively.

The manufacturers need to increase the use of alkaline electrolyzers in hydrogen production processes relying on a wind energy conversion system by extending the partial load range. Therefore, even at low wind speeds, alkaline electrolyzers can produce hydrogen using the electricity generated by the wind turbine [10].

The NEL company proposes alkaline electrolyzers with the best performance in terms of operating pressure (up to 200 bar), hydrogen flow rate (up to 3880 $Nm^3.h^{-1}$), specific energy consumption (3.8-4.4 $kWh.Nm^{-3}$), partial load range (15-100 %), and stack power (up to 2.2 MW), among all the manufacturers mentioned in Table 1-1. The A-series (as given in Table 1-1) can connect two 2.2 MW stacks in series to boost power and hydrogen flow rates while reducing specific energy consumption and providing a wide partial load range.

1.2.2. PEM electrolyzers

In the 1960s, General Electric (GE) Company has developed the first PEM electrolyzer. This technology aims to solve the limitations of alkaline electrolyzers technology introduced in the last subsection [3].

PEM electrolyzers are made up of a solid polymer electrolyte (SPE) that is in charge for transferring protons from the anode to the cathode, separating the produced gas at the anode and the cathode, and providing electrical insulation between the two electrodes while also acting as a reactant barrier against gas crossover. The chemical reactions of the PEM water electrolysis process are given as [1]:

$$\text{Anode} \qquad 2H_2O \rightarrow O_2 + 4H^+ + 4e^- \tag{1.4}$$

$$\text{Cathode} \qquad 4H^+ + 4e^- \rightarrow 2H_2 \tag{1.5}$$

$$\text{Global} \qquad 2H_2O \rightarrow 2H_2 + O_2 \tag{1.6}$$

As a result of the chemical reaction (1.4), the water molecules break at the anode side to produce oxygen and positively charged protons. Afterward, in the chemical reaction (1.5), protons travel through the SPE and merge with electrons to form hydrogen at the cathode side. The principle of operation of PEM electrolyzers is illustrated in Figure 1-3.

In comparison to alkaline technology, PEM electrolyzers feature higher current densities, a suitable partial load range (0-100%), a compact stack architecture, high-pressure operation, and quicker dynamic response times. At present, SPE is based on the DuPont Company's fluoropolymer (PFSA) Nafion membranes, that are most widely used for this technology due to their excellent thermal stability, thin membrane (25–254 µm), and proton conductivity (i.e., 0.1 $S.cm^{-1}$ at 100 °C). The membrane thickness is chosen to achieve a balance of predicted operating pressures across the membrane, minimal gas crossover, ohmic resistance, and mechanical resistance [21].

In [3], [22], it has been emphasized that a very thin membrane allows reducing ohmic losses and high-pressure operation. However, crossover currents increase when employing thin membranes [23], [24]. Therefore, the rise in faradaic losses is related to the increase in hydrogen and oxygen crossover. At low current densities, Faradaic losses due to Faraday's efficiency become especially important.

To deal with this issue, PEM electrolyzers must operate at medium and high current densities to decrease Faradaic losses.

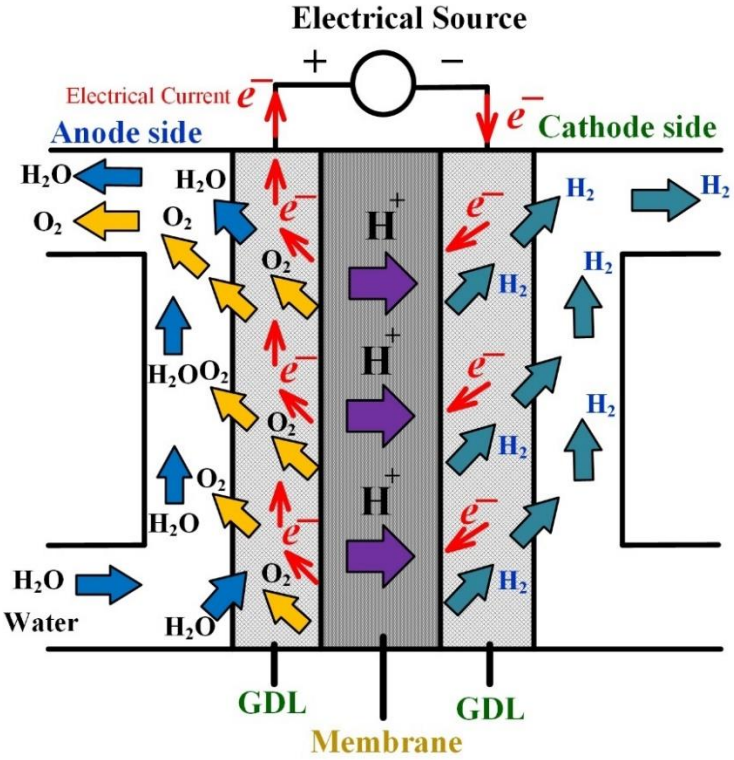

Figure 1-3: Principle of operation of PEM electrolyzers.

The main disadvantage of this technology is its high price since rare elements (e.g., iridium, platinum, and titanium) are required for both the anode and cathode catalysts. The remaining challenges rely on minimizing costs by replacing noble materials and high-cost components, improving long-term stability, and scaling up single cells (>1000 cm^2) [22].

Like alkaline electrolyzers, PEM electrolyzers are produced by a few manufacturers and an overview of the most important specification for various PEM electrolyzers models are given in Table 1-2. The same specifications data were collected to compare them to those for alkaline electrolyzers.

It can be seen from the data in Table 1-2 that only three manufacturers (NEL, GREEN Hydrogen, and Hydrogenics) manufacture both alkaline and electrolyzers, through with different specifications. The operating pressures of PEM electrolyzer range from 1 to 50 bar, that are lower than pressures reported for commercial alkaline electrolyzer (up to 200 bar).

The range of hydrogen flow rate is between 0.22 and 5000 $Nm^3.h^{-1}$, while the specific energy consumption is around 4.5 and 7.3 $kWh.Nm^{-3}(H_2)$, depending on the electrolyzer stack power (from kW to MW).

In the same way as alkaline electrolyzers, the NEL manufacturer develops PEM electrolyzers (e.g., M Series) with the best performance: operating pressure (up to 30 bar), hydrogen flow rate (up to 5000 $Nm^3.h^{-1}$), specific energy consumption (4.5 $kWh.Nm^{-3}$), partial load range (0-100 %), and stack power (up to 2 MW). Moreover, PEM electrolyzers have a partial load range of 0-100 %, making them suitable for hydrogen generation pathways based on wind turbines. They can generate hydrogen during operations at low wind speeds and especially absorb the energy in cases of fast intermittent energy discontinuities due to their fast dynamical response time and wide partial load range.

Nevertheless, in terms of specific energy consumption, PEM electrolyzers is less effective than alkaline electrolyzers.

In fact, a minimum specific energy consumption of 4.5 kWh.Nm^{-3} (against 3.8 kWh.Nm^{-3} for A-series from NEL). In conclusion, PEM electrolyzers must be enhanced further to compete with alkaline electrolyzers in terms of specific energy consumption and system size.

Table 1-2. Summary of leading manufacturers of PEM electrolyzers.

Manufacturer	Series and Operating Presure	Hydrogen Flow Rate ($Nm^3 \cdot h^{-1}$)	Energy Consumption ($kWh.Nm^{-3}$ H_2)	Load Range (%)	Electrolyte	Power
H-TEC Systems [25]	H-TEC Series-S 20 bar	0.22–1.1	No details	No details	SPE	1–5 kW
H-TEC Systems [26]	ME100/350 15-30 bar	15–46.3	4.9	32-100	SPE	225kW nominal
H-TEC Systems [27]	ME450/1400 15-30 bar	42-210	4.8	20-100	SPE	1MW nominal
Hydrogenics [28]	HyLYZER 0–7.9 bar	1–2	6.7	0–100	SPE	No details
ITM Power [29]	HGas1SP, HGas2SP, HGas3SP, HGasXMW 20 bar	11-36 kg/h 4050 kg/24h	No details	No details	SPE	700kW - 1.07MW
Siemens [30]	SILYZER 300	100-2000 kg/h	No details	0-100	SPE	>1MW
Green Hydrogen [31]	P–series 15–50 bar	1	No details	25–100	SPE	4.95 kW
Elogen [32]	-/ Min 2000	4.3 stack and 4.8 system	No details	No details	No details	No details
NEL [33]	S Series 13.8 bar	0.27-1.05	6.1 system	0-100	PEM Caustic Free	No details
NEL [34]	H Series 15 bar	2-6	6.8-7.3 system	0-100	PEM Caustic Free	No details
NEL [35]	C Series 30 bar	10-30	5.8-6.2 system	0-100	PEM Caustic Free	No details
NEL [36]	M Series Containerized 30 bar	264-492	4.5 Stack	0-100	PEM Caustic Free	No details
NEL [37]	M Series 30 bar	2000–5000	4.5 Stack	0–100	PEM Caustic Free	No details

1.2.3 State-of-the-art of the specifications for alkaline and PEM electrolyzers

A state-of-the-art of alkaline and PEM electrolyzers technologies have been assessed based on technical information collected from each electrolyzer manufacturer and is presented in Table 1-3. As can be seen from Table 1-3, PEM electrolyzers are competitive against alkaline electrolyzers since they have similar cell voltage efficiency and system energy efficiency. Furthermore, the energy efficiency of ancillaries such as power electronics, which are mostly based on AC-DC converters with thyristors and have high energy efficiency, is included in the system energy efficiency (around 97 %). Therefore, the challenging issue of both

technologies is to enhance energy efficiency. Additionally, power electronics (i.e., AC-DC and DC-DC converters), that can be based on thyristors, or a three-phase diode rectifier coupled to a DC chopper, are used to obtain the required DC current (about a thousand amps) and voltage (a hundred volts) from the electrolyzer. Finally, alkaline electrolyzers have a longer lifespan compared to PEM electrolyzers and the understanding of the interactions between power electronics and electrolyzers is a major issue particularly from the lifetime point of view.

Table 1-3. State-of-the-art of alkaline and PEM electrolyzers.

Specification	Alkaline Electrolyzer	PEM Electrolyzer
Cell temperature	60–80 °C	50–80 °C
Pressure	1–200 bar	0–50 bar
Current density	0.2–0.8 $A.cm^{-2}$	0.6–2.0 $A.cm^{-2}$
Cell voltage	1.5–2.5 V	1.8–2.2 V
Cell voltage efficiency (LHV[1], HHV[2])	52–85%	57–83%
Stack voltage	18–522 V	4–125 V
Stack Current	60–5250 A	9–75 A
System efficiency	Up to 76.5%	Up to 75%
Spec. energy consumption stack	3.8–5.4 $kWh.Nm^{-3}$	4.2–5.6 $kWh.Nm^{-3}$
Spec. energy consumption system	4.17–5.9 $kWh.Nm^{-3}$ H_2	4.53–7.3 $kWh.Nm^{-3}$ H_2
Load range	15–100%	0–100%
Cell area	≤ 4 m²	≤ 300 cm²
Hydrogen flow rate	1.5–3880 $Nm^3.h^{-1}$	0.22–5000 $Nm^3.h^{-1}$
Lifetime stack	< 90,000 h (more than 10 years)	< 60,000 h
Lifetime system incl. maintenance	20 + years	35,000–80,000 h (around 9 years)

[1] Lower Heat Value (alkaline electrolyzers), [2] Higher Heat Value (PEM electrolyzers),

1.3 Hydrogen production system supplied by low-carbon energy sources

Hydrogen production systems can be classified based on the type of low-carbon energy sources and grid systems configurations (i.e., AC or DC configuration). In the literature, it has been reported four types of hydrogen production systems based on water electrolysis supplied by solar energy, wind energy, DC microgrid system, and the power grid. Nevertheless, power electronics topologies are needed for the system, to convert for example high DC voltage (more than 100V) from low-carbon energy sources to a very low voltage (less than 10V) [38], [39] enabling supplying the electrolyzer.

Firstly, the hydrogen production systems based on solar energy is presented in Figure 1-4. This system is composed of photovoltaic (PV) panels, step-down DC–DC buck converter, and electrolyzer. The PV panels collect sunlight to produce DC voltage, which is then interfaced with the classic buck converter to deliver DC current to the electrolyzer, that generates hydrogen gas. It should be observed that on performing with PV panels, the available power depends on solar irradiance. All of power must be utilized to feed the electrolyzer for the conversion chain to keep its high efficiency. The maximum power point (MPPT) algorithm can be employed to control the step-down converter and to supply the appropriate current to the electrolyzer [40].

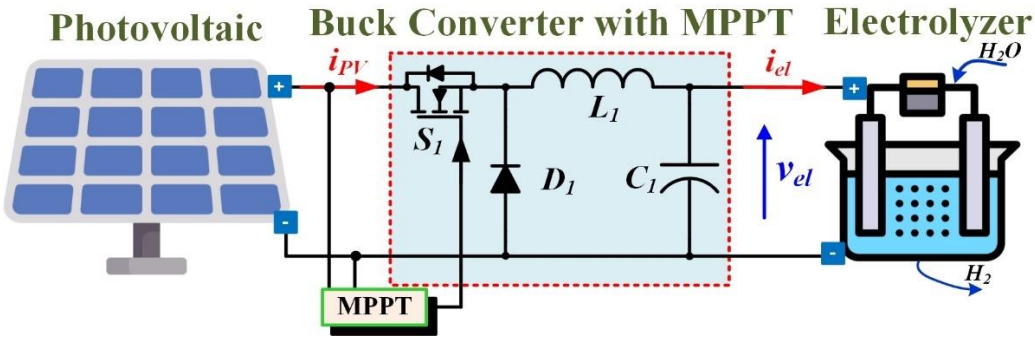

Figure 1-4: Hydrogen production systems based on solar energy.

Second, wind energy conversion systems (WECS) for hydrogen production systems consist of a wind turbine, a step-down DC-DC converter, and an electrolyzer. In addition, wind turbines enable converting kinetic energy from the wind into AC voltage at a three-phase generator output. As a result, an AC-DC three-phase bridge rectifier, a DC-DC buck converter are required for the system. The architecture of this system is illustrated in Figure 1-5.

Due to gusts, WECS has a fast dynamic response. Hence, the capacitor C_{DC} at the DC bus helps to minimize this effect. However, it must be operated with delivering power to the electrolyzer. On one hand, if the power production increases suddenly and is not supplied to the electrolyzer, the capacitor C_1 can protect the electrolyzer against likely damages with the suitable rated capacitor voltage. On the other hand, the power feeding the electrolyzer must be adjusted without causing voltage overshoots, that may degrade the electrolyzer.

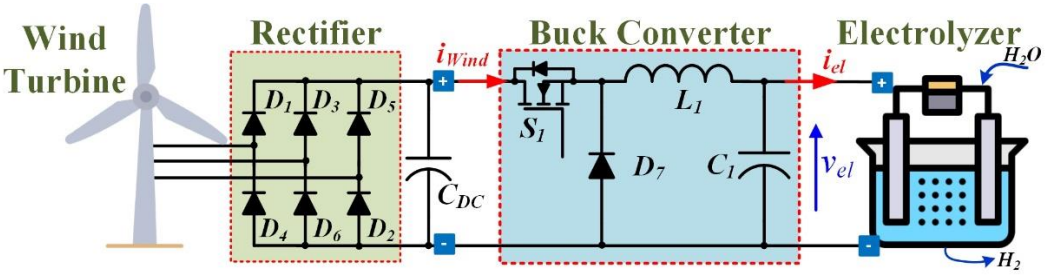

Figure 1-5: Hydrogen production systems supplied by wind energy with uncontrolled rectifier as passive front-end.

As shown in Figure 1-5, WECS relies on the use of permanent magnet synchronous generator (PMSG). On the generator side, a traditional 3-phase diode rectifier provides a cost-effective solution because active power flows unidirectionally and reactive power is not needed. Unfortunately, an uncontrolled rectifier could result in low-frequency torque pulsing, which leads up to shaft resonance. The availability of low-cost controlled power electronics devices and microprocessor platforms enable designing more complex schemes with improved performance. An active pulse width modulation (PWM) rectifier can be used to replace the uncontrolled rectifier, as displayed in Figure 1-6. In fact, it allows obtaining a complete power control (four-quadrant operation). Moreover, it is a basic architecture (available as an interfaced power module), robust and reliable [41]–[43].

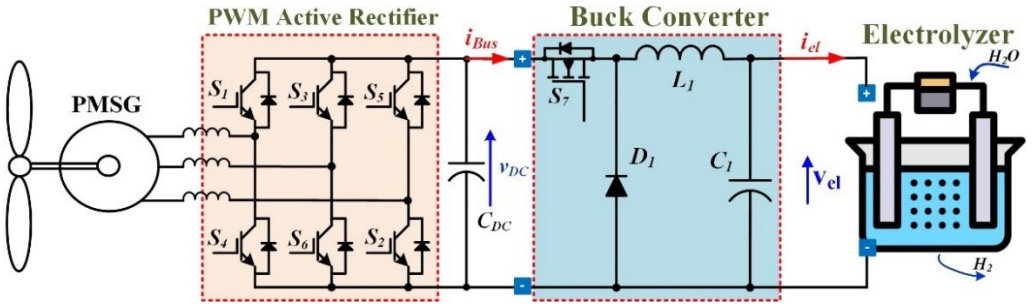

Figure 1-6: Hydrogen production systems supplied by wind energy with front-end based on active rectifier.

In addition, the three-phase high-frequency semi-controlled rectifier, as illustrated in Figure 1-7, is attractive for low-power wind turbines with a PMSG due to it is simplicity and robustness. Furthermore, all operational switches are connected to a common point, avoiding consequently a short-circuit via a leg [44].

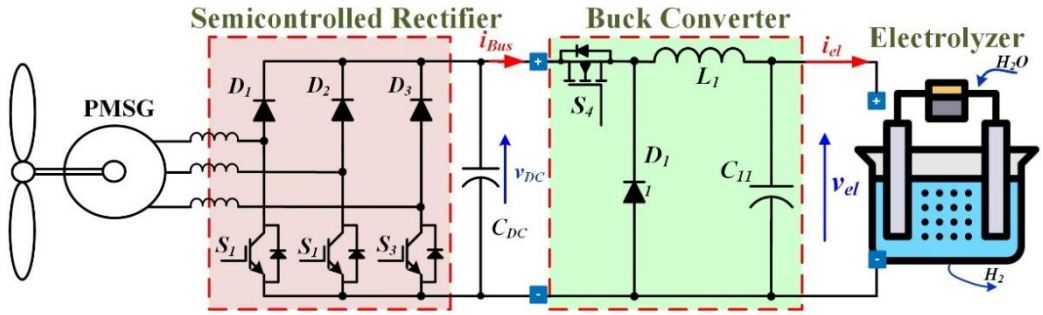

Figure 1-7: Hydrogen production systems fed by wind energy with front-end based on semi-controlled rectifier.

One of the most commercial multilevel converters for the wind turbines available in the market is a three-level neutral-point diode clamped front-end topology (3L-NPC). The 3L-NPC provides two DC output voltages; so, it can be interfaced with two electrolyzers. Both DC output voltage level has half of the voltage level generated by the two levels active rectifier.

The schematic diagram of this topology is presented in Figure 1-8. However, the midpoint voltage inconstancy of the DC bus is a major disadvantage. Thus, this issue may be mitigated by controlling the redundant switching state [41], [42], [45].

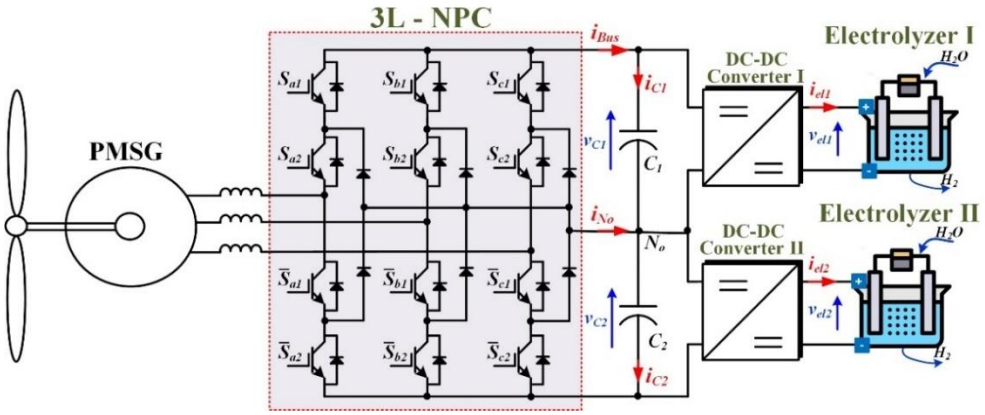

Figure 1-8: Hydrogen production systems supplied by wind energy with front-end based on multilevel rectifier.

Third, the hydrogen production based on the DC microgrid system, like hydrogen production systems powered by solar energy, is illustrated in Figure 1-9. In this system, the input of the buck converter is coupling with the DC bus in the DC microgrid, and the output is connected to electrolyzers [46]. The dynamic behavior in this case is determined by the requirement to store hydrogen due to microgrid limitations.

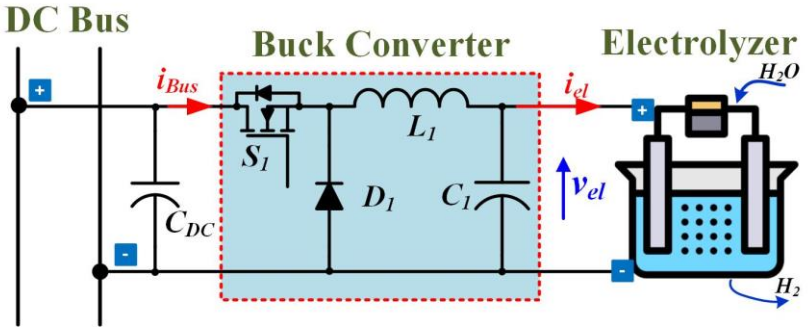

Figure 1-9: Hydrogen production systems with DC micro grid system.

Four, the hydrogen production system coupled with the power grid is depicted in Figure 1-10. This system is connected to the power grid with an electrolyzer by using a delta-star transformer and a 3-phase rectifier. However, the output current of the rectifier for the electrolyzer needs to be controlled, 6-pulse thyristors-based rectifiers are typically employed [47]–[49] as sketched in Figure 1-10. Recently, thyristor-based rectifiers have commonly been used in industrial and power-to-gas applications where high voltage and current to supply electrolyzers are required.

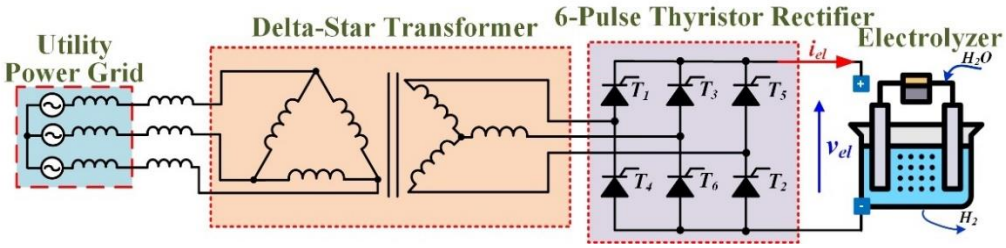

Figure 1-10: Hydrogen production systems connected to the power grid.

Finally, the output voltage of RESs may fluctuate rapidly due to the strong intermittent characteristics. Therefore, suitable power electronics for each hydrogen production system are mandatory to manage hydrogen flow rate, energy efficiency, and reliability. In the next subsection, many types of power electronics topologies are introduced and analyzed.

1.4 Power Electronics for Electrolyzer Applications

In the literature, different types of power electronic topologies are applied for alkaline and PEM electrolyzers depending on the power sources and the electrical requirements to feed electrolyzers. They can be categorized into two groups: AC-DC converter and DC-DC converter. It can be seen from the data in Table 1-3 that the desired stack voltage can range from a few to hundreds of volts, while the current can range from tens to thousands of amps, depending on the rated power (i.e., from watt to megawatt range). Furthermore, many requirements and parameters must be considered before selecting the appropriate power electronics topologies for electrolyzer applications.

1.4.1. AC-DC converter

Currently, the large-scale hydrogen production system is based on wind turbines and the utility power grid. Accordingly, AC-DC converters are mandatory for the system [50]. The major issues facing AC-DC converters in hydrogen production systems are summarized below [38], [49], [51], [52]:

1. The DC current must be controlled to handle the hydrogen flow rate and energy efficiency of the electrolyzer.
2. Strong interaction with the AC power supply in terms of power quality (e.g., high power factor, compensation of reactive power).
3. Input current harmonics fed from the AC power supply must follow international standards and requirements such as IEEE 519-2014.
4. High overall efficiency.
5. High reliability to guarantee the power supply in the case of electrical malfunctions.
6. High-frequency and low current ripples from specific energy consumption and life span point of view.
7. Low cost to decrease the capital cost of the system.

Normally, large current controlled rectifiers are used for high-power applications, and they are mainly divided into two categories: thyristor-based rectifiers with hybrid filters and diode rectifiers with a DC chopper [50], [53]. The availability of power switches for power electronics that can handle high voltage and high currents, such as thyristors and IGBTs, have allowed the development of such circuits. In this subsection, the controlled rectifier (i.e., thyristor-based rectifiers with hybrid filters and diode rectifiers with a DC chopper) are summarized from output current ripple, energy efficiency, power quality, reliability, control, and capital cost point of view.

1.4.1.1 Thyristor-based rectifiers with hybrid filters

Thyristor-based rectifiers are the most commercialized AC-DC converters in the market for industrial applications that can supply high current and voltage to the electrolyzer.

Especially compared to diode-based rectifiers, the usage of thyristors enables the supply of a controlled current, which is needed to handle the hydrogen flow rate and the energy efficiency of the electrolyzer when connecting with renewable energy sources. On one hand, thyristor-based rectifiers are controlled by their firing angle technique. The thyristor-based rectifier operates in rectifier mode if its firing angle is lower than $\frac{\pi}{2}$ rad; whereas it functions in inverter mode if its firing angle is between $\frac{\pi}{2}$ rad and π rad. Nevertheless, the reactive power is generated when the rectifier is controlled by firing angles, the current harmonic content rises and the power factor falls [50], [51]. The power quality is a key issue for thyristor-based rectifier topologies. As a result, to improve the power factor, compensation of the produced reactive power is required. Two types of thyristor-based rectifiers are presented and analyzed in terms of power quality in this subsection.

A. Six-Pulse thyristor bridge rectifier

The architecture of a six-pulse thyristor bridge rectifier is shown in Figure 1-11, which is composed of six thyristors. The anode of the thyristors (i.e., T_1, T_3, and T_5) are connected to a phase of the AC power grid based on a three-phase delta-star transformer. The average output voltage value (i.e., V_{el}) of the rectifier neglecting the parasitic elements of the thyristors is determined by the following equation according to the firing angle α, [54]:

$$V_{el} = \frac{3V_{max}\sqrt{3}}{\pi} cos\alpha \tag{1.7}$$

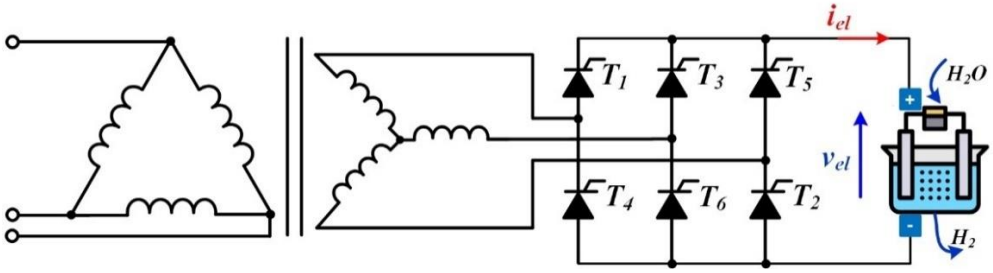

Figure 1-11: Six-pulse thyristor bridge rectifier.

From Equation (1.7), At α = 0°, the maximum DC output voltage (V_{el} = 538 V if V_{rms} = 230 V) is achieved, which is the same as a six-pulse diode bridge rectifier. The firing angle α must not exceed 90° to maintain the operation in rectifier mode. It means that the DC output voltage decreases when increasing the firing angle. Although the six-pulse thyristor bridge rectifier provides excellent energy efficiency and controllable current, it has several weaknesses from power quality and current ripple point of view. The firing angle has a direct impact on reactive power generation. The higher the firing angle, the larger the current harmonics content. Thus, the power factor of the system is reduced dramatically. Besides, in previous work reported in [48], this architecture has a high ripple factor, ranging from 14% to 71% depending on the load range. The current ripple at the large load is very small. Consequently, the low-load operation must be neglected to avoid high current ripple. However, the enhancement of the power quality remains a challenging issue.

The literature indicates in [47]–[49] that a high current ripple raises the specific energy consumption. In other words, more power is required to produce the same volume of hydrogen that could be generated with a pure DC current. The purity of hydrogen gas produced by electrolyzers is also influenced by current ripple [48].

On the other side, this topology produces odd order rank harmonics (i.e., 5, 7, 11, 13, 17, etc.). To face this issue, several strategies have been proposed in the literature to enhance the power factor by compensating the reactive power. The most common approach is to employ passive filters (AC power supply side) since they are developed and designed to eliminate a specific harmonic frequency. Another approach is to use a static synchronous compensator (STATCOM) and a distribution static synchronous compensator (D-STATCOM) [49], [50]. This methodology is suitable for the compensation of fluctuating reactive power. Furthermore, the utilization of these technologies increases costs and causes additional losses. Finally, to address the cost issue, hybrid systems integrating passive filters and STATCOMs have been recommended [50].

B. 12-Pulse thyristor bridge rectifier

To overcome the power quality and current ripple issues, a 12-pulse thyristor bridge rectifier is proposed and illustrated in Figure 1-12. The outputs of two thyristor bridge rectifiers are connected in parallel and the input is interfaced with two secondaries of an inter-phase transformer in delta (upper part) and in star (lower part) to enhance output current, but it can also be set up in series to improve output voltage. In addition, the two secondaries provide a natural phase shift of $\pi/6$ between output voltage. The parallel architecture of this topology is specifically fit for high-power applications since it can supply the electrolyzer with a high voltage and a high current as emphasized in Table 1-3.

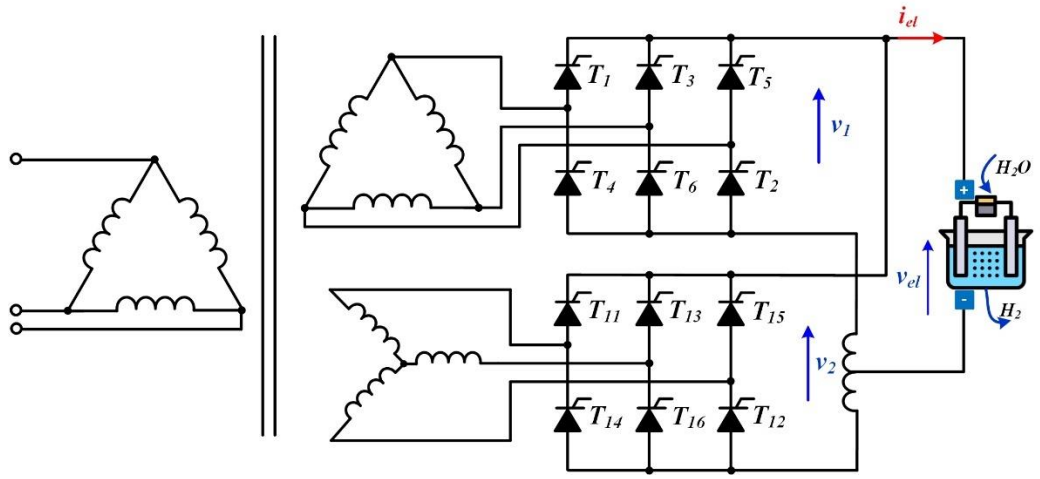

Figure 1-12: 12-pulse thyristor bridge rectifier.

This topology has benefits over the six-pulse thyristor bridge rectifier in terms of current ripple and power quality. Indeed, as discussed in [48], the ripple factor is small, varying from 3.2% to 4.8% depending on the load range. Therefore, the specific energy consumption is reduced, and the quality of the hydrogen generated is improved. However, despite the decrease in specific energy consumption, it remains higher than the reference of specific energy consumption at constant DC current [47].

Finally, a 12-pulse thyristor bridge rectifier allows eliminating odd rank harmonics, decreasing consequently reactive power, and enhancing power factor. However, a hybrid filter consisting of a shunt passive filter and D-STATCOM has been presented and investigated in [55] to satisfy international standards and requirements such as IEEE 519-2014 (offering a recommended harmonic limit for current distortion). This hybrid filter achieves a 0.98 input power factor and a 4.8 % THD (total harmonic distortion).

1.4.1.2 Diode rectifiers with a DC chopper

The combination of diode-based rectifier with DC chopper enables enhancing the power factor while reducing the cost of the system. Indeed, this topology does not need the use of bulky and expensive passive filters.

Usually, the classical combination consists of a six-pulse diode bridge rectifier coupled with a traditional step-down DC-DC buck converter as shown in Figure 1-13.

The six-pulse diode bridge rectifier is employed to convert the AC to DC voltage, enabling an average DC voltage to be supplied according to the voltage specifications of the AC power source (i.e., utility power grid, wind turbine).

From the hydrogen flow rate and energy efficiency points of view, a step-down DC-DC buck converter is used to control the current via the single power switch (i.e., IGBT) since the three-phase diode bridge rectifier cannot be controlled due to the use of diodes. The cost of the system is cheap due to the use of a few components.

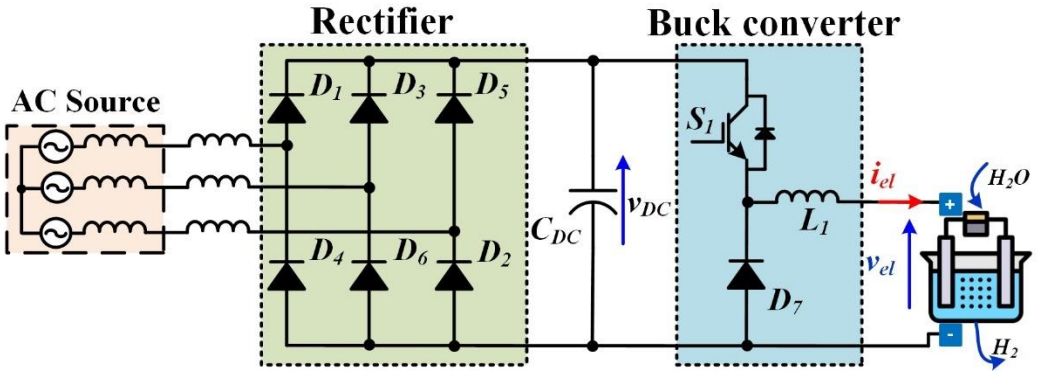

Figure 1-13: Six-pulse diode bridge rectifier with a buck converter.

The output voltage of the step-down converter neglecting the parasitic elements is given by [54]:

$$V_{el} = DV_{DC} \tag{1.8}$$

where D is the duty cycle of the power switch S_1, (defined as the ratio of its conduction time and the switching period), which the values vary from 0 to 1 and V_{DC} is the DC output voltage of the rectifier. The capacitor C_{DC} allows smoothing the voltage ripple.

The output current ripple Δi_{el} is given by [54]:

$$\Delta i_{el} = \frac{DV_{DC}(1-D)}{L_1 f_s} \tag{1.9}$$

where L_1 is the inductor in (H), and f_s is the switching frequency in (Hz) of the converter.

From equation (1.9), it can be observed that the output current ripple is low in the case of a high value of the inductor and switching frequency. Low current ripple is one of the most significant features for electrolyzers in terms of minimizing their specific energy consumption and increasing their reliability [49], [53]. On one hand, when increasing the inductor values, it raises the cost and volume of the component. It can be noted that the whole current i_{el} passes through the inductor, which is a design limitation for electrolyzers requiring high currents. However, the increasing of switching frequency leads to a lower value of the inductor. On the other hand, high switching losses occur when the power switch operates at a high switching frequency. As a result, a balanced solution must be made to enhance energy efficiency while decreasing current ripple [51]. Moreover, other methods have been proposed to reduce the switching losses such as the utilization of soft-switching methods and wide-bandgap semiconductors (GaN, SiC) [56].

Whereas a step-down DC-DC buck converter enables the voltage to be reduced, high currents can be achieved by improving energy efficiency. For high-power applications, this architecture suffers from high voltage stress on the power

electronics devices. Additionally, the power level is limited due to the use of a single power switch. Besides, the converter cannot operate in case of power switch failures since it includes a single power switch.

The fast current dynamic response is another important feature provided by this converter because of the use of a high switching frequency (i.e., >20 kHz) compared to the general frequency for thyristor-based rectifiers (around a few kHz). In terms of power quality, a high value of the capacitor C_{DC} required to reduce rectifier voltage ripple indicates a pulse-shaped current. The reactive power can be decreased and so, the power factor is improved [49]. Passive filters can be added on the power supply side to improve the power factor even further.

1.4.2. DC-DC converter

Generally, medium-scale and small-scale hydrogen production systems are based on photovoltaic power and DC bus configuration. DC-DC converters topologies are consequently compulsory for these applications. The main expected features of a DC-DC converter for electrolyzer applications are summarized below:

1. High energy efficiency.
2. Low or medium, step-down conversion ratio (depending on the characteristics of the system).
3. Reduced output current ripple (to optimize the performance of the electrolyzer from an energy point of view).
4. Low electromagnetic interference.
5. Reduced cost.
6. Ability to operate when electrical failures occur.

Nowadays, classical step-down DC-DC buck converters are employed for electrolyzer application due to their low cost and ease of control [40], [57]–[60]. However, these topologies are not suitable for electrolyzers because of their weaknesses such as limited conversion ratio, low energy efficiency, high output current ripple, and unavailability in case of power switch failures. In this subsection, several DC-DC converter topologies are discussed to overcome the above issues. They are categorized into two types: non-isolated and isolated DC-DC converter

1.4.2.1 Non-isolated DC-DC converter

A. Quadratic buck converter

After introducing the advantage and drawback of classical step-down DC-DC buck converter, quadratic buck converter topology has been proposed in the literature over the last decade [61], [62]. In fact, it allows improving the step-down conversion ratio over the traditional DC-DC buck converter. It is shown is Figure 1-14. This converter consists of using two buck converters connected in series using a single power switch. As a result, better voltage conversion gain can be obtained compared to a conventional buck converter.

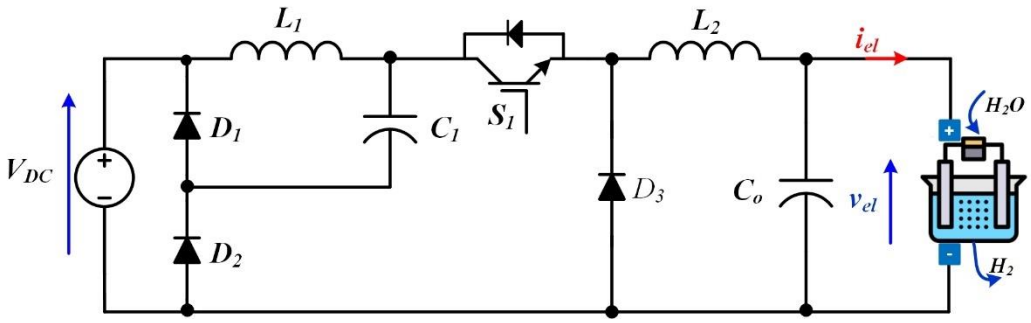

Figure 1-14: Quadratic buck converter.

The voltage ratio and the output current ripple are given by the following expressions:

$$\frac{V_{el}}{V_{\mathrm{DC}}} = D^2 \tag{1.10}$$

$$\Delta i_{L_2} = \frac{V_{DC} D^2 (1 - D)}{L_2 f_s} \tag{1.11}$$

However, this topology cannot operate in the event of an electrical failure due to the use of a single power switch. According to Equation (1.10), the output current ripple is smaller than classical buck converter. In addition, the voltage stress on the power switch remains high.

B. Three-leg interleaved buck converter

A three-leg interleaved buck converter has been proposed to overcome the output current ripple issue and illustrated in Figure 1-15. Moreover, the use of three-leg architecture achieves a conciliation of output current ripple and volume reduction, energy efficiency, and reliability in the case of power switch failure.

The efficiency can be improved due to the share of the current i_{el} among three inductors because of Joule losses into parasitic resistance are proportional to the square of the current.

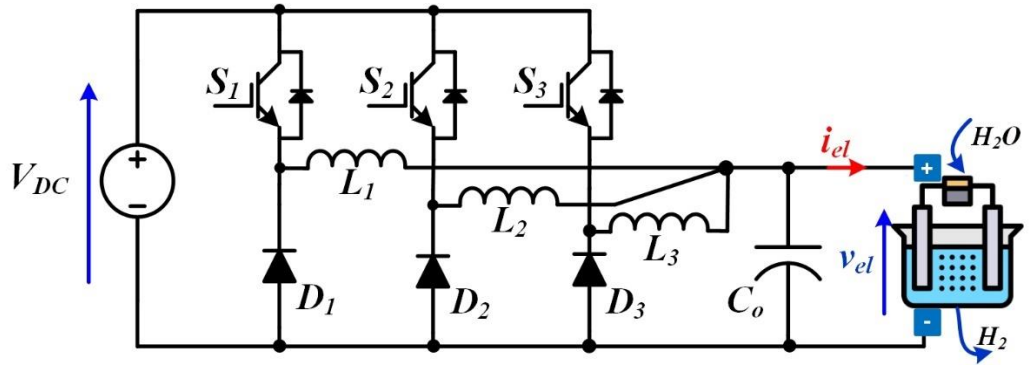

Figure 1-15: Three-legs interleaved buck converter.

The output current ripple and inductor volume are decreased by controlling each power switch (i.e., S_1, S_2, and S_3) with a $\frac{2\pi}{3}$ rad phase shift angle. The output voltage V_{el} is expressed in Equation (1.8). Based on the duty cycle value, the output current ripple is given by the following equation [63].

$$\Delta i_{el} = \frac{V_{el} D(1-3D)}{L f_s} \quad , \quad 0 < D < \frac{1}{3} \tag{1.12}$$

$$\Delta i_{el} = \frac{V_{el}(3D-1)(2-3D)}{3 L f_s} \quad , \quad \frac{1}{3} < D < \frac{2}{3} \tag{1.13}$$

$$\Delta i_{el} = \frac{V_{el}(3D-2)D}{L f_s} \quad , \quad \frac{2}{3} < D < 1 \tag{1.14}$$

From equation (1.12-1.14), it can be observed that the output current ripple is eliminated for specific duty cycles (i.e., 1/3 and 2/3). However, in comparison to a traditional step-down DC-DC buck converter, the three-leg interleaved buck converter can be operated in case of power switch failures and provide energy continuously to the electrolyzer because of its static redundancy. Nevertheless, this topology may suffer from having additional current stresses due to a no fit phase shift angle after fault occurrence. To cope with this issue, the phase shift angle must be modified from $\frac{2\pi}{3}$ rad to π rad to operate as a two-leg interleaved converter [64] and so, the current ripple can be reduced compared to a case without phase-shift angle change.

Despite its limited conversion gain and high voltage stress, this topology is especially well suitable for high-power applications due to the share of the input current across the leg [65]. Compared to a traditional step-down DC-DC buck converter, the energy efficiency can be enhanced, but the high duty cycle value produces major losses at low input DC voltage. Finally, the cost of this configuration is higher than a traditional step-down DC-DC buck converter even if the cost and availability of a single inductor can convince the designer towards the interleaved topology.

C. Two-leg stacked interleaved buck converter

A two-leg stacked interleaved buck converter (SIBC) is an attractive topology for electrolyzer application as depicted in Figure 1-16. It was first proposed in [38], [66] to control the energy from WECS to supply an electrolyzer.

Based on the configuration of the classical step-down DC-DC buck converter, the power diode is replaced by an IGBT power switch to decrease conduction losses since IGBTs have on-state resistance values lower than diodes. However, for low-power applications, the MOSFET devices can be applied [63]. Moreover, an additional classical buck converter has been connected in parallel to take advantage the feature of interleaved topology. Additionally, between the first and second legs, an auxiliary capacitor C_s is employed to block the DC component of the current flowing through the second leg (i.e., s). For this reason, only the AC component of the current passes through the second leg. The two IGBTs (i.e., S_1, S_4, and S_2, S_3) are controlled in the opposite way (rather than π rad in a two-leg interleaved buck converter). Therefore, both AC components of current passing through the first and second legs can be eliminated. Irrespective of the operational state, only a pure DC current passes through the electrolyzer, enhancing its reliability and energy

efficiency [38]. The SIBC can continue to perform when a power switch failure occurs. However, since the SIBC operates with only a single leg, output current ripple increases and is expressed by the expression (1.9) as a basic buck converter. Compared to a three-leg interleaved buck converter, the SIBC has the same weaknesses, especially losses at low DC input voltage.

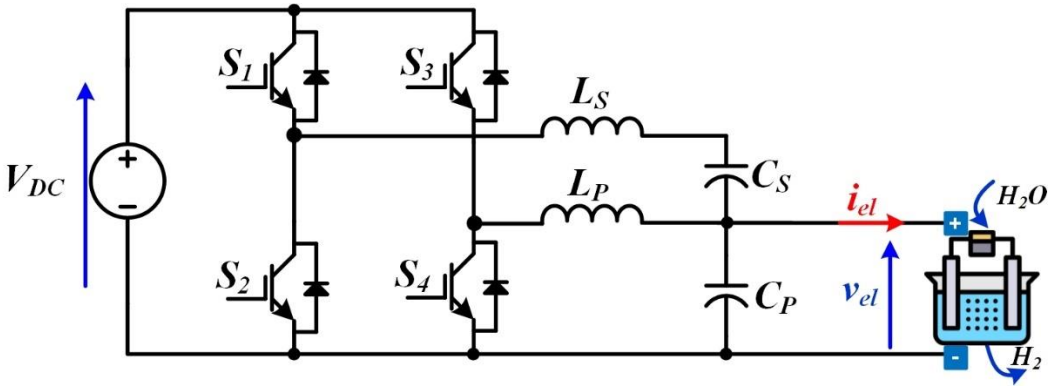

Figure 1-16: Two-leg Stacked Interleaved Buck Converter.

D. Three-level interleaved DC-DC buck converter

One of the most attractive non-isolated DC-DC converter topologies for electrolyzer application is the three-level interleaved buck converter. The configuration of this topology is shown in Figure 1-17 [67]. Based on Figure 1-17, each power switch must withstand only a portion of the input voltage, allowing operation with input voltages higher than the maximum voltage constraints of the power switches. Moreover, the four addition inductors (L_1, L_2, L_3, L_4) enable a significant reduction in losses associated with the phenomenon of diodes reverse recovery and zero-current switching during the on-state phases of the switches. In summary, this topology features these following advantages: the voltage stress on the power switch can be decreased while maintaining low output current ripple, low step-down voltage conversion, ability to operate in case of power switch failures and high energy efficiency. Thus, it has been decided to carry out this Ph.D. work by using this topology. Further details about this topology are provided in Chapter 3.

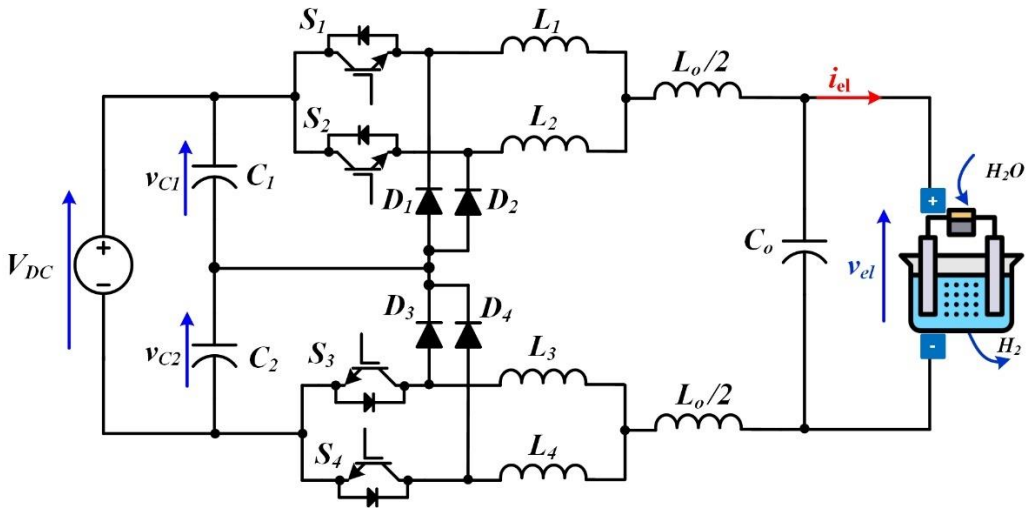

Figure 1-17: Three-level interleaved buck converter

1.4.2.2 Isolated DC-DC converter

In addition to non-isolated DC-DC converters, isolated DC-DC converter topologies with a high-frequency transformer can be employed to meet the expectations for electrolyzer applications (see Table 1-3). Isolated DC-DC converters consist of four parts: an inverter, a high-frequency transformer, a rectifier, and an LC filter. The switching frequency of isolated topologies is typically included between ten and one hundred kilohertz, that allow them to be small and compact. Four types of isolated DC / DC converter topologies have been proposed in the literature to interface electrolyzers and are presented in this subsection. A particular attention is given about the step-down voltage ratio and energy efficiency point of view.

A. Half-bridge isolated DC-DC converter

A half-bridge isolated DC-DC converter has been proposed for electrolyzer applications. The architecture of this topology is shown Figure 1-18 and the voltage gain is provided by the following equations:

$$\frac{V_{el}}{V_{DC}} = \frac{d}{2n} \tag{1.15}$$

where n is the turn ratio of the transformer.

This topology can use soft switching techniques in terms of zero voltage switching (ZVS) to reduce switching losses [56], [68]. This technique is carried out using capacitive dampers on the input side. Furthermore, Equation (1.15) indicates that by properly designing the converter transformer, a high voltage ratio can be achieved. However, the major disadvantage of this topology is the turn ratio transformer; the magnetic flux increases with the turn ratio. Consequently, the inductance leakage would be too high, resulting in extra power losses. For this reason, the voltage gain is not low enough to optimize the value of the turn's ratio. Furthermore, this architecture is not reliable in case of power switch failures.

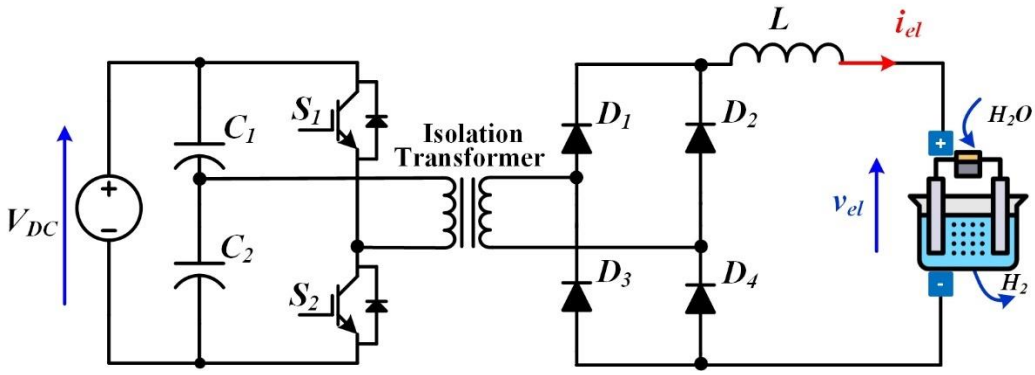

Figure 1-18: Half-bridge isolated DC-DC converter

B. Full-bridge isolated DC-DC converter

Based on the half-bridge isolated DC-DC converter, a Full-bridge isolated DC-DC converter has been developed for high-power electrolyzer applications. The configuration of this technology is displayed in Figure 1-19. The primary transformer is driven symmetrically by two couples of power switches (i.e., MOSFETS). In the first switching period, power switches S_1 and S_4 conduct,

whereas power switches S_2 and S_3 conduct in the second switching period. The second couple stays in the off state while the first couple operates [69]. The main benefit of this topology is a wide range of input and output voltage levels that can be handled, reliability, high power density, and low power losses. However, some weaknesses are presented such as the voltage ratio (not fit to supply low-power electrolyzers) compared to the half-bridge isolated DC-DC converter, high cost because of the use of many elements, and losses in transformer depending on its design [70].

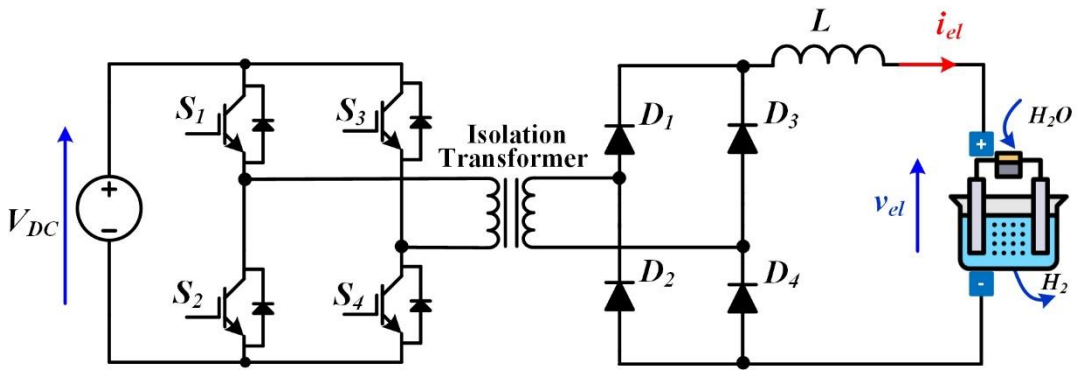

Figure 1-19: Full-bridge isolated DC-DC converter.

C. Push-pull isolated DC-DC converter

The other isolated DC-DC converter topology for electrolyzer application is the push-pull DC-DC converter [71]. The schematic diagram is depicted in Figure 1-20 and the voltage conversion ratio is expressed by the following equation:

$$V_{el} = 2D\frac{N_s}{N_p}V_{DC} \tag{1.16}$$

where D is the duty cycle in the primary switches and N_s/N_p is the transformer turns ratio.

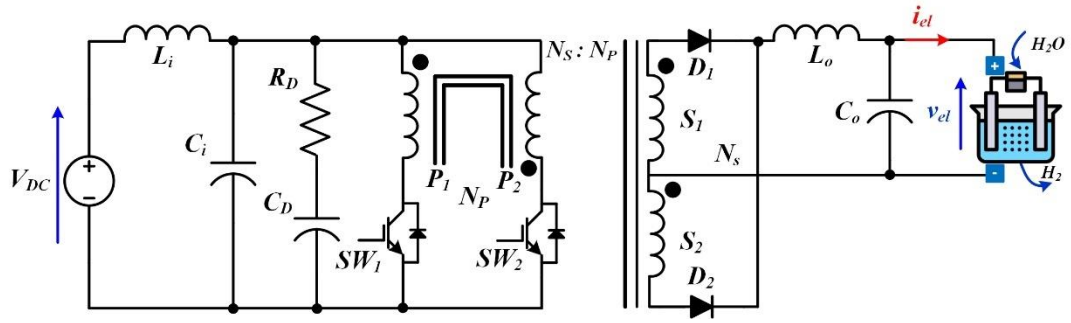

Figure 1-20: Push-pull DC-DC converter.

The major feature of the topology is the output frequency is twice higher than the primary power switching frequency. Besides, the power switches on the primary side must be able to block a voltage twice higher than the input voltage. Indeed, the high input voltage is based on the transformer leakage inductance, and it can be eliminated by a snubber circuit surrounding the power switch [71].

In conclusion, this topology offers effective, simple, and low-cost converters due to the use of two power switches on the primary side with a basic driving technique. Also, the input capacitor voltage is decreased, reducing consequently the cost and volume of the system. Switching operation is enhanced by a simple hard-

switching system utilizing snubber networks, that improve stability and dynamic responses. Nevertheless, the main drawbacks are large blocking voltage components on the primary side, low efficiency due to the hard-switch configurations, and increase of complexity because of the center-tap power transformer.

D. Multi-resonant isolated DC-DC converter

In the same way, multi-resonant DC-DC converters are attractive topologies for electrolyzer applications since they can exhibit many benefits such as low voltage conversion ratio, high energy efficiency, and high adaptability. Basically, multi-resonant DC-DC converters consist of a high-frequency inverter half or full-bridge structure, a resonant tank (i.e., resonant inductor, resonant capacitor, and a high-frequency transformer), and a center-tapped full-wave rectifier [72], [73]. The electrical scheme is illustrated in Figure 1-21.

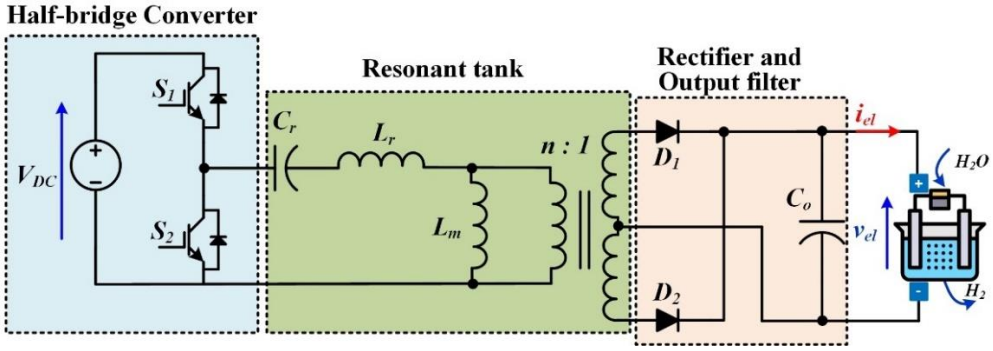

Figure 1-21: Multi-resonant DC-DC converter based on half-bridge LLC resonant converter [74].

Figure 1-21 presents the LLC resonant converter relying on a half-bridge configuration to power the electrolyzer [59]. The resonant tank is located between the half-bridge converter and the output side. It combines a leakage inductor, excitation inductor, resonant capacitor (LLC), and transformer. The resonant tank enables energy to be supplied to the load as well as ZVS to be obtained. Subsequently, the full-wave rectifier with a center-tap architecture allows converting AC voltage into DC voltage. Finally, the ripple of the output voltage is filtered by the output capacitor before being supplied the electrolyzer. However, this topology presents some disadvantages such as the output voltage fluctuation when modifying the operation mode of the power switches, that harms system safety [56].

Finally, a suitable control algorithm is needed for power electronics topologies to meet the requirement expected for electrolyzers as highlighted in Table 1-3 in terms of current and voltage. Moreover, by considering RESs to supply electrolyzers through power electronics, it should be noted that two dynamics must interact with each other. For this reason, the modeling of electrolyzers is mandatory to investigate their real behavior according to the operating conditions (static or dynamic). The electrolyzer modeling can allow designing electrolyzer emulators, able to reproduce accurately the real behaviors of electrolyzers. Novel power electronics topologies combined with their control strategies can be tested with the emulator, avoiding the use of a real electrolyzer that could be damaged during experiments (e.g., overshoots, current ripple). In the next section, the modeling of the PEM electrolyzer is investigated and discussed.

1.5 Proton exchange membrane electrolyzer modeling for emulator purpose

The PEM electrolyzer modeling is compulsory for power electronics and its control. The electrical characteristics of PEM electrolyzer must be investigated to simulate the real behavior of PEM electrolyzer (i.e., static, dynamic operations). Indeed, the PEM electrolyzer model must be combined with the power electronics model to design efficient controllers. The objective of this subsection is turned to the overall model (which includes the power electronics and the load) into a transfer function or a state-space model. Based on the literature survey, three types of PEM electrolyzer modeling have been provided and summarized in the following subsection.

1.5.1. Resistive model

As illustrated in Figure 1-22, the PEM electrolyzer can be represented as a variable resistor. The resistor is the simplest model for delivering electric power to the PEM electrolyzer.

This straightforward model has been used to evaluate the power quality of an alkaline electrolyzer [49]. Moreover, it has been employed to design control algorithms for the traditional buck converter [59], a synchronous buck converter [40], the three-level interleaved buck converter [75], soft-switch full-bridge isolated converter [56], [72], and full-bridge resonant isolated converter [73]. Nevertheless, only in [49], [75], the authors have provided information to determine the equivalent resistive value.

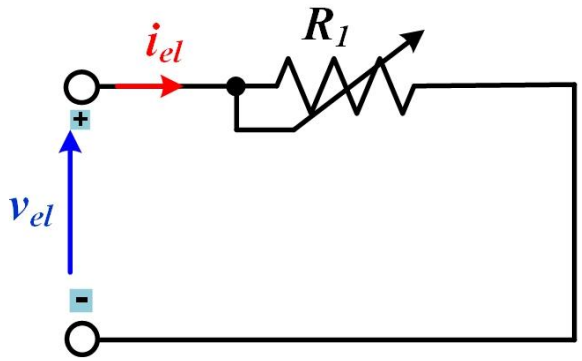

Figure 1-22: Equivalent electric model of PEM electrolyzer by using a variable resistor.

In [49], the equivalent resistance is determined by means of the static voltage-current characteristic as follows:

$$R_1 = \frac{v_{el}}{i_{el}} \tag{1.17}$$

The static voltage-current characteristic curve of the 3MW alkaline electrolyzer is depicted in Figure 1-23. Based on Equation (1.17) and Figure 1-23, the equivalent resistance value according to current has been calculated and is shown in Figure 1-24. It can be observed that the resistance value decreases when increasing the current since the electrolyzer can be seen as a high-current/low-voltage load. An additional curve has been added in Figure 1-24 to highlight the resistance value, that has decreased over a current range of 2000 to 20,000 A.

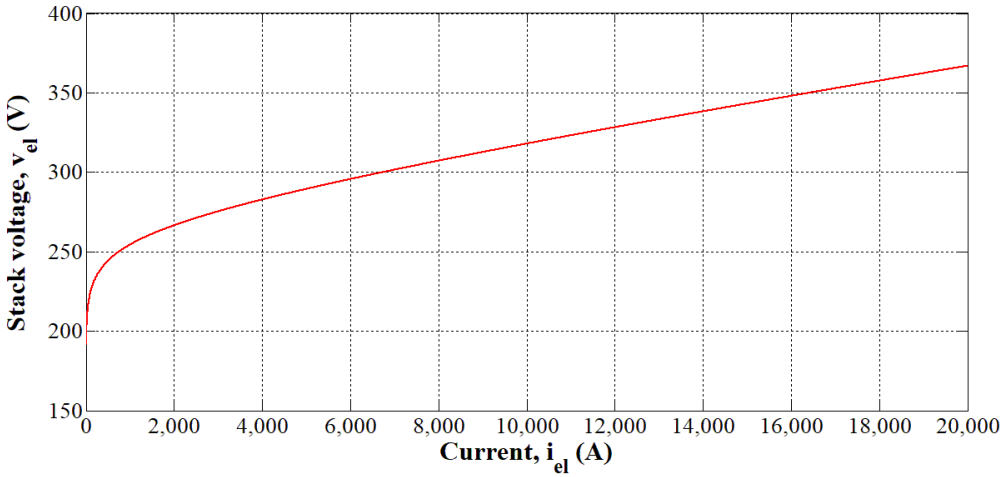

Figure 1-23: Static voltage-current curve of a 3MW alkaline electrolyzer [76].

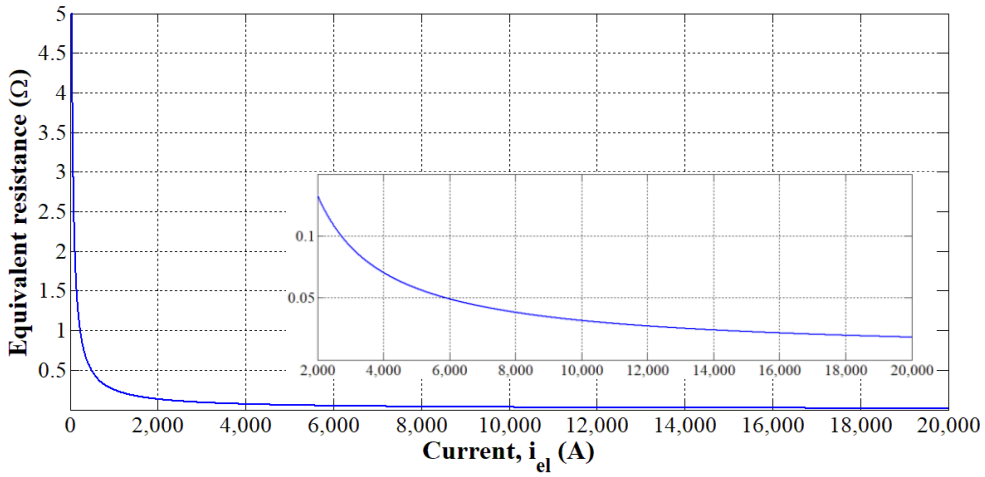

Figure 1-24: Equivalent resistive load according to the current [76].

Furthermore, in [75], the authors have used a dynamic electrical circuit model (presented in subsection 1.5.2) to describe the value of the equivalent resistive. The resistance value is expressed as follows:

$$R_1 = \frac{v_{el} R_{tot}}{v_{el} - E} \tag{1.18}$$

Where:

-V_{el}: PEM electrolyzer voltage (V), depending on the PEM electrolyzer current if the latter is controlled instead of the voltage.

-R_{tot}: the sum of resistances in the equivalent model, taking into considered activation losses (both at the anode and cathode sides) and ohmic losses. The total resistance value is equal to 0.441 Ω.

-E: reversible voltage of the PEM electrolyzer, which is equal to 4.38 V.

As illustrated in Figure 1-25, the value of the equivalent resistive has been assessed using Equation (1.18) and the PEM electrolyzer voltage range of 5 to 8 V (rated stack power of 400 W). It can be noted that the resistive load value decreases when the PEM electrolyzer voltage increases. These results look like those reported in [49].

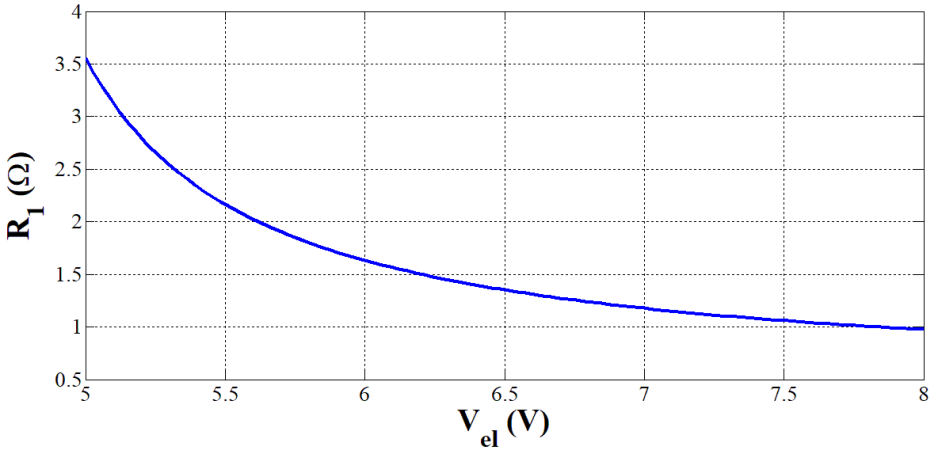

Figure 1-25: Resistance value variation according to PEM electrolyzer voltage.

To summarize, based on these two previous works, the calculation of the resistance is based on the static behavior of the PEM electrolyzer.

1.5.2. Static model

The static model of PEM electrolyzers is mostly used in hydrogen production systems supplied by RESs [57], [58], [77], [78]. It is based on its voltage-current (V–I) characteristic. The V–I characteristic curve can be obtained by performing static tests on a single cell PEM electrolyzer. The parameters of the V–I characteristic curve can be determined through experimental data.

An example of V–I characteristic curve of a 400 W commercial PEM electrolyzer is depicted in Figure 1-26. The operational conditions to acquire this curve are 1 bar of gas pressure and 20 °C of ambient temperature. Moreover, the specifications of the PEM electrolyzer are given in Table 1-4.

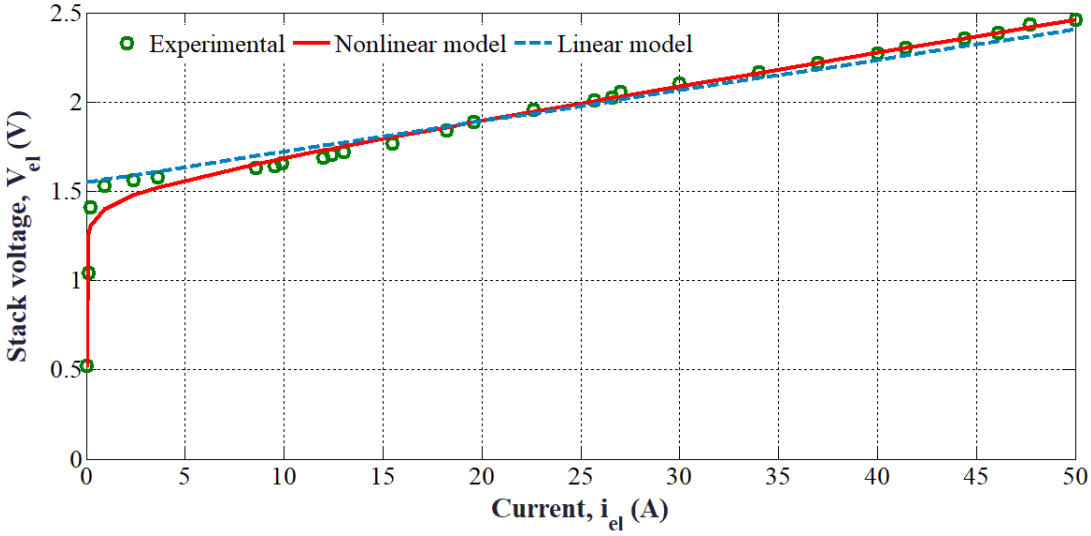

Figure 1-26: The I-V characteristic curve of a PEM electrolyzer with two different modeling (i.e., nonlinear and linear).

Table 1-4. Specifications of the PEM electrolyzer.

Parameters	Value	Unit
Rated electrical power	400	W
Stack operating voltage	8	V
Stack current range	0–50	A
Delivery output pressure	0.1–10.5	bar
Cells number, N	3	-
Active area Section	50	cm^2
Hydrogen flow rate at STP (Standard Temperature and Pressure, 20 °C and 1 bar)	1	slpm (Standard liter per minute) P = 1 bar, T = 20 °C

Based on Figure 1-26, it should be observed that PEM electrolyzer has a nonlinear behavior. For this reason, the model can rely on either a linear or a nonlinear model approach.

First, a linear equation can be applied for static modeling of PEM electrolyzer is provided by the following equations [77]:

$$y = \frac{\Delta y}{\Delta x} x + c$$

$$v_{el} = \frac{\Delta v_{el}}{\Delta i_{el}} i_{el} + 1.545 = \frac{2.407-1.545}{50-0} i_{el} + 1.545 \quad (1.19)$$

$$v_{el} = 0.0172 i_{el} + 1.545 \cong R_1 i_{el} + E$$

The reversible voltage E (electrochemical) is important for electrolysis process and hydrogen production, and can be calculated as follows [3]:

$$E = \frac{\Delta G}{zF} = 1.233\ V \quad (1.20)$$

where:

-R_1 is an equivalent resistance [Ω].

-E is a reversible voltage [V].

-ΔG is the Gibbs energy (238 $kJ.mol^{-1}$ for T = 20 °C) allowing splitting the deionized water into hydrogen and oxygen.

If the water is liquid, ΔG can be determined according to the temperature (°C):

$$\Delta G = 285{,}840 - 163.2(273 + T)\ [J.mol^{-1}] \quad (1.21)$$

-z is the number of electrons exchanged during the reaction. For H_2, z = 2.

-F is the Faraday's constant (96,485 $C.mol^{-1}$).

From Equation (1.19), a static equivalent electrical circuit for a single cell PEM electrolyzer can be assumed as illustrated in Figure 1-27. The model is composed of a constant DC voltage source representing a voltage (E) in series with an equivalent resistance (R_1) [78].

It is composed of an electromotive force (E) in series with an equivalent resistance (R_1) [78].

The electrical power *Pcell* of a single cell is given by:

$$P_{cell} = v_{cell} i_{el} = {i_{el}}^2 R_1 + i_{el} E \quad (1.22)$$

Hence, the total electrical power (P_{el}) is obtained by multiplying the power (P_{cell}) by the number of cells (N):

$$P_{el} = N v_{cell} i_{el} \tag{1.23}$$

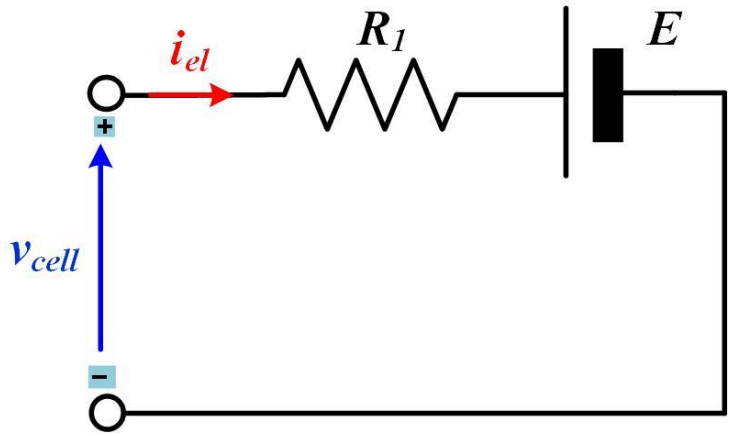

Figure 1-27: Equivalent static electrical model of a PEM electrolyzer single cell.

Based on Figure 1-27, the ratio of the electrochemical hydrogen energy (P_{H2}) to electrical power (Pel) is used to evaluate the energy efficiency of the PEM electrolyzer as follows:

$$\eta_{el} = \frac{P_{H2}}{P_{el}} = \frac{i_{el} E}{v_{cell} i_{el}} = \frac{E}{v_{cell}} \tag{1.24}$$

According to Equation (1.24), the lower the energy efficiency, the higher the cell voltage. Furthermore, the cell voltage efficiency is determined as the ratio of the thermoneutral cell voltage V_{TN} to the cell voltage, v_{cell} [3]:

$$\eta v_{cell} = \frac{V_{TN}}{v_{cell}} \tag{1.25}$$

$$V_{TN} = \frac{\Delta H}{zF} \tag{1.26}$$

where

-ΔH is the variation of enthalpy (285.84 kJ. mol^{-1}).

Finally, the static model of the PEM electrolyzer can be developed based on an empirical current-voltage (I-V) expression. A least-squares regression algorithm can be used to identify the different parameter values. The I-V relationship of the PEM electrolyzer is expressed by the following equations [79]:

$$v_{el} = E + r i_{el} + s log(t i_{el} + 1) \tag{1.27}$$

where

-r is the ohmic resistance of electrolyte (Ω).

-s, t are the coefficients for overvoltage on electrodes

The electrolyzer voltage in Equation (1.27) neglects some operating conditions such as the temperature. As a result, the previous equation can be customized to consider the effects of temperature on the electrode and overvoltage in the electrolyte. The temperature-dependent V–I model can be calculated as follows [79]:

$$v_{el} = E + r_1 + r_2 T i_{el} + (s_1 + s_2 T + s_3 T^2)\ log(t_1 + t_2/T + t_3/T^2 i_{el} + 1) \qquad (1.28)$$

-r_i is the parameters for ohmic resistance of electrolyte (i = 1...2).
-s_i , t_i are the parameters for overvoltage on electrodes (i = 1...3).
-T is the temperature of electrolyte (°C).
The parameters r_i, s_i, t_i are provided in [79].

1.5.3. Dynamic model

The previous two subsections have presented resistive and static models. They do not consider dynamic operations of the PEM electrolyzer. However, the development of dynamic models is crucial to reproduce accurately the real behavior of PEM electrolyzers when coupling them with RESs.

Therefore, the main objective of dynamic models is to reproduce physical phenomena of PEM electrolyzer such as accumulation of charges and losses. Based on the literature review, two dynamic models have been investigated and analyzed [80]–[84].

First, in [80], [81], the dynamic model can be represented by the electrical model. It is characterized by reversible voltage and overvoltage. The operation voltage of a PEM electrolyzer cell is the sum of the reversible voltage and all the irreversibilities within the cell (i.e., activation overvoltage, ohmic overvoltage, and concentration overvoltage).

The dynamic model of cell PEM electrolyzer can be represented by an equivalent electrical circuit which models overvoltage with resistors (R). Moreover, the double layer charge phenomenon that occurs at the electrode-electrolyte interfaces is discussed in detail in [82] regarding the fuel cell; it is modeled by a capacitor (C) in parallel with the activation and mass transport resistors as shown in Figure 1-28.

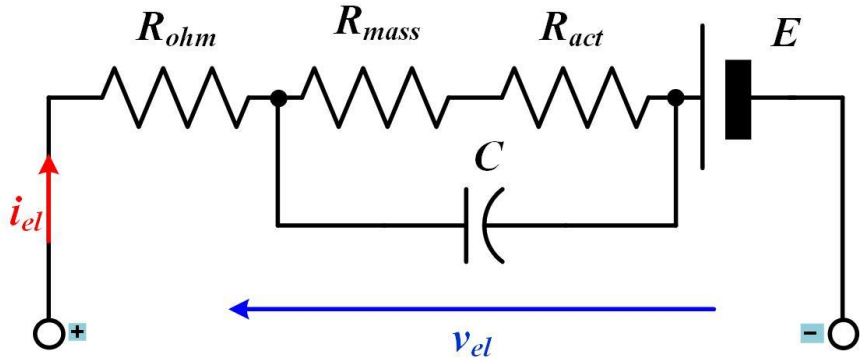

Figure 1-28: Equivalent dynamic electrical model of a PEM electrolyzer [80], [81].

Based on Figure 1-28, which uses three resistors and a capacitor to reproduce the dynamic behavior of PEM electrolyzer. R_{act}, R_{mass} and R_{ohm} represent activation, mass transport and ohmic losses, respectively; the reversible voltage (E) is represented by an electromotive force at a fixed temperature. It is important to note that this dynamic model was developed based on previous research on the fuel cell. Thus, only in [81], the dynamic behavior of PEM electrolyzer has been demonstrated through experiments. Nevertheless, the parameters of dynamic model were not determined from the experimental data.

By comparison, in [83], [84], a second equivalent dynamic model for a PEM electrolyzer has been developed considering the dynamic behavior of the PEM electrolyzer under dynamic operations. In this specific case of operation, the electrolyzer behavior is like a capacitor. The dynamic equivalent circuit model of PEM electrolyzer is shown in Figure 1-29.

The authors have investigated this model by using a methodology for identifying the parameters of the model using the least-squares regression algorithm. The dynamic behavior of the PEM electrolyzer is strongly linked to the operation conditions (i.e., input current) and so, the parameters of the model cannot be considered constant. However, the authors have determined the model parameters valid for a specific operating range. Hence, the parameters are considered constant.

To improve the reliability of the model, the parameters of the latter must be adaptive according to the current supplied to the electrolyzer [85]. More details about this dynamic model will be provided in Chapter 2 focused on the design of a PEM electrolyzer emulator.

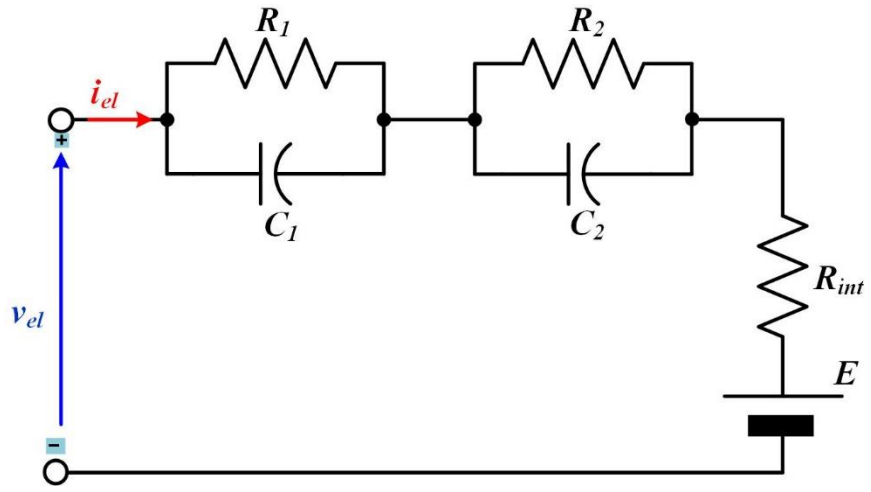

Figure 1-29: Equivalent dynamic electrical model of a PEM electrolyzer [83], [84].

1.6 Objectives of the Thesis

Power electronics topologies and their control algorithm are mandatory for hydrogen production based on the water electrolysis process supplied by a low-carbon energy source as presented in Chapter 1. Moreover, the modeling of the PEM electrolyzer needs to be investigated and analyzed to develop a PEM electrolyzer emulator. Indeed, it can be used to test new power electronics topologies instead of using a real electrolyzer. As the result, the main objectives of this thesis are summarized below:

1. Investigation of real static and dynamic behaviors of a commercial PEM electrolyzer NMH2 1000 from HELIOCENTRIS company to design and realize a PEM electrolyzer emulator (Chapter 2).

2. Design, sizing, and validation of PEM electrolyzer emulator for power electronics test based on the analysis of static and dynamic operations. The emulator relies on an equivalent electrical scheme (Chapter 2).

3. Design, realization, and simulation of a low-voltage high-power DC-DC converter (i.e., 3-level interleaved buck converter) with developing non-linear control laws (i.e., improved sliding mode based-control) (Chapter 3).

4. Development of an experimental test rig including a 3-level interleaved buck converter with improved sliding mode based-control and a PEM electrolyzer emulator to validate the performance of the developed converter and control laws (Chapter 4).

1.7 Conclusion

Chapter 1 aimed to introduce the state-of-the-art of alkaline and PEM electrolyzer technologies in terms of fundamental operation and key features. From this state-of-the-art, it has been emphasized that PEM electrolyzers feature several benefits over alkaline electrolyzers such as high current densities (more compact), fast dynamic responses, and large partial load range. Hence, PEM electrolyzers are perfectly suitable for hydrogen production systems based on RESs since they can capture energy during dynamic operations. For this reason, PEM electrolyzers have been considered in this Ph.D. thesis.

Then, it has been highlighted that hydrogen production systems include power electronics which are classified into two categories, AC-DC converters, and DC-DC converters. AC-DC converters are preferred for high-scale hydrogen production systems, whereas DC-DC converters are suitable for low and medium-scale hydrogen production systems. Different topologies have been presented and analyzed. Within the framework of this Ph.D. thesis, a three-level interleaved buck converter has been selected relying on its features and will be discussed deeply in Chapter 3.

Finally, this Chapter has been concluded in presenting different types of electrolyzer modeling for emulation and control purposes. The development of accurate models is crucial to replicate the real behavior of the PEM electrolyzer and can be useful to develop an emulator for testing applications. In this work, a dynamic model has been considered to take into consideration the dynamic operating conditions of the PEM electrolyzer. The next Chapter will investigate the design, the realization, and the validation of a PEM electrolyzer emulator. Then, it can be combined with the studied DC-DC converter to perform experimental tests and to validate the proposed control laws.

Chapter 2
Design, Realization and Validation of a Proton Exchange Membrane Electrolyzer Emulator

2.1 Introduction

Emulators have been proven to be effective in RESs exploitation research. It's mostly due to the necessity for reproducible test settings, that are difficult to provide since weather conditions frequently change suddenly. Furthermore, the usage of an emulator is advantageous for laboratory experiments since it enables the development of a less expensive test bench. In fact, as compared to the actual plant to be emulated, an emulator is often cheap and less dangerous; no hydrogen is produced throughout the experiment, especially when utilizing electrolyzer emulators. As a result, substantial emulator research has been performed in the recent year to decrease overall costs and increase dynamic performance. An emulator's structure is made up of a model of the system to be simulated, that provides reference parameters to a power conversion system whose output is the feedback to the model.

The photovoltaic (PV) emulators are active circuits that can replicate the current-voltage characteristics of a PV source [86]. Different techniques to evaluate the model have been offered, such as using an equivalent electrical circuit or an interpolation model [38] or identifying the PV source by testing under operating conditions [87]. The objective is to reproduce specified conditions, such as partial shade [88], [89] , to evaluate maximum power tracking methods and acquire a good dynamic that accurately reproduces the natural fluctuation of the plant [88], [90]. In [91], the PV characteristic is determined using a linear circuit for a low-power application; switching converters are recommended to obtain a high-efficiency power conversion system [88], [89], [92].

Likewise, the fuel cell emulator enables the behavior of fuel cell to be reproduced, including all the system's auxiliaries, while avoiding hydrogen waste, cell purchase, and cell injury [93]–[95]. The authors in [96] suggested an emulator based on a model of an equivalent electrical circuit. In contrast, the developed emulators in [93], [97], [98] are based on DC-DC converters, whereas the emulator in [99] uses a low-cost microcontroller. Battery emulators have similar characteristics where the bidirectional flow of energy is replicated by a power switching converter [100], [101].

Several attractive emulators have made it possible to test wind turbines. A fit-controlled motor connected to the generator can be used to simulate the turbine [43], [102], and a suitable controlled three-phase power converter can be used to emulate the generator behavior [102], [103]. Oppositely, as explained in [104], the load emulators leverage a power converter's characteristic to represent a variable impedance that can be used to load PV sources or fuel cells or as an electric machine that can be coupled to a grid and tested under different load situations [105] for microgrid testing [106]–[109]. The electrolyzer is a load for a power converter that must meet the voltage of the supply to the voltage required by the electrolyzer. The utilization of RESs to generate hydrogen has modified the requirement of the model

to be able to emulate accurate behavior in dynamic conditions. Since power grid is supplied energy to high-power industrial alkaline electrolyzers are often operated in stationary mode, an equivalent resistance can be used to simulate them. On the other side, PEM electrolyzers are also available for medium and low-power applications and can be powered by RESs through a power converter [110], however, a more precise model is necessary [111]. Even though the electrolyzer is recognized as a load, using a programmable load for static operating does not duplicate the transients until a reference model is employed. To emulate a PEM electrolyzer, it is desirable to avoid programmable loads based on switching converters to avoid interference from the switching converter. As a result, the design of a PEM electrolyzer emulator differs from the previously mentioned emulators. It is based on an equivalent passive circuit, with components that reproduce the physical behavior of the PEM electrolyzer, including the anode side and cathode side reactions, as well as the membrane's dynamics. Furthermore, a linear circuit is used to rectify the V-I static characteristic and obtain the internal voltage. It allows to acquire the produced hydrogen since the internal voltage for the current is multiplied.

The aim of this chapter is to investigate the static and dynamic behavior of a commercial PEM electrolyzer NMH2 1000 from HELIOCENTRIS company in terms of design and realization of a PEM electrolyzer emulator. Subsequently, the emulator has been designed and sized based on an equivalent electrical circuit. Finally, experimental tests have been carried out to assess the performance of the realized emulator under static and dynamic operating conditions. The obtained results have been compared with the real PEM electrolyzer to justify the use of this emulator to test new DC-DC converter topologies and their control laws.

2.2 Analysis of the PEM electrolyzer behavior

The static and dynamic characterizations of the commercial PEM electrolyzer NMH2 1000 from HELIOCENTRIS company for emulation purposes have been identified by experiment tests. The specifications of the PEM electrolyzer under study are given in Table 1-4 (See chapter 1). On one hand, static characterization can be investigated by collecting the experimental data of the electrolyzer under study (i.e., current, voltage) during static operation (set pressure and temperature) to achieve the voltage-current characteristic curve. On the other hand, the dynamic characterization is performed by providing the dynamic current profiles (simulating the interfacing of the PEM electrolyzer with the RES) to the electrolyzer and then observing the voltage response of the studied PEM electrolyzer, highlighting its dynamics. To better understand the dynamics of the PEM electrolyzer, dynamic characterization is essential, and leading up to its simulation by an equivalent electrical circuit is critical.

Although several contributions to the development of PEM electrolyzer models have been published in the literature [3], [84], in most cases, dynamic operations are not considered while modeling the electrolyzer. Like PEM fuel cells, electrolyzers are electrochemical devices, and they request some time to respond to the dynamic operations because of the charge movement into the electrolyzer. In [84], is reported a first investigation of the PEM electrolyzer responses according to dynamic input energy. By taking their dynamics behavior into account, it allows enhancing the accuracy of the model.

The development of realistic PEM electrolyzer models is critical for simulating hydrogen production systems relying on RESs as well as to developing effective power electronics controllers. When dealing with RESs for hydrogen generation, the dynamics of both systems must be considered. Indeed, the rate at which the energy generated by a RES fluctuates is frequently different from the rate at which the speed of energy is absorbed by the electrolyzer. This phenomenon is replicable only by considering the dynamics of the electrolyzer. Especially when RESs are employed to supply the electrolyzer, the energy fluctuates suddenly. Hence, the electrolyzer takes more time to respond to its operating point; meanwhile, to avoid overvoltage, the intermediate DC-bus of the converter must be well-designed (or supported by an auxiliary storage device). In this subsection, the results of a commercial PEM electrolyzer are investigated based on dynamic current profiles, including rising and falling current.

2.2.1. Static operation

First, the static voltage characteristic curve of the PEM electrolyzer under study has been carried out through experimental tests. It is depicted in Figure 2-1. It can be observed that the stack voltage of the PEM electrolyzer rises when increasing the current feeding the electrolyzer. Nevertheless, the stack voltage remains constant from a current of approximately 7 A (i.e., 0.14 A. cm^{-2}). Normally, a constant voltage zone is not met for electrolyzer. Before performing these tests, the studied PEM electrolyzer stack has been used with power electronics (electrolyzer system) generating low and high-frequency current ripple. Based on the GREEN research team's knowledge and research articles on this topic, these operations could have caused likely degradations and so, the electrolyzer characteristic has been modified letting appear a voltage saturation operation. Before the saturation region, the operation of the emulator was limited to the linear section of the V-I characteristic curve. During the experiments described in this subsection, a pure current source was used to obtain the identification of the static and dynamic curves of the experimental tests. In terms of the static characterization, the virtual control panel of the DC power supply controls the current source to deliver current in a suitable range; the voltage is measured for each operating point to accurately reproduce the static characteristic, as shown in Figure 2-1.

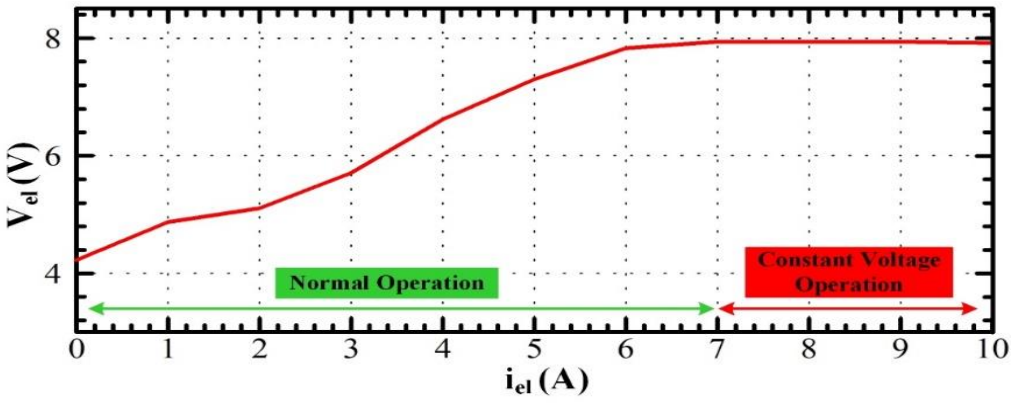

Figure 2-1: Static current-voltage waveform.

Only the PEM electrolyzer stack was utilized in this test, connected directly to a DC power source. It should be noted that, even though the V-I static curve is not theoretically correct, it characterizes our case study, afterward, the emulator was designed to simulate the constant voltage zone as well. It is achieved by an auxiliary circuit whose operation has no effect on the normal operation zone and can be eliminated to simulate an electrolyzer without saturation.

2.2.2. Dynamic operation

The dynamic characterization plays an important role in electrolyzer emulators; in fact, differently from high-power alkaline electrolyzers, the PEM electrolyzers have different behavior when the frequency is changed. Generally, a single-phase diode rectifier combined with a DC-DC buck converter is used in power electronics converters for PEM electrolyzer supplied from the grid. The rectifier is used to convert an AC voltage to a DC voltage; however, the DC output voltage of the rectifier is too high to fulfill the PEM electrolyzer's low DC voltage requirement. As a result, a DC-DC buck converter is required to step-down the voltage and supply the electrolyzer. It is important to emphasize that the usage of power electronics generates current ripples at both low and high frequencies. Usually, the single-phase rectifier produces low-frequency current ripple (approximately to twice the frequency of the power grid; in this case, 100 Hz); while the DC-DC buck converter generates the high-frequency current ripple (due to the high switching frequency; in this case, 20 kHz). The output voltage is affected by both low and high-frequency ripple when employing a commercial power converter; it also affects the current, that suffers from the same distortion. Several studies on the effects of low and high-frequency current ripples have been reported in the literature on PEM FC stacks [112]–[115], and more recently on alkaline electrolyzer [116], [117]. Based on previous relevant works, it has been found that the lifespan and performance of FC and electrolyzer during operation may be affected by low and high-frequency current ripple. The PEM electrolyzer can be identified in the frequency domain by collecting the frequency response in acceptable range or the step response in time domain. The time-domain characterization based on the step current response has been employed since the aim of this emulator is to analyze the performance with an intermittent characteristic of RESs. Several dynamic tests have been carried out; especially, the tests demonstrating operation with a current step from 2 to 7 A and vice versa are presented in this subsection since they are especially challenging for the large range of current supplying the electrolyzer.

The obtained results are illustrated in Figures 2-2 and 2-3. For both experiments, a long-time scale (i.e., 5 $s.div^{-1}$) was tuned to emphasize the dynamics operation of the PEM electrolyzer as well as the steady-state operation. It can be observed that the voltage response of the PEM electrolyzer is fast when step currents are applied (i.e., rise, fall). This behavior is one of the key features of PEM electrolyzers and it is necessary when electrolyzers are connected to RESs since their operations are extremely fluctuating.

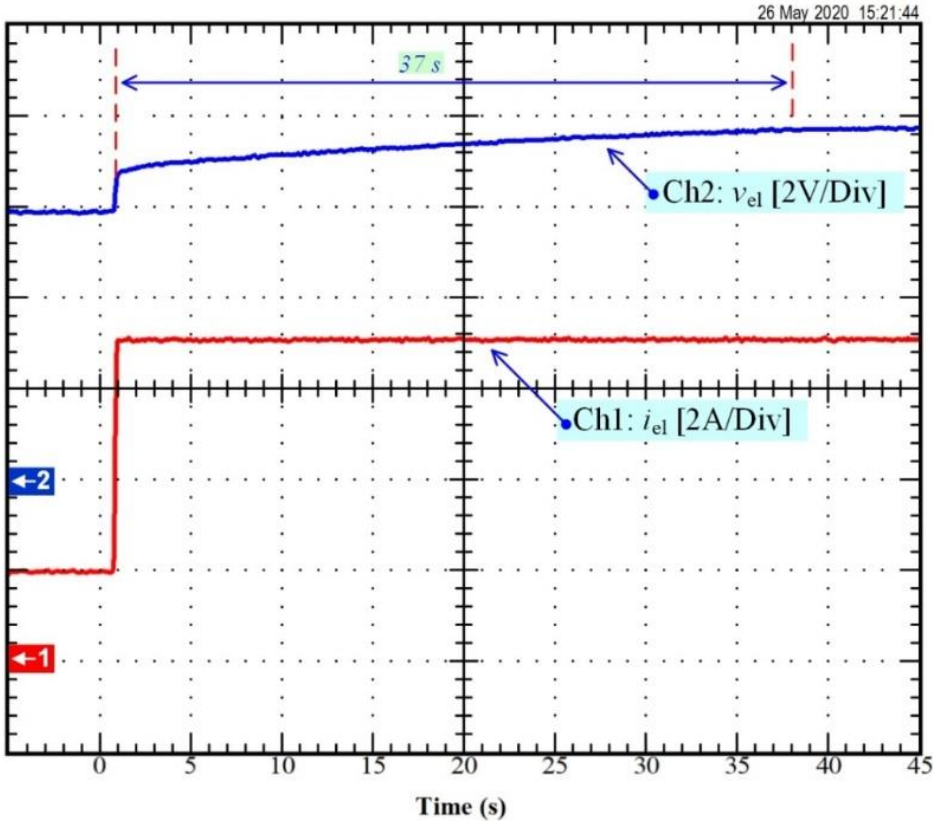

Figure 2-2: Response of the PEM electrolyzer as a result of a rising current.

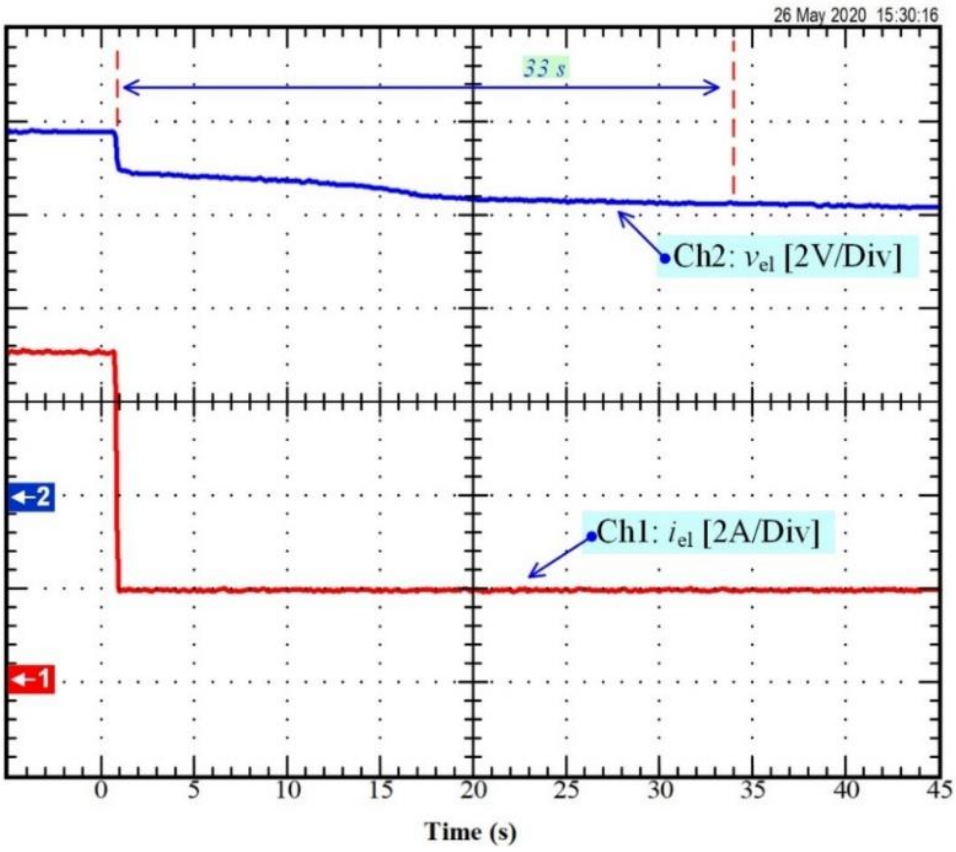

Figure 2-3: Response of the PEM electrolyzer as a result of a falling current.

Based on Figures 2-2 and 2-3, it can be noted that the stack voltage of the PEM electrolyzer increases immediately. Afterward, it rises slowly before achieving its steady-state value as a consequence of a step input current of PEM electrolyzer. The sudden voltage rise is related to the membrane operation because only protons can pass through it.; while the slow voltage rise emphasizes the dynamic behaviors of the PEM electrolyzer at both electrode sides (i.e., anode and cathode side). In the rising up current test (i.e., Figure 2-2), the final steady-state voltage value (around 8 V) is reached roughly in 37 s, whereas for the falling down test (i.e., Figure 2-3), the final steady-state voltage value is reached in 33 s. The small difference in both curves obtained with the current rising and falling is expected because the electrolyzer perceives a varied impedance throughout the step-up and step-down of the supplied current. Furthermore, the electrolyzer current is driven by a power converter during the increased current operation; while during the decreased current operation, the electrolyzer must discharge the extra charge to reduce the voltage level at the terminals. This is achieved by modifying the hydrogen production rate.

2.2.3. Discussion

As mentioned in previous subsection, the two experimental tests of the PEM electrolyzer are identified by different dynamics. On one hand, the steady-state stack voltage is reached sluggishly in the static operation test. On the other hand, for the dynamic operation test, the dynamic behaviors of stack voltage are slightly faster than the static operation test. It can be noted that a long time is needed to stabilize a steady-state operation between two experimental tests. For the static operation test, the chemical reactions within the PEM electrolyzer are slower than the dynamic operation test since the expected steady-state stack voltage is close to the rate (i.e., around 8 V). The time response to achieve the steady-state value should be shorter since the expected steady-state value was lower than the rated stack voltage. These sluggish dynamics are particularly obvious for currents ranging from 4 to 7 A. In comparison, for the dynamic operation test, the required time to reach the steady-state voltage value of the PEM electrolyzer is too long because of the gas diffusion phenomenon. As a result, two dynamics can be highlighted in both experimental tests, one faster relating to the cathode reaction and the other slower relating to the anode side reaction as indicated in a previous work [84]. Indeed, the anode side presents slow reaction, and the cathode side a fast reaction, and one of these reactions can dominate the dynamics depending on the input energy supplying the electrolyzer [84].

Finally, the dynamics are particularly apparent up to a current range of up to 8 A, according to the obtained experiment results. This is related to the static voltage curve obtained in Figure 2-1, where the stack voltage remains constant above 7 A despite the electrolyzer 's rated current of 50 A.

This analysis of the obtained results of PEM electrolyzer is very useful to design a PEM electrolyzer emulator. In the next subsection, the guidelines to design and realize the emulator are provided and analyzed.

2.3 PEM electrolyzer emulator

2.3.1. Design of the PEM electrolyzer emulator

As analyzed in the previous section, PEM electrolyzer under study presents slow and fast dynamics, that are due to the well-known “charge double-layer” effect and gas diffusion phenomenon as described for PEM fuel cells [118]. Normally, there is a charge layer between the electrode and the electrolyte that can store electrical charge as well as energy. This "charge double-layer" represents a capacitor.

On one hand, an electrical voltage is produced by the accumulation of charges, which corresponds to the activation overvoltage at both the anode side and the cathode side. Hence, when the current immediately changes, the activation overvoltage at the anode side and the cathode side need some time to respond to the current change. On the other hand, because of a change in current, the ohmic overvoltage responds immediately, as can be seen in Figures 2-2 and 2-3. Therefore, the proposed equivalent electrical scheme of the PEM electrolyzer emulator is illustrated in Figure 2-4. The proposed scheme can separate the activation overvoltage at the anode side and the cathode side by two RC branches.

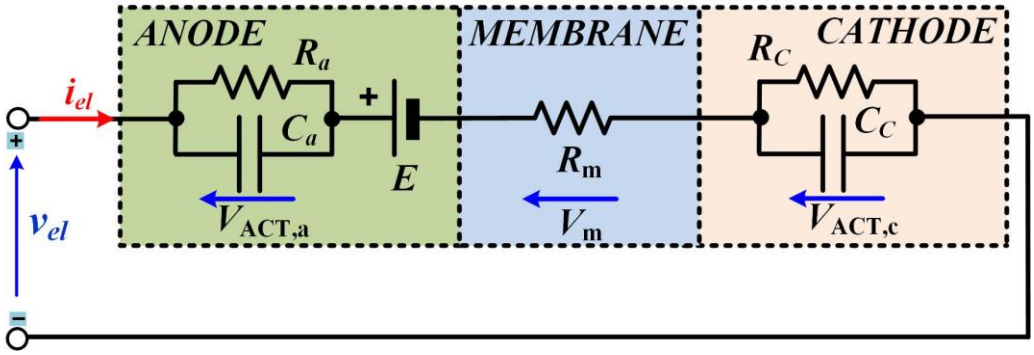

Figure 2-4: PEM electrolyzer equivalent electrical circuit.

Based on Figure 2-4, the electrical circuit model of the PEM electrolyzer emulator consists of two RC branches (i.e., R_a, C_a, and R_c, C_c) to emulate the dynamic reactions at the anode side and the cathode side. The electromotive force at the cathode side is modeled as the energy that is transformed into hydrogen (i.e., reversible voltage E), while the ohmic loss at the membrane is represented by the resistor R_m.

The power losses take place on the anode side and cathode side since the charges flow across the membrane, the end-plates, contacts, and interconnect resistors. This set of losses is well-known as ohmic losses. Losses on the anode side and cathode side are simulated by R_a and R_c respectively. Losses into end-plates, contacts, and interconnect resistors can be improved by a suitable arrangement, consequently, it can be ignored as proposed by [80]. Nevertheless, considering their contribution is mostly ohmic, like that of the membrane, it can be included in R_m.

Finally, while the two capacitances (C_a and C_c) are supposed to be equal, the two resistances (R_a and R_c) differ owing to the different energy needed to reach the cathode and anode reactions, emphasizing two different dynamics (e.g., slow, and fast). The resistor R_a emulates the losses at the anode side; meanwhile the resistor R_c simulates losses at the cathode side [93]. The assumption that the two capacitances are equal, is an approximation because a noticeable change in anode

capacitance relying on current can be seen. This assumption is justified based on a previous investigation for PEM fuel cell modeling [119].

Nevertheless, since it is a second-order effect, and combining this variation in an emulator would have made the circuit too complicated and expensive, the equality has been preserved.

In conclusion, the behavior (activation and ohmic effects) of the real electrolyzer can be reproduced when the emulator is supplied by a step current.

Relying on Figure 2-4, the electrolyzer voltage is expressed by the following equation (usable for normal operations as depicted in Figure 2-1):

$$v_{el} = E + v_{act,a} + v_{act,c} + v_m \tag{2.1}$$

The dynamic activation overvoltage at the anode side and cathode side are given by the following expressions:

$$\frac{dv_{act,a}}{dt} = \frac{1}{C_a} i_{el} - \frac{v_{act,a}}{R_a C_a} \tag{2.2}$$

$$\frac{dv_{act,c}}{dt} = \frac{1}{C_c} i_{el} - \frac{v_{act,c}}{R_c C_c} \tag{2.3}$$

The time constants that run the dynamics both at the anode side and the cathode side are given as:

$$\tau_{act,a} = R_a C_a = C_a(\frac{v_{act,a}}{i_{el}}) \tag{2.4}$$

$$\tau_{act,c} = R_c C_c = C_c(\frac{v_{act,c}}{i_{el}}) \tag{2.5}$$

The ohmic overvoltage v_m can be written as:

$$v_m = R_m i_{el} \tag{2.6}$$

The energy efficiency (i.e., ratio of the power converted into hydrogen to the electrical power) can be calculated relying on the electrical model [84] as follows:

$$\eta_{el} = \frac{P_{H2}}{P_{el}} = \frac{E i_{el}}{V_{cell} i_{el} + (R_c + R_a + R_m) i_{el}^2} \tag{2.7}$$

Therefore, the hydrogen flow rate (mol.s^{-1}) is provided by the following equations [79]:

$$\dot{N}H_2 = \frac{\eta_F . n_C . i_{el}}{z.F} \tag{2.8}$$

-η_F is a Faraday's efficiency resulting in the ratio of the measured hydrogen flow rate to the theoretical hydrogen flow rate which could be generated according to the input energy. Based on an experimental investigation reported in [120], it has been shown that the Faraday's efficiency is roughly equal to η_F = 0.96 for high current densities.

-n_c is number of cells of the electrolyzer (in our case, n_c=3).

-i_{el} is an electrolyzer current (A).

-z is number of electrons exchanged during the reaction. For H_2, z = 2.

-F is a Faraday's constant, 96,485 (C.mol^{-1}).

For a better understanding, the hydrogen flow rate is usually given in standard liter per minute (slpm). In addition, the molar volume of hydrogen V_m can be calculated using the ideal gas law under standard conditions (atmospheric pressure (P=101.3 kPa) and a temperature of 288.15 K (T=15 °C)) as follows:

$$\mathrm{V}_m = \frac{V}{n} = \frac{R_G T}{P} = 0.02365 m^3 \cdot mol^{-1} \tag{2.9}$$

where V is the volume of the gas, n is the number of moles and R_G is the gas constant (8.314 $J.K^{-1}.mol^{-1}$).

Finally, the hydrogen flow rate in slpm can be calculated by the following expression:

$$\dot{\mathrm{V}}H_2 = \mathrm{V}_m \cdot 60 \cdot 1000 \cdot \dot{N}H_2 \tag{2.10}$$

2.3.2. Implementation of PEM electrolyzer emulator

First and foremost, before developing the emulator prototype, the various parameters of the equivalent electrical model illustrated in Figure 2-4 must be evaluated. In brief, there are six parameters to consider: the three resistors of the anode side, cathode side, and membrane R_a, R_c, and R_m respectively, the two capacitors for the anode C_a and cathode C_c, and the reversible voltage E. The literature indicates in [84] that the membrane resistor and reversible voltage can be analyzed from a static model characterization, while the four remaining parameters for both RC branches (i.e., R_a, C_a, R_c, and C_c) can be evaluated by using a dynamic model characterization.

As depicted in Figures 2-2 and 2-3, the transient operation has been analyzed for the characterization of the PEM electrolyzer. A least-squares regression technique has been used to obtain the time constant of the transient operation, subsequently the activation resistances and double-layer capacitances [84]. It must be observed that the values of double-layer capacitors estimated for the studied PEM electrolyzer are roughly equal to 37 F; whereas the value for the PEM fuel cells as reported in [118] is a few Farads. For this reason, the supercapacitors have been employed to make the emulator since the capacitance values are very high. On one hand, the dynamics behavior of the PEM electrolyzer may change depending on the operating conditions (i.e., input current supplying the electrolyzer), according to the experiment tests as shown in Figures 2-2 and 2-3. On the other hand, while the estimated parameters in [84] are not optimal for any operating condition, they have provided excellent agreement with the actual dynamic behavior of the PEM electrolyzer. As a result, these parameters have been considered to develop a PEM electrolyzer emulator prototype. The proposed methodology can be applied to different PEM electrolyzers by implementing the model parameter identification as described in [84]. The estimated parameters for the electrical circuit model of the PEM electrolyzer emulator are given in Table 2-1. It should be noted that the PEM electrolyzer emulator type has been realized for a current range of the studied PEM electrolyzer (i.e., up to 20 A). Hence, all the resistors (i.e., R_a, R_c, and R_m) in the emulator have been selected to dissipate a maximum power of 20 A.

Table 2-1. Values of the estimated parameters for the PEM electrolyzer emulator.

Parameters	Value	Unit
E	4.38	V
R_m	0.088	Ω
R_a	0.318	Ω
R_c	0.035	Ω
C_a	37.26	F
C_c	37.26	F

The reversible voltage E is simulated through a voltage generator circuit that has been designed and configured to meet a value close to that required. The circuit starts working to replicate E as immediately as the emulator is operated. The voltage generator circuit is composed of a power MOSFET, diode, resistor, and voltage regulator. The MOSFET features a current sink, enabling current from the input of the emulator to pass through it while keeping a constant voltage. This configuration has been chosen because it is more precise than a simple resistance (whose voltage varies with current) or a series connection of diodes (whose drop voltage depends on the temperature and cannot be imposed). The schematic diagram of the voltage generator is illustrated in Figure 2-5. It relies on a power MOSFET IRFP064 and a silicon-based diode 1N4148 from Vishay Siliconix Company. Additionally, a 1 kΩ resistor is connected between gate and source of the power MOSFET, while the diode is connected between drain (anode part of the diode) and gate (cathode part of the diode) of the power MOSFET. The power MOSFET IRFP064 and silicon-based diode 1N4148 have been chosen based on the gate-source voltage threshold of the IRPF064 that is equal to 4V, while the forward voltage range of the diode 1N4148 is between 0.6 and 1 V depending on the forward current. For this reason, the sum of both voltages allows achieving the reversible voltage of the PEM electrolyzer under study. Moreover, the 1 kΩ resistor has been selected to flow the current through the diode so that it is low enough not to destroy it. Indeed, the low current enables reaching a forward voltage of approximately 0.6 V. Finally, the circuit board of the voltage generates the reversible voltage E as illustrated in Figure 2-7 (see dotted box B) and the power MOSFET IRFP064 and silicon-based diode 1N4148 are shown in the same figure (see dotted box A).

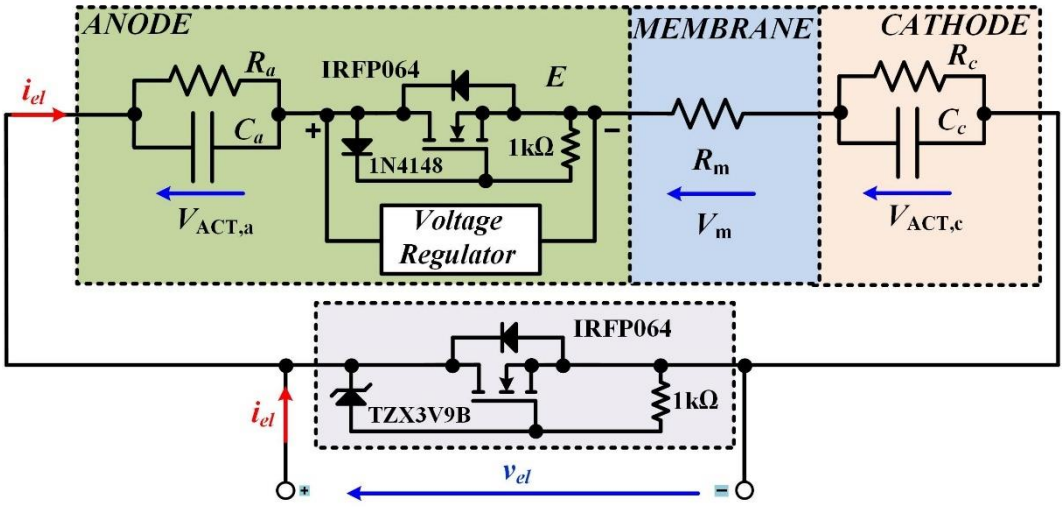

Figure 2-5: The schematic diagram of the voltage generator and stack voltage saturation.

Moreover, a linear voltage regulator LM317 from Texas Instrument Company has been chosen to generate the voltage for the reversible voltage. The architecture of the voltage regulator is illustrated in Figure 2-6. Based on Figure 2-6, the input voltage V_{in} of 12 V is required, it is generated by employing a single-phase transformer and bridge rectifier with a capacitive filter to reduce the ripple.

Therefore, the resistance values of R_1 and R_2 can be calculated by the following expression:

$$E = V_{ref} \times (1 + \frac{R_2}{R_1}) \tag{2.11}$$

where $V_{ref} = 1.25\,V$ By using (2.11), the following values of resistors have been determined: $R_1 = 220\ \Omega$ and $R_2 = 550\ \Omega$.

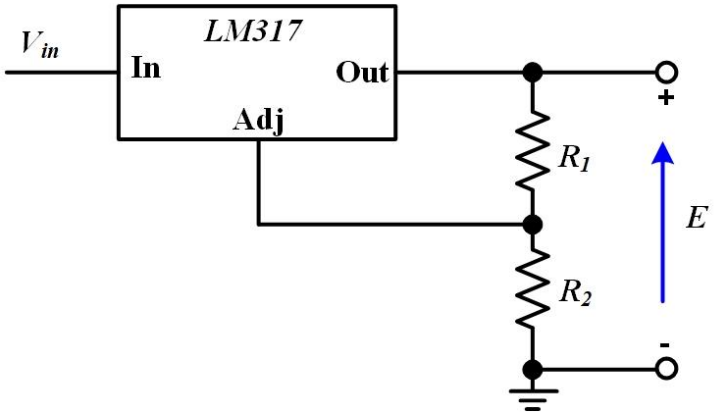

Figure 2-6: The architecture of voltage regulator.

Afterward, three resistors of 0.27 Ω connected in parallel have been employed to realize the resistor modeling the ohmic overvoltage and losses in the membrane. Each resistor can dissipate up to 25 W. Correspondingly, to emulate the overvoltage and losses at the anode side and cathode side, three resistors of 1 Ω (i.e., anode) or 0.1 Ω (i.e., cathode) connected in parallel have been utilized. Each anode and cathode resistor can dissipate 50 W and 10 W respectively. Because the emulator is designed to supply the current up to 20 A, the membrane, anode, and cathode resistors must dissipate power related to the maximum current. As a result, the maximum power it can dissipate is 35.2 W, 127.2 W, and 14 W respectively. Moreover, a 10 Ω auxiliary resistor has been connected in parallel for every part (i.e., anode, membrane, and cathode) to compensate the tolerances. All these resistors can be seen in Figure 2-7, which depicts the completed PEM electrolyzer emulator. Furthermore, all the resistors have been placed on a heatsink for heat dissipation.

In the same way, as mentioned above, the value of both double-layer capacitors at the anode side and cathode side are equal and quite high (i.e., 37 F). We have designed them in different configurations to ensure that the maximum operating voltage was not exceeded. Since the voltage at the anode side is around 6.36 V at 20 A, three supercapacitors of 100 F 2.7V (model EECHL0E107 from Panasonic Company) connected in series have been employed for the anode side. As a result, the capacitance is achieved close to 37 F and the terminal voltage of the supercapacitor is higher than the voltage at the anode side. A resistance of 10 kΩ connected in parallel to each supercapacitor ensures that voltages are partitioned equally. Given that the voltage at the cathode side is lower (around 0.7 V) than

anode voltage, one supercapacitor of 30 F 2.3V (model EECHW0D306 from Panasonic Company)) has been connected in parallel with supercapacitor of 30 F 2.3V (model EECHZ0E335 from Panasonic Company). The connections of the supercapacitors can be seen in Figure 2-8. In addition, the emulator prototype has also two fans to cool the heatsink. The comparison between the estimated and real values of the PEM electrolyzer emulator is given in Table 2-2. It can be observed that the real values of the emulator are quite nearly those of estimated values. Nevertheless, small differences in the values may cause errors in the measurements with the emulator.

Table 2-2. Comparison between the estimated and real values of the PEM electrolyzer emulator.

Parameters	Estimated Values	Real Values	Error
R_m	0.088 Ω	0.09 Ω	0.002 Ω
R_a	0.318 Ω	0.333 Ω	0.015 Ω
R_c	0.035 Ω	0.033 Ω	0.002 Ω
C_a	37.26 F	33.33 F	3.93 F
C_c	37.26 F	33.30 F	3.96 F

Furthermore, relying on Figure 2-1 and the analysis reported in Section 2.1, the maximum voltage at the constant voltage operation is equal 8 V. It has been considered in this PEM electroyzer emulator. The voltage must not exceed 8 V to reproduce such behavior. The voltage clamp circuit that reproduces the saturation is based on the power MOSFET and a Zener diode as illustrated in Figure 2-5.

The operation of this circuit can be expressed as follows: if the voltage between the drain and the source of the MOSFET is less than 8 V, the Zener diode operates as a reverse-biased diode, the current cannot pass through it. The supplied voltage between the gate and the source of the MOSFET is zero and the device remains in the blocking region; signifying it operates in open circuit with high impedance. As a result, it has no effect on the emulator in linear operation since it is a parallel-connected circuit (which shows a low impedance).

By comparison, when the voltage of the emulator attempts to exceed 8 V, the Zener diode acts in the Zener region and operates as a voltage generator, a 5 mA Zener current passing through forces a voltage between the gate and the source of the MOSFET, biasing it to have an 8 V voltage between the drain and the source of the MOSFET. These values have been chosen to best represent the "knee" shape exhibited by the static I-V curve while avoiding an edge caused by sudden transitions, such as from linear to saturation, also in the real circuit. It should be emphasized that this circuit does not need to be turned on from the external since it starts to perform automatically when the voltage electrolyzer approaches 8 V.

To set the rated value of the PEM electrolyzer emulator voltage in the case of a current above 7 A, the same power MOSFET IRFP064 from Vishay Siliconix Company has been employed. A resistor of 1 kΩ is connected between the source and the gate of MOSFET, while a Zener diode TZX3V9B from Vishay Siliconix Company is connected between the drain (cathode part of the Zener diode) and the gate (anode part of the Zener diode) of MOSFET. The power MOSFET IRFP064 and the Zener diode TZX3V9B have been selected because the gate-source threshold voltage of the IRFP064 is equal to 4 V, whereas the maximum Zener voltage of TZX3V9B is equal to 4 V. As a result, the total of both voltages reaches the rated stack voltage of the studied PEM electrolyzer (i.e.,8 V). Similarly to the

voltage generator, a resistor of 1 kΩ has been used for the same purposes. Besides, this small current allows maintaining the Zener diode in avalanche breakdown mode. The power MOSFET IRFP064 and Zener diode TZX3V9B are depicted in Figure 2-7 (see C). The emulator can be applied for different electrolyzer due to the circuitry used to reproduce the reversible voltage and stack saturation. Indeed, the reversible voltage is obtained by a reference voltage that can be modified to the desired value. It may also be adjusted based on the current with an appropriate linear driver. The stack voltage remains constant owing to the stack saturation circuit when the current exceeds a threshold that can be adjusted depending on the behavior of the PEM electrolyzer.

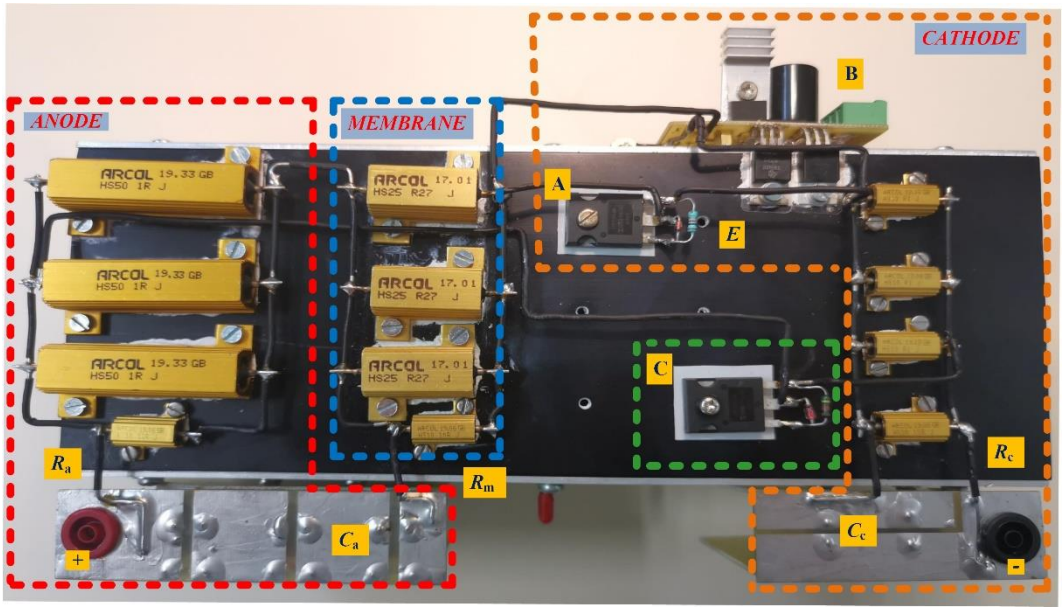

Figure 2-7: Top view of the PEM electrolyzer emulator.

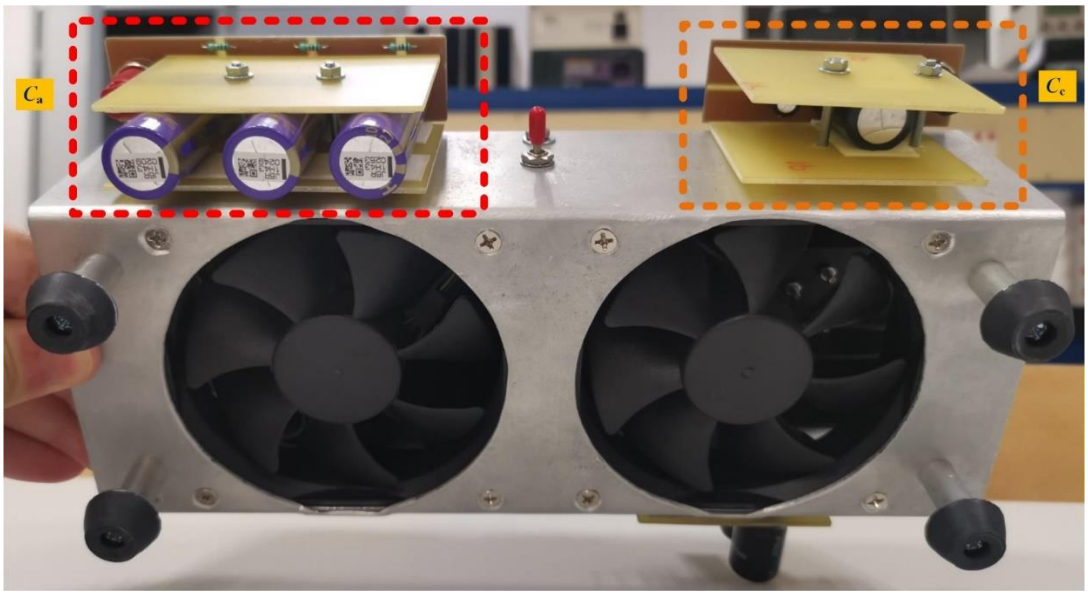

Figure 2-8: Bottom view of the PEM electrolyzer emulator.

The proposed circuit is more general due to these design considerations. Finally, it should be noted that because this is a passive circuit, the power to be dissipated can be handled inexpensively up to a few kW; nevertheless, over this limit, a different emulator solution must be considered. For instance, the proposed circuit can be used to determine the current reference to be extended by a programmable load.

2.3.3. Cost estimation

Based on the previous subsection discussing the realization of the PEM electrolyzer emulator prototype, Table 2-3 summarizes the list of required components and their respective cost. The objective is to estimate the overall cost of the realization of the PEM electrolyzer emulator. All the cost reported in Table 2-3 have been taken from Radiospares components website [121]. From Table 2-3, the overall cost of the emulator is very low (around 160 €) compared to the current costs of PEM electrolyzer stacks. Indeed, based on a PEM electrolyzer manufacturer website FuelCellStore [122], the costs of PEM electrolyzer stacks are quite high. A synthesis of different PEM electrolyzer stack models with their respective costs is provided in Table 2-4. Based on their electrical power and cost, it can be deduced to their cost (€/W). By calculating the average value of the cost (€/W) for each model, an average cost of 18.5€/W has been obtained. Since the developed emulator prototype has been designed for 8 V/ 20 A, the electrical power is equal to 160 W. By combining this power with the average cost of the available electrolyzer in the market, the cost of a PEM electrolyzer at the same power is equal to 2960 €. As a result, an economy of 2800 € can be achieved. It must be noted also that current PEM electrolyzer systems include not only the stack but also ancillaries such as power electronics and hydrogen storage tanks. Therefore, the overall cost of a PEM electrolyzer system must be revised upwards.

Table 2-3. Summary of the required components of the PEM electrolyzer emulator [121].

Element	Number	Unit price (€)	Total price (€)
R_m 270 mΩ 25 W	3	2.7	8.1
R_a 1Ω 50 W	3	3.47	10.41
R_c 100 mΩ 10 W	3	2.05	6.15
R_{aux} 10Ω 10 W	3	2.02	6.06
C_a 100F 2.7V	3	9.654	28.962
C_c 3.3F 2.5V	1	2.85	2.85
C_c 30F 2.3V 2	1	3.94	3.94
Diode 1N4148	1	0.046	0.046
Diode Zener TZX3V9B	1	0.063	0.063
MOSFET IRFP064	2	2.12	4.24
Heat sink 1000 x 120 x 37mm	1	43.57	43.57
Fan 80 x 80 x 32mm	2	12.51	25.02
Red Banana Jack	1	3.56	3.56
Black Banana Jack	1	3.56	3.56
Transformer V_{in} 230V 50 Hz 24 VA, V_{out} 2 x 9V	1	10.11	10.11
Dual High Voltage Schottky Rectifier MBR20150CT	1	0.913	0.913
Linear voltage regulator LM317	1	1.51	1.51
Summary			159.064

Table 2-4. Synthesis of the available PEM electrolyzer models and their respective price [122].

Model	Price (€)	Power (W)	€/W
Titan EZ-60	607	18	33.72
Titan EZ-120	881	36	24.47
Titan EZ-180	1162	54	21.51
Titan EZ-240	1320	72	18.33
Titan EZ-300	1487	80	18.58
Titan EZ-500	1934	160	12.08
Titan EZ-1000	3591	320	11.22
Titan EZ-2000	5179	640	8.1

2.3.4. Errors analysis of the PEM electrolyzer emulator

The components used to realize the PEM electrolyzer emulator on the market are slightly discrepancy from the design value, which might result in a difference between theoretical and experimental results. Consequently, the error in the PEM electrolyzer emulator is discussed and analyzed in this subsection.

The emulator must simulate three main operations are: a) the losses into the electrolyzer, b) the hydrogen production, and c) the transient owing to a rapid current variation. The first two operations are related to steady-state condition, whereas the third is related to the dynamics of the emulator.

In steady-state behavior, the two capacitances can be ignored, the losses are provided by the following equation:

$$P_J = {I_{el}}^2 \, (R_a + R_c + R_m) \tag{2.12}$$

Supposing that the error has no effect on the current since it is supplied by the laboratory DC power source, the error on the losses is expressed by the following equation:

$$\Delta P_j = {I_{el}}^2 \left[\left(\frac{\partial P_J}{\partial R_a}\right)\Delta R_a + \left(\frac{\partial P_J}{\partial R_c}\right)\Delta R_c + \left(\frac{\partial P_J}{\partial R_m}\right)\Delta R_m\right] = {I_{el}}^2 \, [\Delta R_a + \Delta R_c + \Delta R_m] \tag{2.13}$$

This error relies only on resistance tolerances, and it can be further reduced by connecting more resistances in parallel. In fact, the error is divided by *n* by connecting *n* resistances of the same value in parallel. In this emulator, a tolerance $\Delta R = 5\%$ of resistance have been selected, moreover, three resistances have been employed in parallel for the anode side, cathode side, and membrane resistance. The error on losses evaluation can be calculated by:

$$\Delta P_j = \frac{{I_{el}}^2}{n} \, [\Delta R_a + \Delta R_c + \Delta R_m] = {I_{el}}^2 \Delta R \tag{2.14}$$

The equivalent power of hydrogen is determined by:

$$P_H = I_{el} \, E \tag{2.15}$$

And the error depends on *E* is given by:

$$\Delta P_H = I_{el} \, (\Delta E) \tag{2.16}$$

The reversible voltage *E* is supposed by the LM317 voltage regulator, which features a load regulation accuracy of 1.5%.

Subsequently, the error on the transient due to a step current is mostly determined by cathode behaviors because the anode voltage remains constant at first owing to the high time constant. The electrical configuration scheme to assess the error during transient operation is depicted in Figure 2-9.

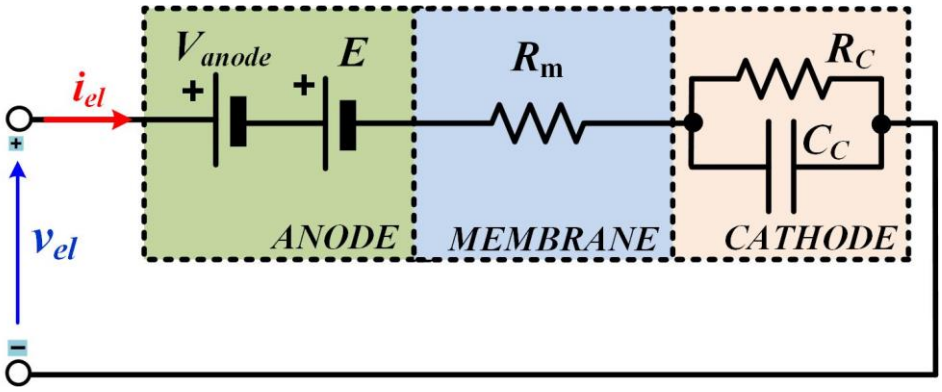

Figure 2-9: Equivalent electric scheme to evaluate the error on the voltage after a step current solicitation.

The voltage after a step supplied current is given by:

$$V(t) = E + V_{anode} + I_{el} * \left[R_m + \left(1 - e^{-\frac{t}{\tau}}\right) * R_c\right] \tag{2.17}$$

The error on the voltage depends only on the internal resistance and it occurs immediately after the current change, meaning for t = 0^+. The error on the voltage can be expressed by:

$$V\Delta(t = 0^+) = I_{el}\,\Delta R_m \tag{2.18}$$

Therefore, a slight error is expected, differently during the transient, the contribution of the cathode side must be considered:

$$\begin{aligned} \Delta V(t > 0^+) &= I_{el}\left[\Delta R_m + \left|\frac{\partial V}{\partial R_c}\right|\Delta R_c + \left|\frac{\partial V}{\partial C_c}\right|\Delta C_c\right] \\ &= I_{el}\left[\Delta R_m + \left|1 - \left(1 + \frac{t}{R_c C_c}\right)e^{-\frac{t}{R_c C_c}}\right|\Delta R_c + \left|\frac{t}{{C_c}^2}e^{-\frac{t}{R_c C_c}}\right|\Delta C_c\right] \end{aligned} \tag{2.19}$$

The two coefficients multiplied by ΔRc and ΔCc are displayed in Figure 2-10 according to the time. It can be observed that despite the coefficient due to capacitance being affected by the high tolerance of supercapacitor (80% in the worst case), it is less than the error due to cathode resistance. After the step current roughly 10s, the error is expected to slightly increase due to the non-linearity of the supercapacitor.

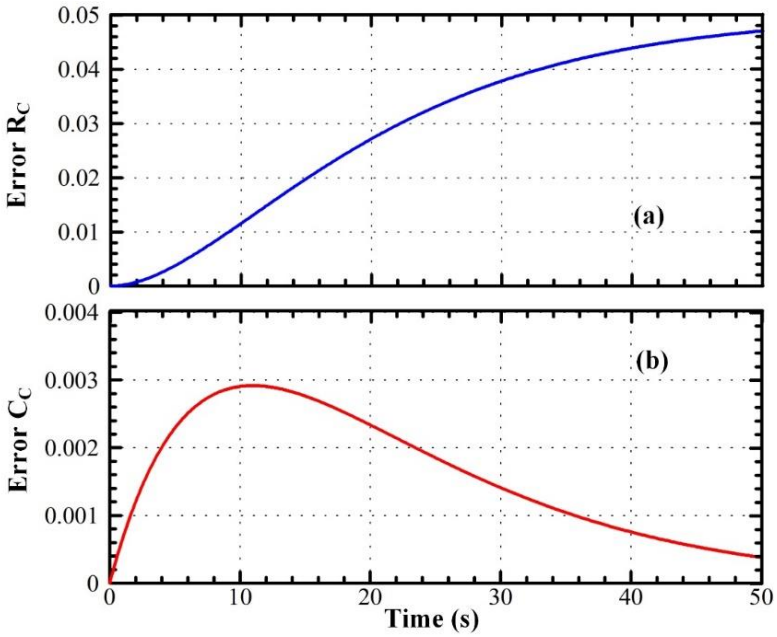

Figure 2-10: Error due to the cathode resistance (a) and due to the cathode capacitance (b).

2.4 Experimental validation of PEM Electrolyzer emulator

2.4.1. Description of the experimental test bench

This subsection aims to evaluate the performance of the PEM electrolyzer emulator in replicating the static-dynamic behavior of a real PEM electrolyzer once it has been analyzed, designed, and implemented. Therefore, an experimental platform has been developed in the laboratory as illustrated in Figure 2-11. The experimental platform consists of the following component: (1) a dSPACE control desk, (2) a DS1104 controller board, (3) a 4-channel oscilloscope, (4) a DC power supply, (5) a laptop with a virtual control panel controlling the DC power supply, (6) the developed PEM electrolyzer emulator, (7) a measurement board, (8) the real PEM electrolyzer stack, and (9) a transformer 230 V/9 V 50 Hz.

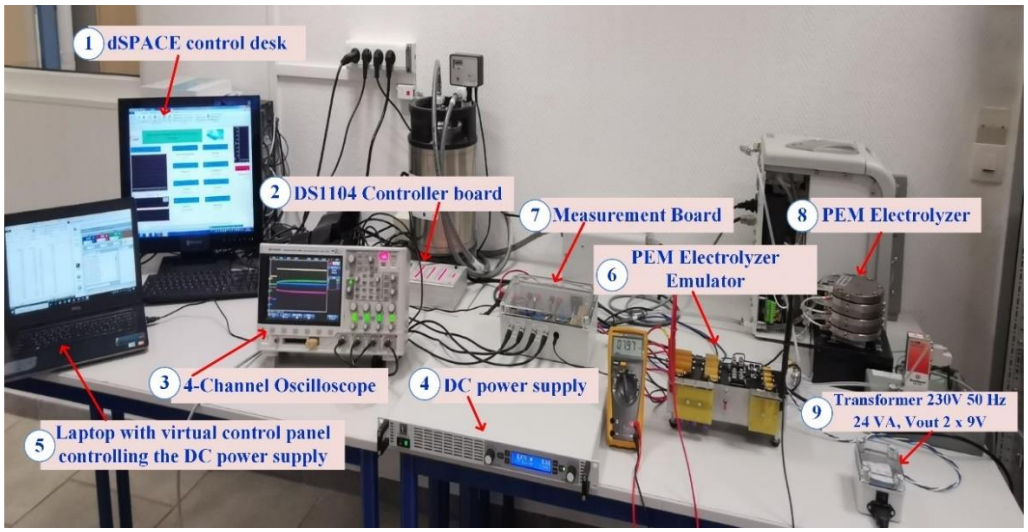

Figure 2-11: Realized experimental test bench to validate the PEM electrolyzer emulator.

Equations (2.7) and (2.10) have been performed into a dSPACE DS1104 controller board by employing Matlab/Simulink software. By measuring the electrolyzer current, these equations enable for real-time calculation of the hydrogen flow rate and the energy efficiency of the electrolyzer. Besides, the electrical power P_{el} of the electrolyzer is determined through the electrolyzer voltage and current. A configuration illustration of this implementation is depicted in Figures 2-12 and 2-13. On one hand, the experimental test rig designed to obtain the data by the real electrolyzer is shown in Figure 2-12. The current is supplied from the DC power supply to the electrolyzer. The dSPACE™ board is employed to handle the supply as well as to plot data by the oscilloscope and collect it for comparison with the emulator. On the other hand, the test rig configuration to assess the emulator is displayed in Figure 2-13; the dSPACE™ board receives voltage and current from the emulator, which controls the same power supply. Finally, the dSPACE™ board allows for the visualization of output signals. Indeed, the dSPACE™ control desk interface can monitor all data related to the PEM electrolyzer emulator or the real electrolyzer (i.e., current, voltage, power, hydrogen flow rate, and energy efficiency).

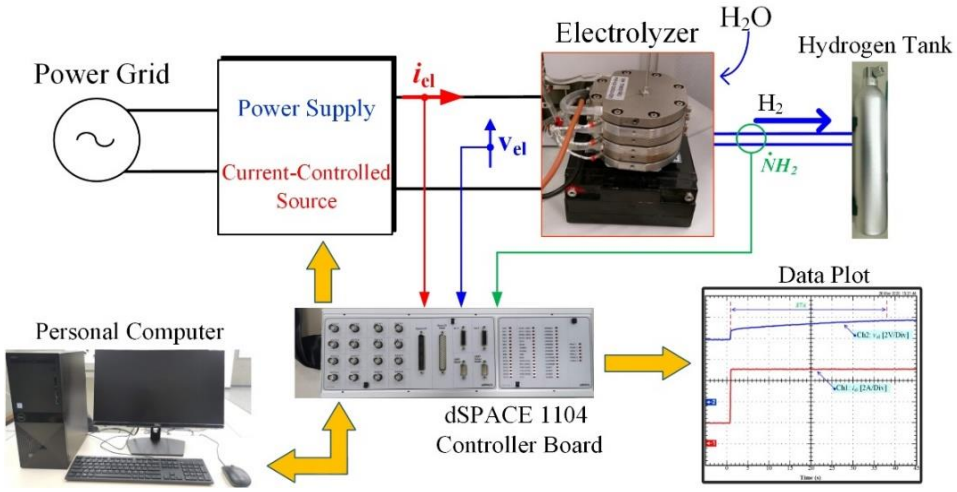

Figure 2-12: Block diagram of the test rig to acquire data by the electrolyzer.

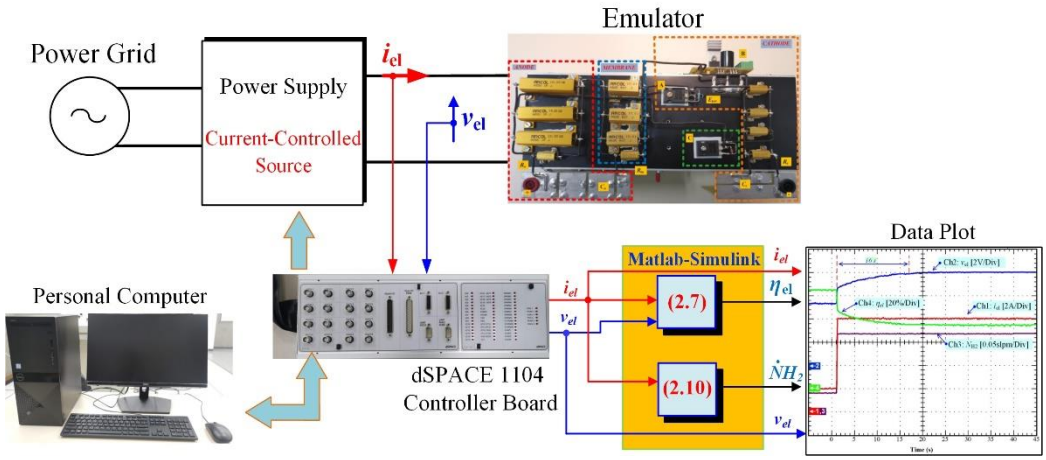

Figure 2-13: Block diagram of the test rig to test the emulator.

Besides, the current and voltage of the PEM electrolyzer emulator and the real electrolyzer are obtained by a measurement board (6). It is composed of a current and voltage sensor as well as a low-pass filter. To supply the linear voltage regulator LM317 with a DC voltage of 12 V, the transformer 230 V/9 V 50 Hz is connected to a single-phase diode rectifier (as indicated in subsection 2.3.2). Finally, the DC power supply is controlled via a laptop control panel to provide different current profiles to the PEM electrolyzer emulator and the real electrolyzer.

2.4.2. Experimental results

Firstly, the response of the PEM electrolyzer emulator to a step current from 2 to 8 A and vice versa has been investigated through experimental tests. In addition, the experimental tests have considered the hydrogen flow rate and energy efficiency acquired from the DS1104 controller board. The obtained results are illustrated in Figures 2-14 and 2-15. In particular, the response of the emulator because of a step-up current from 2 up to 8 A is shown in Figure 2-14; while the response of the emulator because of step-down current from 8 down to 2 A is shown in Fig. 2-15. A time scale of 5 s has been selected to highlight the dynamic response of the PEM electrolyzer emulator and steady-state operation.

Based on Figures 2-14 and 2-15, it can be noted that the PEM electrolyzer emulator can replicate the sudden increase voltage in the ohmic part, as well as the slow and rapid dynamics of the activation part. Hence, the steady-state voltages at the end of the obtained results are equal to 8 V and 5 V in Figures 2-14 and 2-15, respectively.

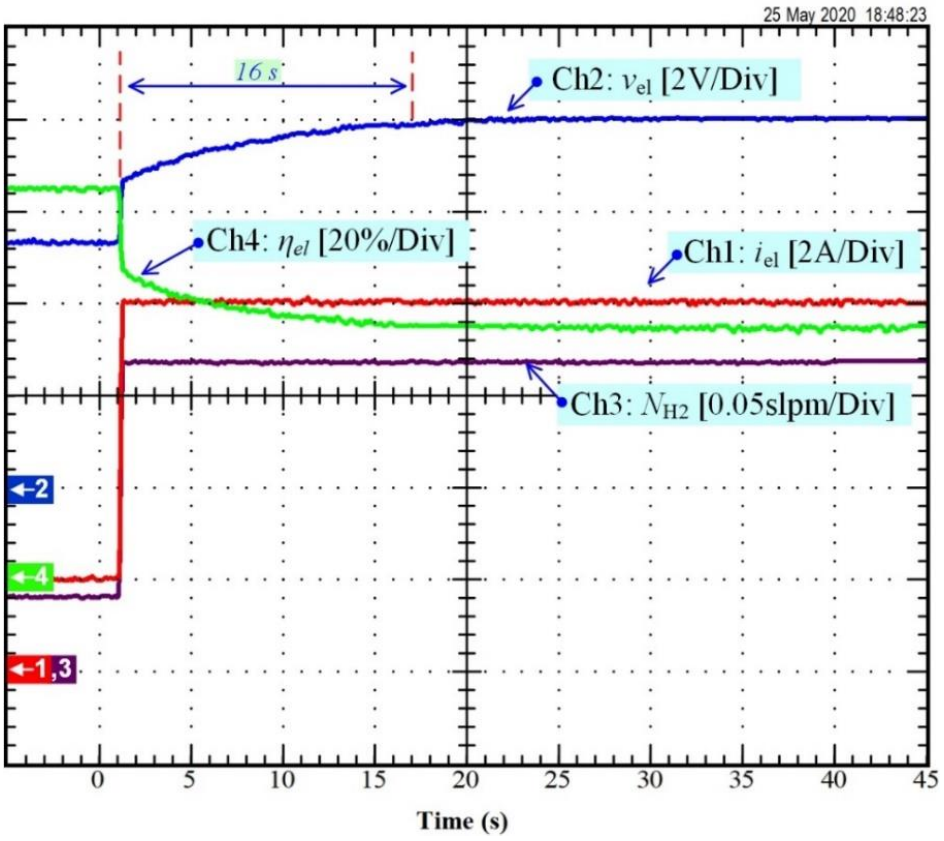

Figure 2-14: Voltage response because of a rising step current from 2 to 8 A.

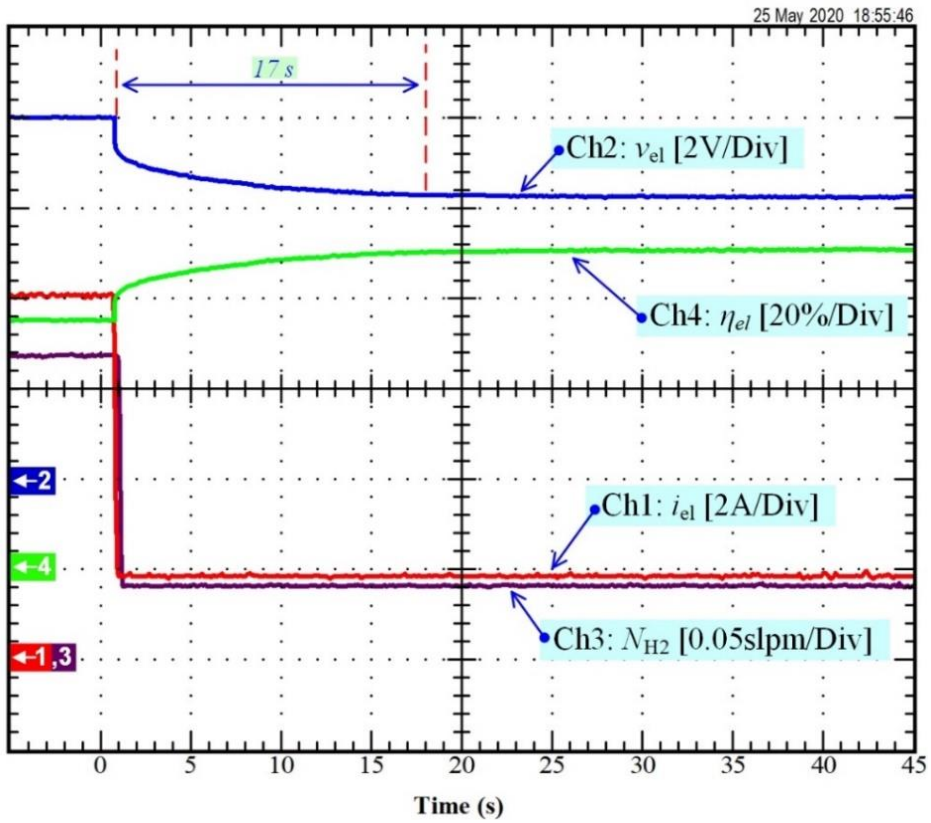

Figure 2-15: Voltage response because of a falling step current from 8 to 2 A.

For the first test reported in Figure 2-14, the steady-state operation is reached in 16 s; while for the second test in Figure 2-15, the steady-state operation is reached in 17 s. Moreover, based on Figure 2-14, it can be observed that the voltage of the PEM electrolyzer emulator is limited to the threshold voltage (i.e., 8 V) as emphasized in subsection 2.3.2 with the obtained static voltage-current curve. Relying on equations (2.7) and (2.10), the hydrogen flow rate increases when the electrolyzer current is increased; while since energy efficiency is inversely related to voltage, it decreases when voltage increases.

Afterward, the obtained static characterization of the realized PEM electrolyzer emulator has been compared with the static characterization of the real studied PEM electrolyzer as depicted in Figure 2-16. It can be noted that the emulated static characterization of realized PEM electrolyzer emulator is similar to the real studied PEM electrolyzer. Indeed, the voltage operation of the developed PEM electrolyzer emulator at a constant stack voltage (i.e.,8 V) when the current over 7 A has been considered.

Based on Figure 2-16, the voltage of the designed PEM electrolyzer emulator is restricted at 8 V for a current higher than 7 A. In conclusion, the developed PEM electrolyzer emulator can reproduce the static characterization precisely and meet the constant stack voltage region. The percentage errors of the worst-case range from 5% to 10%.

It is a minor inaccuracy in absolute terms, but it is acceptable for the purpose for which the emulator has been designed, which is to test power converters designed to supply electrolyzers because the voltage provided by a switching converter is impacted by a few percent ripple due to switching.

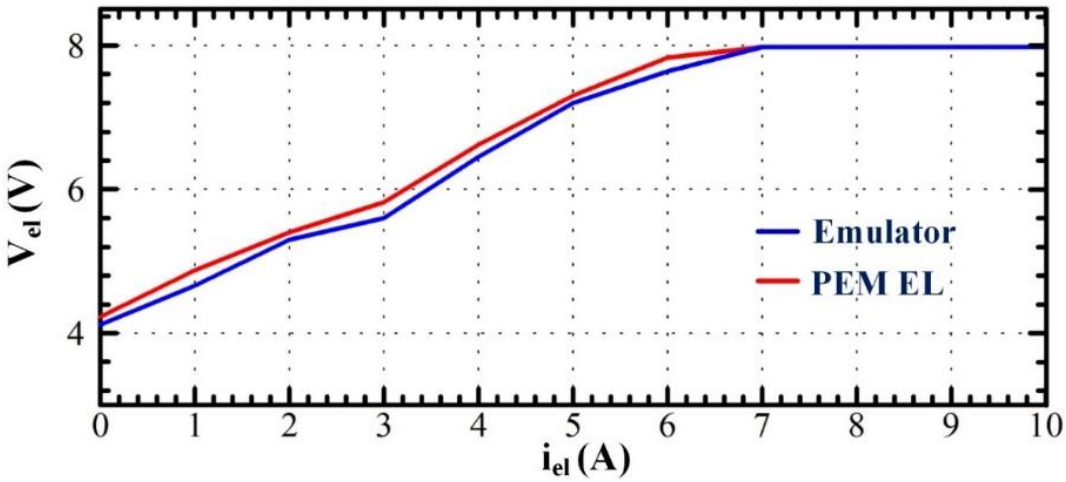

Figure 2-16: Comparison of the static characteristic between the developed emulator and real electrolyzer.

Finally, the same current steps that those applied for the first experimental test have been employed to assess the effectiveness of the developed PEM electrolyzer emulator. The comparison for dynamic operations between the obtained results with the designed PEM electrolyzer emulator and the real studied PEM electrolyzer are analyzed and provided in Figures 2-17 and 2-18. On one hand, for step current rising from 2 to 8 A as illustrated in Figure 2-17, the designed emulator can replicate the real voltage response of the electrolyzer despite some noticeable errors. During the transient operation, the error of voltage ε between the emulator and real electrolyzer less than 1 V (approximately 7.5 % of the steady-state value, 8 V) is especially noticeable. However, the beginning and steady-state voltages meet the stack voltage of the real electrolyzer. On the other hand, for the step current falling from 8 to 2 A as depicted in Figure 2-18, the obtained voltage result of the emulator presents an excellent precision in comparison to the voltage of the real electrolyzer response. In fact, the maximum voltage error less than 0.5 V (roughly 4 % of steady-state value, 8 V) is perceptible in transient and steady-state operations. These additional errors can be described by the fact that the direct dynamics (i.e., when increasing the current) and inverse dynamics (i.e., when decreasing the current) are different as analyzed in subsection 2.2.2 (i.e., Figures 2-2 and 2-3).

Nevertheless, direct dynamics are particularly significant when testing DC/DC converters to feed an electrolyzer since one of the objectives of the test is to minimize voltage overshoots without decreasing the dynamic of the converter. These tests are harmful to a real electrolyzer. For the additional investigation, it would be interesting to study the direct and inverse dynamics of several PEM electrolyzers models to draw conclusions regarding dynamics modeling. However, this emulator enables an accurate reproduction of the real voltage response of the electrolyzer while minimizing errors (the maximum percentage error is equal to 8.75 %).

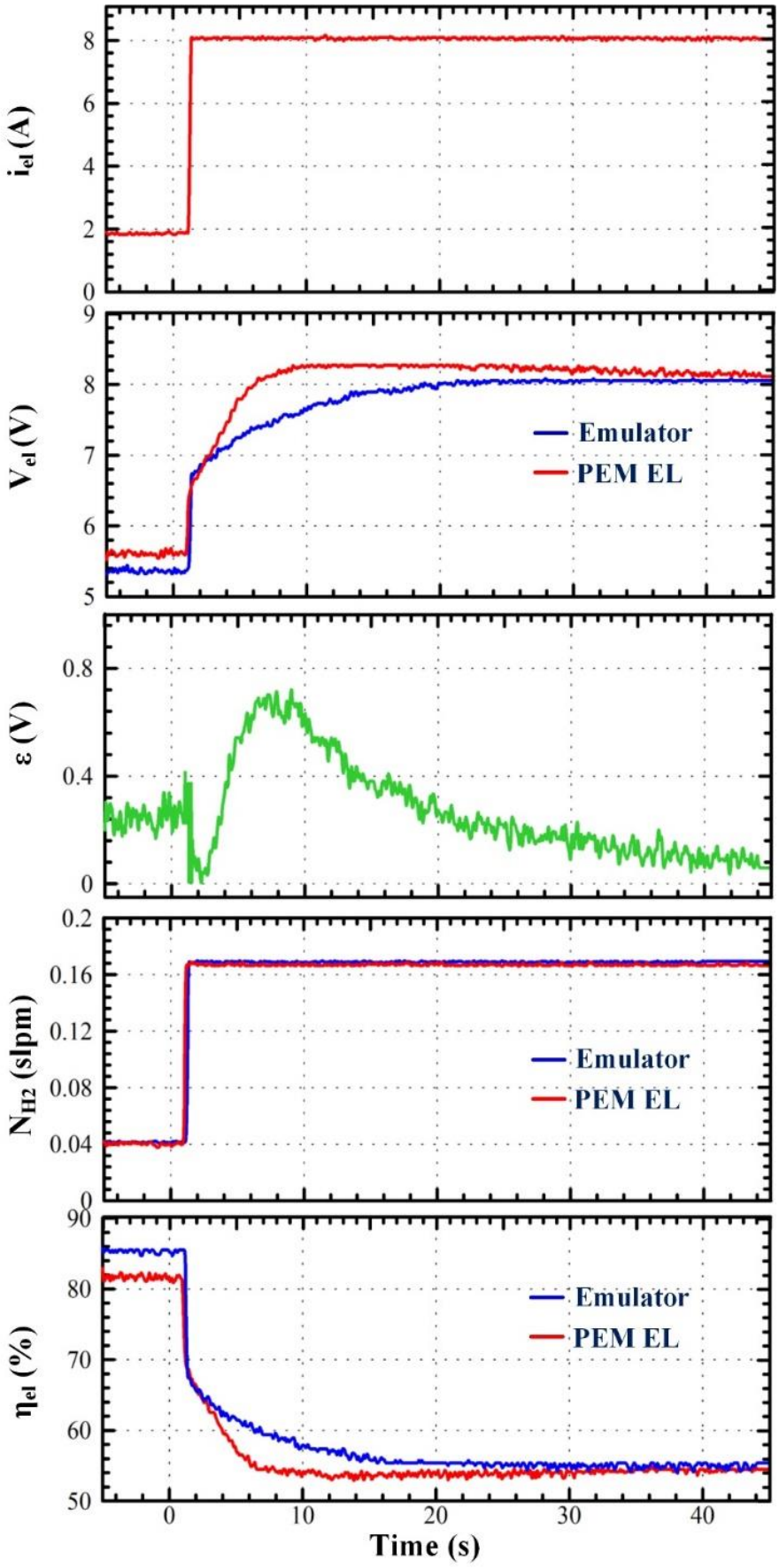

Figure 2-17: Comparison between the developed emulator and real electrolyzer for a step current from 2 to 8 A.

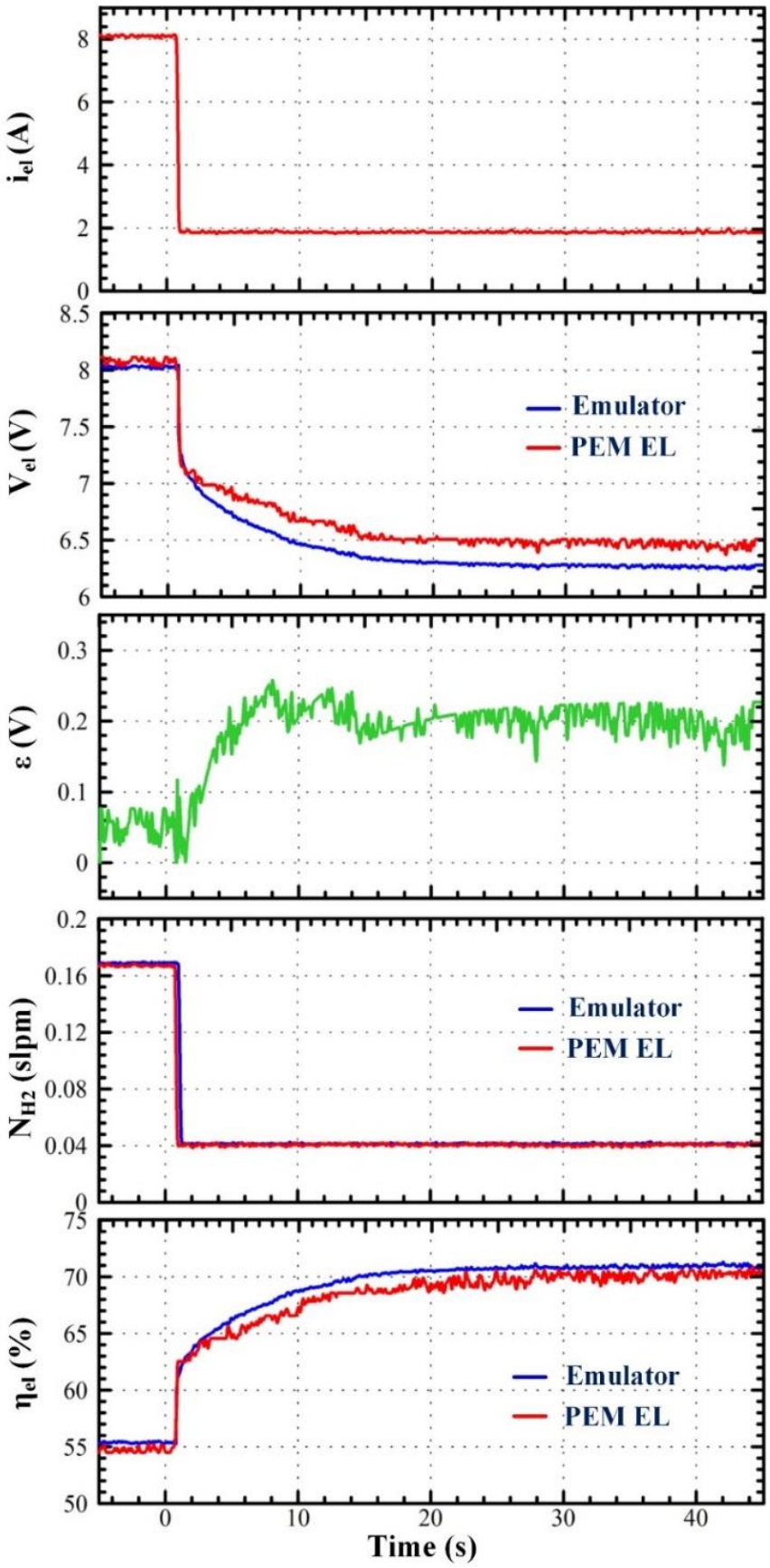

Figure 2-18: Comparison between the developed emulator and real electrolyzer for a step current from 8 to 2 A.

As predicted, the maximum error happens during the transient operation following the step current for t = 10 s. It is consistent with the use of constant capacitances and the error analysis in Figure 2-10, which illustrates that the maximum error occurs around t = 10 s.

As concerns, the voltage differential that occurs during rising and falling current, it can be highlighted that they depend on the different behavior of the electrolyzer as well as the different impedance of the power current supply. This behavior has not affected the stability when power converters are employed with a constant parameter emulator as a load. Indeed, the hypothesis of similar dynamic characteristics is enough to analyze the transfer function of a power converter loaded by an emulator [38].

The percentage maximum error has been estimated for several experiments with a 1A step current. Moreover, the root-mean-square-error normalized as nRMSE and the coefficients of variation root-mean-square-error as CV(RMSE) are provided in Equation 18 and 19, respectively since they have been used to measure the difference between prediction values (sample or population values) by a model or estimator and the observation values.

$$nRMSE = \frac{1}{Y_{max} - Y_{min}} \sqrt{\frac{\sum_{i=1}^{N} (Y_i - \widehat{Y}_i)^2}{N}} \tag{2.20}$$

$$CV(RMSE) = \frac{1}{Y} \sqrt{\frac{\sum_{i=1}^{N} (Y_i - \widehat{Y}_i)^2}{N}} \tag{2.21}$$

Based on (2.20) and (2.21), Y_i is the voltage of the designed emulator (corresponding to the predicted time series) and $\widehat{Y}_i$ is the voltage of the real electrolyzer.

The comparison in terms of errors of voltage profiles acquired by the developed emulator and the real electrolyzer is given in Table 2-5. It can be observed that in the worst-case situation, which corresponds to a current step from 2 to 8 A, the maximum percentage inaccuracy is 8.75 %. By comparison, the error percentage of other cases is always less than the worst-case (i.e., from 2.2 % to 4.3%). The fluctuations of the percentage error in the other cases are owing to the fixed equivalent capacitance, which implies a distinct trend after around 10 s of the current step is employed. In addition, the case of step current from 5 to 4 A presents the worst obtained result of both nRMSE and CV(RMSE) while there are small differences in the other cases. It is the optimal trade-off that can be achieved with the selected component values. In terms of minimizing errors, it should be recognized that a switching converter is used to power the power supply, which is a current-controlled current source. Therefore, switching noise effects the voltage and it is also difficult to decrease the error below a few percent. For instance, a ripple of 0.4 V is noticed on a voltage of 7.66 V. Finally, in comparison to using a circuit without dynamics operation, as discussed in [84], the observed errors are significantly reduced.

Since the real PEM electrolyzer stack is quite expensive, and to minimize deterioration, this developed emulator could be useful for testing new DC-DC converter topologies and their control. Indeed, the design and control of DC-DC converters are now critical issues in the widespread adoption of PEM electrolyzer technology.

It should be noted that a single cell and a full-stack PEM can be emulated using the proposed model. The equivalent model in the first case describes the physical behavior of the cell, otherwise, the stack is represented by an equivalent circuit. The supplementary circuit parallel connected to the equivalent model can be eliminated if the electrolyzer static characteristic does not show voltage saturation region.

Table 2-5. Comparison among errors between voltage profiles obtained by the emulator and by the electrolyzer.

CURRENT STEP	Maximum % Error	nRMSE	CV(RMSE)
From 2 up to 8 A	8.75%	0.1162	0.0451
From 8 down to 2 A	3.125%	0.0948	0.0225
From 3 up to 4 A	2.375%	0.2797	0.0204
From 4 up to 5 A	3.625%	0.1830	0.0125
From 5 up to 6 A	4.375%	0.2196	0.0141
From 6 up to 7 A	2.867%	0.2268	0.0151
From 7 down to 6 A	3.375%	0.1851	0.0113
From 6 down to 5 A	2.212%	0.2017	0.0138
From 5 down to 4 A	4.075%	0.4512	0.0331
From 4 down to 3 A	3.125%	0.1861	0.0162

2.5 Conclusion

The objective of Chapter 2 was to design and develop a prototype of a PEM electrolyzer emulator based on the static and dynamic behavior of a commercial PEM electrolyzer NMH2 1000 from HELIOCENTRIS company, to avoid employing a real PEM electrolyzer that might be damaged during experiments. This developed emulator is based on an equivalent electrical model that enables reproducing electrolyzer dynamics as a result of step input current. The comparison between the obtained voltage response with the realized emulator and the real electrolyzer has presented an acceptable result, notwithstanding non-negligible errors on the voltage that have been observed during the transient state, when employed as a load, the proposed circuit enhances the precision of a power converter feeding an electrolyzer. The error of voltage is increased when the current is decreased due to the dynamics of the electrolyzer being special and complicated to model.

Besides, the hydrogen flow rate and energy efficiency of the electrolyzer can be evaluated through a real-time DS1104 controller board. The designed emulator is very useful for performing experiments test. Indeed, it can be applied for a variety of purposes such as assessing new DC-DC converters topologies and their control algorithm. The investigation of new topologies of DC-DC converters and their control laws are currently significant challenges to ease the dissemination of PEM electrolyzers at large scale. The main benefits of this developed emulator are its simplicity and low cost since it implies a few components that can be found easily on the market. Compared to the previously reported PEM electrolyzer emulators, which are mostly dependent on power electronics, these emulators are more complex for practical implementations due to the use of power electronics combined with their control. Besides, these emulators have been designed considering only static operating conditions, whereas dynamic operations are crucial when coupling PEM electrolyzers with RESs.

Finally, a trade-off is essential to replicate transients in different operational conditions to reduce the error between the real system and the designed emulator because the realized emulator reproduces both rising and falling transients in the same way. For future works, it would be interesting to improve the performance of the emulator to replicate the inverse dynamic for falling step currents. In addition, the proposed methodology can be employed to simulate a single cell or a whole stack of the PEM electrolyzer. In the next Chapter, a low-voltage high-power DC-DC converter (i.e., three-level interleaved buck converter) with its control algorithm (i.e., improved sliding mode based-control) is investigated including the principle of operation, the design, and the simulation. The aim is to couple it between RESs with the developed PEM electrolyzer emulator.

Chapter 3
Design, Sizing and Simulation of a Low-Voltage High-Power DC-DC Converter

3.1 Introduction

The main objective of this chapter is to design a three-level interleaved buck converter (TLIBC) according to the specifications of the system, develop a control strategy to ensure the performance of the PEM electrolyzer, and finally confirm its performances through simulations carried out with Matlab Simulink® software. Hence, this chapter is divided into three parts. First and foremost, the state-of-the-art of a TLIBC is introduced. Afterward, the TLIBC operation has been analyzed and detailed (i.e., the mathematical model, the operational, and the switching diagram). Subsequently, the designing, sizing, of TLIBC are carried out for the hydrogen production systems based on low-carbon energy sources. Second, non-linear sliding mode control approaches are presented. Furthermore, improved sliding mode control has been applied and analyzed for TLIBC. Third, the simulation of TLIBC with improved sliding mode control is performed using Matlab Simulink® to evaluate and confirm the performance of the converter and proposed controller.

3.2 The state-of-the-art of a three-level interleaved buck converter

A three-level zero voltage switching (ZVS) pulsed-width-modulation (PWM) has been already proposed in 1992 [123]. The main features of a three-level converter consist on the reduction of the voltage stress of the power switch that is half of the input voltage, and it is very suitable for high and medium power applications [63], [123]–[127]. Normally, the insulated gate bipolar transistor (IGBT) and the metal-oxide-semiconductor field-effect transistor (MOSFET) are used as power switches for high and medium scale respectively [123], [124]. Given that this Ph.D. thesis work is focused on a medium scale, the use of MOSFET has been considered. Two power switches in series are used to substitute a single power switch to decrease the voltage stress on the power switches. Moreover, to guarantee that the two series power switches are subjected to the same voltage stress, a clamping diode and a clamping voltage source are utilized [128], [129]. The three-level power switch cells can be classified into two types based on the connection with the clamping diode and the clamping voltage source [128], [129]. On one hand, the anode of the clamping voltage source is coupled with the drain of the power switch S_1, whereas the anode of the diode is connected at the middle-point of the clamping voltage source and the cathode of the diode is connected at the middle-point of two series power switches [128], [129]. The well-known anode three-level power switch cells is shown in Figure 3-1(a). On the other hand, the cathode of the clamping voltage source is interfaced with the source of the power switch S_2, while the cathode of the diode is interfaced at the middle-point of the clamping voltage source and the anode of the diode is coupled at the middle-point

of two series power switches. It is named cathode three-level power switch cells as shown in Figure 3-1(b) [128], [129].

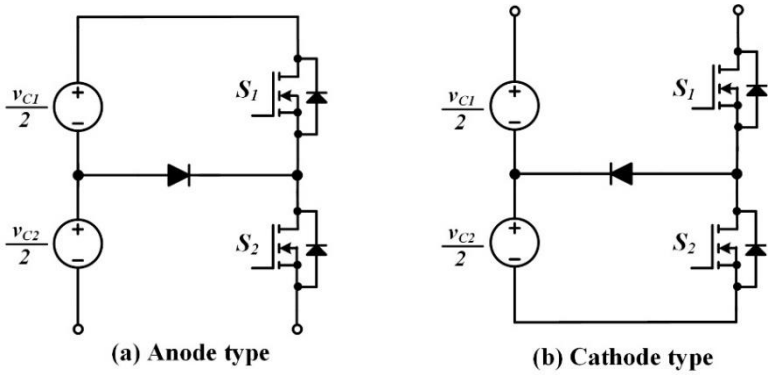

Figure 3-1: Three-level power switch cell [128], [129].

A three-level buck converter (TLBC) can be developed based on a classical buck converter (Figure 3-2(a)) by connecting the additional power switch in series with the original power switch as illustrated in Figure 3-2(b). As a result, the voltage stress of the power switch is decreased. Indeed, the voltage stress of power switch *S* in classical buck converter is equal to input voltage v_{DC}. To divide the half equally of input voltage ($v_{DC}/2$), the two capacitors in series are connected in parallel with an input voltage as depicted in Figure 3-2(c). However, between the two series power switches, there may be minor differences in turn-off characteristics. Therefore, the voltage stress on the two series power switches can be unbalanced. For this reason, the diode has been connected the between middle-point of two capacitors (anode part) and the middle-point two series power switches (cathode part) to ensure that the two series power switches withstand only $v_{DC}/2$ as shown in Figure 3-2(d) [128], [129].

Based on Figure 3-2(d), this circuit is named TLBC with anode three-level power switch cells. On one hand, supposing that the two power switches (S_1 and S_3) of TLBC turn on and off concurrently, the obtained output voltage across the inductor and the capacitor (like the traditional buck converter) is illustrated in Figure 3-3(a). On the other hand, if the power switch S1 is controlled by a PWM and the power switch S3 is still turned on, the output voltage curve across the inductor and the capacitor is depicted in Figure 3-3(b). Thus, three voltage levels are obtained ((+1) v_{DC}, (+1/2) v_{DC}, and 0). Indeed, only ((+1) v_{DC} and (+1/2) v_{DC} are employed [128], [129].

Furthermore, if the inductance value of both classical buck and TLBC is the same, the output current ripple of the TLBC is significantly smaller than classical buck converters. For this reason, the dynamic response of the TLBC has been increased [128], [129].

Nevertheless, the unbalanced voltage in both input capacitors (C_1 and C_2) occurs from this operation. Indeed, when both power switches are turned on, the two-input capacitors supply energy to the load. Afterward, when S_1 is turned off, only the capacitor C_2 supplies energy to the load. It can be noted that the capacitor C_1 supplies energy less than the capacitor C_2 in the duty cycle period. The voltage of the capacitor C_1 is increased equal to the input voltage v_{DC}, while the voltage of the capacitor C_2 is decreased to 0. For this reason, the TLBC as depicted in Figure 3-2(d) cannot perform effectively [128], [129].

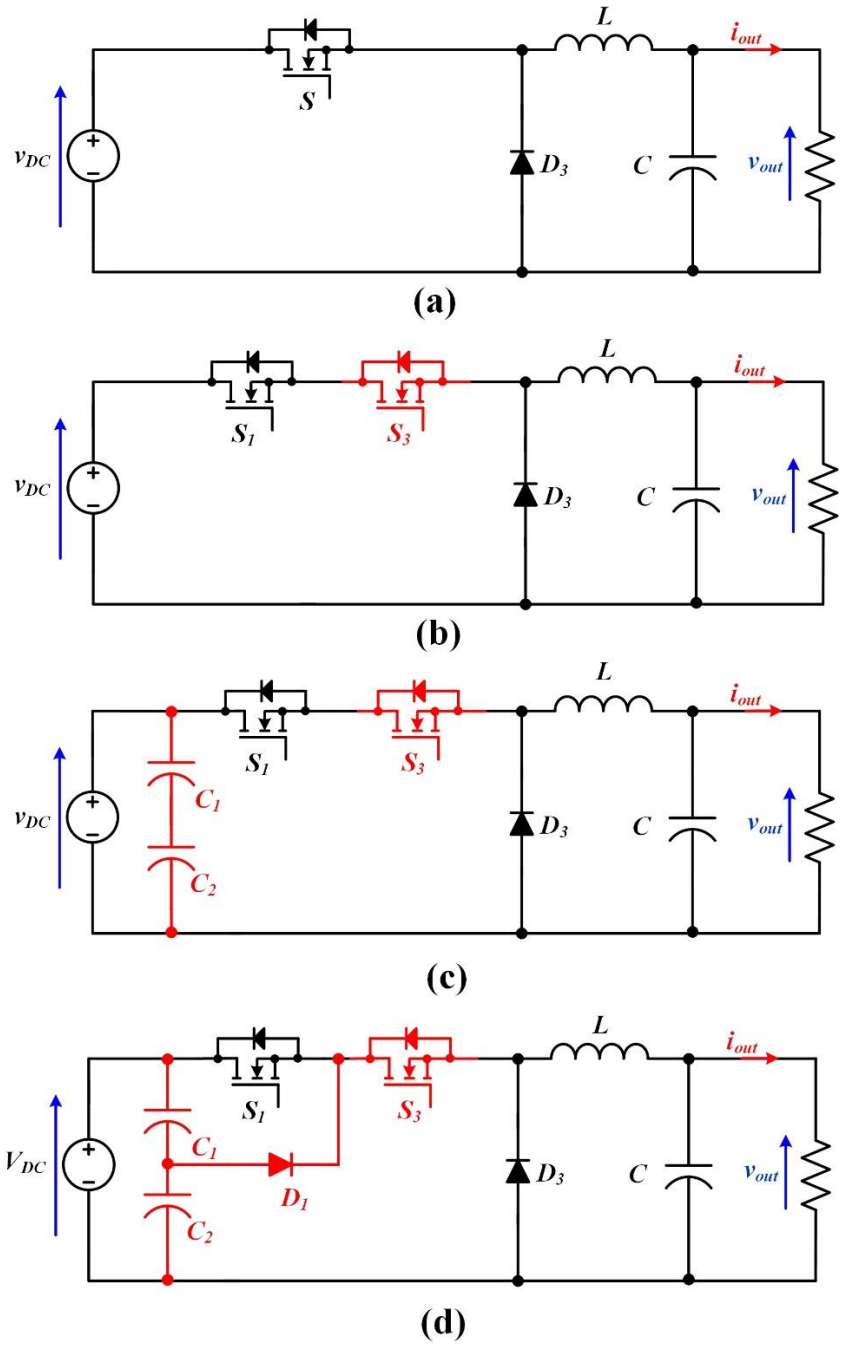

Figure 3-2: Development of three-level buck converter [128], [129].

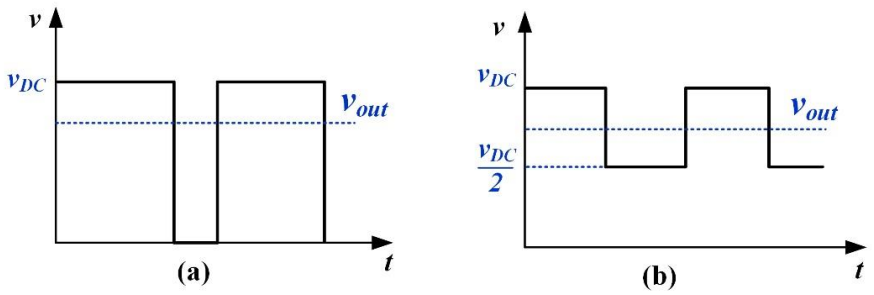

Figure 3-3: The output voltage across the inductor and the capacitor
(a) traditional buck converter, (b) three-level buck converter [128], [129].

In comparison, cathode three-level power switch cells can be applied for a TLBC as depicted in Figure 3-4. Supposing that the operation of the power switch S_4 is always turned on and the power switch S_2 is controlled by PWM, the output voltage waveform across the inductor and the capacitor is similar to a three-level interleaved converter with anode three-level power switch cells. However, during the duty cycle period, the capacitor C_1 supplies more energy than the capacitor C_2. It should be noted that it is opposite to TLBC with anode three-level power switch [128], [129].

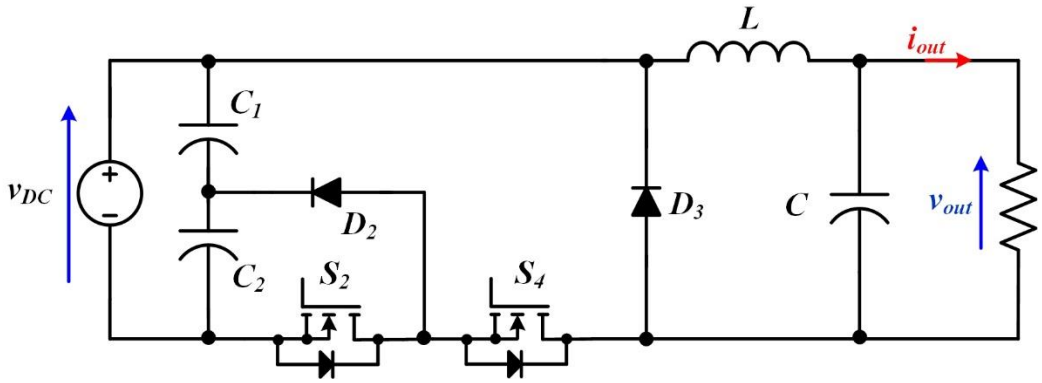

Figure 3-4: Three-level buck converter with cathode three-level power switch cells [128], [129].

To improve the three-level buck converter described above, two types of TLBC (Figure 3-2(d) and Figure 3-4) can be combined into one circuit as illustrated in Figure 3-5. The timing diagram of the combined TLBC is sketched in Figure 3-6. At the first switching period (T'), S_1 is controlled by a PWM, while S_2, S_3, and S_4 are turned on, the C_2 supplies energy more than the capacitor C_1. Subsequently, at the second switching period (2T'), S_2, S_3, and S_4 are turned on, whereas S_1 is controlled by PWM, the C_1 supplies energy more than the capacitor C_2. For this reason, during the next two switching periods, the two input capacitors supply the same amount of energy. Thus, the voltage of the input capacitors is balanced [128], [129].

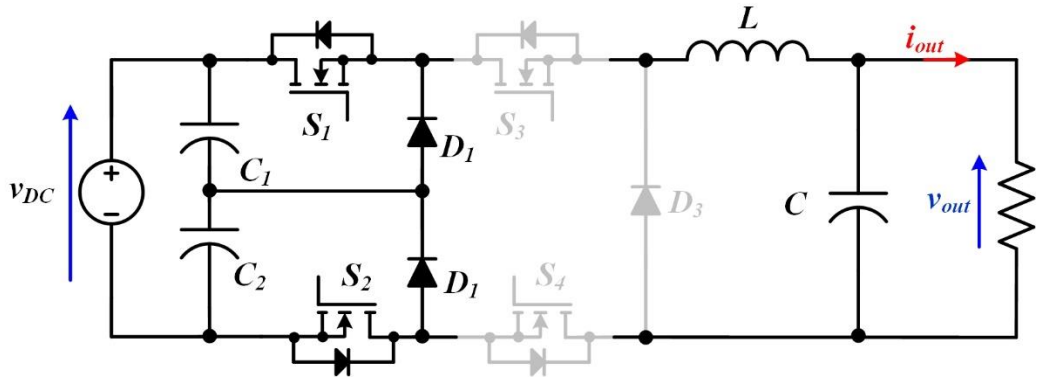

Figure 3-5: Combination of two types three-level buck converter [128], [129].

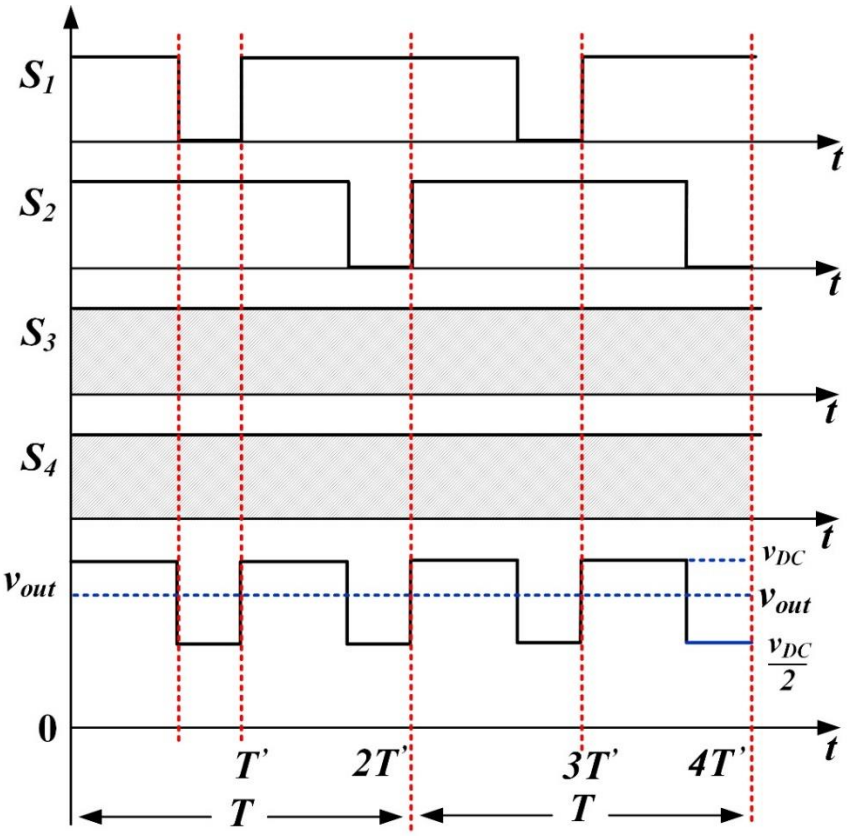

Figure 3-6: The timing diagram of the combined three-level buck converter [128], [129].

It can be observed that the power switches S_3 and S_4 are always turned on, they can be short-circuited directly, allowing S_3 and S_4 to be eliminated. In addition, D_3 is redundant and can be deleted because it is connected in parallel with D_1 and D_2. As a result, the new version of TLBC is improved as depicted in Figure 3-7 [128], [129].

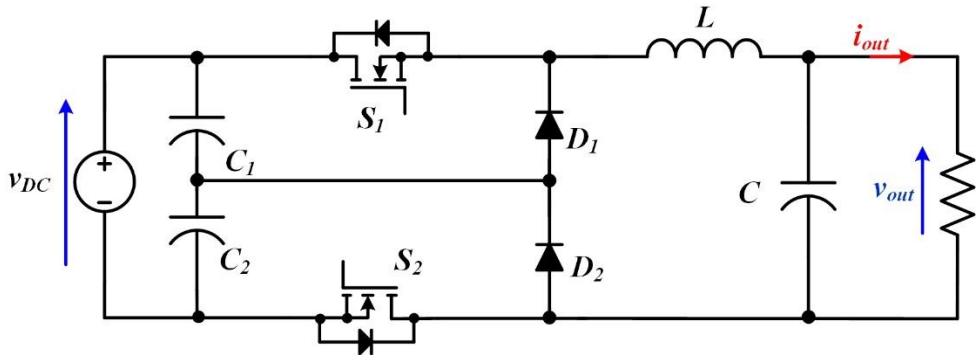

Figure 3-7: Improved three-level buck converter [128], [129].

It should be noted that the control signals of S_1 during the adjoining two switching periods are coupled together. Thus, it can be merged into one switching period. For this reason, the switching frequency of control signals S_1 is decreased to half of the primary switching frequency. The switching periods of control signals S_2 are the same as S_1 [128], [129]. The new switching diagram of improved TLBC is illustrated in Figure 3-8. Based on Figure 3-8, the control signals of S_1 and S_2 are interleaved switching techniques.

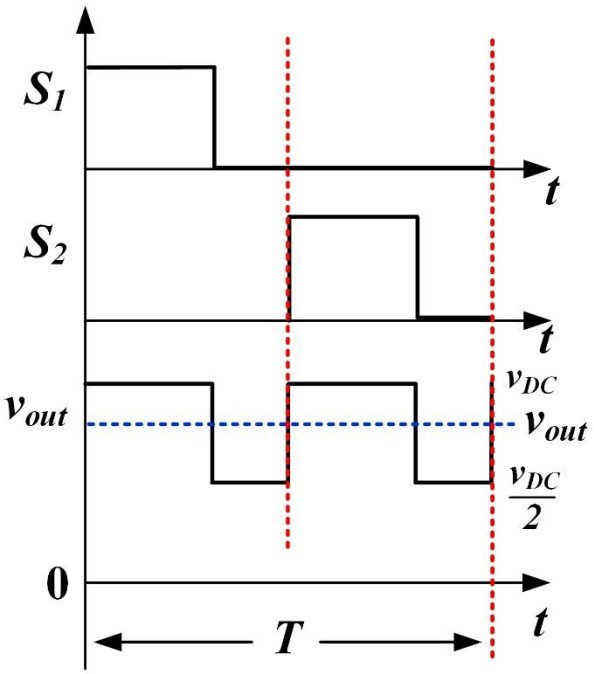

Figure 3-8: The switching diagram of improved three-level buck converter.

The comparison of the normalized inductor current ripple of the classical buck converter and the TLBC is depicted in Figure 3-9 when the inductance value and the switching frequency of both converters are equal. The normalized inductor current ripple is expressed by the following expression [128], [129]:

$$normalized\ \Delta i_L of\ Classic\ Buck = \frac{\Delta i_L\ of\ Classic\ Buck}{Maximum\ \Delta i_L\ of\ Classic\ Buck} \tag{3.1}$$

$$normalized\ \Delta i_L of\ TLB = \frac{\Delta i_L of\ TLB}{Maximum\ \Delta i_L\ of\ Classic\ Buck} \tag{3.2}$$

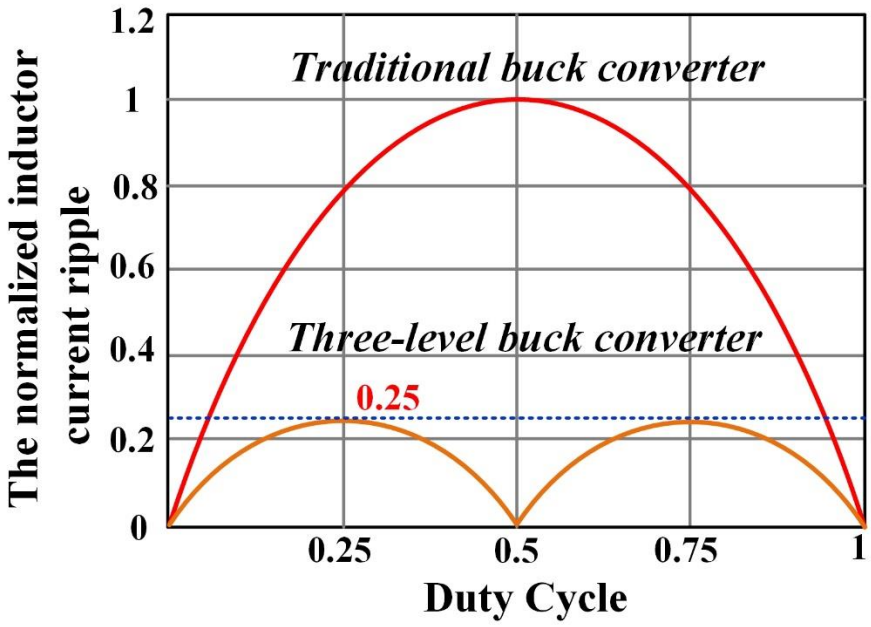

Figure 3-9: The comparison of the inductor current ripple between classic buck converter and three-level buck converter [128], [129].

Referring to Figure3-9, it can be observed that the maximum normalized inductor current ripple of TLBC is a quarter of the traditional buck converter. Moreover, the maximum current ripple of TLBC happens when power switches are performed at a duty cycle equal to 0.25 and 0.75. In comparison, the ripple of the inductor current is canceled when the power switches operated at a duty cycle equal to 0.5.

3.3 Three-level interleaved buck converter

The interleaved technique has been widespread in power electronic topologies to improve dynamic performance, decrease current ripple, increase the power rating, reduce power switching losses, reduce the size of passive components, and enhance the availability in case of power switch failures due to the static redundancy [38], [130]–[132]. For this reason, this technique can be applied for TLBC to meet the requirement of PEM electrolyzer applications as mentioned in Chapter 1, subsection 1.4. The proposed TLIBC configuration is depicted in Figure 3-10.

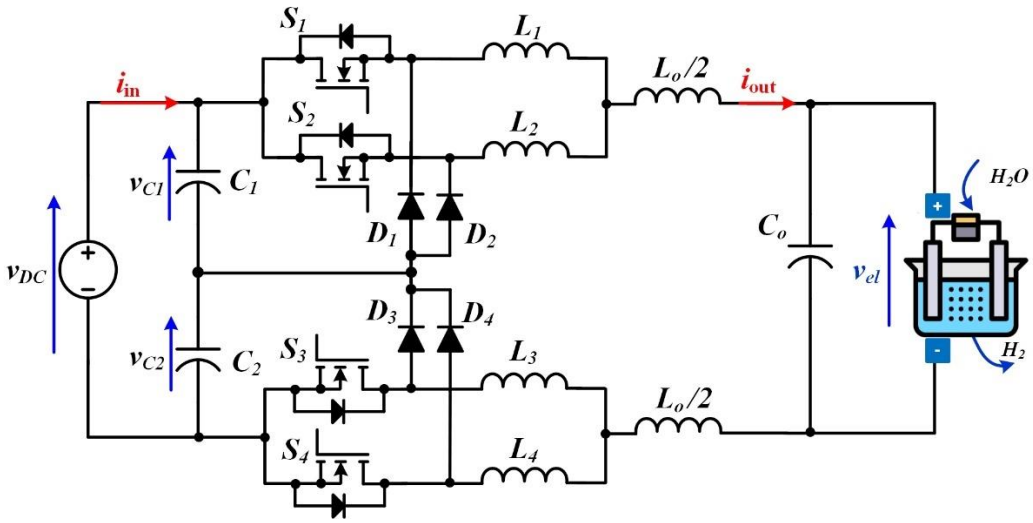

Figure 3-10: Three-level interleaved buck converter [67].

Based on Figure 3-10, the small commutation inductors (L_1, L_2, L_3, and L_4) are used with an interleaved structure to minimize switching turn on and diode reverse recovery losses [67]. In comparison with the original TLBC (Figure 3-7), the voltage stresses of power switches are identical, and the current stresses are only slightly increased. Furthermore, two output inductors $L_{0/2}$ have been added in the output parts of the converter to obtain the zero-current transition (ZCT) feature that achieves the soft switching [67]. Indeed, L_1 and L_2 are connected with $L_{0/2}$ in the upper part, and L_3 and L_4 are interfaced with $L_{0/2}$ in the lower part of TLIBC. The sum of commutation inductors of each part is defined as the commutation inductance L_C and the sum of inductance values is less than the inductance of output inductors $L_{0/2}$ [67].

Moreover, the power of the converter is shared equally among all 4-power switches in the TLIBC ZCT configuration [67]. In the next subsection, the operations of TLIBC are introduced and detailed.

3.3.1 The operations of TLIBC

The control operation signals of the TLIBC rely on the interleaved switching techniques and they are shifted π rad between the power switches located either in the upper part or lower part. It can be noted that in the upper part, the shift of power switches S_1 is stated at 0 rad, while in the lower part the shift of power switches S_3 is stated at $\frac{\pi}{2}$ rad. As a result, the original shift of power switches S_1, S_2, S_3, and S_4 in one switching period are 0 rad, π rad, $\frac{\pi}{2}$ rad, and $\frac{3\pi}{2}$ rad respectively [67].

Indeed, the operations of TLIBC are divided into two modes, (i.e., duty cycle less than 0.25 (D<0.25) and duty cycle range between 0.25 to 0.5 (0.25>D<0.5)) [67].

A. The operations of TLIBC at duty cycle less than 0.25 (D<0.25)

The ideal timing diagram to describe the operation of TLIBC at duty cycle less than 0.25 is depicted in Figure 3-11.

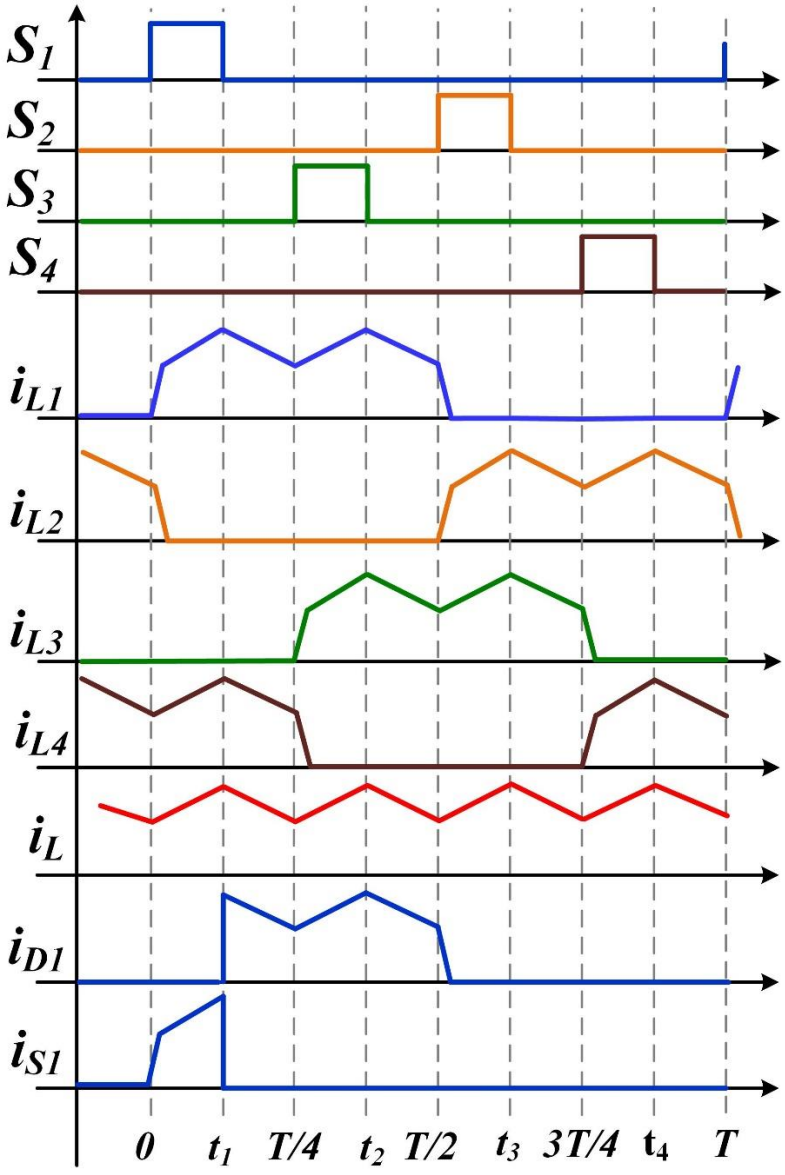

Figure 3-11: Timing diagram of operation for TLIBC at duty cycle less than 0.25 [67].

At the beginning (t= 0), the power switch S_1 turns ON and the diode D_1 is supposed to still turn OFF, the current commutates from L_2 to L_1 with a slope of v_{DC} / 2L_c. As a result, this slope decreases the recovery losses of the diode D_2 and achieved zero current turns ON of the power switch S_1. Moreover, the total current passes via L_1 and the main inductor L_o, while no current flows through the inductor L_2. The current has been increased with a slope of $v_{DC}/2(L_1+L_4+L_0) = v_{DC}/2(L_c+L_0) \approx v_{DC}/2L_0$ [67].

At t_1, power switch S_1 is turned OFF, the main inductor current L_o compels the diode D_1 to turn ON. In addition, the current reduces with the slope v_{el}/L_0. This slope is quite small, and the voltage across L_1 is roughly zero, because of main inductance L_0 is rather large. The consequence is that the current flows through inductor L_2 stills zero and the voltage across L_2 is approximately zero [67].

Afterward, at T/4, the power switch S_3 turns ON and the current commutates from L_4 to L_3 with a slope of v_{DC}/ 2L_c. In the same way as period t=0, the recovery losses of the diode D_4 are decreased and the power switch S_3 turns ON with zero current condition. In this period, the diode D_3 assumes to remain in turn OFF state, the whole current passes through the inductor L_3 and the main inductor L_0, whereas the current flows through the inductor L_3 is equal to zero. Finally, the current has been increased with a slope of $v_{DC}/2(L_1+L_3+L_0) = v_{DC}/2(L_c+L_0) \approx v_{DC}/2L_0$ [67].

At t_2, power switch S_3 is turned OFF, the diode D_3 turns on by the main inductor current, and the current decreases with the slope v_{el}/L_0. Like period t_1, the current slope is rather small due to the main inductance L_0 being quite large and the voltage across L_3 is closed to zero. As a result, the current flows through inductor L_4 and the voltage across L_4 is roughly zero [67].

Subsequently, at T/2, the power switch S_2 turns ON at zero current condition and the diode D_2 turns OFF with no reverse recovery losses. The commutating current switches from L_1 to L_2 with a slope of v_{DC}/ 2L_c from zero. When power switch S_2 turns ON, the converter operates like when power switch S_1 turns ON, with the exception that the current goes through the inductor L_2 replacing L_1 [67].

At t_3, it can be observed that when power switch S_3 is turned OFF, the whole current remains to pass through the inductor L_2, while the current at the inductor L_1 and the diode D_1 are still equal to zero. Consequently, when power switch S_1 turns ON again, the diode D_1 does not suffer from reverse recovery losses and power switch S_1 turns ON at zero current condition [67].

At 3T/4, the power switch S_4 turns ON with zero current condition and the current commutates from L_3 to L_4 with a slope of v_{DC}/ 2L_c, whereas the diode D_4 turns OFF with no reverse recovery losses. Like period $t_{s/2}$ when power switch S_4 turns ON, the converter behaves like when power switch S_3 turns ON. However, the current flows through the inductor L_4 replacing L_3 [67].

Finally, at t_4, when power switch S_4 is turned OFF, the total current continues to flow through the inductor L_4, whereas the current through the inductor L_3 and the diode D_3 is approximately zero. Hence, the reverse recovery losses do not occur when power switch S_3 turns again and power switch S_3 turns ON with zero current condition [67].

As a result, the ideal operation of the converter achieves turns ON zero-current condition of the four power switches and does not have reverse recovery losses of the four diodes [67].

B. The operations of TLIBC at duty cycle range between 0.25 to 0.5 (0.25>D<0.5))

If the duty cycle of the power switches is more than 0.25 as illustrated in Figure 3-12, one of the power switches in the upper part and the lower part are turned ON overlapping. When the duty cycle reaches 0.5, the maximum output voltage is achieved. However, to maintain the main advantage and the efficiency of the TLIBC, the duty cycle must be limited to less than 0.5 to provide time for the diodes to commutate. Moreover, the soft-switching technique will be lost if the duty cycle is too high [67].

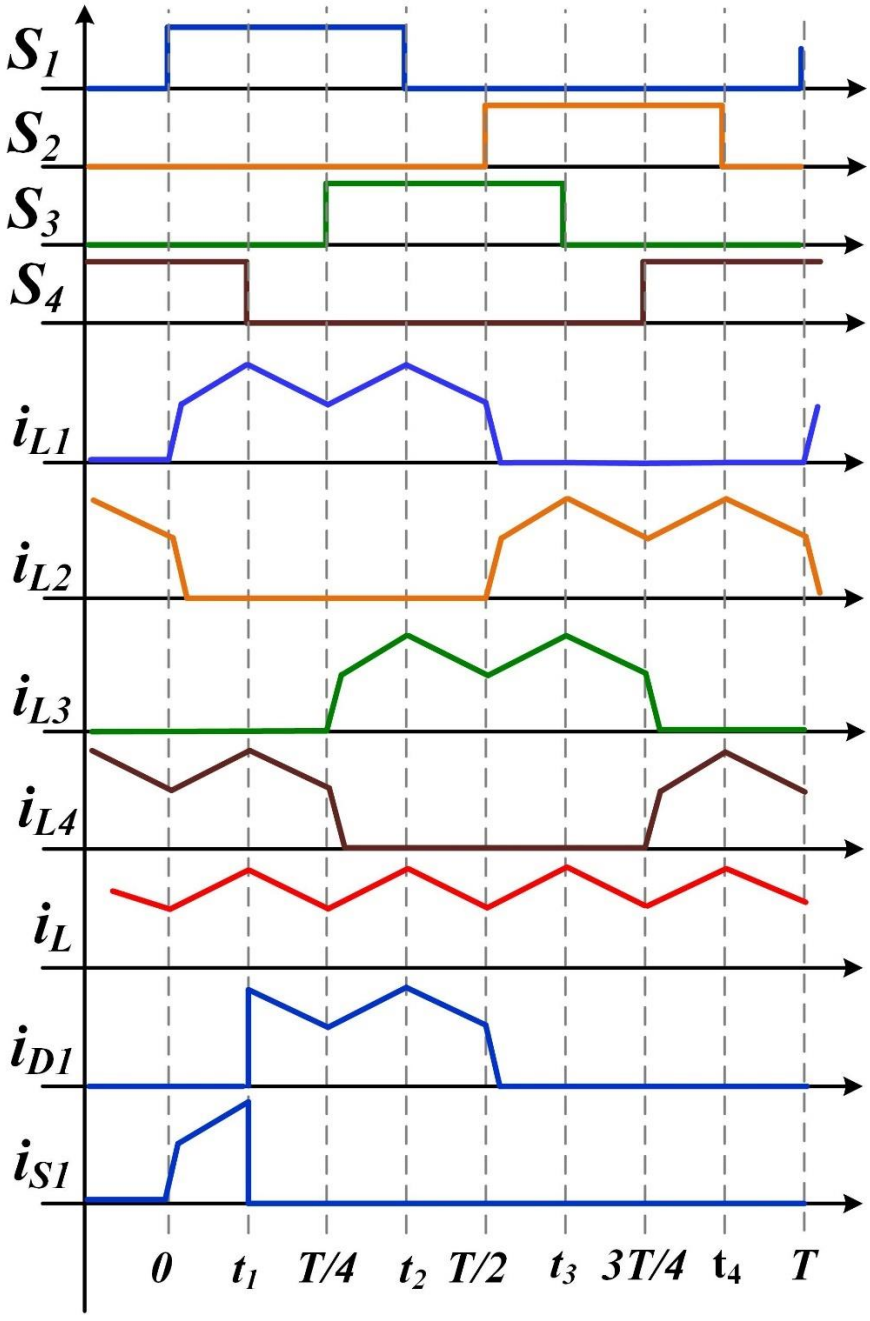

Figure 3-12: Timing diagram of operation for TLIBC at duty cycle higher than 0.25 [67].

3.3.2 Analysis of TLIBC to define step-down voltage conversion ratio

Based on Figure 3-10, it can be observed that the upper part of the TLIBC is the interleaved ZCT buck converter as depicted in Figure 3-13 [133], [134]. For this reason, the voltage conversion ratio of TLIBC can be defined and analyzed based on the interleaved ZCT buck converter.

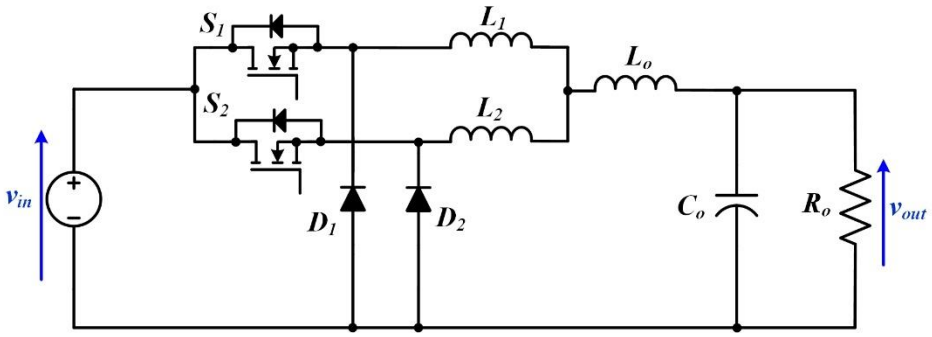

Figure 3-13: Schematic diagram of interleaved ZCT buck converter [133], [134].

The large-signal average switching model has been applied to define the conversion ratio gain of the converter due to its simplicity to model dynamics in a wide range of converters with various control strategies [133], [134]. Hence, the switching network of interleaved ZCT buck converter is sketched in Figure 3-14. Afterward, the input current and the output voltage waveforms have been defined.

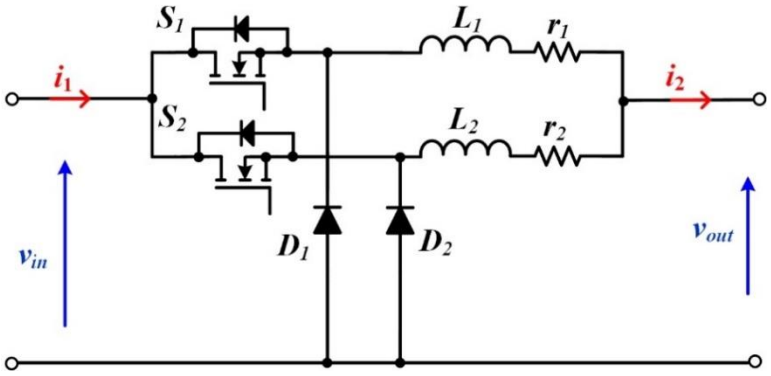

Figure 3-14: Switch network of the interleaved ZCT buck converter [133], [134].

To sketch the input current and the output voltage waveforms, Kirchhoff's current law (KCL) and Kirchhoff's voltage law (KVL) have been used in the switch network of the interleaved ZCT buck converter. In addition, the power switches S_1, S_2, and the diode D_1, D_2 are considered ideal.

The first step is to determine t_1 which means considering the circuit when S_2 turned OFF and S_1 starting turn ON. The KCL and KVL are applied as presented in Figure 3-15.

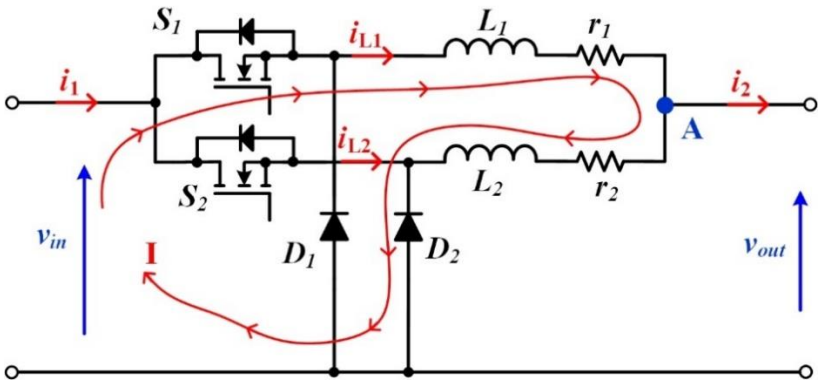

Figure 3-15: Sketch of KCL and KVL in the switch network to determine t_1.

At node A:

$$i_{L1} + i_{L2} = i_2 = I \tag{3.3}$$

Applying KVL along path *I*:

$$L_1 \frac{di_{L1}}{dt} - L_2 \frac{di_{L2}}{dt} + r_1 i_{L1} - r_2 i_{L2} = v_{in} \tag{3.4}$$

If $L_1 + L_2 = L_o$ and $r_1 + r_2 = r$

$$L_o \left(\frac{di_{L1}}{dt} - \frac{di_{L2}}{dt}\right) + r(i_{L1} - i_{L2}) = v_{in} \tag{3.5}$$

Based on Equation 3.3

$$\frac{di_{L1}}{dt} = -\frac{di_{L2}}{dt} \tag{3.6}$$

Substituting (3.6) into (3.5), it yields to:

$$L_o \left(\frac{di_{L1}}{dt} - \left(-\frac{di_{L1}}{dt}\right)\right) + r(i_{L1} - i_{L2}) = v_{in}$$

$$L_o \left(2\frac{di_{L1}}{dt}\right) + r(i_{L1} - i_{L2}) = v_{in} \tag{3.7}$$

$$2L_o \frac{di_{L1}}{dt} = v_{in} - r(i_{L1} - i_{L2})$$

$$\frac{di_{L1}}{dt} = \frac{v_{in} - r(i_{L1} - i_{L2})}{2L_o} \tag{3.8}$$

$$\int_0^I \left(\frac{di_{L1}}{dt}\right) = \int_0^{t_1} \left(\frac{v_{in} - r(i_{L1} - i_{L2})}{2L_o}\right) dt$$

$$I = \frac{v_{in} - r(i_{L1} - i_{L2})}{2L_o} t_1$$

$$\therefore t_1 = \frac{2L_o I}{v_{in} - r(i_{L1} - i_{L2})} \tag{3.9}$$

Afterward, to find output voltage (v_{out}) during $0 < t < t_1$, KCL and KVL have been applied along a path *I* as shown in Figure 3-16.

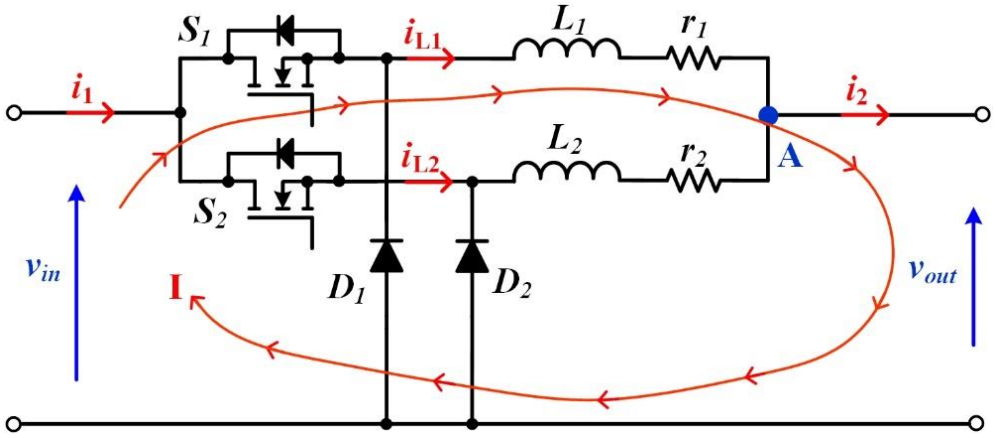

Figure 3-16: Drawing of KCL and KVL in the switch network to determine v_{out}.

The following expression has been retrieved involving v_{out}:

$$L_1 \frac{di_{L1}}{dt} + r_1 i_{L1} + v_{out} = v_{in} \quad ; L_1 = L_o$$

$$v_{out} = v_{in} - L_o \frac{di_{L1}}{dt} - r_1 i_{L1} \tag{3.10}$$

Replacing (3.8) into (3.10), it leads to:

$$v_{out} = v_{in} - L_o \left(\frac{v_{in} - r(i_{L1} - i_{L2})}{2L_o} \right) - r_1 i_{L1}$$

$$v_{out} = v_{in} - \frac{v_{in}}{2} + \frac{r}{2}(i_{L1} - i_{L2}) - r_1 i_{L1}$$

$$v_{out} = \frac{v_{in}}{2} + \frac{r}{2} i_{L1} - \frac{r}{2} i_{L2} - r_1 i_{L1} \quad ; r_1 = r$$

$$v_{out} = \frac{v_{in}}{2} - \frac{r}{2} i_{L1} - \frac{r}{2} i_{L2}$$

$$v_{out} = \frac{v_{in}}{2} - \frac{r}{2}(i_{L1} + i_{L2}) \tag{3.11}$$

Substituting (3.1) into (3.11), it yields to:

$$v_{out} = \frac{v_{in}}{2} - \frac{r}{2} I \tag{3.12}$$

Thus, relying on equations 3.6 and 3.9, the input current and the output voltage waveforms can be drawn as illustrated in Figure 3-17.

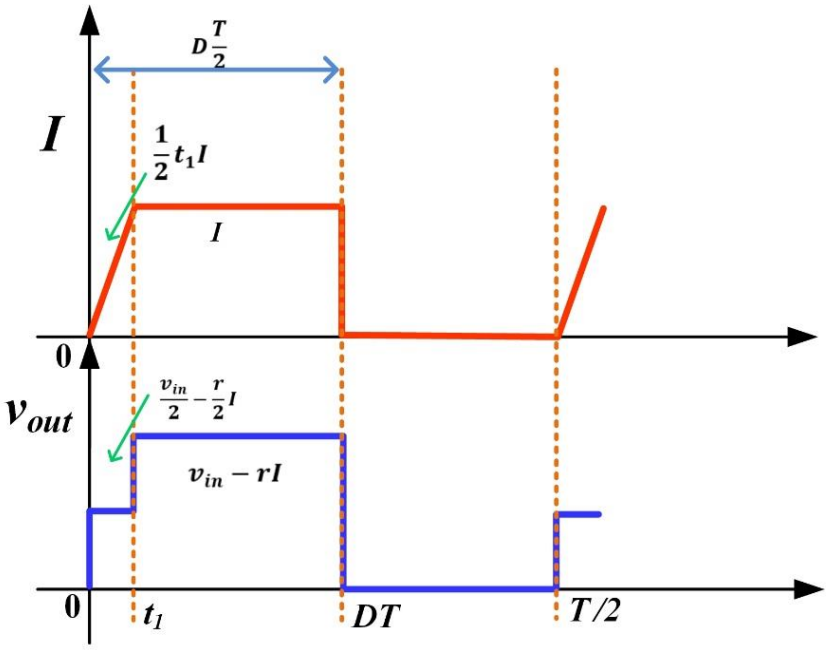

Figure 3-17: Input current and the output voltage waveforms [133], [134].

Where *T* is the switching period of the TLIBC, and D is the duty cycle.

Referring to Figure 3-17, the averaged quantities of input current $\langle i_1 \rangle$ and output voltage $\langle v_{out} \rangle$ can be analyzed as follows:

$$\langle i_1 \rangle = \frac{2}{T} I t_1 + \frac{2I}{T}(DT - t_1)$$

$$\langle i_1 \rangle = 2DI - \frac{I t_1}{T} \tag{3.13}$$

Replacing (3.9) into (3.13), it leads to:

$$\langle i_1 \rangle = 2DI - \frac{I}{T}\left(\frac{2L_o I}{v_{in} - r(i_{L1} - i_{L2})}\right) \tag{3.13}$$

$$\langle i_1 \rangle = 2DI - \frac{2L_o}{T}\left(\frac{I^2}{v_{in} - r(i_{L1} - i_{L2})}\right)$$

Then, one considers $R_e = \frac{2L_o}{T}$.

$$\therefore \langle i_1 \rangle = 2DI - R_e \frac{I^2}{v_{in} - r(i_{L1} - i_{L2})} \tag{3.14}$$

The average output voltage $\langle v_{out} \rangle$ can be found as:

$$\langle v_{out} \rangle = \left[\left(\frac{v_{in}}{2} - \frac{rI}{2}\right) t_1 + (v_{in} - rI)(DT - t_1)\right] \frac{2}{T} \tag{3.15}$$

Substituting (3.9) into (3.15), it yields to:

$$\langle v_{out} \rangle = \left[\frac{1}{2}(v_{in} - rI)\left(\frac{2L_o I}{v_{in} - r(i_{L1} - i_{L2})}\right) + (v_{in} - rI)\left(DT - \frac{2L_o I}{v_{in} - r(i_{L1} - i_{L2})}\right)\right] \frac{2}{T}$$

$$\langle v_{out} \rangle = \left[\frac{(v_{in} - rI)L_o I}{v_{in} - r(i_{L1} - i_{L2})} + (v_{in} - rI)DT - \frac{2(v_{in} - rI)L_o I}{v_{in} - r(i_{L1} - i_{L2})}\right] \frac{2}{T}$$

$$\langle v_{out} \rangle = \frac{2(v_{in} - rI)DT}{T} - \frac{2L_o}{T} \frac{(v_{in} - rI)I}{v_{in} - r(i_{L1} - i_{L2})}$$

$$\langle v_{out} \rangle = 2D(v_{in} - rI) - R_e \frac{(v_{in} - rI)I}{v_{in} - r(i_{L1} - i_{L2})} \tag{3.16}$$

One defines $R_e{}' = R_e \frac{(v_{in} - rI)}{v_{in} - r(i_{L1} - i_{L2})}$

$$\therefore \langle v_{out} \rangle = 2D(v_{in} - rI) - R_e{}' I \tag{3.17}$$

Finally, the conversion ratio gain can be defined by using Equation 3.17 as follows:

$$\langle v_{out} \rangle = 2D(v_{in} - rI) - R_e{}' I$$

where I is the output voltage $\langle v_{out} \rangle$ divided by the output resistance R_0.

$$\langle v_{out} \rangle = 2Dv_{in} - 2Dr\left(\frac{\langle v_{out} \rangle}{R_0}\right) - R_e{}'\left(\frac{\langle v_{out} \rangle}{R_0}\right)$$

$$\langle v_{out} \rangle + 2Dr\left(\frac{\langle v_{out} \rangle}{R_0}\right) + R_e{}'\left(\frac{\langle v_{out} \rangle}{R_0}\right) = 2Dv_{in}$$

$$\langle v_{out} \rangle \left(1 + \frac{2Dr}{R_0} + \frac{R_e{}'}{R_0}\right) = 2Dv_{in}$$

$$\frac{\langle v_{out} \rangle}{v_{in}} = \frac{2D}{1 + \frac{2Dr + R_e{}'}{R_0}} \tag{3.18}$$

If $r = 0$

$$\frac{\langle v_{out} \rangle}{v_{in}} = \frac{2D}{1 + \frac{R_e}{R_0}} \tag{3.19}$$

3.3.3 Design and sizing of TLIBC for hydrogen production systems based on low-carbon energy sources

This Ph.D. work comes within the scope of a collaboration between the Group of Research in Electrical Engineering of Nancy (GREEN), Université de Lorraine, IUT de Longwy section, France, and Renewable Energy Research Centre (RERC), Thai French innovation institute, King Mongkut's University of Technology North Bangkok, Thailand. As a result, the hydrogen production system for this thesis work has been designed based on the available equipment in both laboratories.

First, a 5-kW horizontal axis wind turbine from the FORTIS company is installed at the IUT de Longwy campus, and its specifications have been employed to design in the best conditions the studied system [135]. The wind power turbine versus the wind speed is illustrated in Figure 3-18 and the specifications are given in Table 3-1.

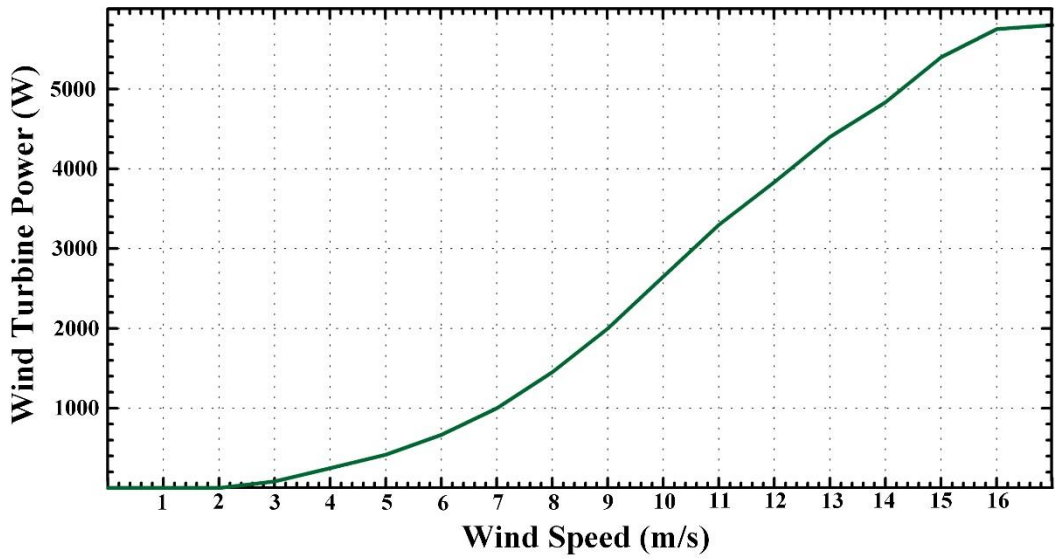

Figure 3-18: Output power of the wind turbine according to the wind speed [135].

Table 3-1. Wind turbine technical specifications [135].

Specification	Value
Rated power	5800 W
Cut in wind speed	2.5 $m.s^{-1}$
Rated wind speed	17 $m.s^{-1}$
Rotor blades number	3
Rotor blades diameter	5 m
Rotor blades swept area	19.63 m^2
Rotor blades tip speed ratio	7
Rotor blades material Generator type	Glas-fibre reinforced epoxy Brushless permanent magnet 9-pole
Rounds per minute operation range	120-450 RPM
Generator frequency	0-70 Hz
Gearbox	None

In addition, this wind turbine is interfaced with a brushless permanent magnet synchronous generator (PMSG), which generates a three-phase AC voltage whose amplitude and frequency are related to wind speed. Afterward, a three-phase diode rectifier and capacitor filter are connected to the output of PMSG to achieve DC voltage. The fluctuation of DC bus voltage at the output of the three-phase diode rectifier depending on the wind speed is presented in Figure 3-19. It can be observed that the DC bus voltage fluctuates from 75 V to 500 V. However, according to the measurement of wind speed in IUT de Longwy, the obtained range of wind speed is 2.5 to 6 ms^{-1}. Thus, the DC output voltage of the wind turbine is generated ranges between 100 to 200V [135].

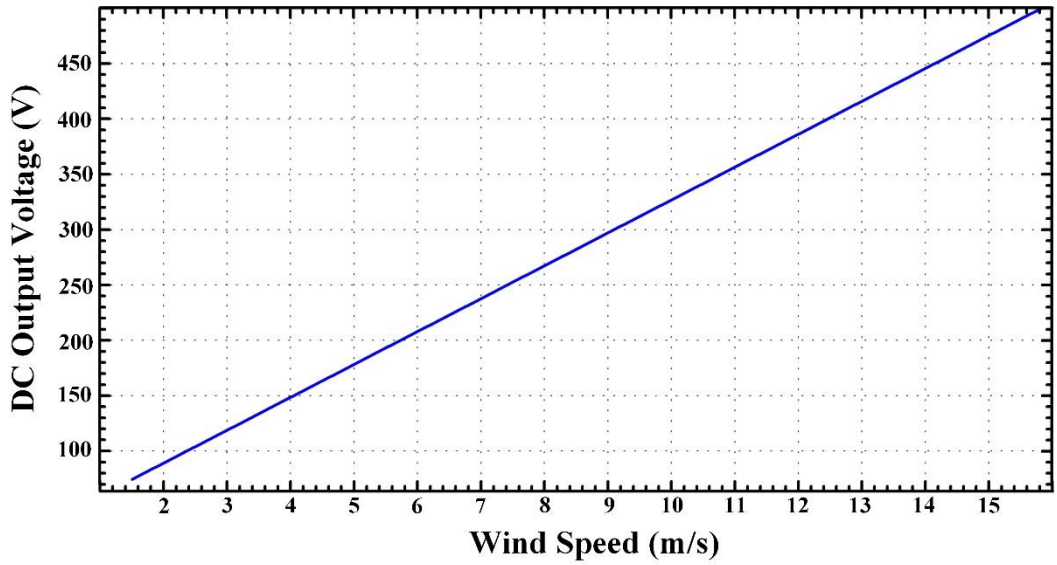

Figure 3-19: Variation of the DC bus voltage according to wind speed [135].

Second, a PEM electrolyzer emulator (investigated in Chapter 2) has been utilized as the load of the system. It has been conceived to reproduce the real behavior (static and dynamic operations) of the commercial PEM electrolyzer NMH2 1000 from HELIOCENTRIS company as mentioned in Chapter 2 and the specifications are given in Table 1-4.

For this reason, the passive components and power electronics devices in TLIBC have been designed accordingly to meet the requirements of input and output of the converter and are detailed in the following subsection.

A. Design of output inductor and 4 commutation inductors

Firstly, to design the output inductor $L_{0/2}$, the inductance values can be designed based on the expected maximum output current ripple flowing through the PEM electrolyzer. Besides, according to the range of input voltage and output voltage as mentioned above, the duty cycle range of the TLIBC in this system can be calculated based on Equation 3.19. Furthermore, the switching frequency of the TLIBC has been set to 10 kHz to optimize the energy efficiency by decreasing switching losses. As a result, the obtained duty cycle is roughly equal to 0.1. It means that the TLIBC understudy operates at a duty cycle lower than 0.25. For this reason, the output current ripple Δi_{el} of the TLIBC can be determined by using the following expression valid for a duty cycle lower than 0.25 [136]:

$$\Delta i_{L_0} = \frac{v_{el}(1-4D)}{L_0 f_s} \tag{3.20}$$

Thus, the expected maximum output current ripple at a duty cycle equal to 0.25 is approximately 1 A. As a result, the output inductance value can be calculated by using equation 3.20 and the obtained value is 0.8mH.

Referring to Figure 3-10, to achieve the best performance from the output current ripple and current stress point of view, the commutation inductances of each leg must be of same value to share equally the current between the 4-legs. They can be designed relying on the obtained output inductance $L_{0/2}$. Indeed, by dividing the output inductance value by the number of legs (i.e., 4), the commutation inductance value can be evaluated. Hence, the commutation inductances are equal to 200µH (L_1=L_2=L_3=L_4= 200µH).

B. Selected the values of both input capacitors and the output capacitor.

Second, the two input capacitance values of the TLIBC have been selected according to the strong intermittent behavior of the RES (i.e., wind energy). Thus, high capacitance values have been chosen for TLIBC to relieve the effect of fast dynamics due to gusts of wind. In addition, the maximum rate of input voltage is mandatory to choose capacitance values. In this case, as mentioned above the range of input voltage generated from the specification of the wind turbine is between 100 to 200V. Moreover, the normal input capacitor voltage rate of TLIBC is half of the input voltage (i.e.,100V). As a result, the maximum input capacitor voltage rate is chosen double of the normal voltage rate. Finally, a capacitance 4400 µF at 200V as available in the markets has been selected for both input capacitance values.

On the other side, a high output capacitor value has been used for the TLIBC to decrease voltage overshoots that may degrade the PEM electrolyzer. Moreover, if the available power increased immediately, a fit voltage rate of the output capacitor would enable to protect of the PEM electrolyzer against high voltage stresses. As a result, based on the components existing in the market, a capacitance 3300 μF at 50 V has been chosen for the output capacitance value.

Finally, the summary of the specification of the TLIBC for this thesis work is given in Table 3-2.

Table 3-2. Specifications of the TLIBC

Parameters	Value
Rated Input voltage, v_{DC}	100-200 V
Electrolyzer voltage, v_{el}	8 V
Maximum output power	5 kW
Input Capacitors $C_1 = C_2$	4400 μF, 200 V
Inductor $L_1 = L_2 = L_3 = L_4$	200 μH
Inductor $L_0/2$	800 μH
Output Capacitors C_0	3300 μF, 50 V
Switching Frequency, f_S	10 kHz

3.4 Improved sliding mode-based control

The control strategy is mandatory for power electronics in hydrogen production based on low-carbon energy sources to control current or voltage to meet the expectations of PEM electrolyzers as mentioned in Chapter 1, subsection 1.2.2. In the literature, traditional linear control laws such as proportional-integral (PI) and proportional-integral-derivative (PID) are usually used as reported in [38], [40], [57], [68], [75], [132], [137]. These control algorithms are designed to provide the best results that can be obtained under specific operating conditions. On the other side, power electronics are strongly sensitive to nonlinearities, disturbances, and uncertainties. As a result, the classic linear controller is not fit to provide high performance for dynamic operating conditions met in using intermittent energy sources.

Therefore, to design and develop a control law with a strong robustness feature, a non–linear controller must be considered to provide optimal performance throughout a wide operating range of RES and PEM electrolyzers [138].

The non-linear sliding-mode control (SMC) approach is an attractive controller to achieve suitable performance during dynamic operations. The SMC is a type of variable structure system (VSS). The SMC was first proposed in the 1950s by Emelyanov from the former Soviet Union and it has been widespread in the field of power electronics because it is an efficient technique for complex higher-order nonlinear systems [139].

The main concept of SMC is to design the sliding surface and attractive law through the required dynamic of the system. Hence, the system state impels from outside of sliding surface slide on the sliding surface [140].

In the beginning, the SMC named direct SMC was not of particular interest to researchers due to some inconveniences, especially the chattering issues and non-constant operating switching frequency. However, there are some benefits of using this approach since the dynamic behavior of the systems are modified by choosing the suitable switching frequency function [139], [140].

In recent years, the weaknesses of the direct SMC have been overcome by introducing a new control method known as indirect SMC. It enables eliminating chattering issues, adapting the uncertain system, and compensating for the influence of nonlinear dynamics. In conclusion, the dynamic performances in a closed-loop system are improved [139], [140].

The main features of indirect SMC over the linear control approach and other non-linear control approaches are high dynamic response, robustness against parameters uncertainties and low influence of external disturbances, and easy to implement. However, the indirect SMC presents some drawbacks from sensors requirement point of view [138]–[140].

Thus, this control algorithm has been selected to ensure the performance of the TLIBC. The principle of indirect SMC is introduced and analyzed in the following subsection.

3.4.1 Principle of the indirect sliding mode-based control

The indirect SMC is based on the equivalent control method. The dynamics of the system along the sliding surface (S) are described by this technique. It assures that the variable under control remains on this surface by setting the desired steady-state regime value for the input amount [140]. That means the equivalent vector can be assumed according to invariance conditions as given [140]:

$$S = 0 \; and \; \dot{S} = 0 \tag{3.21}$$

Based on the assumption, the signal of equivalent control can be achieved in terms of state variables. Therefore, the trajectory planning of the state variables is implicitly created to track the desired sliding surface via the formulation of the control signal [139]. The structure of indirect SMC is composed of the calculation of continuous output command signal ($d \in [0,1]$) based on switching function and control model, and the PWM generator by using d to produce switch command ($u \in \{0,1\}$ with a fixed switching frequency for the controlled system as illustrated in Figure 3-20 [139].

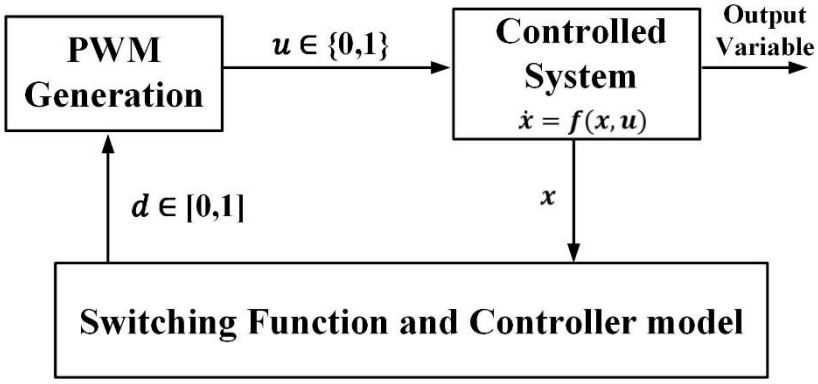

Figure 3-20: Control structure of indirect SMC [139].

All aspects of a nonlinear system with perfect modeling are known [139]:

$$\dot{X} = AX + BU + C \tag{3.22}$$

where $X \in \mathbb{R}^n$ is a state vector, $A \in \mathbb{R}^{n \times n}$ is a matrix, $B \in \mathbb{R}^n$ is a vector, and $U \in \mathbb{R}^n$ is the command.

The control target can be driven using a predetermined trajectory planning known as a sliding surface. That means the state variable X moves along state variable reference X_{ref} can be written as [139]:

$$S(X) = G(X - X_{ref}) \tag{3.23}$$

where G is a constant value that needs to be defined for the required dynamics of the controlled system.

To compel the dynamics of the sliding surface reach null value as an exponential response, the reaching law may be given as [139]:

$$\dot{S}(X) = -\lambda S \tag{3.24}$$

Note that the sliding mode exists when the following equation holds [139].

$$S \cdot \dot{S}(X) < 0 \tag{3.25}$$

By coupling (3.22) and (3.23) to obtain (3.24), the system command U may be found which can force the sliding surface from its original position to zero [139]:

$$U = (GB)^{-1}\left((-\lambda S - GA)X + \lambda G X_{ref} + \lambda G \dot{X}_{ref} - GC\right) \tag{3.26}$$

By evaluating the eigenvalues in respect to the control parameters, the dynamics of the indirect SMC can be investigated, which are λ and G.

Replacing (3.26) into (3.22) yields to [139]:

$$\begin{aligned} \dot{X} = &\underbrace{\left(A + B(GB)^{-1}(-\lambda S - GA)\right)}_{M} X \\ &+ B(GB)^{-1}\left(\lambda G X_{ref} + \lambda G \dot{X}_{ref} - GC\right) + C \end{aligned} \tag{3.27}$$

The eigenvalues of the controlled system may be obtained using the Laplace transformation by evaluating the determinant of the given equation [139]:

$$dt(sI - M) = 0 \tag{3.28}$$

The eigenvalues of the controlled system are determined as λ and G by setting λ and G to the same value. It can be observed that the eigenvalues of the controlled system, such as parasitic components do not depend on system parameters under the matching condition [139].

3.4.2 TLIBC modeling and design of controller

Before designing the control algorithm for TLIBC, the mathematic model of TLIBC has been analyzed. Afterward, the improved indirect SMC approach has been applied to control TLIBC. Both analyses are detailed in the next subsection.

A. Mathematic model of TLIBC

According to Figure 3-10, two power switches and two inductors of two ZCT power switching cells are assumed ideal. Therefore, it indicated that the switching commutation period of each ZCT cell is relatively small compared to the switching

frequency period. For this reason, the large-signal average model approaches can be applied to model the TLIBC as follows [141]:

$$\frac{di_o}{dt} = \frac{1}{L_o}(v_{C1}d_1 + v_{C1}d_2 + v_{C2}d_3 + v_{C1}d_4 - v_{el}) \tag{3.29}$$

$$\frac{dv_{el}}{dt} = \frac{1}{C_o}(i_o - i_{el}) \tag{3.30}$$

$$\frac{dv_{C1}}{dt} = \frac{1}{C_1}(i_{in} - i_o d_1 - i_o d_2) \tag{3.31}$$

$$\frac{dv_{C2}}{dt} = \frac{1}{C_2}(i_{in} - i_o d_3 - i_o d_4) \tag{3.32}$$

where: $v_{C1}$and v_{C2} are the voltages of input capacitor C_1 and C_2 (V) respectively, i_{in} is input current (A), i_o is inductor current of L_0 (A), $C_o$is the output capacitor (F), v_{el} and i_{el} are the voltage (V) and the current (A) of the electrolyzer respectively, and $d_1, d_2, d_3, d_4$are the duty cycle of power switches S_1, S_2, S_3, S_4, respectively.

B. Design of the improved indirect SMC

An improved indirect SMC has been applied for the TLIBC due to its attractive features as mentioned above. Furthermore, it enables the performance of the PEM electrolyzer to be improved during transient conditions such as the input voltage variation owing to the intermittence characteristic of RESs. In conclusion, the aim of this control algorithm is proposed to control two variables:

1. To control the hydrogen flow rate through the inductor current (i_o)
2. To control the balance of both input capacitor voltages (v_{c1} and v_{c2}).

In comparison to classic improved SMC, the indirect SMC for the considered system contains two additional variables, input capacitor voltage (v_{c1} and v_{c2}) with the goal of ensuring constant balance of both input capacitors.

From Equation 3.29-3.32, it is supposed that $d_1 = d_2$ and $d_3 = d_4$.

According to subsection 3.4.1, firstly, to control the inductor current i_o can be applied by using an improved sliding equation as given:

$$S_i = i_o - I_{oref} + k_i \int (i_o - I_{oref})\, dt \tag{3.33}$$

Based on Equation (3.24), to force S_i to obtain zero as an exponential response, a reaching law is expressed by:

$$\dot{S}_i = -\lambda_i * S_i \tag{3.34}$$

The time-derivative of (3.33) is given as follow:

$$\dot{S}_i = \frac{di_o}{dt} - \frac{dI_{0ref}}{dt} + k_i * (i_o - I_{oref}) \tag{3.35}$$

Replacing (3.35) into (3.34), it leads to:

$$\frac{di_o}{dt} - \frac{dI_{0ref}}{dt} + k_i * (i_o - I_{oref}) = -\lambda_i * S_i \tag{3.36}$$

Second, to ensure that the input capacitor voltages are balanced, the improved sliding equation can be used in the same manner as the inductor current control. It can be written as:

$$S_V = v_{C1} - v_{C2} + k_V \int (v_{C1} - v_{C2})\, dt \tag{3.37}$$

To compel S_v to reach a null value as an exponential response, a reaching law is given by:

$$\dot{S_V} = -\lambda_V * S_V \tag{3.38}$$

The time-derivative of (3.37) is defined as:

$$\dot{S_V} = \frac{dv_{C1}}{dt} - \frac{dv_{C2}}{dt} + k_V * (v_{C1} - v_{C2}) \tag{3.39}$$

Substituting (3.39) into (3.38), it yields to:

$$\frac{dv_{C1}}{dt} - \frac{dv_{C2}}{dt} + k_V * (v_{C1} - v_{C2}) = \dot{S_V} = -\lambda_V * S_V \tag{3.40}$$

Finally, Equation (3.29-3.32), (3.36), and (3.40) are used to define the duty cycle of the TLIBC as following equations:

$$d_1 = d_2 = -\frac{1}{-\frac{4i_o v_{C1}}{C_1 L_o} - \frac{4i_o v_{C2}}{C_1 L_o}} \left(\frac{2\left(\frac{i_{in}}{C_1} - \frac{i_{in}}{C_2} + k_V(v_{C1} - v_{C2}) + \lambda_V(\int (v_{C1} - v_{C2})\, dt k_V + v_{C1} - v_{C2})\right) v_{C2}}{L_o} - \frac{2i_o\left(-\frac{dI_{oref}}{dt} + (i_o - I_{oref})k_i + (i_o - I_{oref} + \int (i_o - I_{oref})\, dt k_i)\lambda_i - \frac{v_{el}}{L_o}\right)}{C_2} \right) \tag{3.41}$$

$$\begin{aligned} d_3 = d_4 = -\frac{1}{2i_o(C_1 v_{C1} + C_2 v_{C2})} (& -C_2 \frac{dI_{oref}}{dt} i_o L_o + L_o C_2 {i_o}^2 k_i - C_2 i_o I_{oref}\, k_i L_o + C_2 {i_o}^2 \lambda_i L_o - C_2 i_o I_{oref}\, \lambda_i L_o \\ & + C_2 \int (i_o - I_{oref})\, dt i_o k_i \lambda_i L_o - C_1 i_{in} v_{C1} + C_2 i_{in} v_{C1} \\ & + C_1 C_2 \int (v_{C1} - v_{C2})\, dt k_V\, \lambda_V v_{C1} + C_1 C_2 k_V {v_{C1}}^2 + C_1 C_2\, \lambda_V {v_{C1}}^2 - C_1 C_2 k_V v_{C1} v_{C2} \\ & - C_1 C_2\, \lambda_V v_{C1} v_{C2} - C_2 i_o v_{el})) \end{aligned} \tag{3.42}$$

In addition, the bandwidth of the controller is an important issue because it set the speed of the control loop and is linked to controlling parameters (k_i, λ). Indeed, the bandwidth of the inductor current control is selected faster than the balancing input voltage control loop because it handles the hydrogen flow rate of the PEM electrolyzer and divides the controller into two dynamics. As a result, it can be selected as $k_i = \lambda_i = \frac{2\pi f_s}{\approx 50}$. Thus, the bandwidth of the balancing input voltage control loop is selected as $k_V = \lambda_V = \frac{2\pi f_s}{\approx 500}$ [139].

Finally, the control diagram of improved SMC for TLIBC can be drawn based on equations 3.41 and 3.42 as illustrated in Figure 3-21.

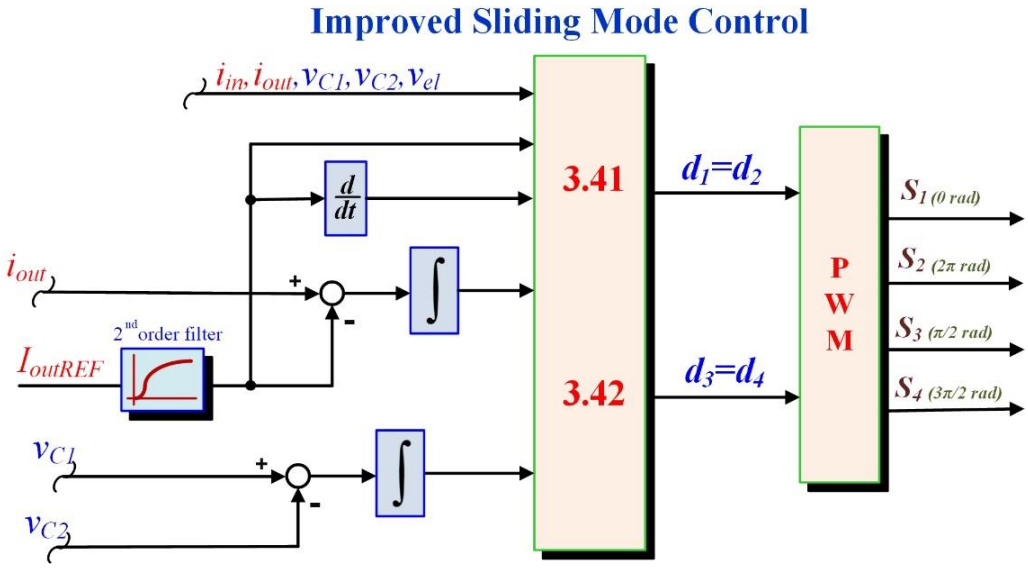

Figure 3-21: Control diagram of improved SMC.

3.5 Simulation of TLIBC with improved SMC

The aim of this section is to validate the effectiveness of improved SMC applied to the studied TLIBC for PEM electrolyzer applications. Simulations have been carried out by using MATLAB®—Simulink as depicted in Figure 3-22. Indeed, the improved SMC was implemented relying on Figure 3-21 and the MATLAB® function code of the improved SMC also as illustrated in Figure 3-23 and 3-24 respectively. The schematic diagram emphasizing the measurement points of the TLIBC for the improved SMC and to display the measured signals is shown in Figure 3-25. Moreover, the converter circuit parameters provided in Table 3-2 and the control parameters of improved SMC given in Table 3-3 have been considered to perform simulations. A variable-step ode45 solver with a step size of 1 µs was used to simulate the whole system. Additionally, the system has been trigged every switching period $T_s = \frac{1}{f_s}$.

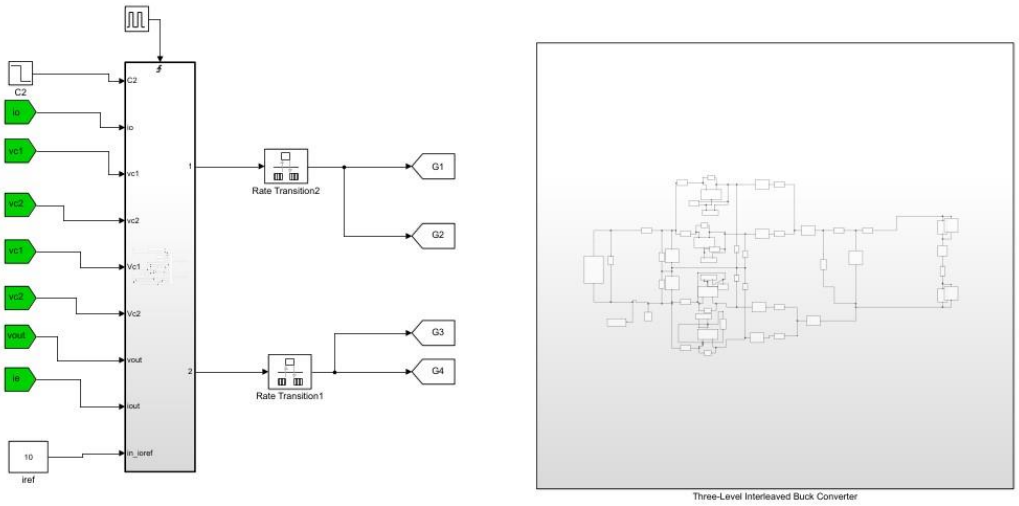

Figure 3-22: Simulation of TLIBC with improved SMC in MATLAB® programming.

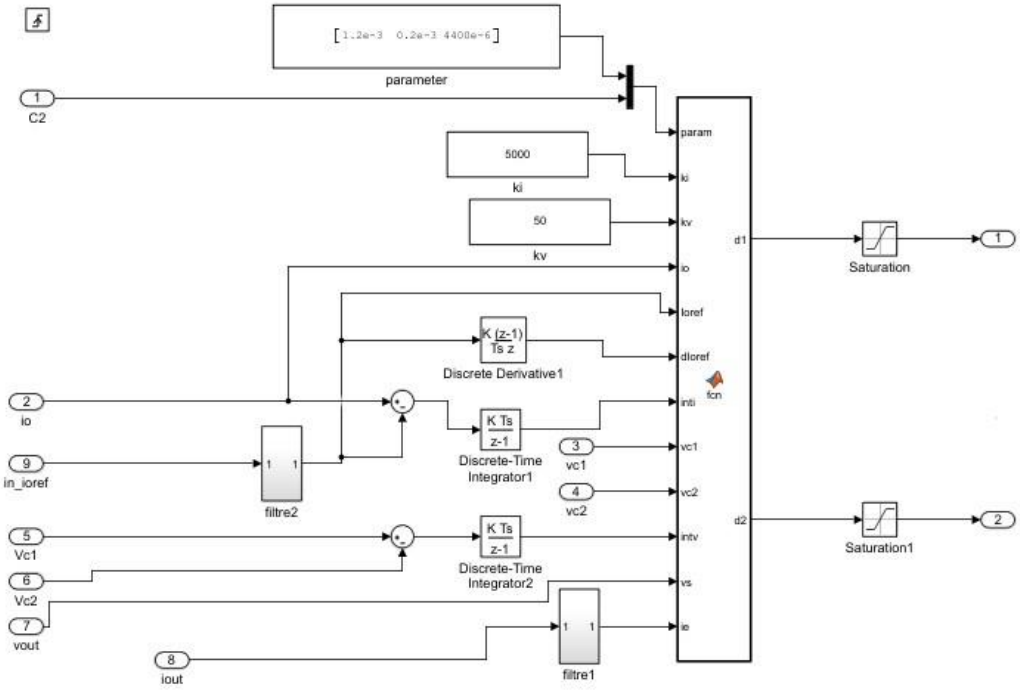

Figure 3-23: Implementation of improved SMC in MATLAB®—Simulink.

```
function [dl,d3]  = fcn(param,ki,kv,io,Ioref,dIoref,inti,vcl,vc2,intv,vs,ie)
Lo=param(1);
ro=param(2);
Cl=param(3);
C2=param(4);
lambda1=ki;
lambda2=kv;

dl=(-1).*((-4).*C2.^(-1).*io.*Lo.^(-1).*vcl+(-4).*Cl.^(-1).*io.*Lo.^( ...
  -1).*vc2).^(-1).*(2.*Lo.^(-1).*(Cl.^(-1).*ie+(-1).*C2.^(-1).*ie+ ...
  kv.*(vcl+(-1).*vc2)+lambda2.*(intv.*kv+vcl+(-1).*vc2)).*vc2+(-2).* ...
  C2.^(-1).*io.*((-1).*dIoref+(io+(-1).*Ioref).*ki+(io+(-1).*Ioref+ ...
  inti.*ki).*lambda1+(-1).*Lo.^(-1).*vs));
d3=(-1/2).*io.^(-1).*(Cl.*vcl+C2.*vc2).^(-1).*((-1).*C2.*dIoref.*io.* ...
  Lo+C2.*io.^2.*ki.*Lo+(-1).*C2.*io.*Ioref.*ki.*Lo+C2.*io.^2.* ...
  lambda1.*Lo+(-1).*C2.*io.*Ioref.*lambda1.*Lo+C2.*inti.*io.*ki.* ...
  lambda1.*Lo+(-1).*Cl.*ie.*vcl+C2.*ie.*vcl+Cl.*C2.*intv.*kv.* ...
  lambda2.*vcl+Cl.*C2.*kv.*vcl.^2+Cl.*C2.*lambda2.*vcl.^2+(-1).*Cl.* ...
  C2.*kv.*vcl.*vc2+(-1).*Cl.*C2.*lambda2.*vcl.*vc2+(-1).*C2.*io.*vs) ...
  ;
```

Figure 3-24: MATLAB® function code of improved SMC.

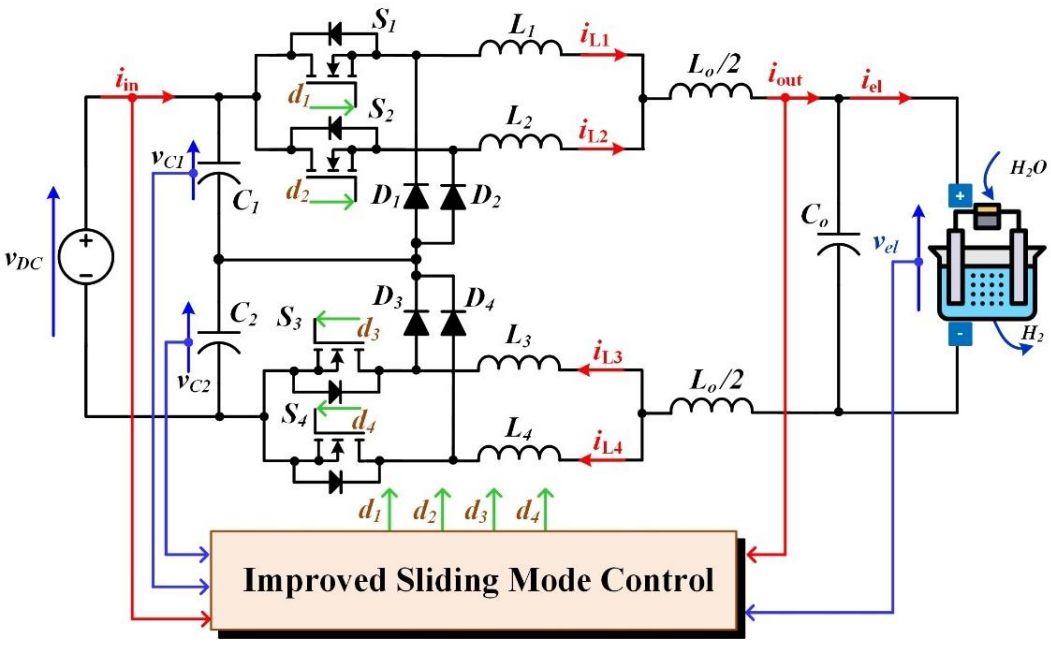

Figure 3-25: Schematic diagram of the measurement points of TLIBC for improved SMC and to display them.

On the other side, the TLIBC and PEM electrolyzer emulator (as mentioned in Chapter 2) have been realized by using the Simscape library in MATLAB®—Simulink as shown in Figure 3-26. All the power switches (MOSFET) and diodes in the converter have been considered ideal.

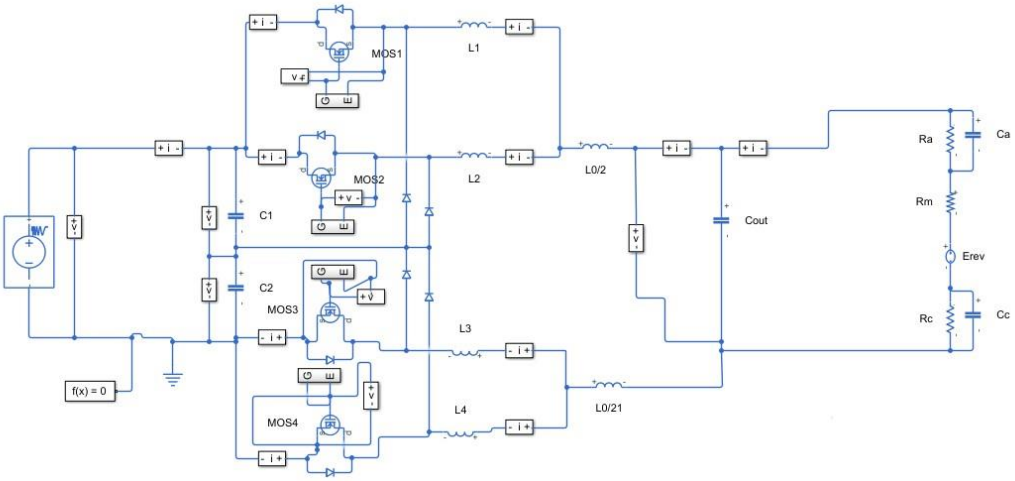

Figure 3-26: Implementation of TLIBC with PEM electrolyzer emulator by using Simscape library.

Table 3-3. Controller Parameters.

Parameters	Value
$k_i = \lambda_i$	5000
$k_V = \lambda_V$	50

The simulation tests to assess the performance of improved SMC for TLIBC have been divided into three tests. The first simulation tests have been performed to adjust the output inductor current reference to control the hydrogen flow rate of the PEM electrolyzer. Afterward, the second simulation tests have been operated under input voltage variation conditions to balance the voltage of both input capacitors. Finally, the third simulation tests have been carried out when a power switch failure occurs. Indeed, as pointed out in the literature [142], power switches are one of the most delicate components in DC-DC converters. For this reason, they have been considered as likely failures to investigate the performance of improved SMC. The availability of the DC-DC converter in case of electrical failures is one of the most important features requested for electrolyzer applications. The obtained results of the three simulation tests are provided and analyzed in the following subsections.

3.5.1 Simulation tests of output inductor current control

First simulation tests have been carried out to evaluate the behavior of the output inductor current i_{ut}, and the electrolyzer voltage v_{el} by modifying output inductor current reference I_{outREF} from 3 to 10 A and vice-versa at a constant DC input voltage of 100V. Moreover, the inductor current reference is filtered by a 2nd order filter to avoid the aggressive current of the output capacitor. The obtained results are reported in Figures 3-27 and 3-28.

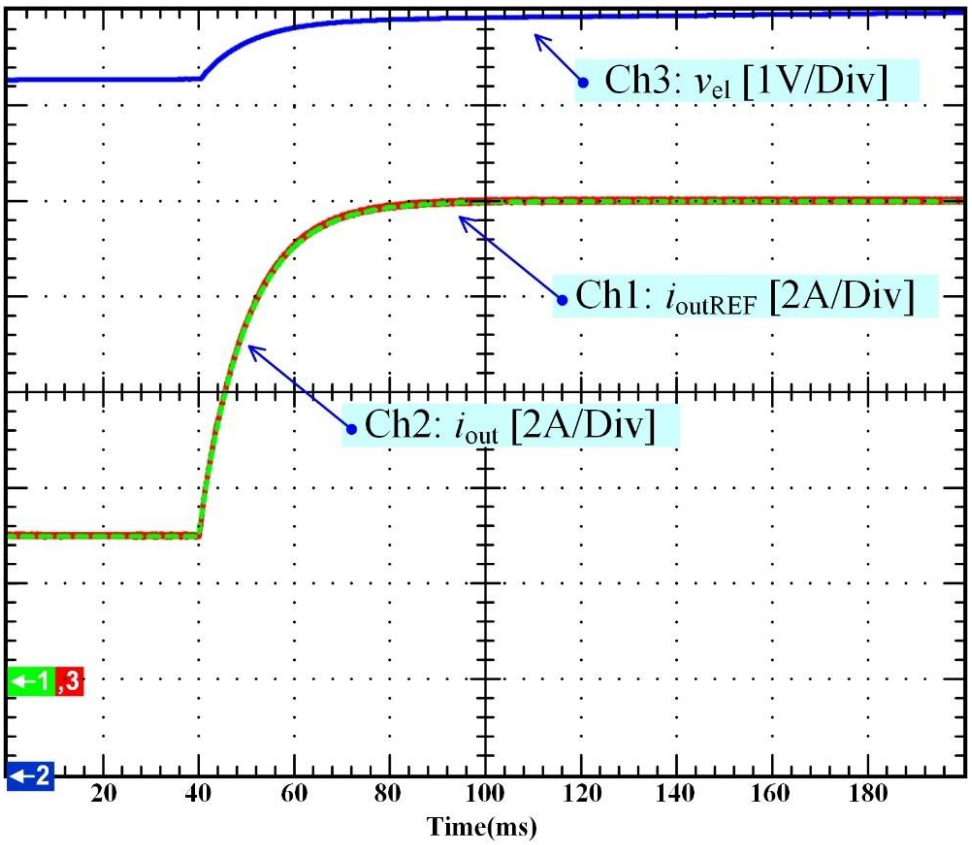

Figure 3-27: Simulation results: v_{el} and i_{out} response during the increase of I_{outREF} from 3 to 10 A.

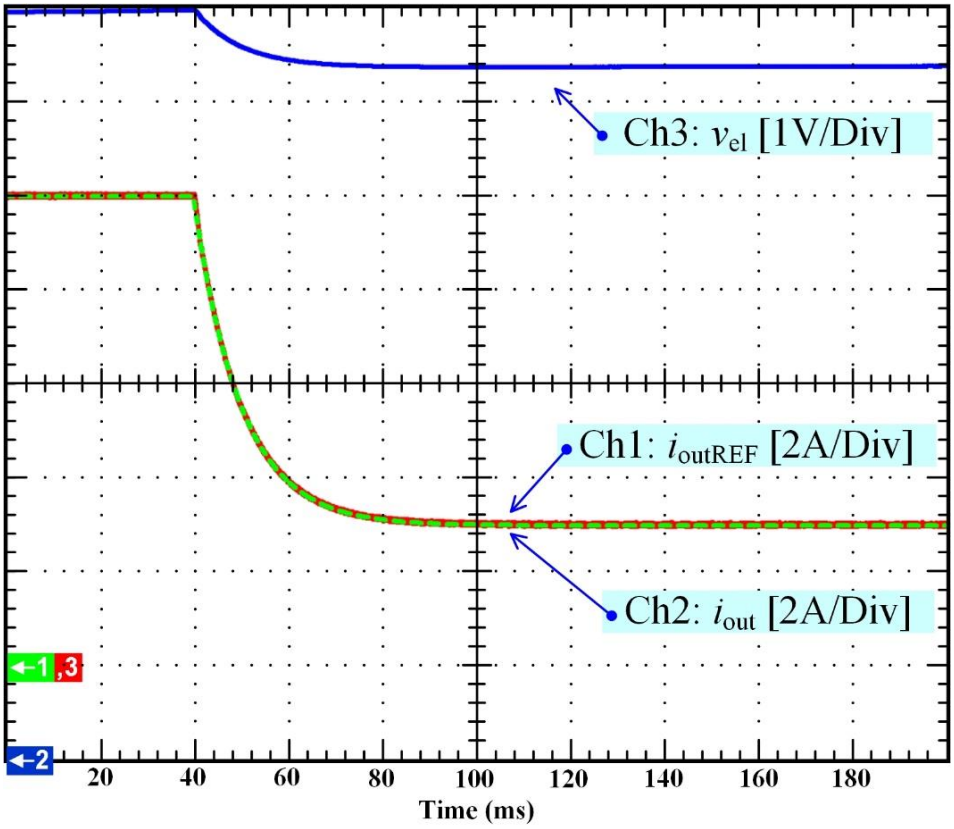

Figure 3-28: Simulation results: v_{el} and i_{out} response during the decrease of I_{outREF} from 10 to 3 A.

According to Figures 3-27 and 3-28, it can be observed that the output inductor current i_{out} tracks perfectly the output inductor current reference I_{outREF}. Furthermore, the PEM electrolyzer emulator is operated in normal voltage operation at I_{outREF} equal to 3 A. Finally, the PEM electrolyzer emulator is performed at a constant voltage operation (i.e., maximum voltage equal to 8V) when I_{outREF} is higher than 7 A relying on Figure 2-1 (Chapter 2).

3.5.2 Simulation tests of balancing input capacitor voltages control

Afterward, the second simulation tests have been performed under input voltage fluctuation conditions to simulate the intermittence behavior of RES by changing the input voltage from 100 to 150 V and vice-versa, whereas the output inductor current reference I_{outREF} is maintained constant at 10 A. The responses of the input voltage v_{in}, both input capacitor voltages v_{C1}, v_{C2}, the electrolyzer voltage v_{el}, and of the output inductor current i_{out} have been analyzed at the time scale of 0.05 s. The obtained results are presented in Figures 3-29 and 3-30.

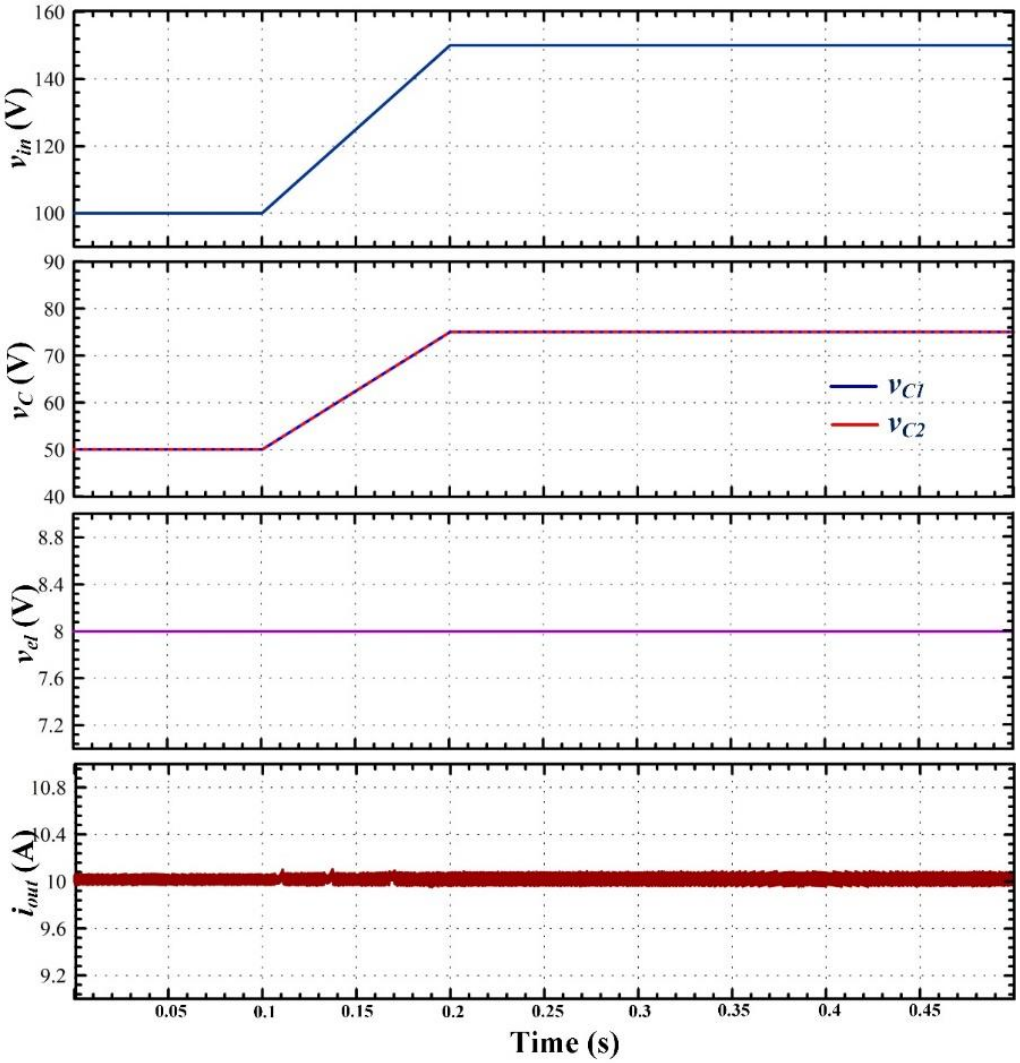

Figure 3-29: Simulation results: v_{in} change from 100 to 150V at I_{outREF} = 10A.

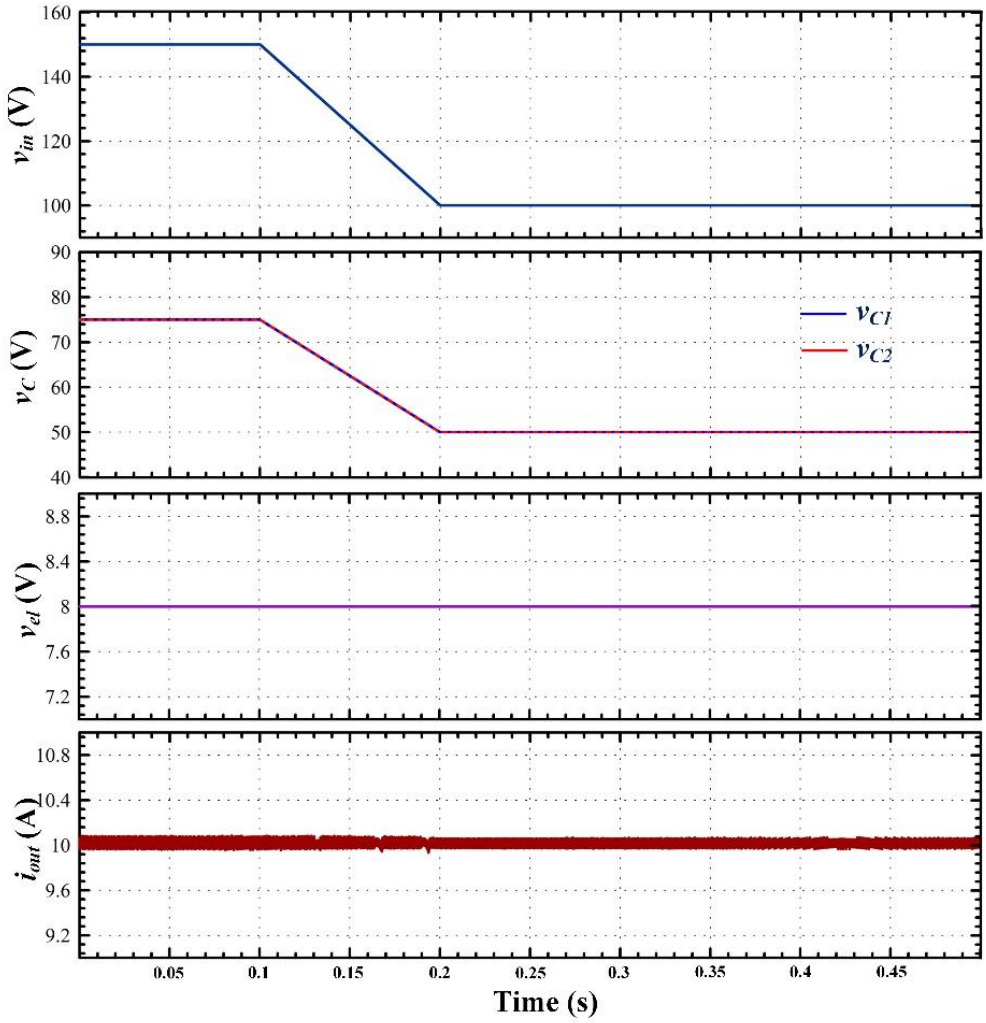

Figure 3-30: Simulation results: v_{in} fluctuation from 150 to 100V at I_{outREF} = 10A.

Based on Figures 3-29 and 3-30, the input voltage has risen from 100 to 150V or has fallen from 150 to 100V at 0.1 s. In both cases, the steady-state value has been reached in 0.2 s. During input voltage variation, it can be noted that input capacitor voltages v_{C1}, v_{C1} are a half of input voltage and the output inductor current is kept constant at 10 A with a very small current ripple (i.e., less than 0.1A). Moreover, the PEM electrolyzer is performed at a constant voltage operation. As a result, the electrolyzer voltage is equal to 8 V.

Additional simulation tests have been performed to check the balance of both input capacitor voltages when the values of input capacitors C_1 and C_2 are changed. The purpose of these additional tests is to analyze the reliability of the improved SMC of guaranteeing the balance of both input capacitors. For these tests, the output inductor current reference I_{outREF} is kept constant at 10 A. A time scale of 0.1 s and the same responses as the second simulation tests have been selected to emphasize the dynamic and steady-state operation of the simulation systems. The response of the system when changing the capacitance value of input capacitor C_1 is provided in Figure 3-31; whereas the response of the system when modifying the input capacitor C_2 value is presented in Figure 3-32.

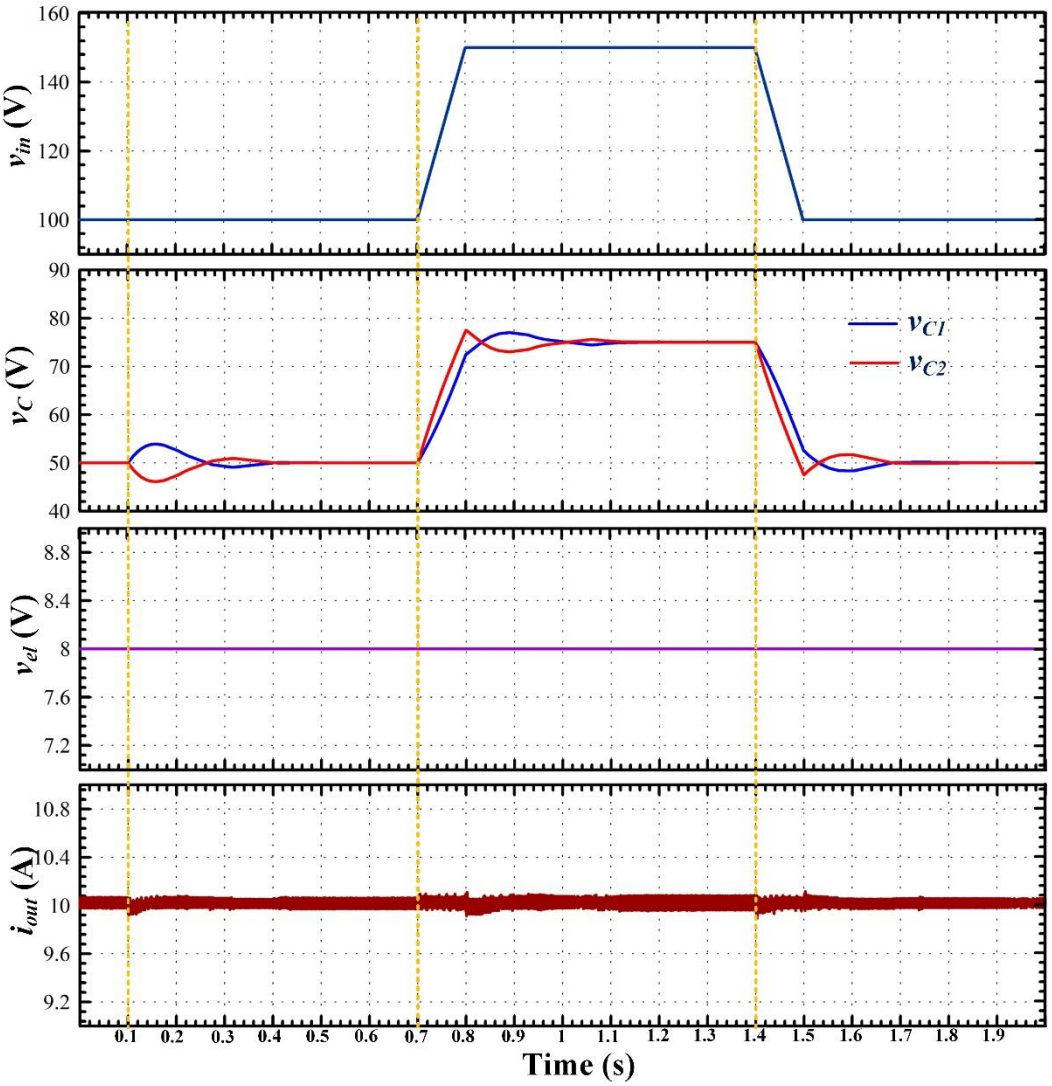

Figure 3-31: Simulation results: change input capacitance C_1 from 4400µF to 1000µF at I_{outREF} = 10A.

Referring to Figure 3-31, in the beginning, the capacitance values of input capacitors C_1 and C_2 are 4400µF and the input voltage is equal to 100V. After that at t = 0.1 s, the capacitance value of input capacitor C_1 is dropped to 1000µF, while the capacitance value of input capacitor C_2 and the input voltage have kept their initial values 4400µF and 100V respectively. It can be observed that the input capacitor voltages v_{C1}, v_{C2} present small fluctuations and a balance is achieved at t = 0.4 s.

Subsequently, at t = 0.7 s, the input voltage is increased from 100 to 150V and reached the steady-state value in 0.8 s. As a result, the input capacitor voltages v_{C1}, v_{C2} show fluctuations because the capacitance of C_1 and C_2 are not equal, and the proposed control algorithm forced them to reach the balance condition at t = 1.1 s.

Finally, at t = 1.4s, the input voltage is decreased from 150 to 100V and achieved the steady-state value in 1.5 s. Thus, the obtained results are like the previous operation (i.e., t =0.7 s to t =1.4 s). It can be noted that during this operation, the electrolyzer voltage and output inductor current are kept constant at 8V and 10A respectively. Indeed, the output inductor current has a very small current ripple approximately equal to 0.1A.

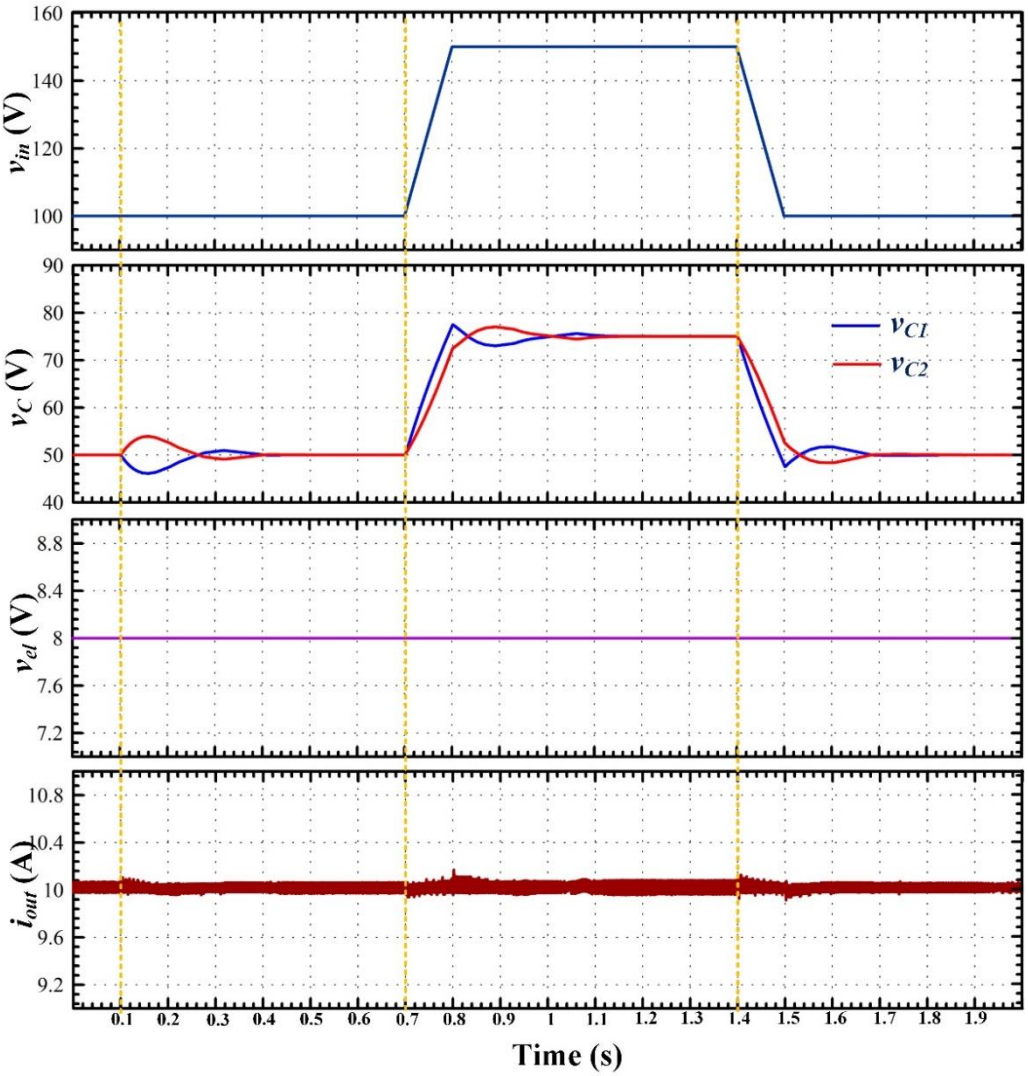

Figure 3-32: Simulation results: change input capacitance C_2 from 4400µF to 1000µF at I_{outREF} = 10A.

In Figure 3-32, the simulation tests condition and the obtained results are like in Figure 3-31. However, one condition difference is the capacitance values of input capacitor C_2 is changed from 4400µF down to 1000µF instated of C_1, while the capacitance value of input capacitor C_1 remains the same, equal to 4400µF.

3.5.3 Study of degraded operating conditions

To assess the reliability of TLIBC and the effectiveness of improved SMC, the third simulation tests have been operated when one of the power switches is faulty, while the input voltage and the output inductor current reference I_{outREF} are constant at 100V and 10 A respectively. The obtained results are depicted in Figures 3-33, providing the inductor current of 4 legs (i_{L1}, i_{L2}, i_{L3}, i_{L4}) and the output inductor current i_{out}.

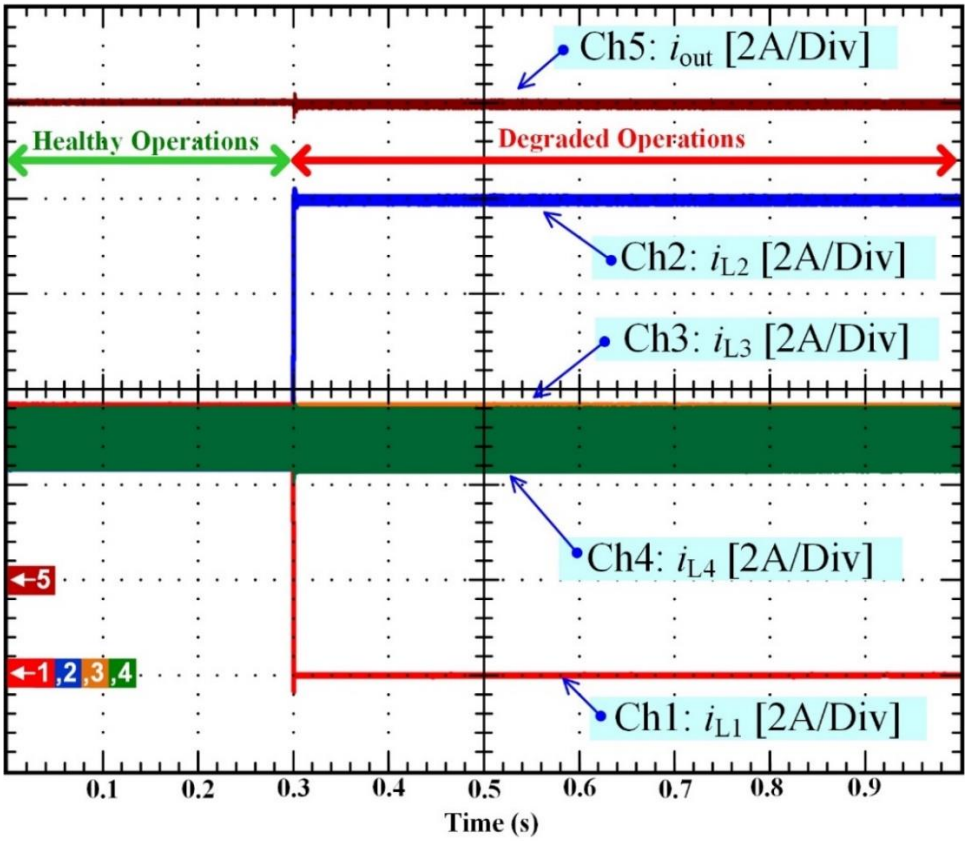

Figure 3-33: Simulation results: the response of i_{L1}, i_{L2}, i_{L3}, i_{L4}, and i_{out} during TLIBC operated in cased of power switch failure.

According to Figures 3-33, at the beginning of the simulation tests, the converter is performed in healthy operations, which means that the converter operates without power switch failure. Afterward, the converter is operated in degraded operations, which means that the converter is performed with a failure occurring on one of the power switches. In this simulation test, an open-circuit failure of S_1 has been simulated at t =0.3 s. To create this failure, the PWM gate control signal of S_1 has been forced to 0.

On one hand, during the healthy operations, it can be highlighted that the inductor current of 4 legs is roughly equal to 5A depending on the phase-shift duty cycle. Hence, the output inductor current (Ch:5) is equal to 10 A with a very small current ripple due to the cancellation of the commutation inductor by the interleaved technique. On the other hand, during the degraded operations, the power switch of leg 1 is faulty, it can be observed that the inductor of leg 1 (Ch:1) has decreased immediately to zero, whereas the inductor current of leg 2 (Ch:2) has increased instantly to 10A to compensate the failure of S_1. This compensation allows balancing the upper and lower circuits of TLIBC. By comparison, the inductor currents of leg 3 and leg 4 are kept constant at 5 A. Consequently, the current ripple of the output inductor has grown up slightly because of the loss of one leg leading up to an unsuitable PWM gate control signals shifts. However, the output inductor is maintained constant at 10 A.

For this reason, the converter can continue to supply the current without interruption to the PEM electrolyzer with the same current reference I_{outREF} during degraded operations. To emphasize all the responses in Figure 3-33 when the healthy operations changed to degraded operations, the time scale range on 0.298 to 0.305 s of Figure 3-33 has been plotted as illustrated in Figure 3-34.

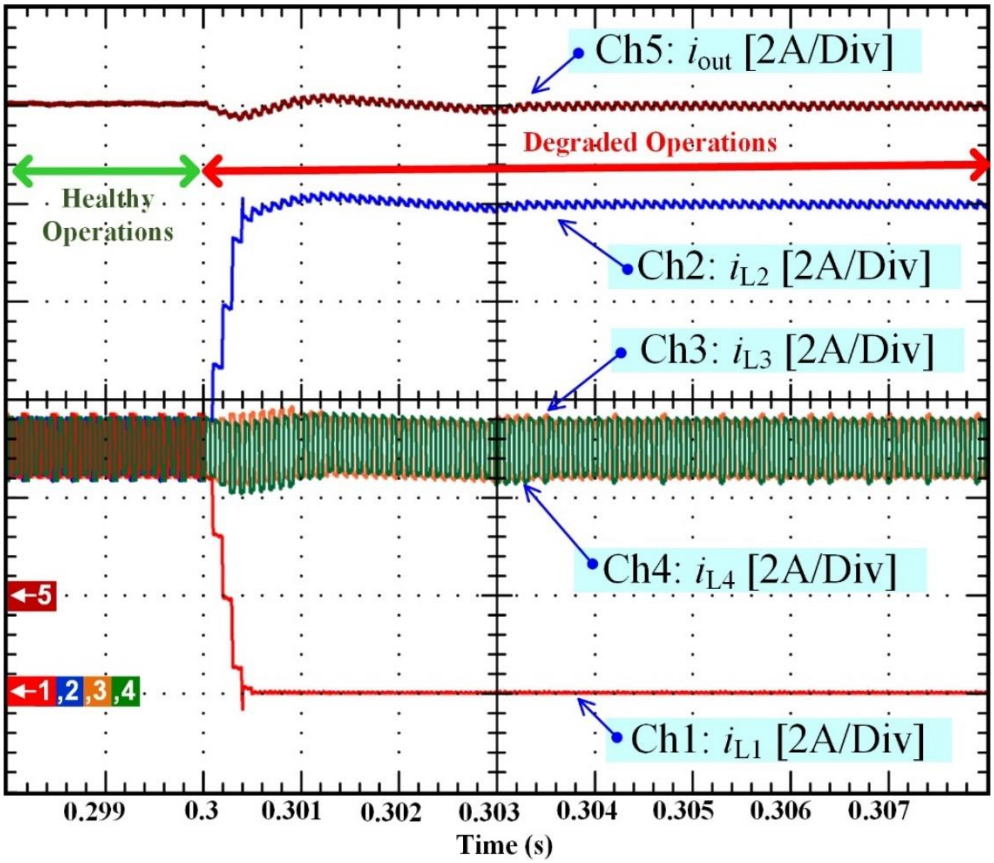

Figure 3-34: Highlight of the response of i_{L1}, i_{L2}, i_{L3}, i_{L4}, and i_{out} when TLIBC changed operations from healthy to degraded operations

Based on the obtained results (Figure 3-34), to decrease the output current ripple when the TLIBC operates in a degraded mode, control strategies can be applied to the PWM gate control signals shifts according to the location of the leg failure. These control strategies are presented in Table 3-4 according to the leg failure.

Table 3-4. Control strategies of PWM according to the leg failure

Leg Failure	Active phase-shift angle to reduce current ripple			
	S_1	S_2	S_3	S_4
Leg 1	-	$Original^2 + \frac{\pi}{6}$	$Original^3$	$Original^4 + \frac{\pi}{3}$
Leg 2	$Original^1$	-	$Original^3 + \frac{\pi}{6}$	$Original^4 - \frac{\pi}{6}$
Leg 3	$Original^1$	$Original^2 - \frac{\pi}{3}$	-	$Original^4 - \frac{\pi}{6}$
Leg 4	$Original^1$	$Original^2 + \frac{\pi}{3}$	$Original^3 + \frac{\pi}{6}$	-

[1] 0 rad, [2] π rad, [3] $\pi/2$ rad, [4] $3\pi/2$ rad,

Then, the TLIBC has been simulated when each power switch is broken to validate the adopted control strategies of PWM according to the leg failure. The obtained output inductor current ripple in healthy operation and degraded operation are given in Table 3-5. The table also includes the comparison of the output inductor current ripple in degraded operation without and with adopted control strategies.

Table 3-5. Comparison of output inductor current ripple

Leg Failure	Healthy Mode	Degraded Mode without phase-shift strategy	Degraded Mode with phase-shift strategy	Reduction of current ripple
Leg 1	0.1 A	0.18 A	0.15 A	16.67 %
Leg 2	0.1 A	0.17 A	0.15 A	11.77 %
Leg 3	0.1 A	0.18 A	0.16 A	11.12 %
Leg 4	0.1 A	0.17 A	0.15 A	11.77 %

According to Table 3-5, it can be observed that the inductor output current ripple in healthy operation is equal to 0.1 A. After that, the inductor output current ripple is increased approximately to 0.075 A when the TLIBC is operated in degraded operation without a phase-shift strategy. Finally, the inductor output current ripple is decreased around 12.83% (average value) in degraded operation when the adopted control strategies are applied.

3.6 Conclusion

The main goal of Chapter 3 was to design and size the TLIBC with a non-linear control algorithm for hydrogen production systems based on low-carbon energy sources. Firstly, before designing and sizing the TLIBC, the development and the operation of TLIBC have been introduced and detailed. Hence, the key features of the TLIBC are achieved as follows: low voltage stress on the power switches, low output current ripple, availability in case of power switch failures, high energy efficiency, suitable for medium scale, and small size of passive components. Afterward, the step-down voltage conversion ratio of TLIBC has been defined by using interleaved ZCT buck converter with the large-signal average model. It can be emphasized that the step-down voltage conversion ratio is very low.

Second, the specifications of the 5-kW wind turbine located at IUT de Longwy and the PEM electrolyzer emulator as designed and realized in Chapter 2 have been utilized to design in the best situations the studied hydrogen production system. For this reason, the passive components of TLIBC have been designed and sized according to the specifications of the power source and load of the system.

Third, the improved SMC has been proposed to be applied to the TLIBC due to the main advantages. Indeed, this control strategy features robustness versus parameters uncertainties, fast dynamic response, and ease of implementation. Besides, the proposed controller has been designed to control the output inductor current and the balance between both input capacitor voltage of TLIBC regardless of the fluctuating operational conditions (the output inductor current reference or input DC voltage).

Finally, the TLIBC with the proposed control algorithm has been evaluated through simulation tests by using MATLAB®—Simulink. The obtained simulation

results have allowed verifying the performance and the robustness of the proposed control algorithm in regulating the output inductor current (i.e., hydrogen flow rate) to supply the PEM electrolyzer while ensuring the balance of both input capacitors voltages regardless of disturbances. Moreover, the last obtained simulation results have enabled demonstrating the reliability of TLIBC with the proposed control algorithm during degraded operating modes (i.e., in case of power switch failures).

In the next and last Chapter, the realized experimental test bench including the TLIBC is presented. The technical specifications of the TLIBC and the design of the improved SMC mentioned in Chapter 3 have been considered to realize the converter and the implementation of the control strategy. Subsequently, experimental tests have been carried out to validate the proposed control algorithm and compare the experimental results with simulation results.

Chapter 4
Experimental Validation of the Three-Level Interleaved DC-DC Buck Converter

4.1 Introduction

In the two previous chapters, the studied hydrogen production system including a PEM electrolyzer emulator and a low-voltage high-power DC-DC converter (TLIBC) has been presented and detailed. On one hand, the PEM electrolyzer emulator has been designed and realized based on an equivalent electrical circuit by considering the static and dynamic behavior of a commercial PEM electrolyzer (as mentioned in Chapter 2). As a result, this emulator is very useful for performing experimental tests with the proposed DC-DC converter with its control laws, to avoid using a real PEM electrolyzer that could be degraded during experiments. On the other hand, the TLIBC has been designed and sized for a studied hydrogen production system (as mentioned in Chapter 3). The main benefits of TLIBC are low step-down voltage conversion ratio, its availability in case of power switch failures, an improved energy efficiency due to its architecture, and low output current ripple. Consequently, the mathematical model of TLIBC has made possible the design of the control strategy. Thus, a non-linear improved SMC has been designed to control this hydrogen system.

In continuity with the previous chapter, the aim of this chapter is to experimentally validate the TLIBC with the developed non-linear control laws. First, the implementation of each component including power electronic devices, passive components, and the acquisition devices of the studied TLIBC have been analyzed and detailed. Second, the realized experimental test rig with the studied TLIBC and the developed PEM electrolyzer emulator is described and presented. Finally, experimental results are provided and analyzed to validate the performance of the proposed control strategy.

4.2 Implementation of TLIBC

First and foremost, before building the experimental test bench, the TLIBC must be implemented based on the technical specification data as analyzed in Chapter 3. Hence, the TLIBC has been designed at a maximum power equal to 5 kW. The specifications of the studied TLIBC have been given in Table 3-2 (see Chapter 3). The details of the developed TLIBC are provided and analyzed in the following subsection.

4.2.1. Selection of the power electronics devices

According to Chapter 3 (subsection 3.3.3), the maximum DC bus voltage (3-phase diode rectifier output) and the rated power of the wind turbine are equal to 200 V and 5 kW, respectively. Given that the maximum voltage and power of the PEM electrolyzer are equal to 8V and 400W, the electrical ratings of both power switches (MOSFETs) and power diodes have been selected based on these specifications. In addition, the normal input voltage of each power switch in the

TLIBC are half of the input voltage (i.e.,100V). On one hand, the Power MOSFETs (N Channel) parts number RCX700N20 from ROHM Semiconductor have been chosen for all power switches in the studied TLIBC. Indeed, for this device, the voltage rating between drain and source is equal to 200V and the drain current is equal to 70A. Moreover, the maximum resistance between drain and source during power switch ON ($R_{DS(ON)}$) is equal to 42.7 mΩ [143]. It can be observed that the rated voltage of RCX700N20 is double of input voltage and the resistance between drain and source is very low, while it can be operated at a high current. On the other hand, to drive the power MOSFET as utilized in the studied TLIBC (RCX700N20), the photocoupler gate drive parts number TLP250 from Toshiba Company have been used.

On the other side, the choice of power diodes is guided by the high input voltage level for connecting the middle-point of input capacitors and providing high efficiency. Thus, the ultra-fast diodes parts number RURG8060 from ON Semiconductor have been selected. The specifications of RURG8060 are high reverse voltage V_F (600V), high forward current I_F (80A), ultrafast recovery (t_{rr} = 85 ns), and high reliability [144].

4.2.2. Realization of the output inductor and 4 commutation inductors

The obtained value of the output inductor and 4 commutation inductors as mentioned in Chapter 3 (subsection 3.3.3) are equal to 0.8mH and 200μH, respectively. To achieve those values, the ferrite cores have been employed to realize the inductors required for the TLIBC. In addition, the output inductor has been realized to withstand a high current and to obtain a high inductance value. As a result, the ETD59-3C90 type magnetic cores have been used for the output inductors as depicted in Figure 4-1. By comparison, the ETD39-3C90 type magnetic cores have been chosen for the commutation inductors due to the inductance values and current stress smaller than those of the output inductors. The ETD39-3C90 is illustrated in Figure 4-2. Both cores are made from ferrite components from the Ferroxcube Company [145].

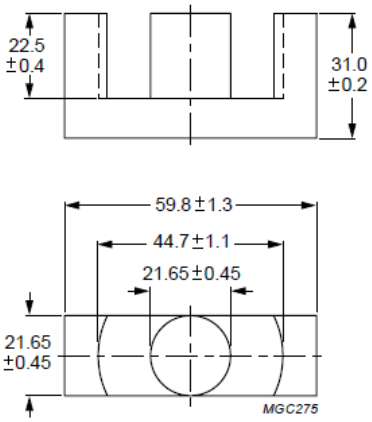

Figure 4-1: The dimension ETD 59-3C90 core half [145].

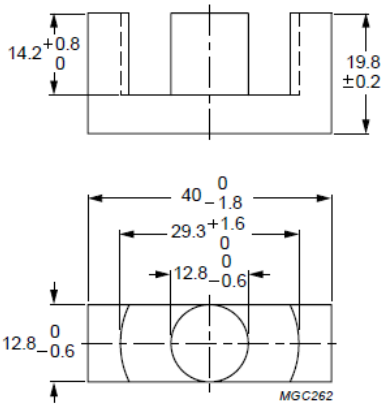

Figure 4-2: The dimension ETD 39-3C90 core half [145].

Furthermore, to reach the obtained value, the number of turns N and air gap d are determined with the following relationships [146]:

$$L = \frac{\mu_o A_e}{2d} N^2 \tag{4.1}$$

$$NI_{Max} \leq 2d \frac{B_{sat}}{\mu_o} \tag{4.2}$$

where L is the inductance value (H), μ_o is the vacuum permeability equal to $4\pi \times 10^{-7}$ (H/m), $A_e$is the effective cross-sectional area of a core (mm^2), N is number of turns, d is the air gap (mm), I_{Max} is the maximum current (A), and B_{sat} is the saturation flux density (mT).

Thus, the effective cross-sectional area of a core A_e of ETD59-3C90 and ETD39-3C90 are equal to 368 and 125 mm^2 [145], respectively. Moreover, the air gap of the main inductor and commutation inductor are set equal to 2 and 1 mm [146], respectively to avoid the saturation of magnetic flux density at high current. As a result, the number of turns N of the main inductor and commutation inductor can be calculated by using equation 4.1 and the obtained values are roughly equal to 26 and 16, respectively.

4.2.3. Design and realize the measurement sensors for TLIBC

Following Chapter 3 (subsection 3.4), to obtain the best performance of the improved SMC approach, more sensors are required to measure the data. For this reason, the sensors are compulsory for this control strategy. The main static features of sensors are high accuracy, sensitivity, linearity, suitable range, and reproducibility. In the proposed improved SMC, 5 sensors are required to measure in the TLIBC as presented in Figure 3-25 (see Chapter 3). There are 3 voltage sensors (both input capacitor voltages (v_{c1}, v_{c2}), and the electrolyzer voltage (v_{el})) and 2 current sensors (input current (i_{in}) and output inductor current (i_{out})). Afterward, the output signals of all sensors are sent to the computation board where the improved SMC is implemented. In this Ph.D. work, the real-time board DS1202 dSPACE–MicroLabBox has been used. The voltage range of analog to digital converter (ADC) of dSPACE–MicroLabBox is between 0 and 10V. As a result, the design of voltage and current sensors are analyzed and detailed in the following subsection.

A. Design and realize the voltage sensors for TLIBC

Firstly, to measure the accuracy of voltage, the voltage transducer LV 25-P from LEM Company has been chosen for all voltage sensors in the studied TLIBC. The range of measurement voltage and output voltage signals of the sensors are selected higher than their maximum measurement voltage and the maximum input voltage signal of the control board. Thus, the maximum of both input capacitor voltages (v_{c1}, v_{c2}) and the electrolyzer voltage (v_{el}) are equal to 100V and 8V, respectively as analyzed in Chapter 3 (subsection 3.3). Therefore, the maximum measurement of both input capacitor voltages (v_{c1}, v_{c2}) and the electrolyzer voltage (v_{el}) are equal to 120V and 10V, respectively. On the other side, the maximum output voltage signals of all voltage sensors are equal to 10 V as mentioned above. The schematic diagram of the voltage sensor is illustrated in Figure 4-3. It relies on the principle circuit of LV25-P and voltage follower circuits.

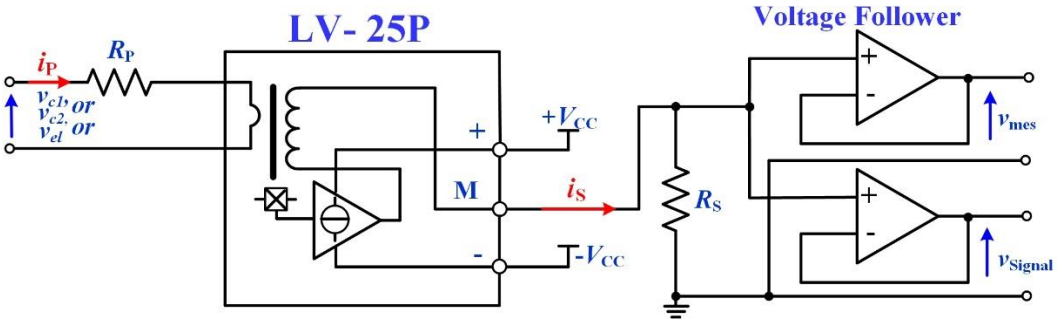

Figure 4-3: The architecture of voltage transducer LV25-P interfaced with voltage follower circuits.

Based on Figure 4-3, to reach the measurement voltage point and to achieve the output voltage signal as chosen, the primary and secondary resistor ($R_{primary}$, $R_{secondary}$) have been calculated by these following equations.

$$R_{primary} = \frac{v_{c1}\ or\ v_{c2}\ or\ v_{el}}{i_{primary}} \tag{4.3}$$

$$R_{secondary} = \frac{v_{signal}}{i_{secondary}} \tag{4.4}$$

where $i_{primary}$ is the primary current of LV-25P equal to 10mA [147], $i_{secondary}$ is the secondary current of LV-25P equal to 25mA [147].

In conclusion, by using equations 4.3 and 4.4, the primary resistors of the voltage sensor circuit ($R_{primary}$) of both input capacitor voltages (v_{c1}, v_{c2}) and the electrolyzer voltage (v_{el}) are equal to 12kΩ and 1kΩ respectively, while the secondary resistors ($R_{secondary}$) are equal 400Ω. The developed voltage sensor is presented in Figure 4-4.

Figure 4-4: Implemented voltage sensor.

B. Design and realize the current sensors for TLIBC

Second, the current transducers LA 55-P from LEM Company have been applied to input current (i_{in}) and output inductor current (i_{out}) of the studied TLIBC. In additional, this current sensor is based on the Hall effect. The Hall effect current sensor offers a better level of safety because of the galvanic isolation between the sensor and the measurement current point. The measured current passes through a conductor within a magnetic core. A magnetic field is generated inside the core as a result of the current. For this reason, the Hall effect sensor is in the core air gap to measure this field. Thus, the Hall sensor generates the output voltage that is proportional to the core magnetic field and the input current. Consequently, the range of both measurement currents is selected equal to 50 A and the output signal voltages are equal to 10V. So, the selected measurement current is met to nominal primary RMS current of LA 55-P is equal to 50 A [148]. The architecture of the current sensor circuit is shown in Figure 4-5.

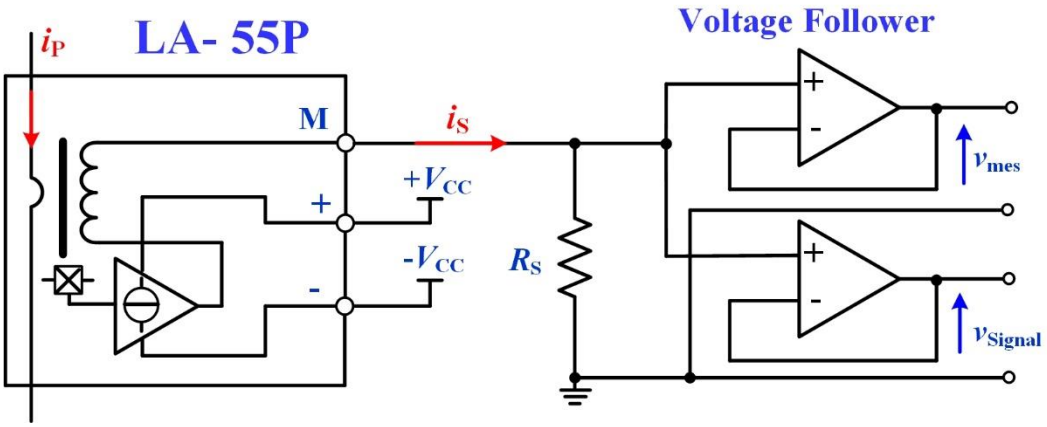

Figure 4-5: Schematic diagram of current transducer LA-55P connected with voltage follower circuits.

As the same manner of the voltage sensor, to obtain the output voltage signal of current sensor as selected, the secondary resistor ($R_{secondary}$) has been determined by using equation 4.4. Hence, the secondary $i_{secondary}$ current of LA-55P is equal to 50mA [148]. Hence, the obtained secondary resistor is equal to 200Ω. The designed current sensor is illustrated in Figure 4-6.

Figure 4-6: Realized current sensor.

Finally, all of components above mentioned have been combined to implement the TLIBC in a suitable box as illustrated in Figure 4-7. In the next subsection, the implementation of the experimental test bench is provided and detailed.

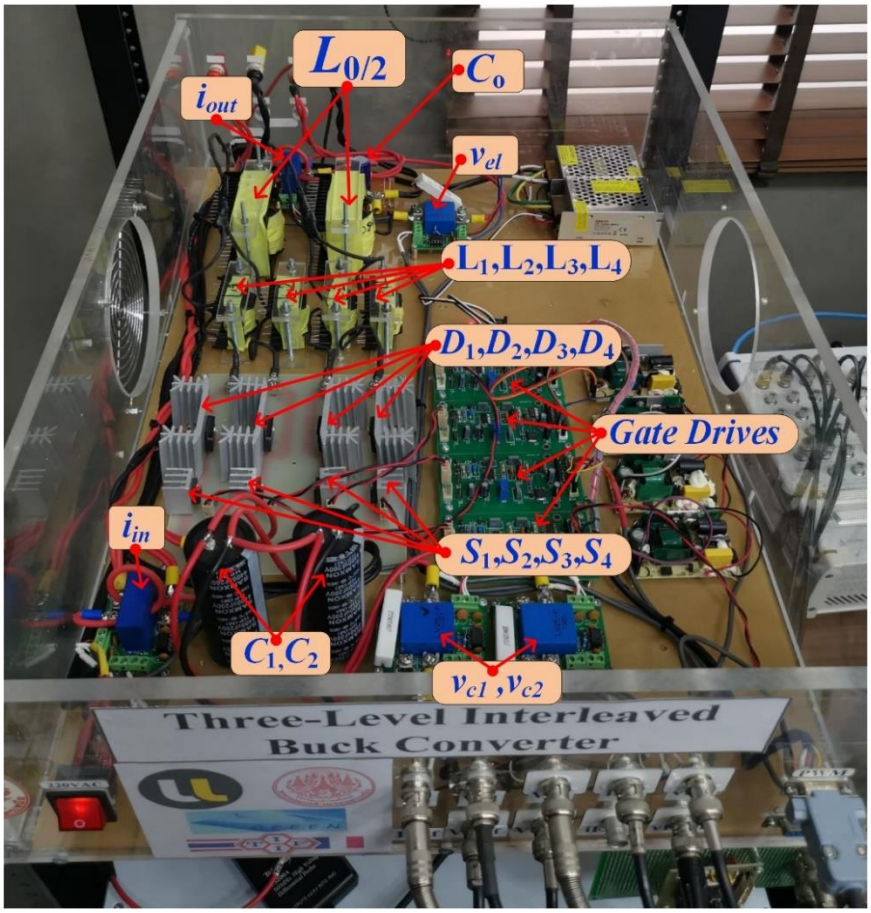

Figure 4-7: Developed TLIBC.

4.3 Experimental test bench and implementation of the proposed non-linear control algorithm

4.3.1. Description of experimental test rig

To validate the control algorithm control developed in Chapter 3, an appropriate experimental test bench was set up in the Renewable Energy Research Centre (RERC), Thai French innovation institute, King Mongkut's University of Technology North Bangkok. The realized experimental test bench is depicted in Figure 4-8.

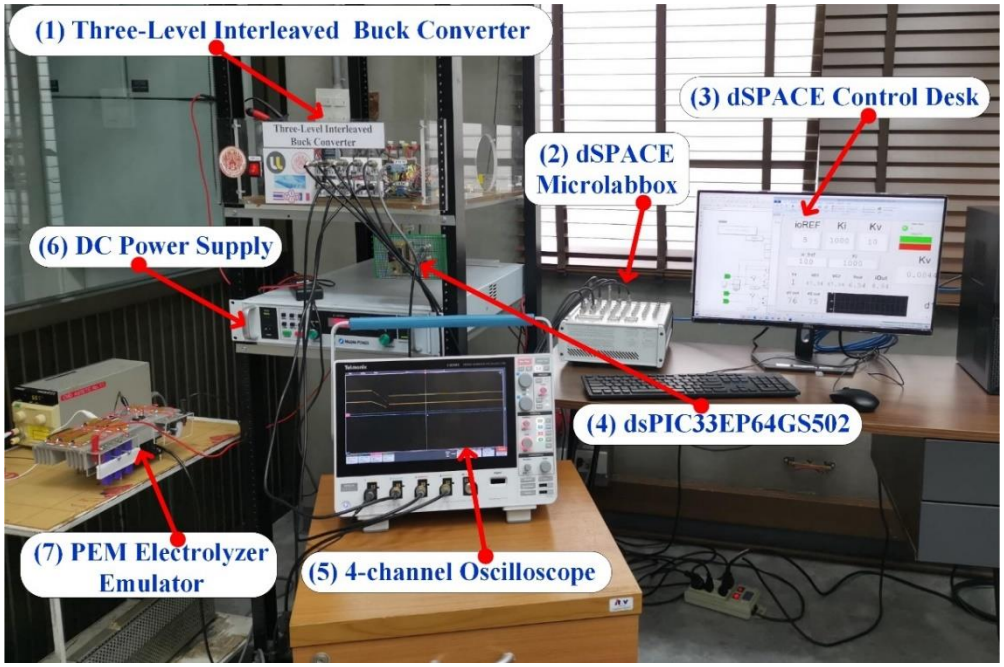

Figure 4-8: Experimental test rig platform with the realized TLIBC.

The experimental test rig consists of the following components: (1) the developed TLIBC, (2) the real-time board DS1202 dSPACE–MicroLabBox, (3) a dSPACE control desk, (4) a microcontroller-based on a dsPIC33EP64GS502 (Microchip Technology Inc., Chandler, AZ, USA), (5) a 4-channel oscilloscope, (6) a programmable DC power supply XR600 from MAGNA-POWER Company (Flemington, NJ, USA), (7) the developed PEM electrolyzer emulator. The programmable DC power supply is used to emulate the electrical features of the 5-kW wind turbine as given in Table 3-1 (see Chapter 3).

The improved SMC as mentioned in Chapter 3 has been realized in MATLAB®—Simulink environment. Then, it has been implemented into the real-time board DS1202 dSPACE–MicroLabBox. However, the phase-shift of the PWM gate control signals required by the converter cannot be made through the DS1202 dSPACE–MicroLabBox. Therefore, a microcontroller-based on dsPIC33EP64GS502 is employed to receive the PWM gate control signals generated by the DS1202 dSPACE–MicroLabBox and to shift them from each other as required by the converter (π rad between S_1 and S_2, S_3 and S_4). A schematic diagram description of this experimental test rig is illustrated in Figure 4-9. Finally, the hydrogen flow rate, V_{H_2}, (given in slpm) and the energy efficiency of the electrolyzer, η_{el}, have been computed in real-time by using the measurement data of the output inductor current i_{out}, and the electrolyzer voltage v_{el}. To obtain those

values, the Equations (2.7) and (2.10) as given in Chapter 2 (subsection 2.3.1) have been realized in MATLAB®—Simulink environment and transferred into the DS1202 dSPACE–MicroLabBox.

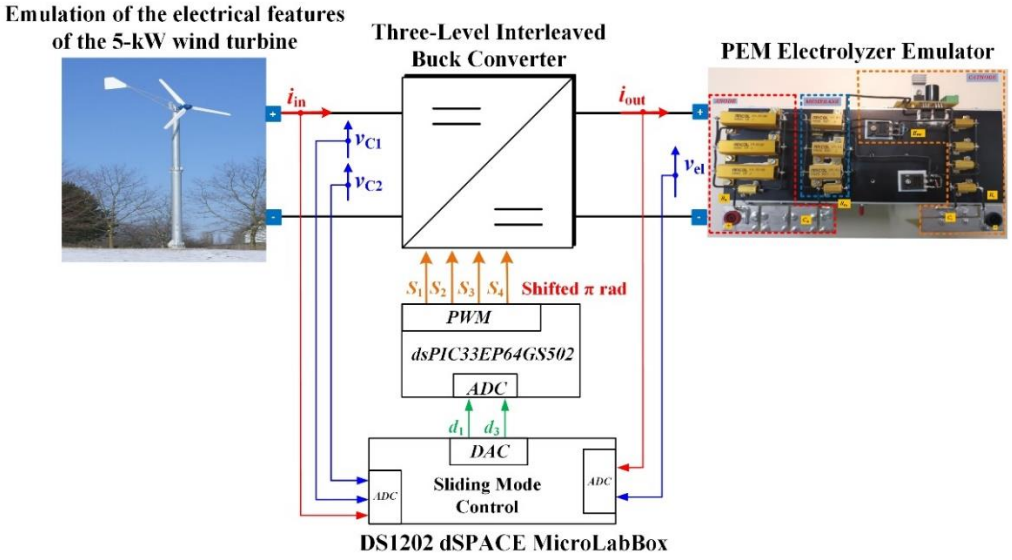

Figure 4 9: Schematic diagram description of the experimental test rig.

4.3.2. Implementation of proposed control laws in the in MATLAB®—Simulink environment

To realize the proposed control strategy, the MATLAB®—Simulink environment has been used. The overall diagram of proposed control strategy implemented in MATLAB®—Simulink is depicted in Figure 4-10. It is composed of the real-time board DS1202 dSPACE–MicroLabBox blocks as follows: (1) the ADC blocks to collect the voltage and current measurement signals of the TLIBC as highlighted in Figure 4-9, (2) implementation of improved SMC (the same as simulation test in Chapter 3, (3) digital to analog converter (DAC) to send the PWM signal to the dsPIC33EP64GS502 based microcontroller enabling generating PWM signals to drive the power switches, (4) interrupt tools block to trick the system every switching period $T_s = \frac{1}{f_s}$ and (5) ON/OFF block. Moreover, a step size of 1 µs and a variable-step ode45 solver have been utilized to compute the developed system.

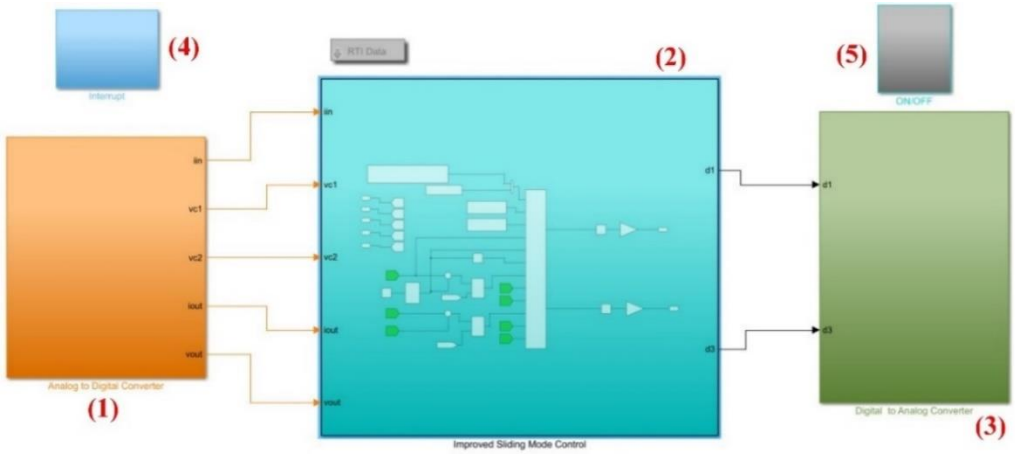

Figure 4-10: Overview of the implemented program in MATLAB®—Simulink environment.

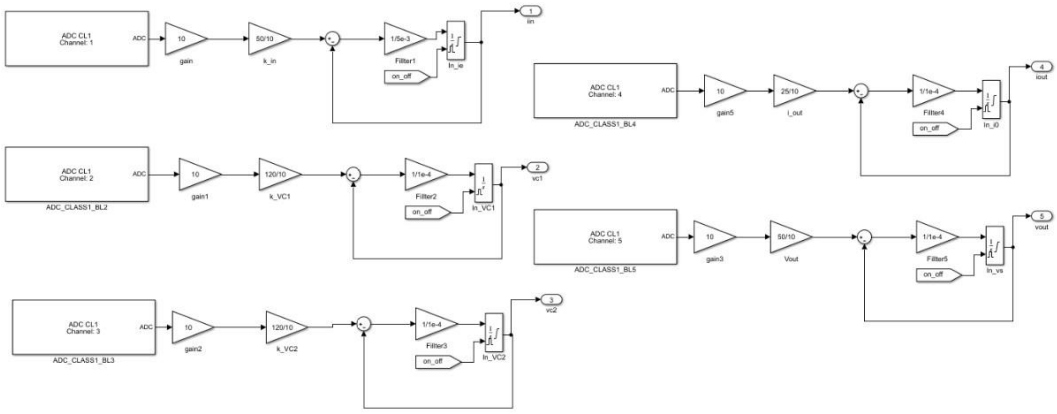

Figure 4-11: Implementation of DS1202 dSPACE–MicroLabBox ADC blocks in MATLAB®—Simulink.

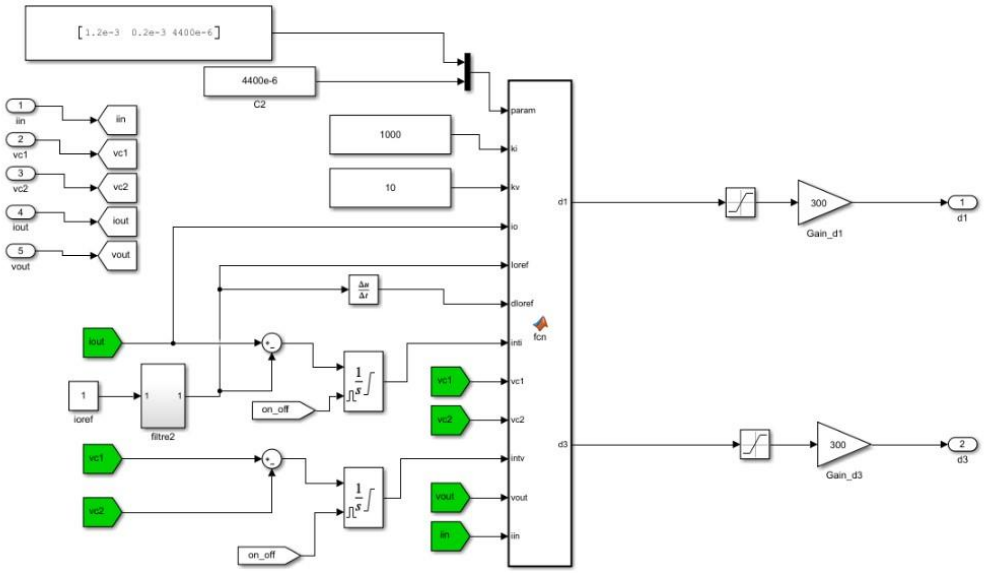

Figure 4-12: Implementation of improved SMC in MATLAB®—Simulink.

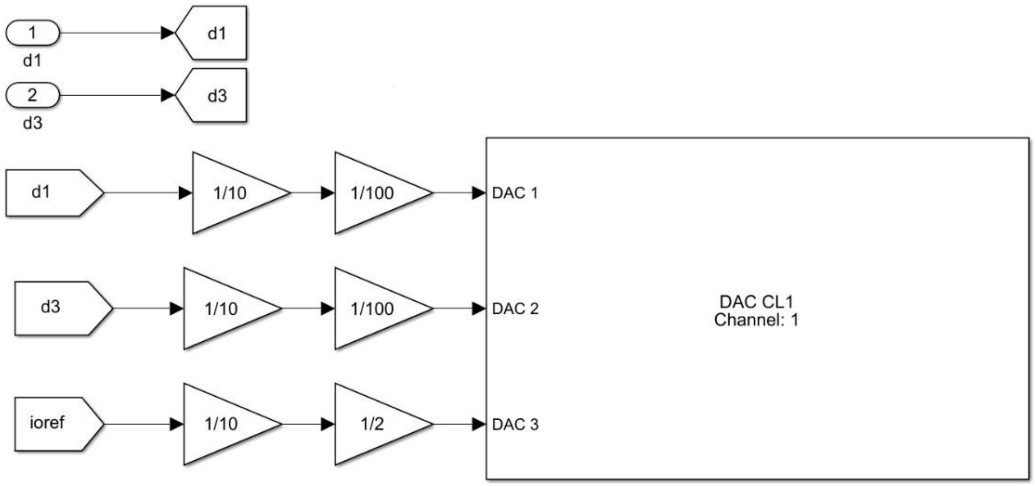

Figure 4-13: Implementation of DS1202 dSPACE–MicroLabBox DAC blocks in MATLAB®—Simulink.

4.3.3. Supervision of experimental test bench.

To monitor the data and control the output current reference of the TLIBC and the PEM electrolyzer in real-time, a ControlDesk dSPACE environment has been interfaced with DS1202 dSPACE–MicroLabBox as illustrated in Figure 4-14. The measurement values as displayed in Figure 4-9 are obtained via the program implemented in block number 1 of Figure 4-10. It can be noted that both input capacitor voltages (v_{c1}, v_{c2}), electrolyzer voltage (v_{el}), input current (i_{in}), output inductor current (i_{out}) and duty cycle (d) are visualized. Moreover, the output inductor current reference I_{outREF} and controller parameter as given in Table3-3 for the closed-loop control by using the proposed improved SMC can be modified through the ControlDesk dSPACE. Finally, the integral block in the implemented control algorithm resets the values by the ON/OFF button.

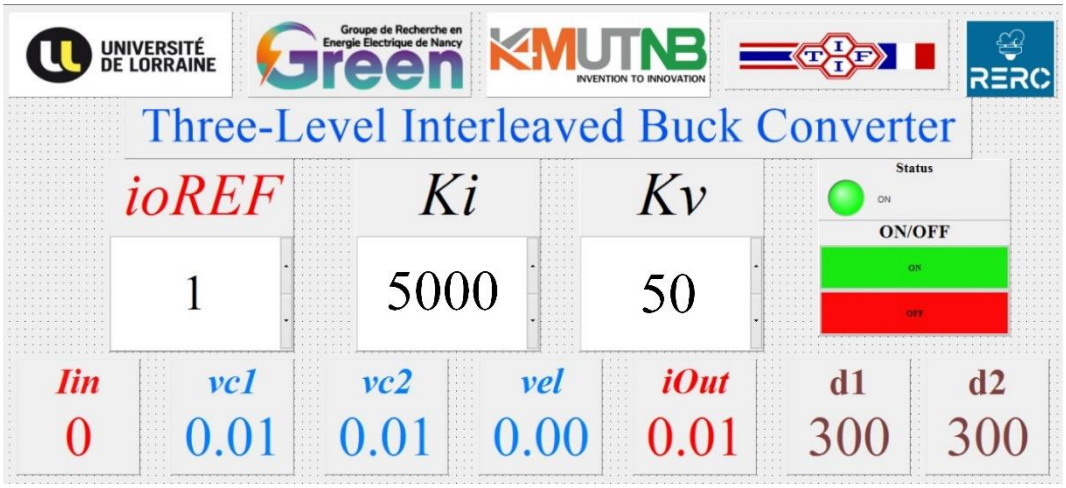

Figure 4-14: dSPACE ControlDesk interface for the experimental test bench.

4.3 Experimental tests of TLIBC with improved SMC

The experimental tests have been split into two tests to evaluate the effectiveness of the improved SMC for TLIBC during dynamic operations. First, the experimental tests have been carried out by modifying the output inductor current reference supplied to the PEM electrolyzer. Second, the experimental tests have been performed during input voltage fluctuation. The obtained experimental results of both experimental tests are presented and analyzed in the next subsections.

4.3.1 Experimental tests of output inductor current control

Firstly, the responses of the output inductor current i_{out}, the electrolyzer voltage v_{el}, and the input capacitor voltage v_{C1} have been assessed through experimental tests. The first experimental tests have been performed with the same conditions adopted for the simulation tests of output inductor current control (Chapter 3 subsection 3.5.1). The output inductor current reference I_{outREF} has been adjusted from 3 up to 10 A and vice-versa and filtered by a 2nd order filter to face the aggressive current of the output capacitor. However, the DC input voltage of experimental tests is higher than that for the simulation tests, it is equal to 150V. The obtained experimental results are presented in Figures 4-15 and 4-16.

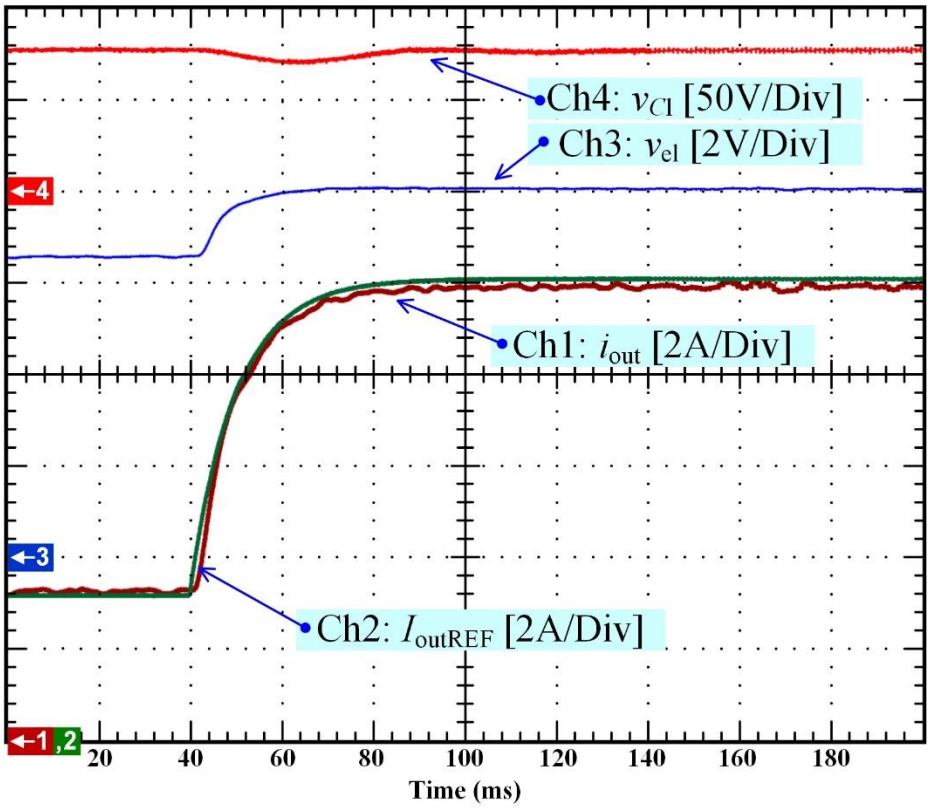

Figure 4-15: Experimental results: responses of v_{C1}, v_{el}, and i_{out} during the increase of I_{outREF} from 3 up to 10 A at a time scale equal to 20 ms.

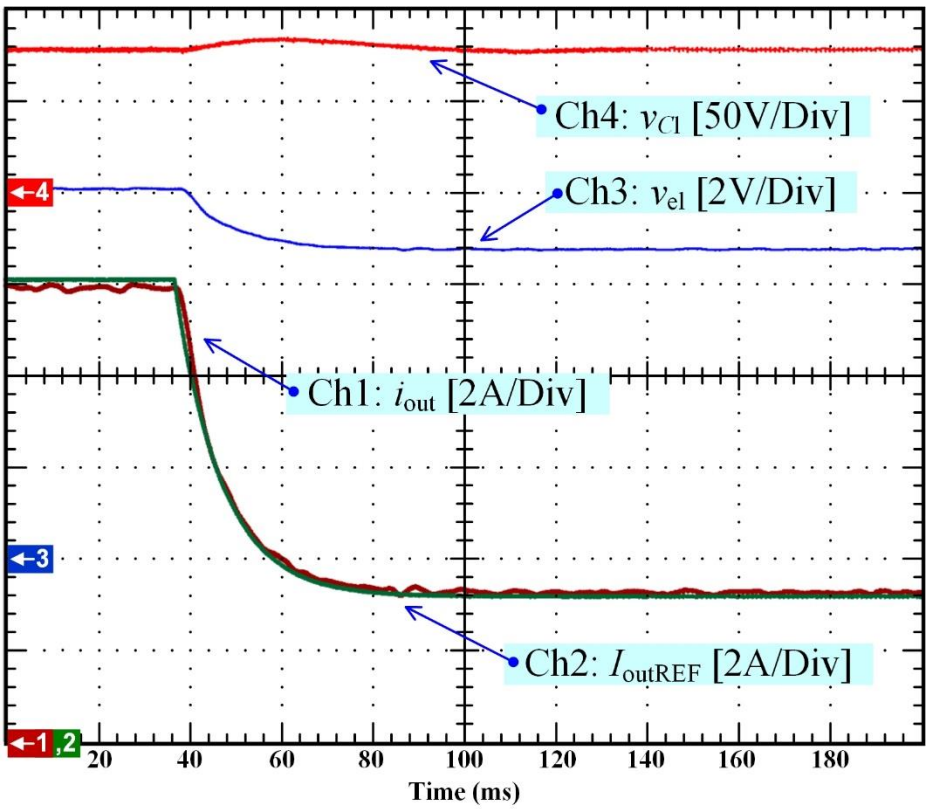

Figure 4-16: Experimental results: responses of v_{C1}, v_{el}, and i_{out} during the decrease of I_{outREF} from 10 down to 3 A at a time scale equal to 20 ms.

According to Figures 4-15 and 4-16, a time scale of 20 ms has been selected to highlight the dynamic responses and steady-state operations of all acquired signals. It can be noted that the obtained output inductor current i_{out} excellently follows the output inductor current reference I_{outREF} like the obtained simulation results (Figures 3-27 and 3-28). Moreover, the input capacitor v_{C1} fluctuates slightly during current variation and kept equal to 75 V. This value is the half of input voltage (i.e.,150V). Additionally, the developed PEM electrolyzer emulator is performed in normal voltage operation during I_{outREF} lower than 7 A. In comparison, the developed emulator is operated at a constant voltage operation when I_{outREF} is higher than 7 A. As a result, the voltage of the designed emulator is limited to 8 V.

Consequently, the hydrogen flow rate, $\dot{V}H_2$ and the energy efficiency of the electrolyzer, η_{el}, obtained from the DS1202 dSPACE−MicroLabBox have been considered throughout the experimental experiments. Thus, the obtained experimental results are illustrated in Figures 4-17 and 4-18.

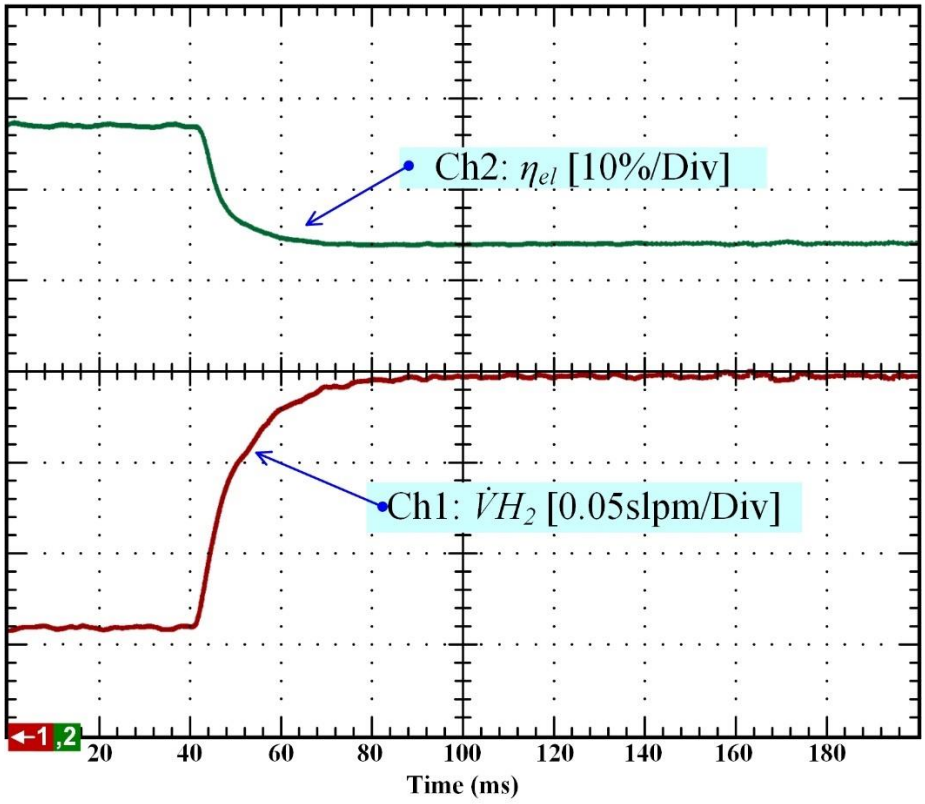

Figure 4-17: Experimental results: curves of $\dot{V}H_2$ and η_{el} during the increase of I_{outREF} from 3 up to 10 A at a time scale equal to 20 ms.

On one hand, according to Figure 4-17, the obtained experimental results of rising output inductor current reference, I_{outREF}, is depicted. It can be observed that the hydrogen flow rate, $\dot{V}H_2$, depends on the output inductor current i_{out}. Hence, this value is grown from 0.06 up to 0.2 slpm. In addition, based on Equation (2.7), the energy efficiency of the electrolyzer, η_{el}, is the reverse of the electrolyzer voltage v_{el}. For this reason, the energy efficiency decreases when the voltage increases. Thus, for this experimental test, the energy efficiency of the electrolyzer, η_{el}, has fallen from 68% down to 55%.

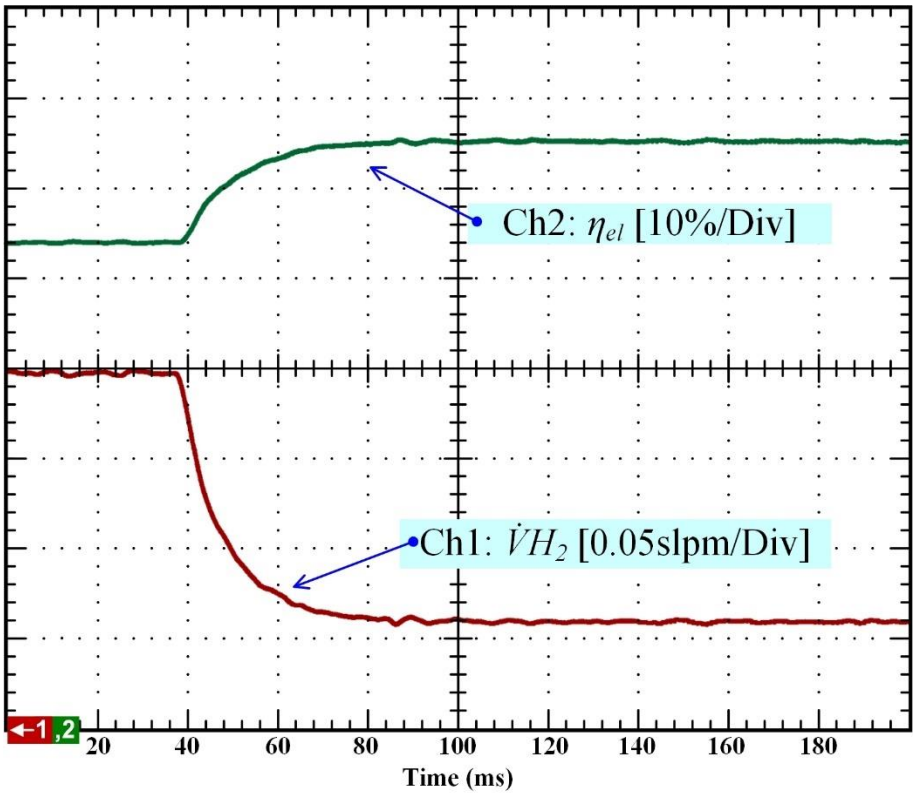

Figure 4-18: Experimental results: curves of $\dot{V}H_2$ and η_{el} during the decrease of I_{outREF} from 10 down to 3 A at a time scale equal to 20 ms.

On the other hand, the obtained experimental results of falling output inductor current reference, I_{outREF}, is shown in Figure 4-18. It can be noted that the obtained results are presented in a contrary way to the previous experimental results (Figure 4-17). Hence, the hydrogen flow rate, $\dot{V}H_2$ is reduced from 0.2 down to 0.06 slpm, while the energy efficiency of the electrolyzer, η_{el}, has risen from 55% up to 66%.

Moreover, to point out the energy efficiency of the electrolyzer η_{el} of both increase and decrease of output inductor current reference, I_{outREF}, both data have been plotted and compared according to the hydrogen flow rate, $\dot{V}H_2$, as demonstrated in Figure 4-19.

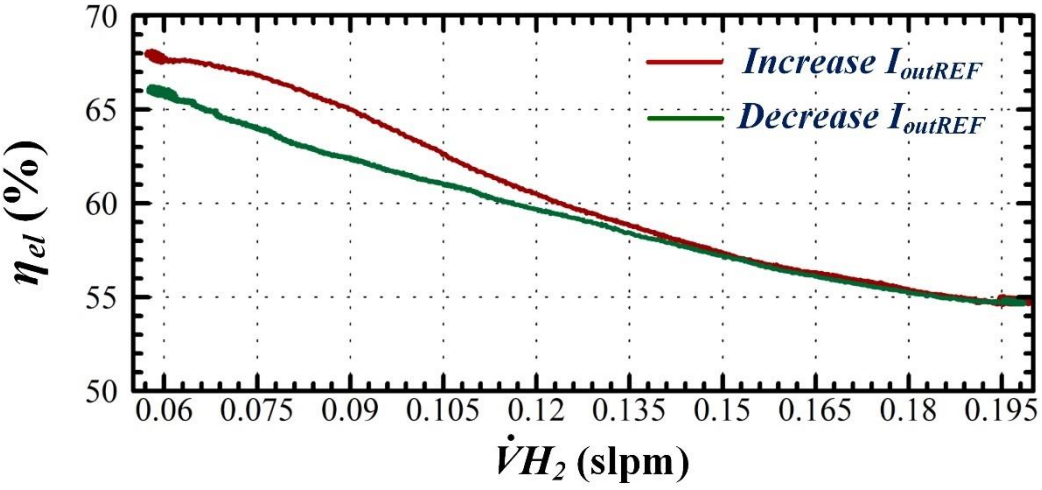

Figure 4-19: Comparison of η_{el} according to $\dot{V}H_2$ between increase and decrease of I_{outREF}.

Based on Figure 4-19, it can be emphasized that the energy efficiency decreases when the hydrogen flow rate increases. Indeed, the comparison of energy efficiency exhibits small errors at a hydrogen flow rate between 0.06 and 0.135 slpm. This error has occurred during the PEM electrolyzer changing mode from normal voltage operation to constant voltage operation or vice-versa.

Afterward, to emphasize the voltage dynamic response of developed PEM electrolyzer emulator combined with the studied TLIBC driven by the improved SMC, the second experimental tests of current control have been performed by modifying the output inductor current reference I_{outREF} from 3 up to 8 A and vice-versa at a constant DC input voltage of 150V. Moreover, a larger time scale of 2 s has been chosen to point out the dynamic responses and steady-state operations of the output inductor current, i_{out}, the electrolyzer voltage, v_{el}, and the input capacitor voltage, v_{C1}. The obtained results are depicted in Figures 4-20 and 4-21.

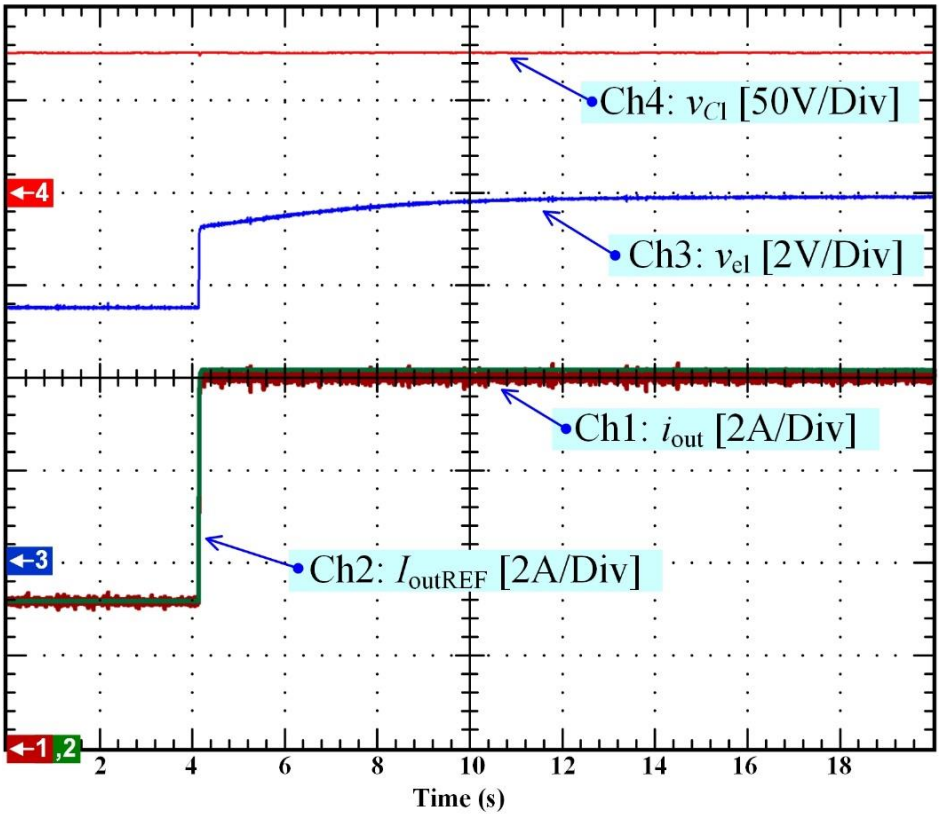

Figure 4-20: Experimental results: responses of v_{C1}, v_{el}, and i_{out} during the increase of I_{outREF} from 3 up to 8 A at a time scale equal to 2s.

Based on Figures 4-20 and 4-21, it can be observed that the improved SMC allows the obtained output inductor current, i_{out}, perfectly tracking the output inductor current reference, I_{outREF}, over a long period (20s), while the input capacitor voltage, v_{C1}, is maintained constant at 75V. Furthermore, the output inductor current, i_{out}, exhibits a small current ripple roughly equal to 0.1 A.

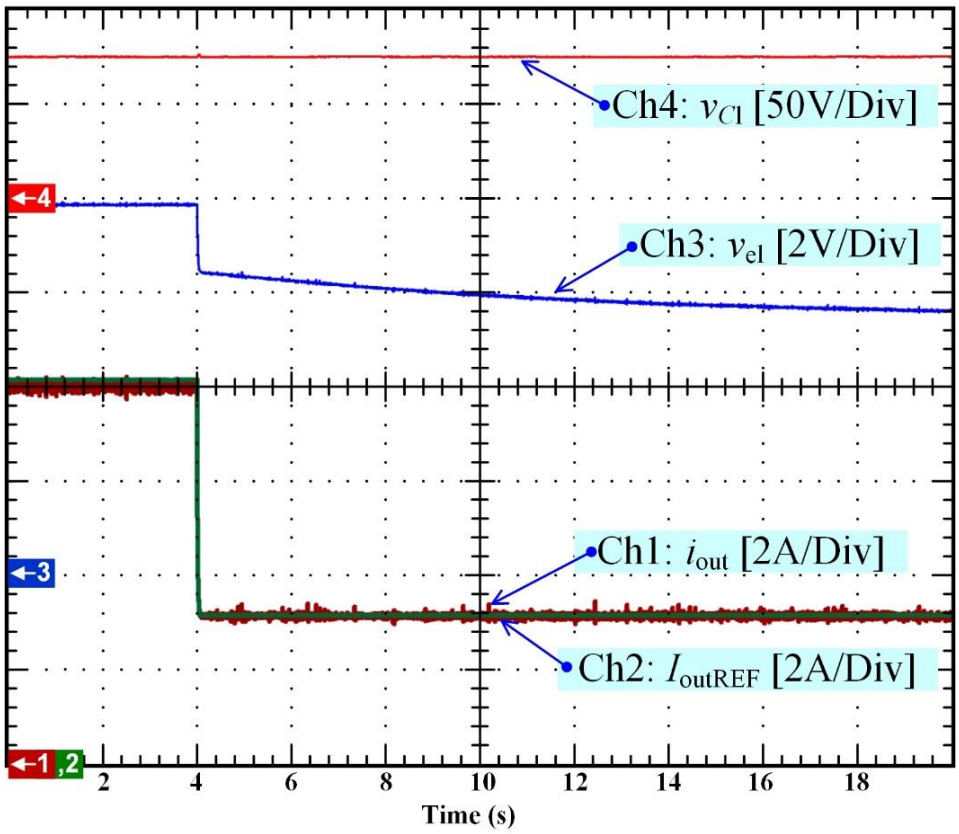

Figure 4-21: Experimental results: responses of v_{C1}, v_{el}, and i_{out} during the decrease of I_{outREF} from 8 down to 3 A at a time scale equal to 2 s.

On the other side, the developed PEM electrolyzer emulator can reproduce the behavior of a commercial PEM electrolyzer with accuracy even connected with the studied TLIBC. For the increase of I_{outREF} presented in Figure 4-17, the electrolyzer voltage v_{el} reaches the steady-state operation (i.e., constant voltage operation) in 10 s; whereas for the decrease of I_{outREF} reported in Figure 4-18, the steady-state operation is achieved in 16 s. Besides, the obtained electrolyzer voltage v_{el} of these experimental tests have reached the steady-state operation faster than the dynamic tests provided in Chapter 2 (subsection 2.4.2) because of closed-loop operations (TLIBC combined with the improved SMC).

Subsequently, as emphasized in the literature [47], [149], power conversion systems play an important role in ensuring the reliability of the power converter and extending the lifespan of the PEM electrolyzer. In addition, the voltage and current ripple produced by the operation of power electronics may cause the increase of specific energy consumption, which also degrade the performance of the PEM electrolyzer [149], [150]. As a result, power electronics (TLIBC) must generate low voltage and current ripple to the PEM electrolyzer.

Hench, the third experimental test of current control has consisted of using the AC coupling function of the oscilloscope to assess the output inductor current ripple and the electrolyzer voltage ripple, while the input voltage and the output inductor current reference I_{outREF} are constant at 150V and 10 A, respectively. The obtained results are reported in Figures 4-19, presenting the output inductor current i_{out}, the electrolyzer voltage, v_{el}, and the input capacitor voltage, v_{C1} at a time scale of 100 µs.

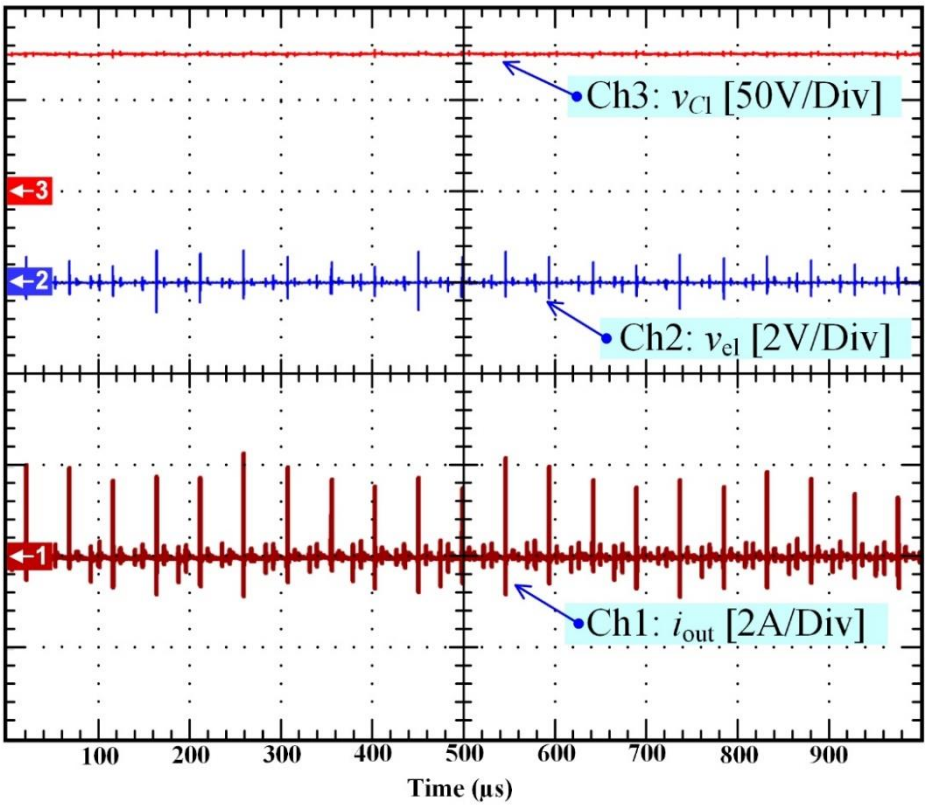

Figure 4-22: Experimental results: responses of v_{C1}, v_{el}, and i_{out} in steady state conditions.

Based on the obtained results in Figure 4-22, both output inductor current ripple and electrolyzer voltage ripple are close to zero during the steady-state operation (i.e., v_{in} = 150V and I_{outREF}= 10 A). It means that the TLIBC guarantees consequently the reliability of the PEM electrolyzer.

4.3.2 Experimental tests of balancing input capacitor voltages control

Second, experimental tests have been carried out during dynamic conditions to analyze the behavior of both input capacitors (C_1 and C_2) of TLIBC from the voltage balancing points of view. The two input capacitors must be balanced to avoid additional stress on passive components and power electronics devices. This additional stress may cause electrical failures and a loss in energy efficiency. Hence, experimental tests to verify input capacitor voltages balancing have been performed under input voltage variation conditions to replicate the intermittent characteristics of RES by modifying the input voltage from 100 up to 150 V and vice-versa, whereas the output inductor current reference I_{outREF} is kept constant at 10 A. The responses of both input capacitor voltages, v_{C1}, v_{C2}, the electrolyzer voltage, v_{el}, and the output inductor current, i_{out} have been investigated at a time scale of 200 ms. The obtained results are displayed in Figures 4-23 and 4-24.

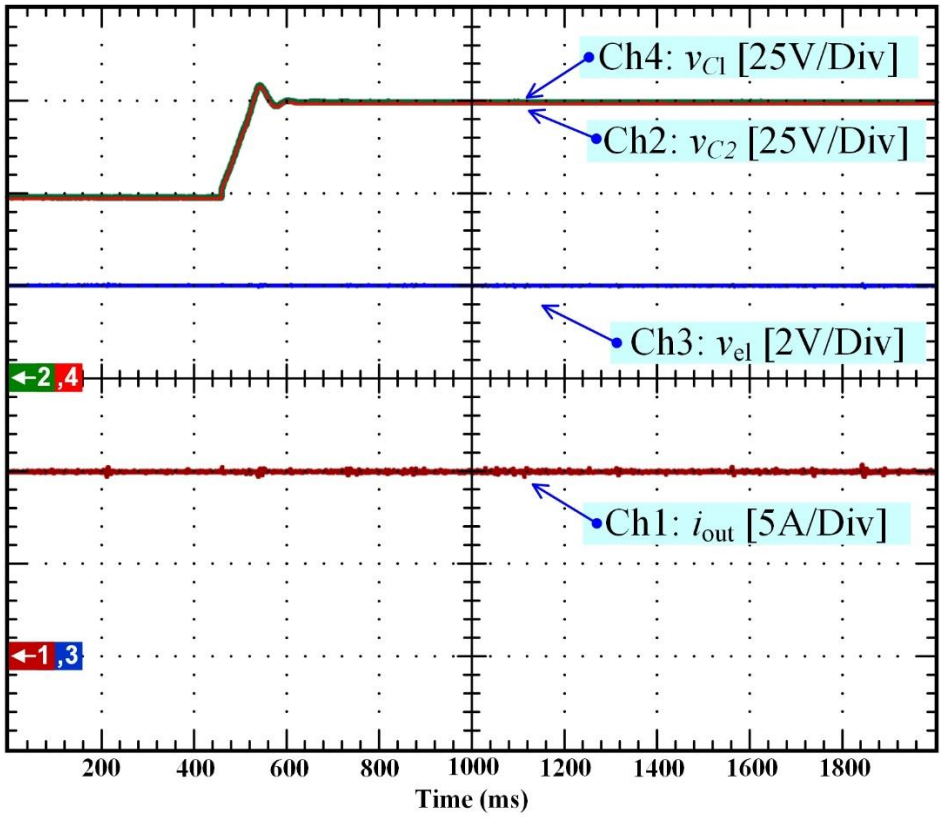

Figure 4-23: Experimental results: v_{in} change from 100 up to 150V at I_{outREF} = 10A.

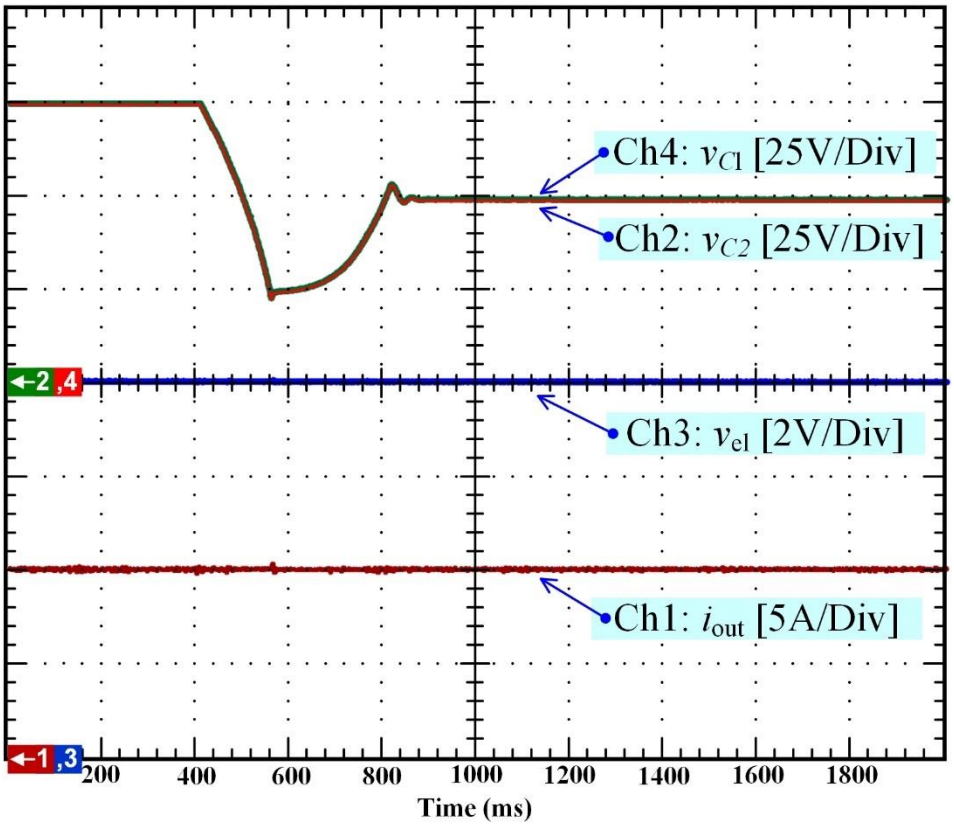

Figure 4-24: Experimental results: v_{in} fluctuation from 150 down to 100V at I_{outREF} = 10A.

According to the obtained experimental results, on one hand, in Figure 4-23, the input voltage has been increased from 100 up to 150V at a time equal to 450 ms and has reached the steady-state value at 600 ms. On the other hand, in Figure 4-24, the input voltage has been decreased from 150 down to 100V at a time equal to 400 ms and has achieved the steady-state value at 820 ms. It can be observed that both input capacitors voltage v_{C1}, v_{C1} are balanced and the value is half of the input voltage value during the input voltage fluctuation. Moreover, the output inductor current, i_{out}, is maintained stable at 10 A with a very small current ripple, while the electrolyzer voltage, v_{el}, is equal to 8 V. In conclusion, both input capacitor voltages do not suffer from balancing issues because of the input voltage variation. Thus, the main advantages of the TLIBC can also be guaranteed, and the reliability of the power electronics components.

4.4 Conclusion

The aim of the last chapter was to implement the experimental test bench platform of the studied hydrogen production system including the emulation of the electrical features of the 5-kW wind turbine (as discussed in Chapter 3), the studied TLIBC, and the developed PEM electrolyzer emulator (as reported in Chapter 2). First, the studied TLIBC has been realized to meet the specifications of the hydrogen production system as mentioned in Chapter 3 (subsection 3.3.3). Hence, the maximum rated of input voltage, output voltage, and electrical power rating is equal to 200V, 8V, and 5 kW, respectively. Thus, the electrical rated of power electronics devices have been selected based on those specifications. In addition, the magnetic ferrite cores ETD59-3C90 and ETD39-3C90 have been used to realize the main inductor and 4 commutation inductors, respectively. Moreover, accurate voltage and current sensors (i.e., LV-25P and LA-55P from LEM Company) have been chosen to measure all the signals in the studied TLIBC as required by the proposed improved SMC control.

Second, a fit experimental test rig platform has been built in the laboratory including the realized TLIBC controlled by the improved SMC. Thus, the proposed improved SMC has been realized in MATLAB®—Simulink environment. Subsequently, it has been implemented into the real-time board DS1202 dSPACE–MicroLabBox.

Finally, to validate the studied TLIBC with the developed control algorithm and assess its performance, two experimental tests have been performed under dynamic operations (i.e., output inductor current control and balancing input capacitor voltages control). The obtained experimental results have demonstrated the effectiveness of the proposed controller to ensure excellent dynamic performance as a result of a modification in the output inductor current reference (i.e., change hydrogen flow rate) and during the fluctuation of input voltage (to simulate the intermittent characteristics of RES). Furthermore, the proposed control laws enable to improve the dynamics of the hydrogen production system by increasing its efficiency. Moreover, the output inductor current ripple is very low, allowing the performance of the PEM electrolyzer to be guaranteed while its life span and energy efficiency are improved.

General Conclusion and Perspectives

The main objective of this work is to develop a high-power low voltage step-down DC-DC converter and a non-linear control algorithm for PEM electrolyzer applications. The main features expected of the developed converter for this application are low step-down conversion ratio gain, low output current ripple, high energy efficiency, reliability in case of electrical power switches failures, and low capital cost. On the other side, to test the proposed step-down DC-DC converter combined with a control strategy, the PEM electrolyzer emulator is very useful to replace a real PEM electrolyzer. Indeed, it can avoid the use of a real PEM electrolyzer that might be damaged when performing experimental tests.

The dissertation starts with the introduction of alkaline and PEM electrolyzer technologies. Thus, the basic operation, important characteristics, advantages, and drawbacks of alkaline and PEM electrolyzers have been compared and summarized. Hence, the PEM electrolyzer has been considered due to several advantages compared to the alkaline electrolyzer. Subsequently, the hydrogen production systems by using the water electrolysis process have been classified according to the type of low-carbon energy sources and bus configuration systems. Afterward, to face the intermittence issue of RES and handle the hydrogen flow rate of the PEM electrolyzer, the power electronic topologies have been deeply investigated to find the suitable topology for PEM electrolyzer applications. As a result, three-level interleaved buck converter (TLIBC) has been chosen to interface with PEM electrolyzer relying on their advantages. Finally, the PEM electrolyzer models have been investigated to precisely reproduce the actual behavior of the PEM electrolyzer. The modeling enables the development of the PEM electrolyzer emulator.

In chapter 2, the PEM electrolyzer emulator has been designed and implemented based on the static and dynamic behavior of a commercial PEM electrolyzer NMH2 1000 from HELIOCENTRIS Company. Hence, the static and dynamic operation of commercial PEM electrolyzers have been investigated. The behavior of real PEM electrolyzer includes slow and fast dynamics. As a result, static and dynamic behaviors are emulated by using an equivalent electrical circuit including six components (DC voltage source, two RC branches, and one resistor). The parameters of these components have been estimated by using a least-squares regression technique. The technical information to realize the electrolyzer emulator have been provided in detail. Moreover, the error of the values between the estimated parameters and the implemented parameters has been analyzed. The error analysis results have shown that the slight error values of each parameter have not affected the performance of the PEM electrolyzer emulator. Finally, to estimate the performance of the realized emulator in reproducing the static and dynamic behavior of a real PEM electrolyzer, an experimental test rig has been realized. The comparison between the obtained results of the developed emulator and real PEM electrolyzer has allowed attesting the performance of the developed PEM electrolyzer emulator.

In chapter 3, the development of the TLIBC has been introduced in detail to take advantage its main features. Thus, the main features of TLIBC have met the requirements for PEM electrolyzers. To explain the operations of TLIBC, two operating modes depending on the range of PWM duty cycle have been analyzed and detailed. In addition, the phase-shift PWM gate signal for the TLIBC is shifted π rad between each power switch. Subsequently, the step-down voltage conversion ratio of the TLIBC has been studied relying on the interleaved ZCT buck converter by using the large-average model. Because of the technical specifications of the investigated system, the obtained duty cycle values are very low by using the step-down voltage conversion ratio. Afterward, the overview of the studied hydrogen production system has been introduced. The system has consisted of the electrical specifications of a 5-kW wind turbine installed at the IUT of Longwy, the developed TLIBC, and the PEM electrolyzer emulator. Hence, the passive components of TLIBC have been sized according to the specifications of the system. Subsequently, the non-linear improved SMC has been introduced and designed to control the output inductor current and the balance of input capacitor voltages of the TLIBC. Finally, simulations of the TLIBC with the proposed improved SMC has been carried out in MATLAB®—Simulink by using the Simscape library. The obtained simulation results have confirmed that the proposed control laws offer excellent performance in controlling the output inductor current. Besides, the controller enables balancing both input capacitor voltages during dynamic operating conditions and the uncertainty of the parameters. Furthermore, it has been demonstrated that the reliability of the system can be ensured in case of power switch failures.

In chapter 4, the TLIBC with improved SMC has been designed and realized based on the technical features of the studied system. Hence, the electrical ratings of power electronics components have been chosen. Afterward, the output inductor and 4 commutation inductors have been realized by using fit magnetic ferrite cores. On the other side, the proposed improved SMC control laws have required 3 voltages and 2 currents measurement points in the developed TLIBC. Thus, LV-25P and LA-55P from LEM Company have been used. Subsequently, an experimental test bench platform has been built to evaluate the performance of the TLIBC controlled by an improved SMC. The improved SMC has been made in MATLAB®—Simulink environment and implemented into the real-time interface DS1202 dSPACE−MicroLabBox. Finally, the obtained experimental results have exhibited the robustness of the proposed controller against dynamic operating conditions (i.e., fluctuation behavior of RES and output current reference change). Moreover, the TLIBC together with the proposed strategy have allowed enhancing the efficiency of the hydrogen production system. Besides, the lifetime and energy efficiency of the PEM electrolyzer have been optimized because of a very low output current ripple.

According to this dissertation work reported in Chapters 1-4, several perspectives can be imagined.

First, from the reliability issue point of view, the studied TLIBC has been investigated in degraded operation (i.e., one power switch failure) only in simulation. Hence, this issue shall be examined thoroughly through tests with the developed experimental platform. This study will be rewarding to enhance the performance of the controller during degraded operating conditions.

Second, the main drawback of using a non-linear SMC approach is the high number of requested sensors. Therefore, it would be interesting to develop other non-linear control approaches with sensorless control applied to the TLIBC, such as flatness-based control, model-free control, and Hamiltonian control.

Finally, the power switches in the studied TLIBC are mainly based on silicon power MOSFET (i.e., RCX700N20) operating at low switching frequency (i.e., 10 kHz). Thus, to increase the power ratings and the efficiency of the TLIBC, the GaN or Sic-based power MOSFET which are able to operate at a high switching frequency (i.e., more than 100 kHz) could be used.

List of Publications

International Journals

1. B. Yodwong, D. Guilbert, M. Phattanasak, W. Kaewmanee, M. Hinaje, and G. Vitale, "Proton Exchange Membrane Electrolyzer Modeling for Power Electronics Control: A Short Review," *C*, vol. 6, no. 2, Art. no. 2, Jun. 2020, doi: 10.3390/c6020029.
2. B. Yodwong, D. Guilbert, M. Phattanasak, W. Kaewmanee, M. Hinaje, and G. Vitale, "AC-DC Converters for Electrolyzer Applications: State of the Art and Future Challenges," *Electronics*, vol. 9, no. 6, Art. no. 6, Jun. 2020, doi: 10.3390/electronics9060912.
3. B. Yodwong, D. Guilbert, M. Phattanasak, W. Kaewmanee, M. Hinaje, and G. Vitale, "Faraday's Efficiency Modeling of a Proton Exchange Membrane Electrolyzer Based on Experimental Data," *Energies*, vol. 13, no. 18, Art. no. 18, Jan. 2020, doi: 10.3390/en13184792.
4. B. Yodwong, D. Guilbert, M. Hinaje, M. Phattanasak, W. Kaewmanee, and G. Vitale, "Proton Exchange Membrane Electrolyzer Emulator for Power Electronics Testing Applications," *Processes*, vol. 9, no. 3, Art. no. 3, Mar. 2021, doi: 10.3390/pr9030498.

International Conferences

1. D. Guilbert, B. Yodwong, W. Kaewmanee, M. Phattanasak, and M. Hinaje, "Hydrogen Flow Rate Control of a Proton Exchange Membrane Electrolyzer," in *2019 Research, Invention, and Innovation Congress (RI2C)*, Dec. 2019, pp. 1–6. doi: 10.1109/RI2C48728.2019.8999963.
2. B. Yodwong, D. Guilbert, W. Kaewmanee, M. Phattanasak, M. Hinaje, and G. Vitale, "Modified Sliding Mode-Based Control of a Three-Level Interleaved DC-DC Buck Converter for Proton Exchange Membrane Water Electrolysis," in *2021 Research, Invention, and Innovation Congress: Innovation Electricals and Electronics (RI2C)*, Sep. 2021, pp. 221–226. doi: 10.1109/RI2C51727.2021.9559790.

Résumé en français

La production d'hydrogène basée sur le procédé de l'électrolyse de l'eau est une alternative intéressante pour faire face au réchauffement climatique et à l'épuisement des ressources fossiles [1]. En effet, la source d'électricité utilisée pour alimenter l'électrolyseur est la principale variable permettant de diminuer l'empreinte carbone [1]. Par exemple, l'électricité du réseau n'est pas un choix définitif pour l'électrolyseur puisque la majeure partie de l'électricité est générée par des centrales électriques basées sur des combustibles fossiles, qui émettent des gaz à effet de serre (c'est-à-dire des centrales électriques au charbon et au gaz naturel). Au contraire, une source d'énergie à faible émission de carbone telle que les sources d'énergie renouvelables (SER) (par exemple, l'énergie éolienne, solaire et hydraulique) et l'énergie nucléaire offrent une solution intéressante pour répondre à la demande croissante d'énergie tout en répondant au désir mondial de réduire les émissions de carbone. Néanmoins, des discontinuités énergétiques intermittentes sont généralement rencontrées lorsque les SER sont utilisés [2], [3].

De plus, le processus d'électrolyse de l'eau permet de générer de l'hydrogène avec une pureté de gaz élevée et en combinant ce processus avec des sources à faible teneur en carbone, de l'hydrogène vert peut être obtenu. Pour cette raison, dans cette thèse de doctorat, les travaux de recherche portent sur l'utilisation de l'électrolyse de l'eau comme moyen de production d'hydrogène.

En conséquence, des dispositifs de stockage d'énergie, tels que le stockage tampon d'hydrogène, peuvent être utilisés pour faire face aux problèmes de discontinuités. Par exemple, l'hydrogène produit et stocké peut être utilisé à diverses fins dans les procédés de production d'hydrogène basés sur les SER, comme le montre la figure A-1 [4], [5].

- Stockage d'énergie : Pour faire face aux interruptions d'énergie intermittentes, l'énergie excédentaire peut être stockée sous forme d'hydrogène pendant les périodes de faible demande d'énergie, puis utilisée pour équilibrer le réseau pendant les périodes de forte demande d'énergie. Par conséquent, le stockage d'hydrogène permet de maintenir un équilibre entre la production et la consommation.

- Transport : l'hydrogène peut être utilisé pour les véhicules électriques à pile à combustible. L'hydrogène est stocké dans des réservoirs sous pression (environ 700 bars) et permet d'alimenter les piles à combustible. Certains constructeurs ont déjà développé des véhicules électriques à pile à combustible tels que Hyundai (modèle Nexo et HDC-6 Neptune), Toyota (modèle Mirai II), et Honda (modèle Clarity).

- Industrie : l'hydrogène peut être utilisé dans un large éventail de processus industriels, y compris chimiques (par exemple, synthèse d'ammoniac, production de méthanol), électroniques (par exemple, fabrication de semi-conducteurs) et métallurgiques (par exemple, travail des métaux, aciers au carbone)

- Le Power-to-Gas : il consiste à convertir l'hydrogène en gaz méthane vert pouvant être pompé dans des canalisations et des installations souterraines via le procédé de méthanisation. Il s'agit d'une capacité de stockage alternative qui peut être utilisée où et quand elle est nécessaire, permettant au système d'alimentation d'être plus flexible.

Le processus d'électrolyse de l'eau consiste à utiliser de l'électricité provenant de sources d'énergie à faible teneur en carbone pour séparer l'eau déminéralisée en

oxygène et en hydrogène. Elle est réalisée par un électrolyseur. À l'heure actuelle, il existe quatre principaux types d'électrolyseurs : l'électrolyseur alcalin, l'électrolyseur à membrane échangeuse de protons (PEM), l'électrolyseur à oxyde solide (SO) et plus récemment les électrolyseurs à membrane échangeuse d'anions (AEM). L'électrolyseur alcalin et l'électrolyseur PEM sont disponibles dans le commerce, tandis que l'électrolyseur SO et l'électrolyseur AE restent encore en recherche et développement.

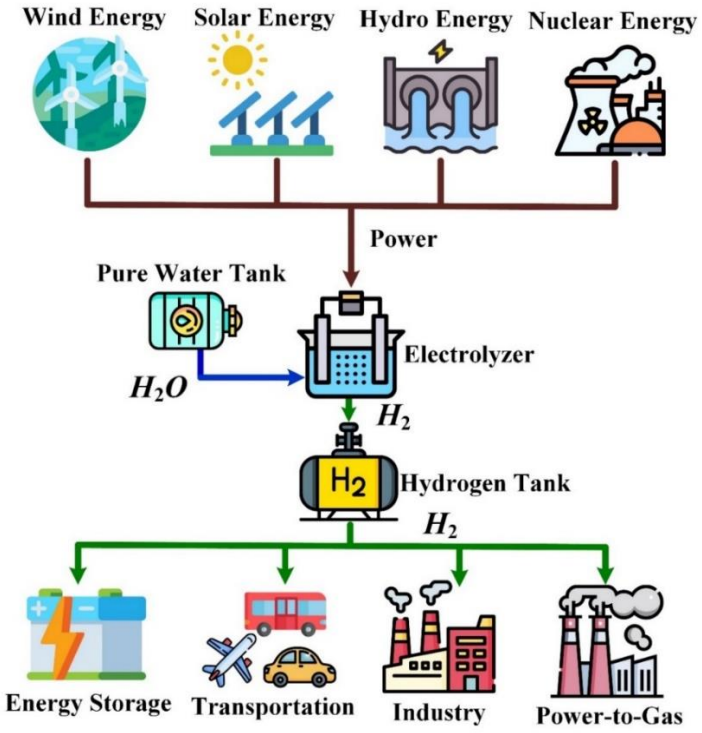

Figure A-1 : Vue d'ensemble des applications utilisant de l'hydrogène produit par électrolyse de l'eau alimenté par des sources d'énergie bas carbone.

D'une part, l'électrolyseur alcalin est la technologie la plus mature et la plus répandue pour les systèmes à grande échelle. Les points forts de cette technologie sont un coût d'investissement bon marché, une durée de vie élevée grâce au matériau du catalyseur à base de nickel et une efficacité énergétique élevée. Cependant, les électrolyseurs alcalins présentent plusieurs inconvénients tels que la faible densité de courant, la flexibilité, la maintenance (du fait de l'utilisation d'une solution liquide pour l'électrolyte), et ils ne sont pas adaptés aux fonctionnements dynamiques (lenteur du transport des ions hydroxydes (OH-)).

D'autre part, les électrolyseurs PEM ont été développés depuis les années 1960 pour faire face aux problèmes des électrolyseurs alcalins. Cette technologie fournit une densité de courant élevée, une plage de charge partielle élevée (0-100%), une réponse rapide aux conditions de fonctionnement dynamiques, ce qui les rend aptes à être couplées avec des SER. Néanmoins, le principal inconvénient est le coût d'investissement élevé dû à l'utilisation de matériaux catalyseurs nobles (par exemple l'iridium, le platine). Étant donné que l'électrolyseur PEM a des caractéristiques intéressantes, cette technologie est considérée dans cette thèse de doctorat.

De plus, l'électronique de puissance est obligatoire pour interfacer les SER et les électrolyseurs. Elle doit répondre à plusieurs problématiques tels que le faible gain du rapport de conversion abaisseur, la faible ondulation du courant de sortie,

le rendement énergétique élevé, la fiabilité en cas de défaillances des interrupteurs de puissance et le faible coût d'investissement. Habituellement, les SER génèrent une tension continue élevée (une centaine de volts environ) tandis que les électrolyseurs nécessitent une tension continue faible (une dizaine de volts). Pour cette raison, l'objectif principal de ce travail est de développer un convertisseur DC-DC abaisseur basse tension haute puissance et un algorithme de contrôle non linéaire pour les applications d'électrolyseur PEM afin de surmonter les problèmes ci-dessus et d'augmenter la production d'hydrogène, la fiabilité du système et la durée de vie de l'électrolyseur PEM. D'autre part, pour tester le convertisseur DC-DC abaisseur proposé combiné à une stratégie de contrôle, l'émulateur d'électrolyseur PEM est très utile pour remplacer un véritable électrolyseur PEM. En effet, cela peut éviter l'utilisation d'un véritable électrolyseur PEM qui pourrait être endommagé lors de la réalisation de tests expérimentaux.

La thèse de doctorat est divisée en quatre chapitres comme suit :

Dans le chapitre 1, les technologies d'électrolyseurs alcalins et PEM ont été introduites. Ainsi, le fonctionnement de base, les caractéristiques importantes, les avantages et les inconvénients des électrolyseurs alcalins et PEM ont été comparés et résumés. Par conséquent, l'électrolyseur PEM a été envisagé en raison de plusieurs avantages par rapport à l'électrolyseur alcalin. Par la suite, les systèmes de production d'hydrogène utilisant le procédé d'électrolyse de l'eau ont été classés selon le type de sources d'énergie à faible émission de carbone et les systèmes de configuration du bus continu. Par la suite, pour faire face au problème d'intermittence des SER et gérer le débit d'hydrogène de l'électrolyseur PEM, les topologies d'électronique de puissance ont été étudiées pour trouver la topologie appropriée pour les applications d'électrolyseurs PEM. En conséquence, le convertisseur abaisseur entrelacé à trois niveaux (TLIBC) a été choisi pour s'interfacer avec l'électrolyseur PEM tenant compte de leurs avantages. Enfin, les modèles d'électrolyseurs PEM ont été étudiés pour reproduire précisément le comportement réel de l'électrolyseur PEM. La modélisation permet le développement de l'émulateur d'électrolyseur PEM.

Dans le chapitre 2, l'émulateur d'électrolyseur PEM a été conçu et implémenté sur la base du comportement statique et dynamique d'un électrolyseur PEM commercial NMH2 1000 de la société HELIOCENTRIS. Par conséquent, le fonctionnement statique et dynamique des électrolyseurs PEM commerciaux a été étudié au moyen d'un banc d'essai expérimental. D'une part, la courbe caractéristique statique obtenue de l'électrolyseur PEM étudié est illustrée à la figure A-2. On peut souligner que la courbe statique montre deux fonctionnements différents : le fonctionnement à tension normale et le fonctionnement à tension constante. De plus, le fonctionnement à tension constante est dû à la dégradation de l'électrolyseur PEM.

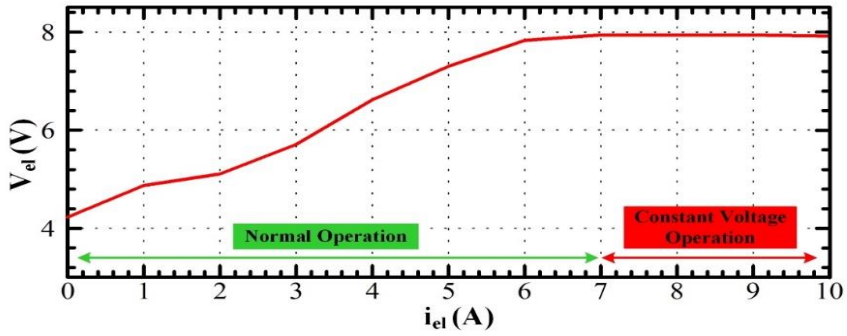

Figure A-2 : Caractéristique statique de l'électrolyseur PEM.

D'autre part, les réponses dynamiques obtenues à la suite d'un échelon de courant de 2 à 7 A sont représentées sur les figures A-3. Pour les résultats des tests, une longue base de temps (c'est-à-dire 5 s.div-1) a été fixée pour souligner le fonctionnement dynamique de l'électrolyseur PEM ainsi que le fonctionnement en régime permanent.

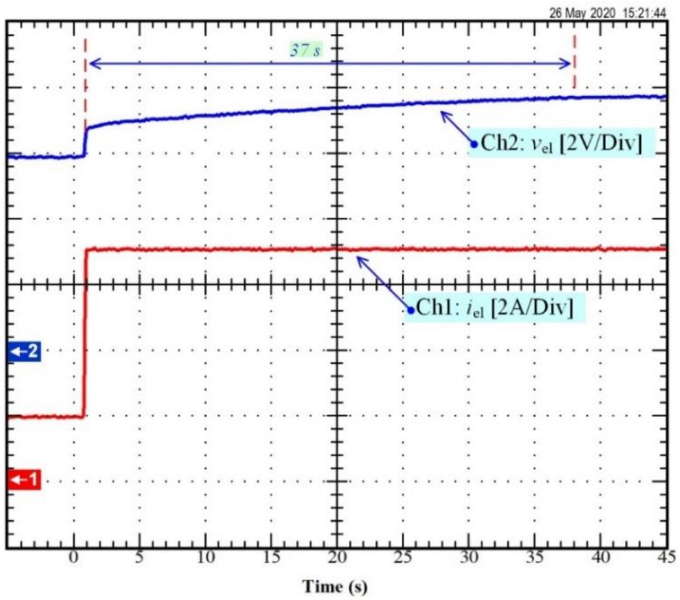

Figure A-3 : Réponse de l'électrolyseur PEM suite à un échelon de courant.

En conclusion, le comportement de l'électrolyseur PEM réel comprend une dynamique lente et rapide. Par conséquent, les comportements statiques et dynamiques sont émulés en utilisant un circuit électrique équivalent comme illustré à la Figure A-4.

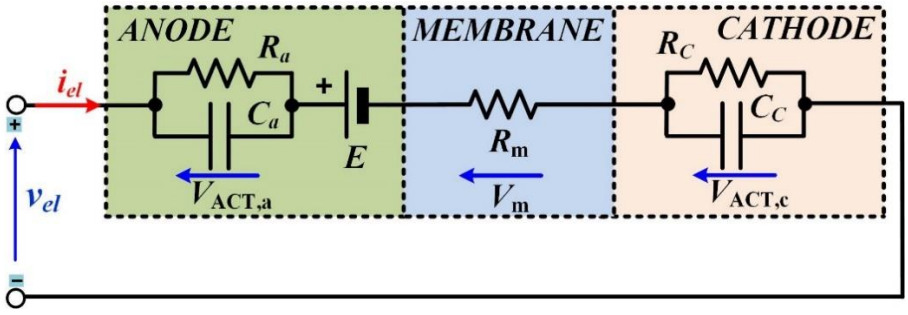

Figure A-4 : Circuit électrique équivalent de l'électrolyseur PEM.

Sur la base de la figure 2-4, le modèle de circuit électrique de l'émulateur d'électrolyseur PEM se compose de deux branches RC (c'est-à-dire Ra, Ca et Rc, Cc) pour émuler les cinétiques chimiques du côté anode et du côté cathode. La force électromotrice côté anode est modélisée comme l'énergie qui est transformée en hydrogène (c'est-à-dire la tension réversible E), tandis que la perte ohmique au niveau de la membrane est représentée par la résistance Rm. Les paramètres de ces composants ont été estimés en utilisant une technique de régression des moindres carrés. Les informations techniques pour réaliser l'émulateur d'électrolyseur ont été fournies en détail. Par conséquent, l'émulateur d'électrolyseur PEM mis en œuvre est illustré à la Figure A-5.

De plus, l'erreur des valeurs entre les paramètres estimés et les paramètres implémentés a été analysée. Les résultats de l'analyse des erreurs ont montré que les légères valeurs d'erreur de chaque paramètre n'ont pas affecté les performances de l'émulateur d'électrolyseur PEM.

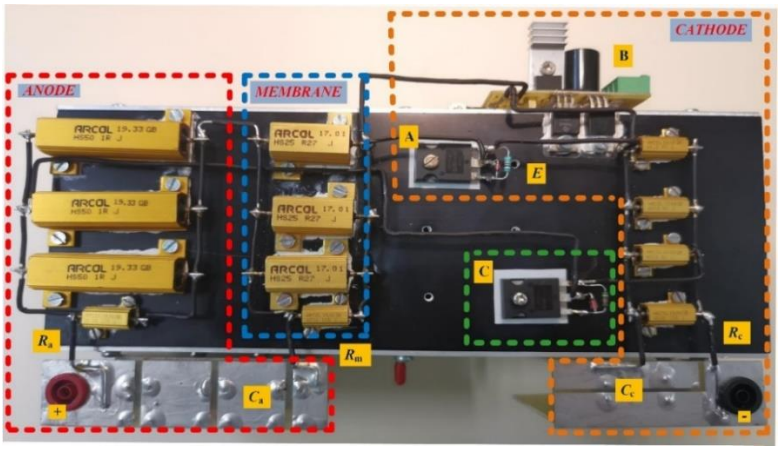

Figure A-5 : Emulateur d'électrolyseur PEM développé.

Enfin, pour estimer les performances de l'émulateur réalisé en reproduisant le comportement statique et dynamique d'un électrolyseur PEM réel, un banc d'essai expérimental a été réalisé. La comparaison entre les résultats obtenus de l'émulateur développé et de l'électrolyseur PEM réel a permis d'attester les performances de l'émulateur d'électrolyseur PEM développé.

Dans le chapitre 3, premièrement, le développement et le fonctionnement du TLIBC ont été introduits et détaillés. De plus, les signaux de commande pour le TLIBC sont décalés de π rad entre chaque interrupteur de puissance. Par conséquent, les principales caractéristiques du TLIBC sont obtenues comme suit : faible tension sur les interrupteurs de puissance, faible ondulation du courant de sortie, disponibilité en cas de défaillances des interrupteurs de puissance, rendement énergétique élevé, adapté à une échelle moyenne et petite taille de composants passifs. Ensuite, le rapport de conversion de tension abaisseur de TLIBC a été défini en utilisant un convertisseur abaisseur entrelacé avec le modèle moyen à grand signal. On peut souligner que le rapport de conversion de tension abaisseur est très faible. La TLIBC proposée est illustrée sur Figure A-6.

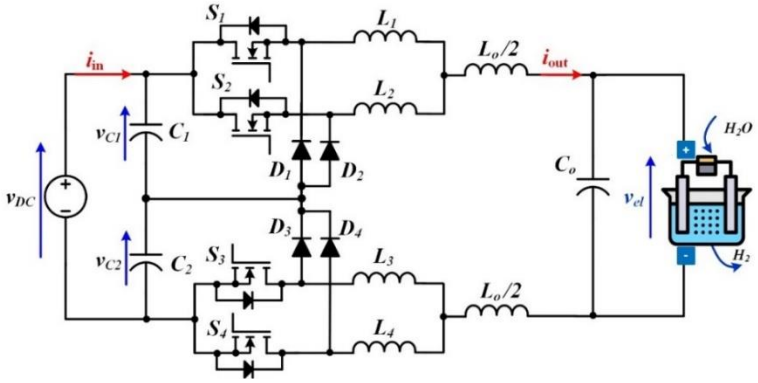

Figure A-6 : Convertisseur entrelacé buck trois niveaux (TLIBC)

Deuxièmement, les spécifications de l'éolienne de 5 kW située à l'IUT de Longwy et de l'émulateur d'électrolyseur PEM telles que conçues et réalisées au chapitre 2 ont été utilisées pour concevoir dans les meilleures situations le système

de production d'hydrogène étudié. Pour cette raison, les composants passifs de TLIBC ont été conçus et dimensionnés en fonction des spécifications de la source d'alimentation et de la charge du système.

Troisièmement, la commande de mode glissant améliorée (SMC) a été proposée pour être appliquée au TLIBC en raison des principaux avantages. En effet, cette stratégie de contrôle présente une robustesse face aux incertitudes des paramètres, une réponse dynamique rapide et une facilité de mise en œuvre. En outre, le contrôleur proposé a été conçu pour contrôler le courant de l'inductance de sortie et l'équilibre entre les tensions des deux condensateurs d'entrée de TLIBC, quelles que soient les conditions de fonctionnement fluctuantes (la référence de courant de l'inductance de sortie ou la tension continue d'entrée).

Enfin, le TLIBC avec l'algorithme de contrôle proposé a été évalué par des tests de simulation en utilisant MATLAB®—Simulink. La première simulation obtenue en modifiant la référence de courant de l'inductance de sortie I_{outREF} de 3 à 10 A par une tension d'entrée continue constante de 100 V est présentée sur Figure A-7.

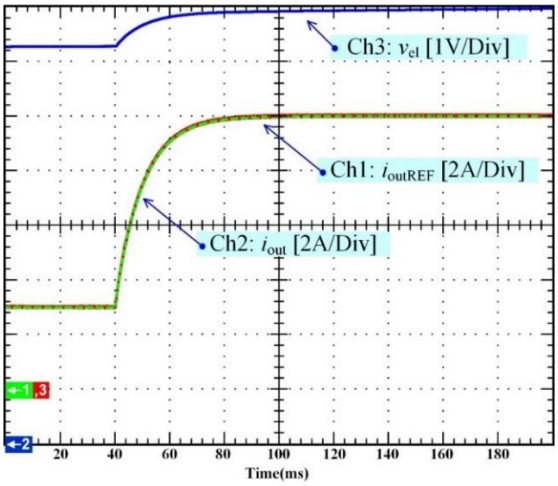

Figure A-7 : Résultats de simulation : réponse de v_{el} et i_{out} durant la variation de I_{outREF} de 3 à 10 A.

Le deuxième résultat de simulation obtenu en modifiant la tension d'entrée de 100 V à 150 V et vice-versa et en modifiant la valeur de capacité de C1 de 4400 µF à 1000 µF est illustré en Figure A-8.

On peut observer que les résultats de simulation obtenus ont permis de vérifier les performances et la robustesse de l'algorithme de contrôle proposé dans la régulation du courant d'inductance de sortie (c'est-à-dire le débit d'hydrogène) pour alimenter l'électrolyseur PEM tout en assurant l'équilibre des tensions des deux condensateurs d'entrée quelles que soient les perturbations.

De plus, les derniers résultats de simulation obtenus, tels que représentés sur la figure A-9, ont permis de démontrer la fiabilité de TLIBC avec l'algorithme de contrôle proposé pendant les modes de fonctionnement dégradés (c'est-à-dire en cas de défaillance de l'interrupteur de puissance).

Les résultats de simulation obtenus ont confirmé que les lois de commande proposées offrent d'excellentes performances dans le contrôle du courant d'inductance de sortie. En outre, le contrôleur permet d'équilibrer à la fois les tensions des condensateurs d'entrée dans des conditions de fonctionnement dynamiques et l'incertitude des paramètres. De plus, il a été démontré que la fiabilité du système peut être assurée en cas de panne de l'interrupteur d'alimentation.

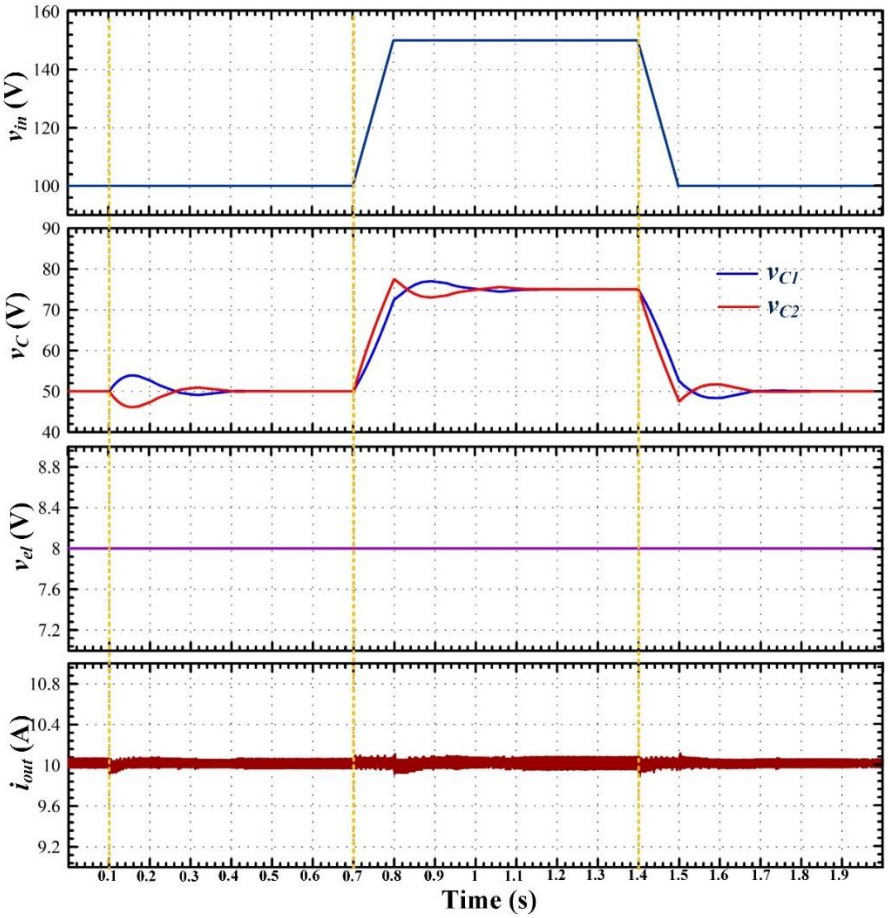

Figure A-8 : Résultats de simulation : variation de la valeur du condensateur d'entrée C_1 de 4400µF à 1000µF à I_{outREF} = 10A.

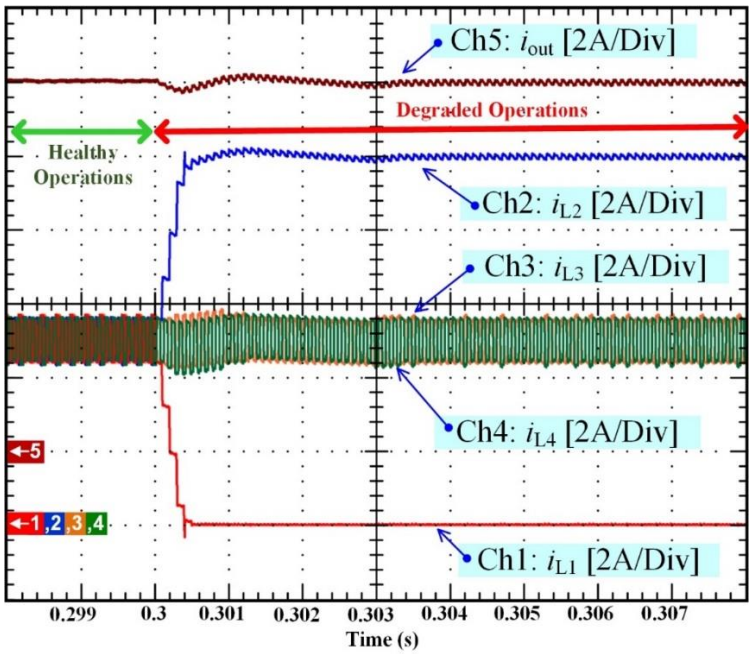

Figure A-9 : Réponses de $i_{L1}, i_{L2}, i_{L3}, i_{L4}$, et i_{out} lorsque le convertisseur passe d'un fonctionnement en mode sain (sans défauts) à un fonctionnement en mode dégradé (défaut de circuit ouvert sur l'interrupteur de la phase 1).

Dans le chapitre 4, en premier lieu, le TLIBC étudié a été réalisé pour répondre aux spécifications du système de production d'hydrogène comme mentionné au chapitre 3. Par conséquent, la tension nominale maximale d'entrée, de tension de sortie et de puissance électrique est égale à 200V, 8V, et 5 kW, respectivement. Ainsi, les caractéristiques électriques nominales des appareils électroniques de puissance ont été sélectionnées sur la base de ces spécifications. De plus, les noyaux magnétiques en ferrite ETD59-3C90 et ETD39-3C90 ont été utilisés pour réaliser respectivement l'inductance principale et les 4 inductances de commutation. De plus, des capteurs de tension et de courant précis (c'est-à-dire LV-25P et LA-55P de la société LEM) ont été choisis pour mesurer tous les signaux dans le TLIBC étudié, comme l'exige le contrôle SMC amélioré proposé.

En second lieu, une plateforme expérimental adaptée composée de l'émulation des caractéristiques électriques de l'éolienne de 5 kW (comme discuté au chapitre 3), du TLIBC étudié et de l'émulateur d'électrolyseur PEM développé (comme indiqué au chapitre 2) a été réalisé en laboratoire, y compris le TLIBC réalisé et contrôlé par le SMC amélioré, comme illustré sur la Figure A-10.

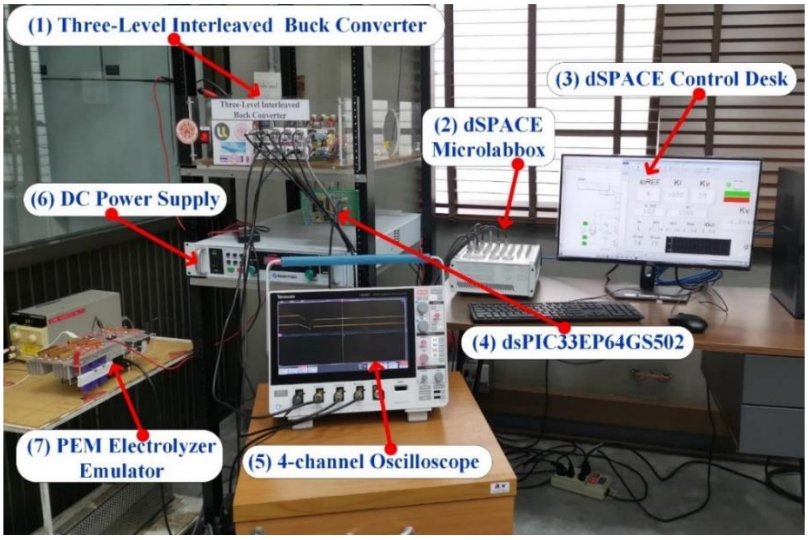

Figure A-10 : Plateforme expérimentale réalisée avec le convertisseur et l'émulateur d'électrolyseur PEM.

Ainsi, le SMC amélioré proposé a été réalisé dans l'environnement MATLAB®—Simulink. Par la suite, il a été implémenté dans la carte temps réel DS1202 dSPACE–MicroLabBox.

Cependant, le déphasage des signaux de commande PWM requis par le convertisseur ne peut pas être effectué via le DS1202 dSPACE-MicroLabBox. Par conséquent, un microcontrôleur basé sur dsPIC33EP64GS502 est utilisé pour les décaler de π rad comme requis par le convertisseur proposé. Une description schématique de ce banc d'essai expérimental est illustrée à la figure A-11.

Enfin, pour valider le TLIBC étudié avec l'algorithme de contrôle développé et évaluer ses performances, deux tests expérimentaux ont été effectués sous des opérations dynamiques (c'est-à-dire le contrôle du courant de l'inducteur de sortie et le contrôle des tensions du condensateur d'entrée d'équilibrage). Le premier test expérimental a été ajusté référence de courant de l'inducteur de sortie I_{outREF} de 3 à 10 A à la tension d'entrée est égale à 150V. Le résultat obtenu est illustré sur la Figure A-12.

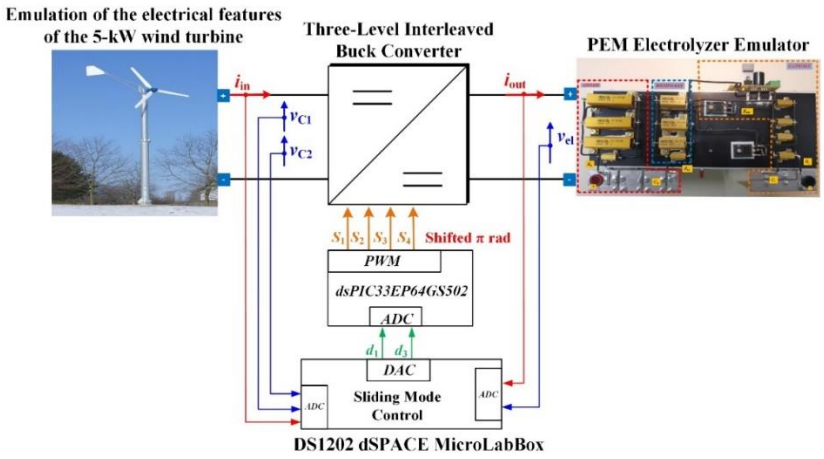

Figure A-11 : Description du banc de test développé.

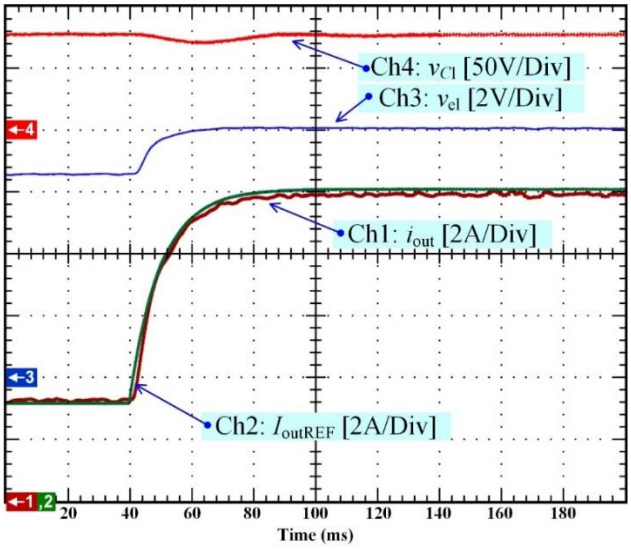

Figure A-12 : Résultats expérimentaux : réponses de v_{C1}, v_{el}, et i_{out} durant la variation de I_{outREF} de 3 à 10 A à une échelle de temps de 20 ms.

Selon la figure A-12, une échelle de temps de 20 ms a été sélectionnée pour mettre en évidence les réponses dynamiques et le fonctionnement en régime permanent de tous les signaux acquis. On peut noter que le courant d'inductance de sortie i_{out} obtenu suit parfaitement la référence de courant d'inductance de sortie I_{outREF} comme les résultats de simulation obtenus.

Ensuite, pour évaluer l'ondulation du courant de l'inductance de sortie et l'ondulation de la tension de l'électrolyseur, le test expérimental supplémentaire de contrôle du courant a été effectué en utilisant la fonction de couplage AC de l'oscilloscope, tandis que la tension d'entrée et la référence de courant de l'inductance de sortie I_{outREF} sont constantes à 150 V. et 10 A, respectivement. Les résultats obtenus sont reportés dans les figures A-13.

Sur la base des résultats obtenus en Figure A-13, l'ondulation du courant de l'inductance de sortie et l'ondulation de la tension de l'électrolyseur sont proches de zéro pendant le fonctionnement en régime permanent (c'est-à-dire v_{in} = 150 V et I_{outREF}= 10 A). Cela signifie que le TLIBC garantit, par conséquent, la fiabilité de l'électrolyseur PEM.

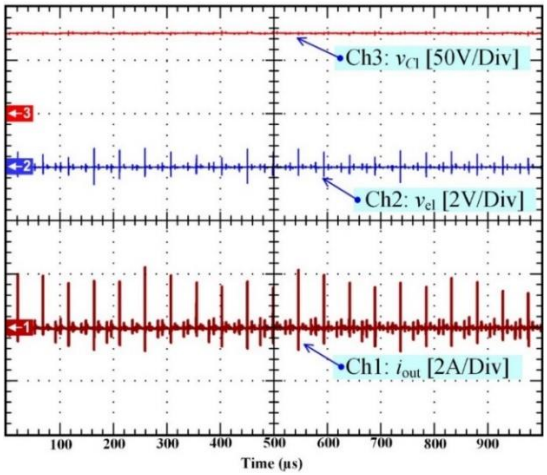

Figure A-13 : Résultats expérimentaux : réponses de v_{C1}, v_{el}, et i_{out} en conditions statiques.

Enfin, deuxièmement, des tests expérimentaux pour vérifier l'équilibrage des tensions des condensateurs d'entrée ont été effectués dans des conditions de variation de tension d'entrée pour reproduire les caractéristiques intermittentes de RES en modifiant la tension d'entrée de 100 à 150 V. Les résultats obtenus sont affichés en Figure A-14.

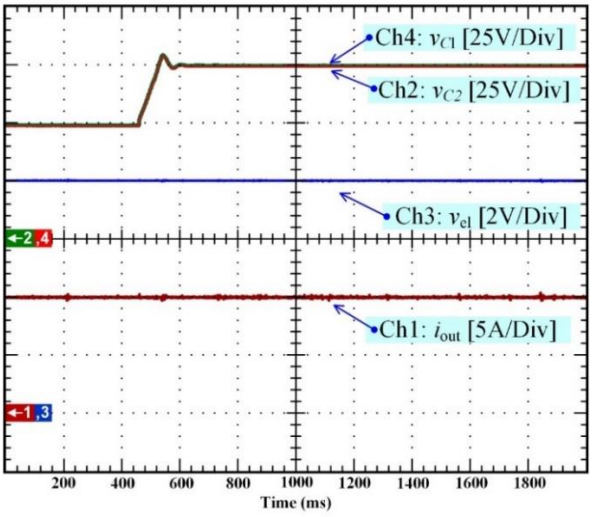

Figure A-14 : Résultats expérimentaux : variation de v_{in} de 100 à 150V à I_{outREF} = 10A.

Selon la Figure A-14, on peut observer que la tension des deux condensateurs d'entrée v_{C1}, v_{C1} est équilibrée et que la valeur est la moitié de la valeur de la tension d'entrée pendant la fluctuation de la tension d'entrée.

En conséquence, les résultats expérimentaux obtenus ont démontré l'efficacité du contrôleur proposé pour assurer d'excellentes performances dynamiques à la suite d'une modification de la référence de courant de l'inducteur de sortie (c'est-à-dire un changement de débit d'hydrogène) et lors de la fluctuation de la tension d'entrée (à simuler les caractéristiques intermittentes du SER). De plus, les lois de commande proposées permettent d'améliorer la dynamique du système de production d'hydrogène en augmentant son efficacité. S'ajoute à cela l'ondulation du courant de l'inducteur de sortie qui est très faible, permettant ainsi de garantir les performances de l'électrolyseur PEM tout en améliorant sa durée de vie et son efficacité énergétique.

Bibliography

[1] S. Shiva Kumar and V. Himabindu, “Hydrogen production by PEM water electrolysis – A review,” *Mater. Sci. Energy Technol.*, vol. 2, no. 3, pp. 442–454, Dec. 2019, doi: 10.1016/j.mset.2019.03.002.

[2] M. Carmo, D. L. Fritz, J. Mergel, and D. Stolten, “A comprehensive review on PEM water electrolysis,” *Int. J. Hydrog. Energy*, vol. 38, no. 12, pp. 4901–4934, Apr. 2013, doi: 10.1016/j.ijhydene.2013.01.151.

[3] D. S. Falcão and A. M. F. R. Pinto, “A review on PEM electrolyzer modelling: Guidelines for beginners,” *J. Clean. Prod.*, vol. 261, p. 121184, Jul. 2020, doi: 10.1016/j.jclepro.2020.121184.

[4] A. Buttler and H. Spliethoff, “Current status of water electrolysis for energy storage, grid balancing and sector coupling via power-to-gas and power-to-liquids: A review,” *Renew. Sustain. Energy Rev.*, vol. 82, pp. 2440–2454, Feb. 2018, doi: 10.1016/j.rser.2017.09.003.

[5] D. Apostolou, “Optimisation of a hydrogen production – storage – re-powering system participating in electricity and transportation markets. A case study for Denmark,” *Appl. Energy*, vol. 265, p. 114800, May 2020, doi: 10.1016/j.apenergy.2020.114800.

[6] M. David, C. Ocampo-Martínez, and R. Sánchez-Peña, “Advances in alkaline water electrolyzers: A review,” *J. Energy Storage*, vol. 23, pp. 392–403, Jun. 2019, doi: 10.1016/j.est.2019.03.001.

[7] M. Carmo and D. Stolten, “Chapter 4 - Energy Storage Using Hydrogen Produced From Excess Renewable Electricity: Power to Hydrogen,” in *Science and Engineering of Hydrogen-Based Energy Technologies*, P. E. V. de Miranda, Ed. Academic Press, 2019, pp. 165–199. doi: 10.1016/B978-0-12-814251-6.00004-6.

[8] L. M. Gandía, G. Arzamedi, and P. M. Diéguez, Eds., *Renewable hydrogen technologies: production, purification, storage, applications and safety*. Amsterdam ; Boston: Elsevier, 2013.

[9] C. Wulf, J. Linssen, and P. Zapp, “Chapter 9 - Power-to-Gas—Concepts, Demonstration, and Prospects,” in *Hydrogen Supply Chains*, C. Azzaro-Pantel, Ed. Academic Press, 2018, pp. 309–345. doi: 10.1016/B978-0-12-811197-0.00009-9.

[10] J. Brauns and T. Turek, “Alkaline Water Electrolysis Powered by Renewable Energy: A Review,” *Processes*, vol. 8, no. 2, Art. no. 2, Feb. 2020, doi: 10.3390/pr8020248.

[11] “https://pdf.directindustry.com/pdf/hydrogen-systems/hystat/14703-642454.html.”

[12] “https://cellar-c2.services.clever-cloud.com/com-mcphy/uploads/2020/08/20.05.McPhy_Portfolio_ELY_McLyzer_EN.pdf.”

[13] “http://www.teledynees.com/products/Hydrogen%20Oxygen%20 Generation%20Systems/Product%20Files/TESI_Brochure_TITAN_HMXT_Series_ English_2013.pdf.”

[14] “http://www.teledynees.com/products/Hydrogen%20Oxygen%20Generation%20 Systems/Product%20Files/TESI_Brochure_TITAN_EL_Series_English_2013.pdf.”

[15] “https://docplayer.org/60674771-Elektrolyseure-typ-ev.html.”

[16] “https://nelhydrogen.com/product/atmospheric-alkaline-electrolyser-a-series/.”

[17] “https://www.nubergindia.com/nuberg-hydrogen-brochure.pdf.”

[18] “https://sagim-gip.com/en/products/m/.”

[19] “http://www.cnthe.com/en.”

[20] “https://greenhydrogen.dk/wp-content/uploads/2021/02/A-Series-brochure-120421.pdf.”

[21] D. Bessarabov, H. Wang, H. Li, and N. Zhao, Eds., *PEM Electrolysis for Hydrogen Production: Principles and Applications*. Boca Raton: CRC Press, 2015. doi: 10.1201/b19096.

[22] M. Schalenbach, M. Carmo, D. L. Fritz, J. Mergel, and D. Stolten, “Pressurized PEM water electrolysis: Efficiency and gas crossover,” *Int. J. Hydrog. Energy*, vol. 38, no. 35, pp. 14921–14933, Nov. 2013, doi: 10.1016/j.ijhydene.2013.09.013.
[23] V. Liso, G. Savoia, S. S. Araya, G. Cinti, and S. K. Kær, “Modelling and Experimental Analysis of a Polymer Electrolyte Membrane Water Electrolysis Cell at Different Operating Temperatures,” *Energies*, vol. 11, no. 12, Art. no. 12, Dec. 2018, doi: 10.3390/en11123273.
[24] A. S. Tijani and A. H. A. Rahim, “Numerical Modeling the Effect of Operating Variables on Faraday Efficiency in PEM Electrolyzer,” *Procedia Technol.*, vol. 26, pp. 419–427, Jan. 2016, doi: 10.1016/j.protcy.2016.08.054.
[25] “https://www.h-tec.com/en/products/detail/h-tec-electrolysis-stack-series-s30/s30-10/.”
[26] “https://www.h-tec.com/en/products/detail/h-tec-pem-electrolyser-me100-350/me100-350/.”
[27] “https://www.h-tec.com/en/products/detail/h-tec-pem-electrolyser-me450-1400/me450-1400/.”
[28] “https://pdf.directindustry.com/pdf/hydrogen-systems/hylyzer/14703-642453.html.”
[29] “https://www.itm-power.com/products.”
[30] “https://assets.siemens-energy.com/siemens/assets/api/uuid:a193b68f-7ab4-4536-abe2-c23e01d0b526/datasheet-silyzer300.pdf.”
[31] “https://greenhydrogen.dk/wp-content/uploads/2019/11/HyProvideTM-P-Series.pdf.”
[32] “https://elogenh2.com/wp-content/uploads/2021/04/Elogen_Product_sheet-Multi-MW.pdf.”
[33] “https://nelhydrogen.com/product/s-series/.”
[34] “https://nelhydrogen.com/product/h-series/.”
[35] “https://nelhydrogen.com/product/c10-c20-c30/.”
[36] “https://nelhydrogen.com/product/m-series-containerized/.”
[37] “https://nelhydrogen.com/product/m-series-3/.”
[38] D. Guilbert, D. Sorbera, and G. Vitale, “A stacked interleaved DC-DC buck converter for proton exchange membrane electrolyzer applications: Design and experimental validation,” *Int. J. Hydrog. Energy*, vol. 45, no. 1, pp. 64–79, Jan. 2020, doi: 10.1016/j.ijhydene.2019.10.238.
[39] F. J. Vivas, A. De las Heras, F. Segura, and J. M. Andújar, “A review of energy management strategies for renewable hybrid energy systems with hydrogen backup,” *Renew. Sustain. Energy Rev.*, vol. 82, pp. 126–155, Feb. 2018, doi: 10.1016/j.rser.2017.09.014.
[40] M. E. Şahin, H. İ. Okumuş, and M. T. Aydemir, “Implementation of an electrolysis system with DC/DC synchronous buck converter,” *Int. J. Hydrog. Energy*, vol. 39, no. 13, pp. 6802–6812, Apr. 2014, doi: 10.1016/j.ijhydene.2014.02.084.
[41] H. Abu-Rub, M. Malinowski, and K. Al-Haddad, Eds., *Power electronics for renewable energy systems, transportation, and industrial applications*. Chichester, West Sussex, United Kingdom ; Hoboken, New Jersey: John Wiley & Sons Inc, 2014.
[42] F. Blaabjerg, M. Liserre, and K. Ma, “Power Electronics Converters for Wind Turbine Systems,” *IEEE Trans. Ind. Appl.*, vol. 48, no. 2, pp. 708–719, Mar. 2012, doi: 10.1109/TIA.2011.2181290.
[43] M. Cirrincione, M. Pucci, and G. Vitale, “Growing Neural Gas (GNG)-Based Maximum Power Point Tracking for High-Performance Wind Generator With an Induction Machine,” *IEEE Trans. Ind. Appl.*, vol. 47, no. 2, pp. 861–872, Mar. 2011, doi: 10.1109/TIA.2010.2102994.
[44] D. S. Oliveira, M. M. Reis, C. E. A. Silva, L. H. S. Colado Barreto, F. L. M. Antunes, and B. L. Soares, “A Three-Phase High-Frequency Semicontrolled Rectifier for PM WECS,” *IEEE Trans. Power Electron.*, vol. 25, no. 3, pp. 677–685, Mar. 2010, doi: 10.1109/TPEL.2009.2034263.

[45] R. Teichmann and S. Bernet, “A comparison of three-level converters versus two-level converters for low-voltage drives, traction, and utility applications,” *IEEE Trans. Ind. Appl.*, vol. 41, no. 3, pp. 855–865, May 2005, doi: 10.1109/TIA.2005.847285.
[46] T. Zhou, D. Lu, H. Fakham, and B. Francois, “Power flow control in different time scales for a wind/hydrogen/super-capacitors based active hybrid power system,” in *2008 13th International Power Electronics and Motion Control Conference*, Sep. 2008, pp. 2205–2210. doi: 10.1109/EPEPEMC.2008.4635592.
[47] J. Koponen, V. Ruuskanen, A. Kosonen, M. Niemelä, and J. Ahola, “Effect of Converter Topology on the Specific Energy Consumption of Alkaline Water Electrolyzers,” *IEEE Trans. Power Electron.*, vol. 34, no. 7, pp. 6171–6182, Jul. 2019, doi: 10.1109/TPEL.2018.2876636.
[48] F.-W. Speckmann, S. Bintz, and K. P. Birke, “Influence of rectifiers on the energy demand and gas quality of alkaline electrolysis systems in dynamic operation,” *Appl. Energy*, vol. 250, pp. 855–863, Sep. 2019, doi: 10.1016/j.apenergy.2019.05.014.
[49] V. Ruuskanen, J. Koponen, A. Kosonen, M. Niemelä, J. Ahola, and A. Hämäläinen, “Power quality and reactive power of water electrolyzers supplied with thyristor converters,” *J. Power Sources*, vol. 459, p. 228075, May 2020, doi: 10.1016/j.jpowsour.2020.228075.
[50] J. Solanki, N. Fröhleke, J. Böcker, A. Averberg, and P. Wallmeier, “High-current variable-voltage rectifiers: state of the art topologies,” *IET Power Electron.*, vol. 8, no. 6, pp. 1068–1080, 2015, doi: 10.1049/iet-pel.2014.0533.
[51] J. R. Rodriguez *et al.*, “Large current rectifiers: State of the art and future trends,” *IEEE Trans. Ind. Electron.*, vol. 52, no. 3, pp. 738–746, Jun. 2005, doi: 10.1109/TIE.2005.843949.
[52] Z. Dobó and Á. B. Palotás, “Impact of the current fluctuation on the efficiency of Alkaline Water Electrolysis,” *Int. J. Hydrog. Energy*, vol. 42, no. 9, pp. 5649–5656, Mar. 2017, doi: 10.1016/j.ijhydene.2016.11.142.
[53] J. Solanki, N. Fröhleke, J. Böcker, and P. Wallmeier, “Comparison of Thyristor-Rectifier with Hybrid Filter and Chopper-Rectifier for High-Power , High-Current Application,” 2013. https://www.semanticscholar.org/paper/Comparison-of-Thyristor-Rectifier-with-Hybrid-and-%2C-Solanki-Fr%C3%B6hleke/43786cfac4ceae8e1cb2d8b5e176c213571d5f16 (accessed Mar. 10, 2022).
[54] M. H. Rashid, Ed., *Power electronics handbook: devices, circuits, and applications handbook*, 3rd ed. Burlington, MA: Elsevier, 2011.
[55] J. Solanki, N. Fröhleke, and J. Böcker, “Implementation of Hybrid Filter for 12-Pulse Thyristor Rectifier Supplying High-Current Variable-Voltage DC Load,” *IEEE Trans. Ind. Electron.*, vol. 62, no. 8, pp. 4691–4701, Aug. 2015, doi: 10.1109/TIE.2015.2393833.
[56] D. S. Gautam and A. K. S. Bhat, “A Comparison of Soft-Switched DC-to-DC Converters for Electrolyzer Application,” *IEEE Trans. Power Electron.*, vol. 28, no. 1, pp. 54–63, Jan. 2013, doi: 10.1109/TPEL.2012.2195682.
[57] M. Albarghot and L. Rolland, “Comparison of experimental results with simulation of a PEM Electrolyzer powered by a horizontal wind turbine,” in *2017 International Conference of Electrical and Electronic Technologies for Automotive*, Jun. 2017, pp. 1–6. doi: 10.23919/EETA.2017.7993232.
[58] S. M. Muyeen, R. Takahashi, and J. Tamura, “Electrolyzer switching strategy for hydrogen generation from variable speed wind generator,” *Electr. Power Syst. Res.*, vol. 81, no. 5, pp. 1171–1179, May 2011, doi: 10.1016/j.epsr.2011.01.005.
[59] O. Alavi, A. Hooshmand Viki, M. Tavakoli Bina, and M. Akbari, “Reliability assessment of a stand-alone wind-hydrogen energy conversion system based on thermal analysis,” *Int. J. Hydrog. Energy*, vol. 42, no. 22, pp. 14968–14979, Jun. 2017, doi: 10.1016/j.ijhydene.2017.04.006.

[60] S. Dahbi, R. Aboutni, A. Aziz, N. Benazzi, M. Elhafyani, and K. Kassmi, “Optimised hydrogen production by a photovoltaic-electrolysis system DC/DC converter and water flow controller,” *Int. J. Hydrog. Energy*, vol. 41, no. 45, pp. 20858–20866, Dec. 2016, doi: 10.1016/j.ijhydene.2016.05.111.

[61] E. E. Carbajal-Gutierrez, J. A. Morales-Saldana, and J. Leyva-Ramos, “Modeling of a single-switch quadratic buck converter,” *IEEE Trans. Aerosp. Electron. Syst.*, vol. 41, no. 4, pp. 1450–1456, Oct. 2005, doi: 10.1109/TAES.2005.1561895.

[62] A. Ayachit and M. K. Kazimierczuk, “Steady-state analysis of PWM quadratic buck converter in CCM,” in *2013 IEEE 56th International Midwest Symposium on Circuits and Systems (MWSCAS)*, Aug. 2013, pp. 49–52. doi: 10.1109/MWSCAS.2013.6674582.

[63] V. Guida, D. Guilbert, and B. Douine, “Literature Survey of Interleaved DC-DC Step-Down Converters for Proton Exchange Membrane Electrolyzer Applications,” *Trans. Environ. Electr. Eng.*, vol. 3, no. 1, Art. no. 1, Mar. 2019, doi: 10.22149/teee.v3i1.129.

[64] D. Guilbert, M. Guarisco, A. Gaillard, A. N’Diaye, and A. Djerdir, “FPGA based fault-tolerant control on an interleaved DC/DC boost converter for fuel cell electric vehicle applications,” *Int. J. Hydrog. Energy*, vol. 40, no. 45, pp. 15815–15822, Dec. 2015, doi: 10.1016/j.ijhydene.2015.03.124.

[65] P. Thounthong and B. Davat, “Study of a multiphase interleaved step-up converter for fuel cell high power applications,” *Energy Convers. Manag.*, vol. 51, no. 4, pp. 826–832, Apr. 2010, doi: 10.1016/j.enconman.2009.11.018.

[66] D. Guilbert and G. Vitale, “Improved Hydrogen-Production-Based Power Management Control of a Wind Turbine Conversion System Coupled with Multistack Proton Exchange Membrane Electrolyzers,” *Energies*, vol. 13, no. 5, Art. no. 5, Jan. 2020, doi: 10.3390/en13051239.

[67] M. Ilic, B. Hesterman, and D. Maksimovic, “Interleaved zero current transition three-level buck converter,” in *Twenty-First Annual IEEE Applied Power Electronics Conference and Exposition, 2006. APEC ’06.*, Mar. 2006, p. 7 pp.-. doi: 10.1109/APEC.2006.1620518.

[68] A. Andrijanovitš, D. Vinnikov, I. Roasto, and A. Blinov, “Three-level half-bridge ZVS DC/DC converter for electrolyzer integration with renewable energy systems,” in *2011 10th International Conference on Environment and Electrical Engineering*, May 2011, pp. 1–4. doi: 10.1109/EEEIC.2011.5874703.

[69] C. Cavallaro, V. Cecconi, F. Chimento, S. Musumeci, C. Santonocito, and C. Sapuppo, “A Phase-Shift Full Bridge Converter for the Energy Management of Electrolyzer Systems,” in *2007 IEEE International Symposium on Industrial Electronics*, Jun. 2007, pp. 2649–2654. doi: 10.1109/ISIE.2007.4375026.

[70] S. Chakraborty, M. G. Simões, and W. E. Kramer, *Power Electronics for Renewable and Distributed Energy Systems: A Sourcebook of Topologies, Control and Integration*. Springer Science & Business Media, 2013.

[71] A. Garrigós, J. M. Blanes, J. A. Carrasco, J. L. Lizán, R. Beneito, and J. A. Molina, “5 kW DC/DC converter for hydrogen generation from photovoltaic sources,” *Int. J. Hydrog. Energy*, vol. 35, no. 12, pp. 6123–6130, Jun. 2010, doi: 10.1016/j.ijhydene.2010.03.131.

[72] P. Chandrasekhar and S. Rama Reddy, “Performance of soft-switched DC-DC resonant converter for Electrolyzer,” in *2011 4th International Symposium on Resilient Control Systems*, Aug. 2011, pp. 95–100. doi: 10.1109/ISRCS.2011.6016096.

[73] S. Zorica, M. Vukšić, and T. Betti, “Design considerations of the multi-resonant converter as a constant current source for electrolyser utilisation,” *Int. J. Electr. Power Energy Syst.*, vol. 111, pp. 237–247, Oct. 2019, doi: 10.1016/j.ijepes.2019.04.019.

[74] G. Vitale, F. Castaldi, and D. GUILBERT, “Design of a LLC Resonant Converter for Powering a PEM Electrolyzer,” *Renew. Energy Power Qual. J. REPQJ*, vol. 19, pp. 452–458, Sep. 2021, doi: 10.24084/repqj19.317.
[75] B. Yodwong, D. Guilbert, W. Kaewmanee, and M. Phattanasak, “Energy Efficiency Based Control Strategy of a Three-Level Interleaved DC-DC Buck Converter Supplying a Proton Exchange Membrane Electrolyzer,” *Electronics*, vol. 8, no. 9, Art. no. 9, Sep. 2019, doi: 10.3390/electronics8090933.
[76] “Data for: Power Quality and Reactive Power of Water Electrolyzers Supplied with Thyristor Converters. Available online: http://dx.doi.org/10.17632/ds64k8jjjy.1#file-95f3fd89-f4d6-4922-816f-9d5e07c0191f (accessed 23 April 2020).”
[77] O. Atlam, “An experimental and modelling study of a photovoltaic/proton-exchange membrane electrolyser system,” *Int. J. Hydrog. Energy*, vol. 34, no. 16, pp. 6589–6595, Aug. 2009, doi: 10.1016/j.ijhydene.2009.05.147.
[78] O. Atlam and M. Kolhe, “Equivalent electrical model for a proton exchange membrane (PEM) electrolyser,” *Energy Convers. Manag.*, vol. 52, no. 8, pp. 2952–2957, Aug. 2011, doi: 10.1016/j.enconman.2011.04.007.
[79] Ø. Ulleberg, “Modeling of advanced alkaline electrolyzers: a system simulation approach,” *Int. J. Hydrog. Energy*, vol. 28, no. 1, pp. 21–33, Jan. 2003, doi: 10.1016/S0360-3199(02)00033-2.
[80] P. Ayivor, J. R. Torres, M. V. D. Meijden, R. V. D. Pluijm, and B. Stouwie, “Modelling of Large Size Electrolyzer for Electrical Grid Stability Studies in Real Time Digital Simulation,” *undefined*, 2018, Accessed: Mar. 10, 2022. [Online]. Available: https://www.semanticscholar.org/paper/Modelling-of-Large-Size-Electrolyzer-for-Electrical-Ayivor-Torres/b81d82dc04bd48dde543d772f788cbc99a8c33e2
[81] F. da Costa Lopes and E. H. Watanabe, “Experimental and theoretical development of a PEM electrolyzer model applied to energy storage systems,” in *2009 Brazilian Power Electronics Conference*, Sep. 2009, pp. 775–782. doi: 10.1109/COBEP.2009.5347619.
[82] J. Larminie and A. Dicks, *Fuel cell systems explained*, 2nd ed. Chichester, West Sussex: J. Wiley, 2003.
[83] D. Guilbert and G. Vitale, “Experimental Validation of an Equivalent Dynamic Electrical Model for a Proton Exchange Membrane Electrolyzer,” in *2018 IEEE International Conference on Environment and Electrical Engineering and 2018 IEEE Industrial and Commercial Power Systems Europe (EEEIC / I CPS Europe)*, Jun. 2018, pp. 1–6. doi: 10.1109/EEEIC.2018.8494523.
[84] D. Guilbert and G. Vitale, “Dynamic Emulation of a PEM Electrolyzer by Time Constant Based Exponential Model,” *Energies*, vol. 12, no. 4, Art. no. 4, Jan. 2019, doi: 10.3390/en12040750.
[85] Á. Hernández-Gómez, V. Ramirez, and D. Guilbert, “Investigation of PEM electrolyzer modeling: Electrical domain, efficiency, and specific energy consumption,” *Int. J. Hydrog. Energy*, vol. 45, no. 29, pp. 14625–14639, May 2020, doi: 10.1016/j.ijhydene.2020.03.195.
[86] R. Ayop and C. W. Tan, “A comprehensive review on photovoltaic emulator,” *Renew. Sustain. Energy Rev.*, vol. 80, pp. 430–452, Dec. 2017, doi: 10.1016/j.rser.2017.05.217.
[87] T. D. Mai, S. De Breucker, K. Baert, and J. Driesen, “Reconfigurable emulator for photovoltaic modules under static partial shading conditions,” *Sol. Energy*, vol. 141, pp. 256–265, Jan. 2017, doi: 10.1016/j.solener.2016.11.050.
[88] M. C. Di Piazza and G. Vitale, “Photovoltaic field emulation including dynamic and partial shadow conditions,” *Appl. Energy*, vol. 87, no. 3, pp. 814–823, Mar. 2010, doi: 10.1016/j.apenergy.2009.09.036.
[89] M. C. D. Piazza, A. Ragusa, and G. Vitale, “Identification of photovoltaic array model parameters by robust linear regression methods,” 2009, doi: 10.24084/REPQJ07.268.

[90] R. Ayop and C. W. Tan, “Rapid Prototyping of Photovoltaic Emulator Using Buck Converter Based on Fast Convergence Resistance Feedback Method,” *IEEE Trans. Power Electron.*, vol. 34, no. 9, pp. 8715–8723, Sep. 2019, doi: 10.1109/TPEL.2018.2886927.
[91] D. M. K. Schofield, M. P. Foster, and D. A. Stone, “Low-cost solar emulator for evaluation of maximum power point tracking methods,” *Electron. Lett.*, vol. 47, no. 3, pp. 208–209, Feb. 2011, doi: 10.1049/el.2010.2930.
[92] Y. Kim, W. Lee, M. Pedram, and N. Chang, “Dual-mode power regulator for photovoltaic module emulation,” *Appl. Energy*, vol. 101, pp. 730–739, Jan. 2013, doi: 10.1016/j.apenergy.2012.07.025.
[93] G. Marsala, M. Pucci, G. Vitale, M. Cirrincione, and A. Miraoui, “A prototype of a fuel cell PEM emulator based on a buck converter,” *Appl. Energy*, vol. 86, no. 10, pp. 2192–2203, Oct. 2009, doi: 10.1016/j.apenergy.2008.12.028.
[94] C. de Beer, P. Barendse, and A. Khan, “Development of an HT PEM Fuel Cell Emulator Using a Multiphase Interleaved DC–DC Converter Topology,” *IEEE Trans. Power Electron.*, vol. 28, no. 3, pp. 1120–1131, Mar. 2013, doi: 10.1109/TPEL.2012.2208481.
[95] T. H. Kwan and Q. Yao, “A Cost Effective Experimental Emulator for Fuel Cell Based Combined Heat and Power Systems,” *Energy Procedia*, vol. 158, pp. 1437–1448, Feb. 2019, doi: 10.1016/j.egypro.2019.01.347.
[96] A. S. Samosir, M. Anwari, and A. H. M. Yatim, “A simple PEM fuel cell emulator using electrical circuit model,” in *2010 Conference Proceedings IPEC*, Oct. 2010, pp. 881–885. doi: 10.1109/IPECON.2010.5697090.
[97] F. Gao, B. Blunier, M. G. Simões, and A. Miraoui, “PEM Fuel Cell Stack Modeling for Real-Time Emulation in Hardware-in-the-Loop Applications,” *IEEE Trans. Energy Convers.*, vol. 26, no. 1, pp. 184–194, Mar. 2011, doi: 10.1109/TEC.2010.2053543.
[98] D. Rezzak, F. Khoucha, M. Benbouzid, A. Kheloui, and A. Mamoune, “A DC-DC converter-based PEM fuel cell system emulator,” in *2011 International Conference on Power Engineering, Energy and Electrical Drives*, May 2011, pp. 1–6. doi: 10.1109/PowerEng.2011.6036469.
[99] P. M. García-Vite, B. L. Reyes-García, C. L. Valdez-Hernández, and A. L. Martínez-Salazar, “Microcontroller-based emulation of a PEM fuel cell,” *Int. J. Hydrog. Energy*, vol. 45, no. 26, pp. 13767–13776, May 2020, doi: 10.1016/j.ijhydene.2019.10.034.
[100] T. Li, Y. Chen, H. Y. Gou, X. Y. Chen, M. G. Tang, and Y. Lei, “A DC Voltage Swell Compensator Based on SMES Emulator and Lead-Acid Battery,” *IEEE Trans. Appl. Supercond.*, vol. 29, no. 2, pp. 1–4, Mar. 2019, doi: 10.1109/TASC.2019.2894017.
[101] S. Farag, C. Lerman, S. Lineykin, and A. Kuperman, “Off-the-Shelf Power Supply-Based Battery/Supercapacitor Emulator for Charger Functionality Testing,” *IEEE Trans. Transp. Electrification*, vol. 2, no. 2, pp. 129–139, Jun. 2016, doi: 10.1109/TTE.2016.2543965.
[102] E. Mohammadi, R. Fadaeinedjad, and H. R. Naji, “Using a new wind turbine emulator to analyze tower shadow and yaw error effects,” *Energy Convers. Manag.*, vol. 174, pp. 378–387, Oct. 2018, doi: 10.1016/j.enconman.2018.08.049.
[103] M. Ashourianjozdani, L. A. C. Lopes, and P. Pillay, “Power Electronic Converter Based PMSG Emulator: A Testbed for Renewable Energy Experiments,” *IEEE Trans. Ind. Appl.*, vol. 54, no. 4, pp. 3626–3636, Jul. 2018, doi: 10.1109/TIA.2018.2819618.
[104] D. H. Wollz, S. A. O. da Silva, and L. P. Sampaio, “Real-time monitoring of an electronic wind turbine emulator based on the dynamic PMSG model using a graphical interface,” *Renew. Energy*, vol. 155, pp. 296–308, Aug. 2020, doi: 10.1016/j.renene.2020.03.096.

[105] E. Durán, J. M. Andújar, F. Segura, and A. J. Barragán, "A high-flexibility DC load for fuel cell and solar arrays power sources based on DC–DC converters," *Appl. Energy*, vol. 88, no. 5, pp. 1690–1702, May 2011, doi: 10.1016/j.apenergy.2010.11.002.
[106] Y. Srinivasa Rao and M. C. Chandorkar, "Real-Time Electrical Load Emulator Using Optimal Feedback Control Technique," *IEEE Trans. Ind. Electron.*, vol. 57, no. 4, pp. 1217–1225, Apr. 2010, doi: 10.1109/TIE.2009.2037657.
[107] J. Wang *et al.*, "Static and dynamic power system load emulation in converter-based reconfigurable power grid emulator," in *2014 IEEE Energy Conversion Congress and Exposition (ECCE)*, Sep. 2014, pp. 4008–4015. doi: 10.1109/ECCE.2014.6953947.
[108] M. Kesler, E. Ozdemir, M. C. Kisacikoglu, and L. M. Tolbert, "Power Converter-Based Three-Phase Nonlinear Load Emulator for a Hardware Testbed System," *IEEE Trans. Power Electron.*, vol. 29, no. 11, pp. 5806–5812, Nov. 2014, doi: 10.1109/TPEL.2014.2301815.
[109] A. S. Vijay, M. C. Chandorkar, and S. Doolla, "A System Emulator for AC Microgrid Testing," *IEEE Trans. Ind. Appl.*, vol. 55, no. 6, pp. 6538–6547, Nov. 2019, doi: 10.1109/TIA.2019.2942275.
[110] B. Yodwong, D. Guilbert, M. Phattanasak, W. Kaewmanee, M. Hinaje, and G. Vitale, "AC-DC Converters for Electrolyzer Applications: State of the Art and Future Challenges," *Electronics*, vol. 9, no. 6, Art. no. 6, Jun. 2020, doi: 10.3390/electronics9060912.
[111] B. Yodwong, D. Guilbert, M. Phattanasak, W. Kaewmanee, M. Hinaje, and G. Vitale, "Proton Exchange Membrane Electrolyzer Modeling for Power Electronics Control: A Short Review," *C*, vol. 6, no. 2, Art. no. 2, Jun. 2020, doi: 10.3390/c6020029.
[112] G. Fontes, C. Turpin, S. Astier, and T. A. Meynard, "Interactions Between Fuel Cells and Power Converters: Influence of Current Harmonics on a Fuel Cell Stack," *IEEE Trans. Power Electron.*, vol. 22, no. 2, pp. 670–678, Mar. 2007, doi: 10.1109/TPEL.2006.890008.
[113] B. Wahdame *et al.*, "Impact of power converter current ripple on the durability of a fuel cell stack," in *2008 IEEE International Symposium on Industrial Electronics*, Jun. 2008, pp. 1495–1500. doi: 10.1109/ISIE.2008.4677206.
[114] R. S. Gemmen, "Analysis for the Effect of Inverter Ripple Current on Fuel Cell Operating Condition," *J. Fluids Eng.*, vol. 125, no. 3, pp. 576–585, Jun. 2003, doi: 10.1115/1.1567307.
[115] Y. Zhan, Y. Guo, J. Zhu, B. Liang, and B. Yang, "Comprehensive influences measurement and analysis of power converter low frequency current ripple on PEM fuel cell," *Int. J. Hydrog. Energy*, vol. 44, no. 59, pp. 31352–31359, Nov. 2019, doi: 10.1016/j.ijhydene.2019.09.231.
[116] A. Ursúa, L. Marroyo, E. Gubía, L. M. Gandía, P. M. Diéguez, and P. Sanchis, "Influence of the power supply on the energy efficiency of an alkaline water electrolyser," *Int. J. Hydrog. Energy*, vol. 34, no. 8, pp. 3221–3233, May 2009, doi: 10.1016/j.ijhydene.2009.02.017.
[117] A. Ursúa, P. Sanchis, and L. Marroyo, "Electric Conditioning and Efficiency of Hydrogen Production Systems and Their Integration with Renewable Energies," 2013. doi: 10.1016/B978-0-444-56352-1.00014-3.
[118] J. T. Pukrushpan, "Modeling and control of fuel cell systems and fuel processors.," Thesis, 2003. Accessed: Mar. 10, 2022. [Online]. Available: http://deepblue.lib.umich.edu/handle/2027.42/123461
[119] M. Hinaje, S. Raël, P. Noiying, D. A. Nguyen, and B. Davat, "An Equivalent Electrical Circuit Model of Proton Exchange Membrane Fuel Cells Based on Mathematical Modelling," *Energies*, vol. 5, no. 8, Art. no. 8, Aug. 2012, doi: 10.3390/en5082724.
[120] B. Yodwong, D. Guilbert, M. Phattanasak, W. Kaewmanee, M. Hinaje, and G. Vitale, "Faraday's Efficiency Modeling of a Proton Exchange Membrane Electrolyzer Based

on Experimental Data," *Energies*, vol. 13, no. 18, Art. no. 18, Jan. 2020, doi: 10.3390/en13184792.
[121] "RS, distributeur de composants électroniques & fournitures industrielles, Fr.Rs-Online.Com. (2021)."
[122] "Electrolyzer Stacks, Fuelcellstore.Com. (2021)."
[123] J. R. Pinheiro and I. Barbi, "The three-level ZVS PWM converter-a new concept in high voltage DC-to-DC conversion," in *and Automation Proceedings of the 1992 International Conference on Industrial Electronics, Control, Instrumentation*, Nov. 1992, pp. 173–178 vol.1. doi: 10.1109/IECON.1992.254637.
[124] X. Ruan, L. Zhou, and Y. Yan, "Soft-switching PWM three-level converters," *IEEE Trans. Power Electron.*, vol. 16, no. 5, pp. 612–622, Sep. 2001, doi: 10.1109/63.949494.
[125] V. Yousefzadeh, E. Alarcon, and D. Maksimovic, "Three-level buck converter for envelope tracking applications," *IEEE Trans. Power Electron.*, vol. 21, no. 2, pp. 549–552, Mar. 2006, doi: 10.1109/TPEL.2005.869728.
[126] J. P. Rodrigues, S. A. Mussa, M. L. Heldwein, and A. J. Perin, "Three-Level ZVS Active Clamping PWM for the DC–DC Buck Converter," *IEEE Trans. Power Electron.*, vol. 24, no. 10, pp. 2249–2258, Oct. 2009, doi: 10.1109/TPEL.2009.2022535.
[127] C. Carstensen and J. Biela, "A Three-Level Buck Converter With a Wide Voltage Operation Range for Hardware-in-the-Loop Test Systems," *IEEE Trans. Power Electron.*, vol. 31, no. 9, pp. 6176–6191, Sep. 2016, doi: 10.1109/TPEL.2015.2504402.
[128] X. Ruan, B. Li, Q. Chen, S.-C. Tan, and C. K. Tse, "Fundamental Considerations of Three-Level DC–DC Converters: Topologies, Analyses, and Control," *IEEE Trans. Circuits Syst. Regul. Pap.*, vol. 55, no. 11, pp. 3733–3743, Dec. 2008, doi: 10.1109/TCSI.2008.927218.
[129] X. Ruan, B. Li, and Q. Chen, "Three-level converters-a new approach for high voltage and high power DC-to-DC conversion," in *2002 IEEE 33rd Annual IEEE Power Electronics Specialists Conference. Proceedings (Cat. No.02CH37289)*, Jun. 2002, vol. 2, pp. 663–668 vol.2. doi: 10.1109/PSEC.2002.1022529.
[130] W. Li and X. He, "Review of Nonisolated High-Step-Up DC/DC Converters in Photovoltaic Grid-Connected Applications," *IEEE Trans. Ind. Electron.*, vol. 58, no. 4, pp. 1239–1250, Apr. 2011, doi: 10.1109/TIE.2010.2049715.
[131] O. Garcia, P. Zumel, A. de Castro, and A. Cobos, "Automotive DC-DC bidirectional converter made with many interleaved buck stages," *IEEE Trans. Power Electron.*, vol. 21, no. 3, pp. 578–586, May 2006, doi: 10.1109/TPEL.2006.872379.
[132] V. Guida, D. Guilbert, G. Vitale, and B. Douine, "Design and Realization of a Stacked Interleaved DC–DC Step-Down Converter for PEM Water Electrolysis with Improved Current Control," *Fuel Cells*, vol. 20, Jun. 2020, doi: 10.1002/fuce.201900153.
[133] M. Ilic and D. Maksimovic, "Averaged Switch Modeling of the Interleaved Zero Current Transition Buck Converter," in *2005 IEEE 36th Power Electronics Specialists Conference*, Jun. 2005, pp. 2158–2163. doi: 10.1109/PESC.2005.1581931.
[134] M. Ilic and D. Maksimovic, "Interleaved Zero-Current-Transition Buck Converter," *IEEE Trans. Ind. Appl.*, vol. 43, no. 6, pp. 1619–1627, Nov. 2007, doi: 10.1109/TIA.2007.908175.
[135] S. M. Collura *et al.*, "Design and experimental validation of a high voltage ratio DC/DC converter for proton exchange membrane electrolyzer applications," *Int. J. Hydrog. Energy*, vol. 44, no. 14, pp. 7059–7072, Mar. 2019, doi: 10.1016/j.ijhydene.2019.01.210.
[136] V. Guida, D. Guilbert, and B. Douine, "Candidate Interleaved DC-DC Buck Converters for Electrolyzers: State-of-the-Art and Perspectives," in *2018 IEEE International Conference on Environment and Electrical Engineering and 2018*

IEEE Industrial and Commercial Power Systems Europe (EEEIC / I CPS Europe), Jun. 2018, pp. 1–6. doi: 10.1109/EEEIC.2018.8494457.
[137] D. Concha, H. Renaudineau, M. S. Hernández, A. M. Llor, and S. Kouro, "Evaluation of DCX converters for off-grid photovoltaic-based green hydrogen production," *Int. J. Hydrog. Energy*, vol. 46, no. 38, pp. 19861–19870, Jun. 2021, doi: 10.1016/j.ijhydene.2021.03.129.
[138] F. Blaabjerg, *Control of power electronic converters and systems. Volume 3 Volume 3*. 2021. Accessed: Feb. 12, 2022. [Online]. Available: http://www.vlebooks.com/vleweb/product/openreader?id=none&isbn=9780128194331
[139] M. Phattanasak, *Introduction to Switching Converters: Modeling and Nonlinear Control Techniques*, First edition. King Mongkut's University of Technology North Bangkok Textbook Publishing Center, 2018.
[140] E. Monmasson, Ed., *Power electronic converters: PWM strategies and current control techniques*. London : Hoboken, NJ: ISTE ; Wiley, 2011.
[141] B. Yodwong, D. Guilbert, W. Kaewmanee, M. Phattanasak, M. Hinaje, and G. Vitale, "Modified Sliding Mode-Based Control of a Three-Level Interleaved DC-DC Buck Converter for Proton Exchange Membrane Water Electrolysis," in *2021 Research, Invention, and Innovation Congress: Innovation Electricals and Electronics (RI2C)*, Sep. 2021, pp. 221–226. doi: 10.1109/RI2C51727.2021.9559790.
[142] E. Jamshidpour, P. Poure, E. Gholipour, and S. Saadate, "Single-Switch DC–DC Converter With Fault-Tolerant Capability Under Open- and Short-Circuit Switch Failures," *IEEE Trans. Power Electron.*, vol. 30, no. 5, pp. 2703–2712, May 2015, doi: 10.1109/TPEL.2014.2342878.
[143] "https://www.rohm.com/products/mosfets/high-voltage/nch-200-to-250v/rcx700n20-product."
[144] "https://www.onsemi.com/pdf/datasheet/rurg8060-d.pdf."
[145] "https://megatron.ch/infocenter/FXC_HB2013.pdf."
[146] P. Thounthong, "Conception d'une source hybride utilisant une pile à combustible et des supercondensateurs," These de doctorat, Vandoeuvre-les-Nancy, INPL, 2005. Accessed: Mar. 21, 2022. [Online]. Available: https://www.theses.fr/2005INPL113N
[147] "https://www.lem.com/sites/default/files/products_datasheets/lv_25-p.pdf."
[148] "https://www.lem.com/sites/default/files/products_datasheets/la_55-p_e.pdf."
[149] H. P. C. Buitendach, R. Gouws, C. A. Martinson, C. Minnaar, and D. Bessarabov, "Effect of a ripple current on the efficiency of a PEM electrolyser," *Results Eng.*, vol. 10, p. 100216, 2021, doi: https://doi.org/10.1016/j.rineng.2021.100216.
[150] F. Parache *et al.*, "Impact of Power Converter Current Ripple on the Degradation of PEM Electrolyzer Performances," *Membranes*, vol. 12, no. 2, Art. no. 2, Feb. 2022, doi: 10.3390/membranes12020109.